The Dissertation Committee for Nathan Alan Simmons
certifies that this is the approved version of the following dissertation:

MANTLE HETEROGENEITY AND FLOW

FROM SEISMIC AND GEODYNAMIC CONSTRAINTS

Committee:

____

Stephen Grand, Supervisor

____

Alessandro Forte

____

Clark Wilson

____

Robert Tatham

____

Jay Pulliam

MANTLE HETEROGENEITY AND FLOW
FROM SEISMIC AND GEODYNAMIC CONSTRAINTS

by

Nathan Alan Simmons, B.S.; M.S.

Dissertation

Presented to the Faculty of the Graduate School of
the University of Texas at Austin
in Partial Fulfillment
of the Requirements
for the Degree of

Doctor of Philosophy

The University of Texas at Austin

May 2007

Acknowledgments

I would like to thank Steve Grand for his generous and unyielding support. None of this work would have been possible without his remarkable insight into the problems regarding the Earth and willingness to send me around the world to learn new things.

Most of the work presented here was the result of a close collaborative effort with Alessandro Forte to whom I owe great gratitude for sharing his brilliant ideas and allowing me to act on them.

My beautiful wife, Marie, provided much needed encouragement and emotional support when things seemed untenable. I couldn't have made it without her.

MANTLE HETEROGENEITY AND FLOW FROM SEISMIC AND GEODYNAMIC CONSTRAINTS

Publication No. ________

Nathan Alan Simmons, Ph.D.
The University of Texas at Austin, 2007

Supervisor: Stephen Grand

I have developed 3-D models of mantle heterogeneity that satisfy seismic and geodynamic observations. The seismic constraints include body wave travel times of multi-bounce mantle and core shear waves. The geodynamic constraints include the Earth's gravity field, dynamic surface topography, tectonic plate motions and the excess ellipticity of the core-mantle boundary. These geodynamic observations are directly dependent upon density perturbations in the mantle which are the driving force of mantle flow. Furthermore, the effect of density anomalies on these geodynamic observables is dependent upon the viscosity of the mantle and whether or not there are boundaries to vertical flow within the mantle. Assuming a linear relation between seismic velocity and density, I tested several hypotheses for how the mantle convects by jointly inverting the seismic and geodynamic data. The data were best fit by a model assuming whole mantle convection with no internal layers that strongly inhibit vertical flow.

The simultaneous inversion of seismic and geodynamic observations requires knowledge of the link between seismic velocity and density perturbations in the mantle. Therefore, I have tested several radially-symmetric profiles of density-velocity scaling from mineral physics studies which assume that all lateral heterogeneity is generated by lateral temperature variations. Integration of the optimum density-velocity conversion profile into the joint modeling framework has yielded mantle-scale models of seismic velocity and thermally-induced density perturbations. These models satisfy the combined dataset to a reasonably high degree implying that variations of temperature are the primary cause of mantle seismic heterogeneity outside of the roots of continental cratons. Using inversion techniques, I have also found a 3D density-velocity relationship in the mantle thereby revealing density perturbations associated with compositional variability. Compositional buoyancy of the cratons is clearly detected and intrinsically-dense material is found within the mid-mantle extension of the rising African superplume structure. This high-density component within the superplume hinders the buoyancy of the structure and possibly redirects the flow within. Collectively, these models yield a better understanding of the dynamics of the mantle.

Table of Contents

Chapter 1

Introduction

1.1 Seismic Tomography and mantle flow

Earthquake-generated seismic waves that travel through the Earth provide the most direct information available on the structure of the interior of our planet. Therefore, measurements of these waves recorded at the surface provide a means to understand the Earth's internal makeup and evolution. Seismic tomography is the process of 3-D spatial mapping of seismic properties (most often wave velocity) using these surface observations. The first attempts at developing 3-D global images of seismic velocity in the upper mantle were done by *Woodhouse & Dziewonski* (1984) and in the lower mantle by *Dziewonski* (1984). Since these early studies, several techniques and datasets have been developed to compute global seismic tomographic images. These techniques include simple travel time tomography where expected arrival times for particular seismic phases are compared to the measured travel times thus generating "travel time residuals". The inversion of the travel time residuals is often performed assuming the time of arrival of a wave is only sensitive to velocity along a curvilinear ray path through the mantle (e.g. Grand 2002). However, some recent approaches involve "finite frequency" analysis where the energy is not assumed to travel along simple ray paths but rather along a three-dimensional kernel (e.g. Montelli *et al*. 2004). Even more sophisticated approaches involve full waveform inversion where complete time series are modeled rather than just arrival times of particular seismic phases. Romanowicz (2003) reviews the recent progress of global seismic tomography with particular emphasis on full waveform inversion.

Most global compressional wave (*P*) and shear wave (*S*) tomography studies show several common large-scale features. These include higher than average *P* and *S* velocities beneath old cratons to depths of at least 200 km. Most models also show large fast seismic anomalies at depths near 600 km associated with western Pacific subduction zones. Within the lower mantle several linear high velocity anomalies are seen that can be geographically related to past subduction locations beneath the Americas and southern Asia; but their continuity through the lower mantle is variable. Finally, in the deepest lower mantle, two large scale slow anomalies are observed beneath the southwest Pacific Ocean and Africa that broaden with depth to the base of the mantle. Although global seismic tomography models show many common features, they still differ significantly in detail and it is still unclear what these images are telling us about the dynamics and evolution of the Earth as a whole. This is due to the non-uniqueness of the seismic problem and also the difficulty in interpreting the seismic anomalies in terms of thermal and compositional variations. Therefore, a number of fundamental questions remain unresolved. For example, we do not know whether the mantle flows continuously from shallow depths to the core-mantle boundary (whole-mantle convection) or if there are boundaries within the mantle restricting mass transport. Such boundaries could be generated by compositional layering, high pressure phase transitions, or changes in rock properties with depth such as viscosity and thermal expansivity. Based on seismic tomography, arguments can be made for both whole-mantle and bounded flow scenarios.

Grand et al. (1997) and *van der Hilst et al*. (1997) have interpreted the linear high-velocity anomalies in the lower mantle beneath the Americas and southern Asia as sinking lithosphere. Parts of these anomalies appear to extend to the core-mantle boundary (CMB). Moreover, the correlation of high-velocity zones at the base of the mantle with regions of ancient subduction suggests that plates may descend through the entire mantle and form slab graveyards near the CMB (Richards & Engebretson 1992). This interpretation implies that material descends across the entire mantle and thus whole-mantle convection occurs in the Earth. However, there are concerns that the apparent slabs in the lower mantle seen in tomographic images may be artifacts produced by sampling and processing problems in the inversions (Hamilton 2002). Furthermore, there are many present day subduction zones that do not appear to have lower mantle fast seismic anomalies associated with them as might be expected. Specifically, along the western Pacific, subducted slabs appear to be strongly inhibited near 670 km depth which marks the depth of the deepest earthquakes. This is also the depth where the dissociation of the spinel phase to perovskite and magnesiowustite is known to occur. It is unclear whether this is a temporary phenomenon or whether this is demonstrating permanent layered mantle flow. In addition to a boundary to flow near 670 km, boundaries to flow at other depths within the mantle have been proposed. For example, *Fukao et al*. (2001) propose that a boundary to flow exists near ~1000 km depth. Their proposal is primarily based upon the evaluation of tomographic images of western Pacific subduction zones that show high velocity anomalies to varying depths but never below about 1000 km. However, it has also been suggested that these apparent slab extensions beneath the upper-lower mantle boundary are due to conductive cooling of the mantle below a stagnant slab lying at the base of the upper mantle (Čižková *et al*. 1999).

Seismic studies have also concluded that the lower ~1000 km of the mantle has complex seismic characteristics including anti-correlation of wave speeds and density (e.g. Ishii & Tromp 1999; Masters *et al*. 2000; Trampert *et al*. 2004). These studies have led to the idea that the deepest mantle is chemically-distinct from the overlying mantle implying yet another boundary to flow well within the lower mantle (Kellogg *et al*. 1999; Van der Hilst & Karason 1999). However, these conclusions are primarily based upon joint modeling of *P* and *S* waves that have very different sampling of the deep mantle or the study of normal mode splitting functions that result in very long-wavelength heterogeneity models. These models may satisfy the constraints considered within each of the studies but suffer from the non-uniqueness of the inversion problem.

One of the most notable features in the deep Earth is known as the "African superplume". The African superplume is a large, seismically-slow anomaly from the base of the mantle to mid-lower mantle depths that may be responsible for the uplift of the southern African continent (Lithgow-Bertelloni & Silver 1998; Gurnis *et al*. 2000). The superplume is characterized by slow shear (*S*) wave speeds and exhibits some complex seismic characteristics (Ritsema *et al*. 1998, 1999; Ishii & Tromp 1999; Masters *et al*. 2000; Ni *et al*. 2002; Ni & Helmberger 2003a,b). For instance, detailed waveform analyses have revealed that the superplume possesses very abrupt wave speed reductions near its boundaries which may suggest strong compositional variations (Ni *et al*. 2002; Ni & Helmberger 2003a,b). However, the density variations associated with this anomaly are difficult to determine using seismic information alone and therefore its role in Earth dynamics is debatable. Figure 1.1 illustrates some of the dynamically-significant features detected by seismic waves discussed above.

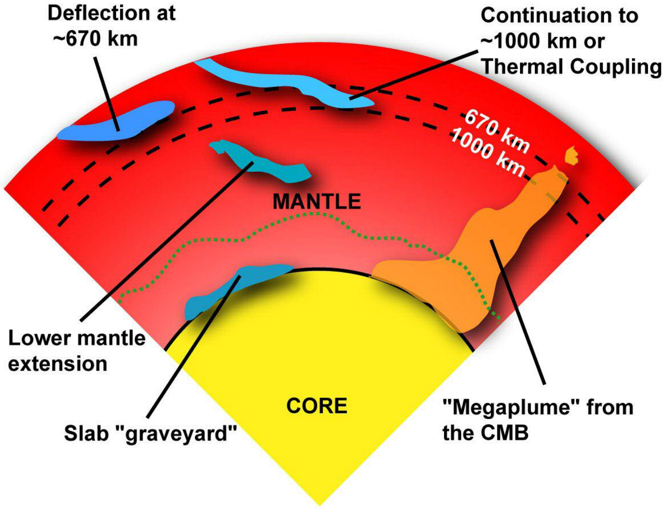

Figure 1.1 Dynamically-significant features detected by seismic waves including possible subducted slabs deflected at the upper-lower mantle boundary and in the lower mantle (blue).

1.2 Inclusion of geodynamic constraints

It is clear that our knowledge of the composition of the mantle and the dynamics of mantle convection are still uncertain. This reveals the limitations of directly interpreting seismic tomography images for mantle flow and compositional variations. To address these issues, we need to consider constraints that are directly related to mantle flow beyond just seismic observations. For instance, the Earth's gravity field, as determined by satellite altimetry, is a direct result of density perturbations in the mantle which are the driving force behind mantle flow. In addition, surface topography not associated with crustal thickness variations (dynamic topography) is also directly related to the flow in the mantle acting to deflect the Earth's surface. Similarly, the motion of tectonic plates and the bulge of the core-mantle boundary are direct results of flow within the mantle. *Richards & Hager* (1984) and *Ricard et al*. (1984) showed that calculating the Earth's gravity field, dynamic topography, and plate motions from a given distribution of density within the mantle depends on the viscosity structure of the mantle as well as whether there exist barriers to flow. Figure 1.2 shows the connection of a buoyant deep mantle density anomaly to the gravity, topography and plate motions. The buoyant anomaly creates a flow field within the mantle that perturbs boundary layers. In this case, viscous stresses cause an uplift of the surface that in turn creates a positive gravity signal over a region underlain by a low density anomaly. If a barrier to vertical flow existed within the model shown in Figure 1.2, the surface uplift would be greatly reduced and this would significantly change the gravity field as well as the other observables. Thus if seismic tomography could give a detailed model of the density structure of the mantle, the observed gravity, dynamic topography, and plate motions could directly place constraints on the nature of mantle flow.

In this thesis, I have performed joint inversions of seismic and geodynamic data to place constraints on the dynamics and chemical composition of the mantle. Firstly, I have updated the travel time dataset presented in *Grand* (2002) and used a new algorithm to produce a shear-wave model of the entire mantle (Chapter 2). The data consist of globally distributed shear body wave travel times including multi-bounce

S-waves, shallow-turning triplicated phases, as well as core reflections and phases traversing the outer core (*SKS* and *SKKS*).

In chapter 3, I present results from simultaneous inversions of the seismic dataset and several flow-related geodynamic observations. The convection-related datasets include global free air gravity, tectonic plate divergence, dynamic surface topography and the excess ellipticity of the core-mantle boundary. The geodynamic observables are linearly related to mantle density perturbations by theoretical, wavelength-dependent kernel functions that represent the viscous flow response of the mantle to internal density loads (Richards & Hager 1984; Ricard *et al*. 1984; Forte & Peltier 1987). Therefore, by defining a link between seismic velocity and density perturbations, we are able to solve for a single density/velocity model that best reconciles all the observations. Fortunately, the geodynamic kernel functions are also strongly dependent upon the style of mantle flow assumed. Therefore, I have directly tested whole-mantle versus layered-mantle flow scenarios in the framework of joint seismic-geodynamic inversion. In this particular analysis, we optimized the scaling factor between velocity and density for each of the models tested (Chapter 3).

Since simultaneously solving seismic and geodynamic datasets requires knowledge of how density and seismic velocity are related, it is important to examine this connection in detail. In chapters 4 and 5, I examine the effect of velocity-density scaling on the results of joint inversion. First, I tested several mineral physics predictions for velocity-density scaling under the assumption that seismic anomalies are due solely to temperature anomalies. I then looked at deviations in the thermal scaling relationships in 3-D to include “non-thermal” effects. In doing so, I estimated the relative contributions of thermal and compositional variations to mantle heterogeneity (Chapter 5). I find chemically-distinct regions in the shallow mantle beneath cratons as well as within the African superplume anomaly in the deep mantle. Using the detailed image of the density and velocity structure of the African superplume region, I discuss the role of the superplume in the dynamics and evolution of the mantle (Chapter 4).

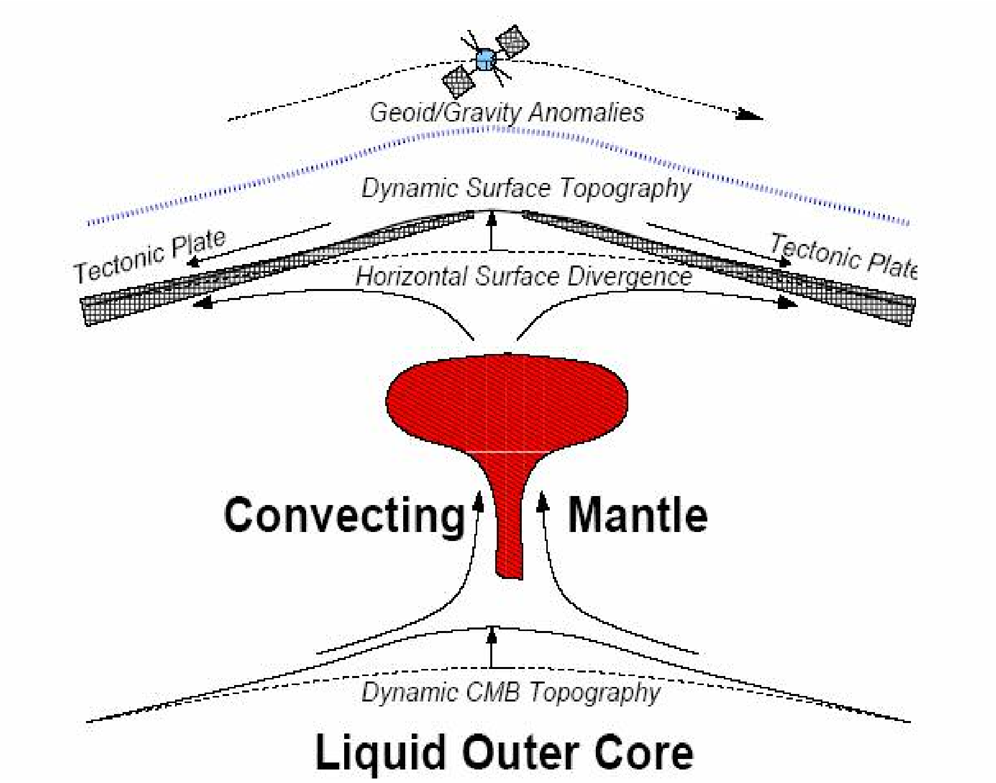

Figure 1.2 Schematic depiction of the effect of a large-scale upwelling on several geodynamic observations. In a viscous Earth, a low-density upwelling deflects boundaries both above and below. In this case, the surface is pushed upward creating dynamic topography and the core-mantle boundary is similarly deflected. These deflections along with the low-density anomaly itself combine to create the total gravity field. As the upwelling reaches the surface, flow is dominant in the lateral direction thereby forcing tectonic plates apart. If a boundary to flow exists at some depth within the mantle (not shown), the new boundary would be deflected in response to the upwelling providing for entirely different observations.

1.3 References

Čižková, H. O. Čadek, A.P. Van den Berg & N.J. Vlaar (1999), Can lower mantle slab-like seismic anomalies be explained by thermal coupling between the upper and lower mantles?, *Geophys. Res. Lett. 26*, 1501-1504.

Dziewonski, A.M. (1984), Mapping the lower mantle: determination of lateral heterogeneity in P velocity up to degree and order 6, *J. Geophys. Res.*, *89*, 5929-5952.

Forte, A.M. & W.R. Peltier (1987), Plate tectonics and aspherical Earth structure; the importance of poloidal-toroidal coupling, *J. Geophys. Res. 92*, 3645-3679.

Fukao, Y., S. Widiyantoro, M. Obayashi (2001), Stagnant slabs in the upper mantle transition region, *Rev. Geophys. 39*, 291-323.

Grand, S.P., R.D. Van der Hilst & S. Widiyantoro (1997), Global seismic tomography: a snapshot of convection in the Earth, *GSA Today*, *7*, 1-7.

Grand, S.P. (2002), Mantle shear-wave tomography and the fate of subducted slabs, *Phil. Trans. R. Soc. Lond. A*, *360*(1800), 2475-2491.

Gurnis, M., J.X. Mitrovica, J. Ritsema & H.J. Van Heijst (2000), Constraining mantle density structure using geological evidence of surface uplift rates: The case of the African Superplume, *Geochem. Geophys. Geosys.*, *1*(7), doi: 1999GC000035.

Hamilton, W.B. (2002), The closed upper-mantle circulation of plate tectonics, in S. Stein, J.T. Freymueller (Eds.), Plate Boundary Zones, AGU, Washington, DC, pp. 359-410.

Ishii, M. & J. Tromp (1999), Normal-mode and free-air gravity constraints on lateral variations in velocity and density of Earth's mantle, *Science*, *285*(5431), 1231-1236.

Kellogg, L.H., B.H. Hager & R.D. Van der Hilst (1999), Compositional stratification in the deep mantle, *Science*, *283*(5409), 1181-1184.

Lithgow-Bertelloni, C. & P.G. Silver (1998), Dynamic topography, plate driving forces and the African superswell, *Nature*, *395*(6699), 269-272.

Masters, G., G. Laske, H. Bolton & A.M. Dziewonski (2000), The relative behavior of shear velocity, bulk sound speed, and compressional velocity in the mantle: implications for chemical and thermal structure, *in Earth's Deep Interior: Mineral Physics and Tomography from the Atomic to the Global Scale*, edited by S.-I. Karato et al., pp. 63-87, AGU, Washington, DC.

Montelli, R., G. Nolet, F.A. Dahlen, G. Masters, R.E. Engdahl & S.H. Hung (2004), Finite-frequency tomography reveals a variety of plumes in the mantle, *Science*, *303*, 338-343.

Ni, S.D., E. Tan, M. Gurnis & D.V. Helmberger (2002), Sharp sides to the African superplume, *Science*, *296*(5574), 1850-1852.

Ni, S.D. & D.V. Helmberger (2003a), Ridge-like lower mantle structure beneath South Africa, *J. Geophys. Res. Solid Earth*, *108*(B2), doi:10.1029/2001JB001545.

Ni, S.D. & D.V. Helmberger (2003b), Seismological constraints on the South African superplume; could be the oldest distinct structure on Earth, *Earth Planet. Sci. Lett.*, *206*(1-2), 119-131.

Richards, M.A. & B.H. Hager (1984), Geoid anomalies in a dynamic earth, *J. Geophys. Res. Solid Earth*, *89*(B7), 5987-6002.

Ricard, Y., L. Fleitout & C. Froidevaux (1984), Geoid heights and lithospheric stresses for a dynamic Earth, Ann. *Geophys. 2*, 267-286.

Richards, M.A. & D.C. Engebretson (1992), Large-scale mantle convection and the history of subduction, *Nature 355*, 437-440.

Ritsema, J., S. Ni, D.V. Helmberger & H.P. Crotwell (1998), Evidence for strong shear velocity reductions and velocity gradient in the lower mantle beneath Africa, *Geophys. Res. Lett.*, *25*(23), 4245-4248.

Ritsema, J., H.J. Van Heijst & J.H. Woodhouse (1999), Complex shear wave velocity structure imaged beneath Africa and Iceland, *Science*, *286*(5446) 1925-1928.

Romanowicz, B. (2003) Global mantle tomography: progress status in the last 10 years, *Ann. Rev. Earth Plan. 31*, 303-328.

Trampert, J., F. Deschamps, J. Resovsky & D. Yuen (2004), Probabilistic tomography maps chemical heterogeneities throughout the lower mantle, *Science*, *306*(5697), 853-856.

Van der Hilst, R.D., S. Widiyantoro & E.R. Engdahl (1997), Evidence for deep mantle circulation from global tomography, *Nature*, *386*, 578-584.

Van der Hilst, R.D. & H. Kárason (1999), Compositional heterogeneity in the bottom 1000 kilometers of the Earth's mantle: Toward a hybrid convection model, *Science*, *283*, 1885-1888.

Woodhouse, J.H. & A.M. Dziewonski (1984), Mapping the upper mantle; three-dimensional modeling of Earth structure by inversion of seismic waveforms, *J. Geophys. Res.*, *89*, 5953-5986.

Chapter 2

Shear-wave Tomography Model of the Mantle

2.1 Introduction

A multitude of tomographic models using a variety of data types and methodologies have provided evidence of significant seismic heterogeneity in the mantle (e.g. Robertson & Woodhouse 1996; Grand *et al*. 1997; Su & Dziewonski 1997; van der Hilst *et al*. 1997; Ritsema *et al*. 1999; Karason & van der Hilst 2000; Masters *et al*. 2000; Megnin & Romanowicz 2000; Gu *et al*. 2001; Zhao 2001; Grand 2002; Ishii & Tromp 2004; Kennett & Gorbatov 2004; Montelli *et al*. 2004; Panning & Romanowicz 2005). Data sets include travel times supplied by the International Seismic Center (ISC) which consists of millions of data points. The bulk of the ISC data consists of *P*-wave travel times that allow for high-resolution images in well-sampled zones. However, the sampling distribution of the ISC data set is limited in parts of the mantle due to the distribution of earthquakes and seismic stations. Other data sets consist of hand-picked travel time measurements as well as data extracted from waveforms. Information extracted from waveforms include surface wave dispersion estimates that provide significant constraints on upper mantle heterogeneity and normal mode splitting functions that constrain the long-wavelength velocity and density heterogeneity throughout the mantle.

Even with the wide variety of data used and the techniques developed to exploit the data, several large-scale features are detected in all recent models of mantle heterogeneity. However, details including the overall shape, intensity and depth extent of some anomalies differ amongst the models. Also, the inherent non-uniqueness of the problem has left the door open for a variety of interpretations of the features visible in existing tomographic images. Therefore, there is still no consensus on the composition and dynamics of the Earth's deep interior and many fundamental questions remain unanswered such as: Do subducted slabs reach the base of the mantle? Where are rising plumes/hotspots initialized? Are there large-scale primitive geochemical reservoirs in the mantle, and if so, where are they?

Improvements to the existing mantle heterogeneity models are required to address these fundamental issues. One way to improve existing tomographic models is the addition of more data to reduce the non-uniqueness of the solutions. This is well within our grasp given the ever-increasing volume of available seismic data recorded at broadband seismic stations around the world. Therefore, I have made additions to the data set of shear body wave travel time residuals described in *Grand* (2002) and developed new techniques to calculate travel times and model the data in the framework of travel time tomography.

Travel time tomography involves calculating the difference between observed seismic wave arrival times and predicted times based on a standardized model, thus generating a data set of travel time residuals. An individual travel time residual can be expressed as:

$$\mathit{residual} = \delta t = \int_{P_a} \frac{\mathrm{d}\mathbf{p}}{v_a(\mathbf{p})} - \int_{P_s} \frac{\mathrm{d}\mathbf{p}}{v_s(\mathbf{p})} = \int_{P_a} s_a \mathrm{d}\mathbf{p} - \int_{P_s} s_s \mathrm{d}\mathbf{p} \tag{2.1}$$

v_a and v_s are the actual (subscript *a*) and starting (subscript *s*) seismic model velocities which are integrated over their corresponding ray paths (P_a and P_s respectively). The seismic velocities can be converted to slowness to attain a simple linear form (i.e. $s_a = 1/v_a$). The starting seismic velocity model is often one-dimensional and the actual model (to be determined) is three-dimensional. In theory, the seismic ray path is a function of the velocity structure itself. However, the time differences due to path changes are of second order and negligible based on Fermat's principle (Aki *et al.* 1977). Therefore, we can approximate Equation 2.1 in the following way:

$$\delta t = \int_P (s_a - s_s)\mathrm{d}\mathbf{p} \tag{2.2}$$

where the path is now assumed to be identical to that predicted for the starting model. The model space can be broken into blocks where we assume that the deviation from the starting model is uniform within each block. The integral in Equation 2.2 can then be written in a discrete form:

$$\Delta t = \sum_{j=1}^{N} l_j \Delta s_j \tag{2.3}$$

where the summation is over all discretized blocks in the model space (*N* number of blocks). l_j and Δs_j are the ray path length and the differential seismic slowness in model block number *j*, respectively. Considering all measured residual times, we can develop a system of linear equations:

$$\Delta t_i = \sum_{j=1}^{N} l_{ij}\Delta s_j \Rightarrow \begin{bmatrix} \Delta t_1 \\ \cdot \\ \cdot \\ \Delta t_M \end{bmatrix} = \begin{bmatrix} l_{11} & \cdot & \cdot & l_{1N} \\ \cdot & \cdot & & \cdot \\ \cdot & & \cdot & \cdot \\ l_{M1} & \cdot & \cdot & l_{MN} \end{bmatrix} \begin{bmatrix} \Delta s_1 \\ \cdot \\ \cdot \\ \Delta s_N \end{bmatrix} \tag{2.4}$$

where *i* is the residual number and *j* is the model block number. *M* and *N* are the total number of measured residuals and the total number of parameterized blocks, respectively. The arrays in Equation 2.4 can be written in a more compact matrix form:

$$\mathbf{Lm} = \mathbf{r} \tag{2.5}$$

In Equation 2.5, **L** is the Fréchet kernel matrix (ray path lengths) and **r** is a vector containing all residual travel times (measurements). The vector **m** is the 3-D differential seismic slowness model to be determined using matrix inversion techniques. In the following sections, I describe the data as well as the measurement and modeling procedures used to obtain an updated mantle-scale tomographic model of shear-wave velocity perturbations. I also point out some of the major features observed in the final model and what they might be telling us about the evolution and dynamics of the Earth's interior.

2.2 Seismic networks and earthquakes

Seismic waveforms recorded at a large number of globally-distributed seismic stations and networks (permanent, semi-permanent and temporary arrays) have been evaluated and are included in the data set. The networks include:

World Wide Standardized Seismographic Network (WWSSN)
    A globally-distributed cold-war era network primarily used in the detection of nuclear weapons testing in the 1960's.
Global Seismographic Network (GSN)
    A globally-distributed network of ~128 permanent broadband stations managed by the Incorporated Research Institutions for Seismology (IRIS) consortium.
GEOSCOPE
    A globally-distributed network of 30+ permanent broadband stations managed by the Institut de Physique du globe de Paris, France.
Canadian National Seismic Network (CNSN)
    Permanent broadband network of stations throughout Canada.
Temporary Arrays
    LaRistra (Texas-New Mexico-Arizona-Utah line), Kaapvaal (southern African continent), Tanzania, Ethiopia, Patagonia, and others.

Ground motion data recorded at all stations in the network are publicly available via internet or emails requests submitted to the IRIS data management center (DMC) which is a centralized data depot funded by the National Science Foundation (NSF). See the website http://www.iris.edu/data/ for the latest data request methods.

A map of all broadband seismic stations used in this study is shown in Figure 2.1. I chose to evaluate data recorded at all available stations in the networks listed above from earthquakes occurring from April 20, 1997 through July 1, 1999 since this is the time span that the Kaapvaal temporary network existed. This was an important network of 54 broadband seismic instruments which occupied 82 different locations near the southern tip of the African continent. The array extended roughly along a SW-NE line almost 1800 km from Cape Town, South Africa to Masvingo, Zimbabwe and SE-NW nearly 600 km from Swaziland into eastern Botswana (Figure 2.2). The importance of this particular network is twofold: 1) stations were located within the southern hemisphere where data coverage is generally limited; and 2) waves recorded at these stations traversed the African superplume structure providing for improved constraints of this significant lower mantle feature which is known to possess extreme lateral velocity gradients and other complexities (e.g. Ritsema *et al*. 1998, 1999; Ishii & Tromp 1999; Masters *et al*. 2000; Ni *et al*. 2002, 2005; Ni & Helmberger 2003a,b). Figure 2.3 is a map of the earthquakes used in this study and Table 2.1 lists the earthquake parameters.

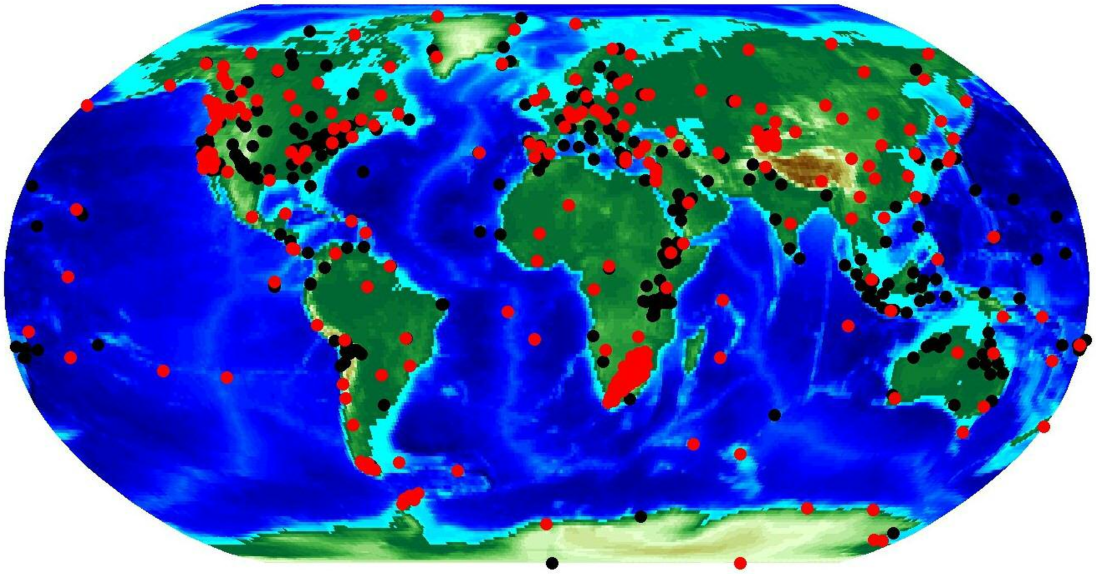

Figure 2.1 Seismic stations used in this study. The red dots are stations used for earthquakes occurring during the timeframe that the Kaapvaal array in southern Africa existed. The black dots are additional stations used in the generation of the previous data set.

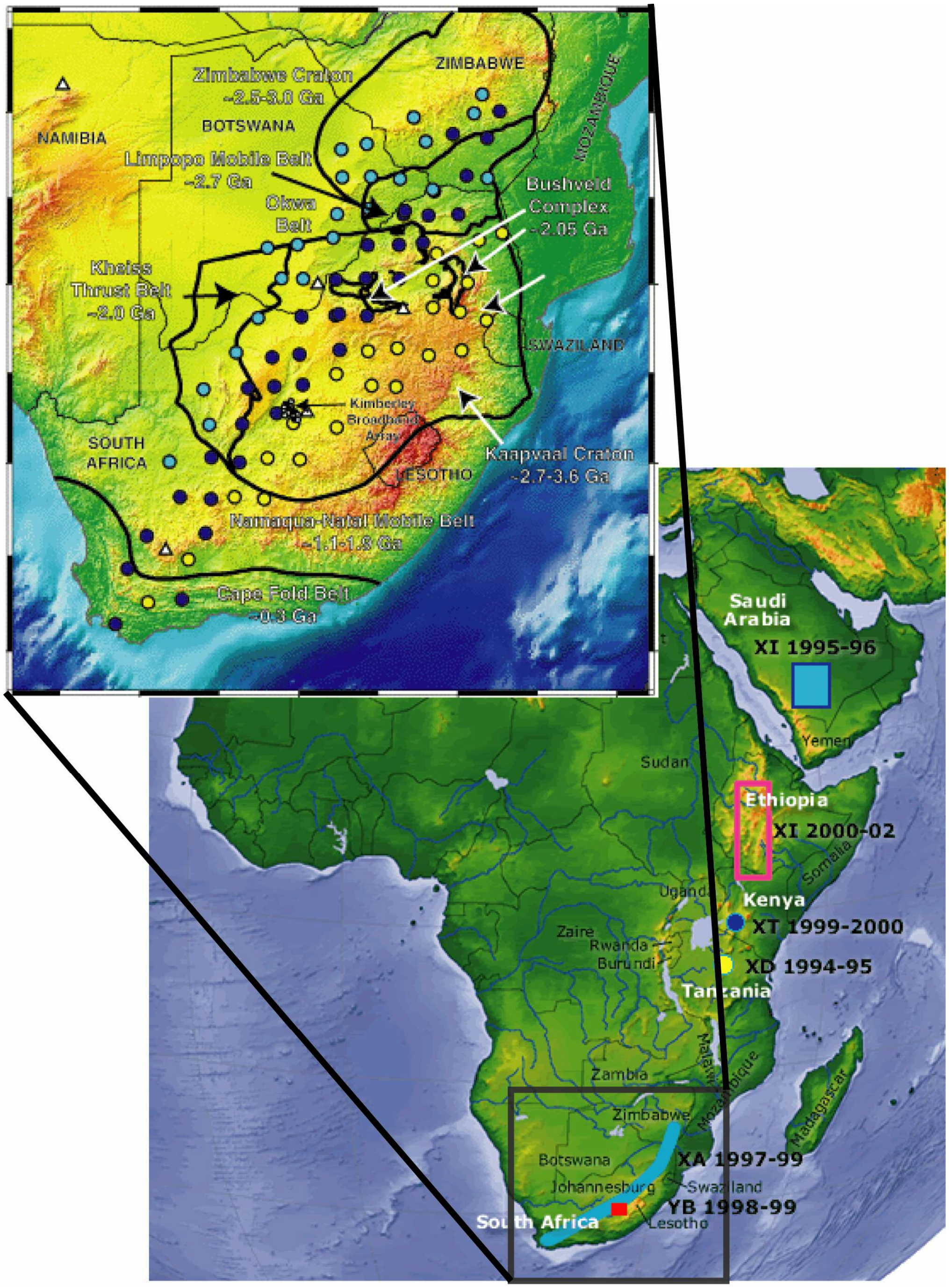

Figure 2.2 Detailed view of the Kaapvaal temporary deployment of broadband seismic stations. The array consisted of 54 instruments occupying 82 distinct locations from April 20, 1997 through July 1, 1999. Significant earthquakes occurring during this time frame were evaluated and added to the data set.

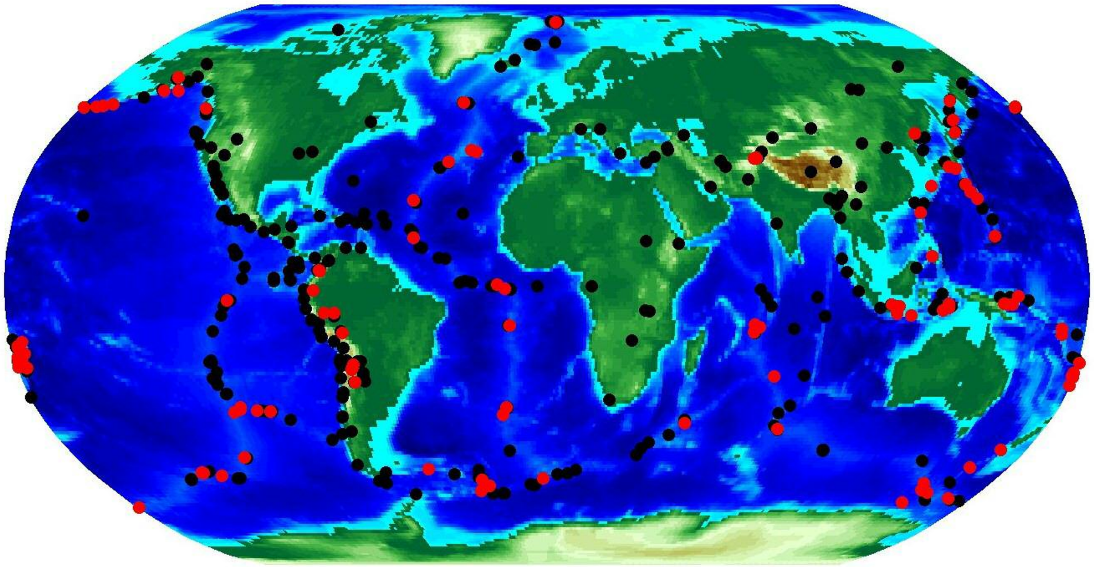

Figure 2.3 A plot of earthquake locations. Red dots mark the earthquakes that I evaluated and the black dots correspond to earthquakes used to develop the pre-existing data.

Table 2.1 List of earthquakes added

Month	Day	Year	Hour	Minute	Second	Latitude	Longitude	Depth (km)	Mw
5	8	97	13	29	24.6	51.72	-170.80	33	6.0
5	13	97	14	13	45.7	36.41	70.94	196	6.4
5	20	97	18	27	6.5	-59.71	150.49	10	5.9
5	27	97	6	10	31.7	-54.92	-136.17	10	6.1
5	29	97	17	2	38.7	-35.96	-102.51	10	6.5
6	10	97	21	53	55.0	-35.81	-108.14	10	6.5
6	11	97	9	29	23.4	-23.97	-177.51	164	5.8
6	17	97	21	3	40.2	51.35	-179.33	33	6.4
6	26	97	19	21	8.8	-49.69	-114.57	10	6.2
6	27	97	4	39	52.7	38.33	-26.68	10	5.9
7	11	97	9	55	12.6	-5.70	110.80	574.4	6.0
7	20	97	0	30	21.0	52.56	-167.48	14.4	6.1
7	20	97	10	14	22.8	-22.98	-66.30	256.1	6.1
8	15	97	7	37	49.1	-4.37	-105.70	10	6.2
8	20	97	13	51	16.6	-41.72	80.13	10	6.5
8	26	97	3	27	46.9	-58.44	-25.05	29	5.6
8	26	97	15	22	9.2	-25.51	178.33	609.6	5.7
9	2	97	12	13	22.9	3.85	-75.75	198.7	6.8
9	3	97	6	22	44.3	-55.19	-128.99	10	6.1
9	4	97	4	23	37.0	-26.57	178.34	624.7	6.8
9	4	97	20	52	58.3	-3.48	151.39	365.6	5.7
9	23	97	17	51	23.5	-65.53	178.81	10	5.8
9	25	97	14	20	48.9	-13.76	66.25	10	6.0
9	26	97	15	48	34.3	-5.39	128.99	253.8	6.1
10	5	97	18	4	30.0	-59.74	-29.20	273.9	6.3
10	8	97	10	47	49.9	-29.25	178.35	617.3	5.7
10	17	97	9	55	15.2	-57.54	147.97	10	6.2
10	17	97	15	2	0.5	-20.89	-178.84	578.9	6.0
10	23	97	1	16	1.8	-8.67	117.02	160	5.7
11	3	97	5	37	48.7	-20.40	-178.74	600	5.6
11	3	97	19	17	58.9	-6.74	129.02	215.6	6.1
11	15	97	7	5	16.6	43.81	145.02	161	6.1
11	28	97	22	53	41.5	-13.74	-68.79	586	6.7
12	11	97	7	56	28.9	3.93	-75.79	177.5	6.4
12	16	97	7	6	56.6	-62.88	163.19	10	5.9
12	17	97	4	38	51.5	51.19	178.87	20	6.6
12	17	97	5	51	29.2	36.39	70.77	207	6.3
12	20	97	13	26	31.6	53.42	152.76	613.8	5.9
12	22	97	2	5	50.1	-5.49	147.87	179.3	7.2
12	26	97	5	34	24.7	-22.34	-179.69	588.4	5.9

Table 2.1 (continued)

Month	Day	Year	Hour	Minute	Second	Latitude	Longitude	Depth (km)	Mw
12	27	97	20	11	1.3	-55.78	-4.22	10	6.2
1	3	98	6	10	8.4	-35.47	-16.19	10	6.3
1	14	98	2	37	3.8	-39.61	46.36	10	5.8
1	26	98	23	6	1.7	-47.51	165.18	33	5.9
1	27	98	2	14	12.9	-20.77	-179.18	642.8	6.0
1	27	98	19	55	1.2	-22.54	179.05	611	6.3
1	27	98	21	5	44.4	-22.41	179.04	610.1	6.5
1	31	98	23	30	42.0	-35.76	-97.06	10	6.0
2	7	98	1	18	59.5	24.82	141.75	525.3	6.4
2	16	98	23	53	19.7	52.72	-33.68	10	6.7
2	20	98	12	18	6.2	36.48	71.09	235.6	6.4
2	28	98	10	46	52.3	-14.42	167.35	184.9	5.8
2	28	98	17	38	48.6	33.46	138.12	291.4	5.7
3	8	98	0	35	42.2	20.58	122.14	157.5	5.7
3	21	98	16	33	11.0	79.89	1.86	10	6.2
3	21	98	18	22	28.5	36.43	70.13	227.8	5.9
3	22	98	1	8	57.5	-11.43	66.25	10	6.1
3	25	98	12	17	22.5	-63.61	147.94	10	6.4
3	25	98	21	2	55.7	-24.34	-66.99	197	5.6
3	29	98	7	14	59.0	-0.24	-17.93	10	6.1
4	1	98	21	37	50.2	35.38	-35.79	10	5.8
4	3	98	22	1	48.2	-8.15	-74.24	164.6	6.6
4	9	98	23	26	52.7	-12.24	67.85	10	5.8
4	10	98	16	40	38.6	-1.32	-15.65	10	6.2
4	14	98	3	41	22.3	-23.82	-179.87	498.6	6.1
4	27	98	23	51	35.7	-6.08	113.10	590.7	5.7
5	15	98	5	58	6.0	14.18	144.88	154.1	6.0
5	16	98	2	22	3.2	-22.23	-179.52	586.1	6.9
5	21	98	22	31	22.9	-43.40	41.39	10	6.3
5	23	98	17	44	47.8	8.14	123.73	657.8	6.0
6	1	98	7	35	50.4	33.94	136.09	398.5	5.9
6	16	98	9	35	11.9	-52.99	159.84	10	6.2
6	18	98	4	17	55.0	-11.57	-13.89	10	6.3
6	24	98	10	44	30.8	-37.29	-17.39	10	6.0
6	29	98	23	37	16.6	-60.35	153.14	10	6.3
7	9	98	5	19	7.3	38.65	-28.63	10	6.2
7	9	98	19	39	44.0	60.53	-153.22	144.8	6.2
8	5	98	12	54	25.7	-54.67	-135.52	10	6.2
8	20	98	6	40	55.8	28.93	139.33	440.5	7.1
8	20	98	15	0	8.1	51.62	175.25	33	6.2

Table 2.1 (continued)

Month	Day	Year	Hour	Minute	Second	Latitude	Longitude	Depth (km)	Mw
8	30	98	7	52	25.3	-23.93	-66.91	219.5	5.7
8	30	98	11	33	33.0	50.91	-130.66	10	6.1
9	7	98	0	39	30.2	-36.24	-97.71	10	6.1
9	12	98	9	3	48.3	-24.51	-67.12	187.2	5.6
9	14	98	4	43	28.9	-34.75	-107.98	10	6.1
9	14	98	23	16	46.8	51.62	-173.15	33	6.1
9	28	98	13	34	30.5	-8.19	112.41	151.6	6.6
10	1	98	3	41	13.1	13.74	-45.56	10	6.0
10	3	98	11	15	42.7	28.50	127.61	226.6	6.1
10	11	98	12	4	54.7	-21.04	-179.11	623.9	5.9
11	8	98	5	0	53.3	-7.26	127.08	263.2	5.7
11	24	98	23	54	46.1	-16.51	-174.75	223.2	6.0
12	10	98	8	21	14.5	-7.95	-71.42	649.4	5.5
1	12	99	2	32	25.6	26.74	140.17	440.6	5.9
1	16	99	10	44	39.5	56.23	-147.43	21	6.0
1	24	99	8	0	8.5	-26.46	74.48	10	6.3
1	25	99	10	37	13.5	-18.03	-178.45	640	5.8
1	27	99	8	9	1.9	-5.32	146.76	230	5.9
2	5	99	11	39	45.2	-12.62	166.97	213	5.9
2	5	99	14	37	53.0	47.51	147.16	407.4	5.9
4	5	99	11	8	4.0	-5.59	149.57	150	7.4
4	6	99	4	51	5.8	24.45	-46.37	10	5.8
4	8	99	13	10	34.1	43.61	130.35	565.7	7.1
4	9	99	12	16	1.9	-26.35	178.22	621.2	6.2
4	13	99	10	38	48.4	-21.42	-176.46	164.2	6.8
4	26	99	18	17	26.2	-1.65	-77.78	172.6	6.1
5	7	99	14	13	52.4	56.42	-152.94	20	6.2
5	11	99	1	0	40.9	-36.10	-110.64	10	6.0
5	25	99	16	42	5.3	-27.93	-66.93	169.3	5.8
6	9	99	4	5	44.5	-53.04	-46.84	10	5.8
6	19	99	9	3	9.1	-5.41	146.88	208.5	5.7
6	26	99	22	5	28.9	-17.96	-178.19	590.4	6.1

2.3 Seismic phases

I used primarily teleseismic, horizontally-polarized shear waves (*SH*) including all detectable surface reflected multiples: *Sn* and *ScSn* where $n = \{1,2,3,4,5\}$ denotes the number of surface reflections and *c* denotes a reflection from the core-mantle boundary (see Figure 2.4). The reason for focusing on *SH* phases is that they are not theoretically coupled to compressional seismic waves (*P*-waves). Therefore, *SH* phases are often clearly visible on the tangential component of the seismogram without significant *P*-wave interference. Additionally, *SH* energy is reflected from the core-mantle boundary without transmitting noteworthy energy into the Earth's outer core making them easily detectable (therefore measurable) at the surface. See Figure 2.5 for an example.

Horizontally-polarized depth phases including all surface multiples (*sSn*, *sScSn*) were also measured for earthquakes deep enough to have phase separation from the direct arrival (greater than about 70km depth). The energy associated with these phases initially travels upward from the source region to the Earth's surface where it is then reflected downward. The significance of these phases is not only do they sample the region above the source, but they also provide a means for locating the depth of the earthquake. See the following section for more discussion on this topic.

In addition to the teleseismic *SH* phases, the data set also contains the teleseismic phases: *SKS* and *SKKS*. *SKS* waves are vertically-polarized phases (*SV*; material displacement in the plane of the wave propagation direction) that travel through the mantle as *S*-waves, convert to *P*-waves in the outer core and return to the surface as *S*-wave energy. *SKKS* waves are similar to *SKS* waves except that they are reflected off the core-mantle boundary from below (Figure 2.4). These phases are detectable at long distances (greater than about 85 arc degrees) and travel nearly vertically through the mantle thereby providing sampling directly below earthquake zones and seismic stations down to the core-mantle boundary. The initial data set (provided by Steve Grand) also includes regional, shallow-turning *SH* phases and surface-reflected multiples that are triplicated due to sharp velocity increases associated with upper mantle phase transformations (Grand 1994). The importance of these complex shallow phases is increased lateral resolution of strongly-varying upper mantle structures that teleseismic body waves do not readily provide due to the general sparseness of station locations. The following sections outline the travel time measurement and inversion techniques used in this study.

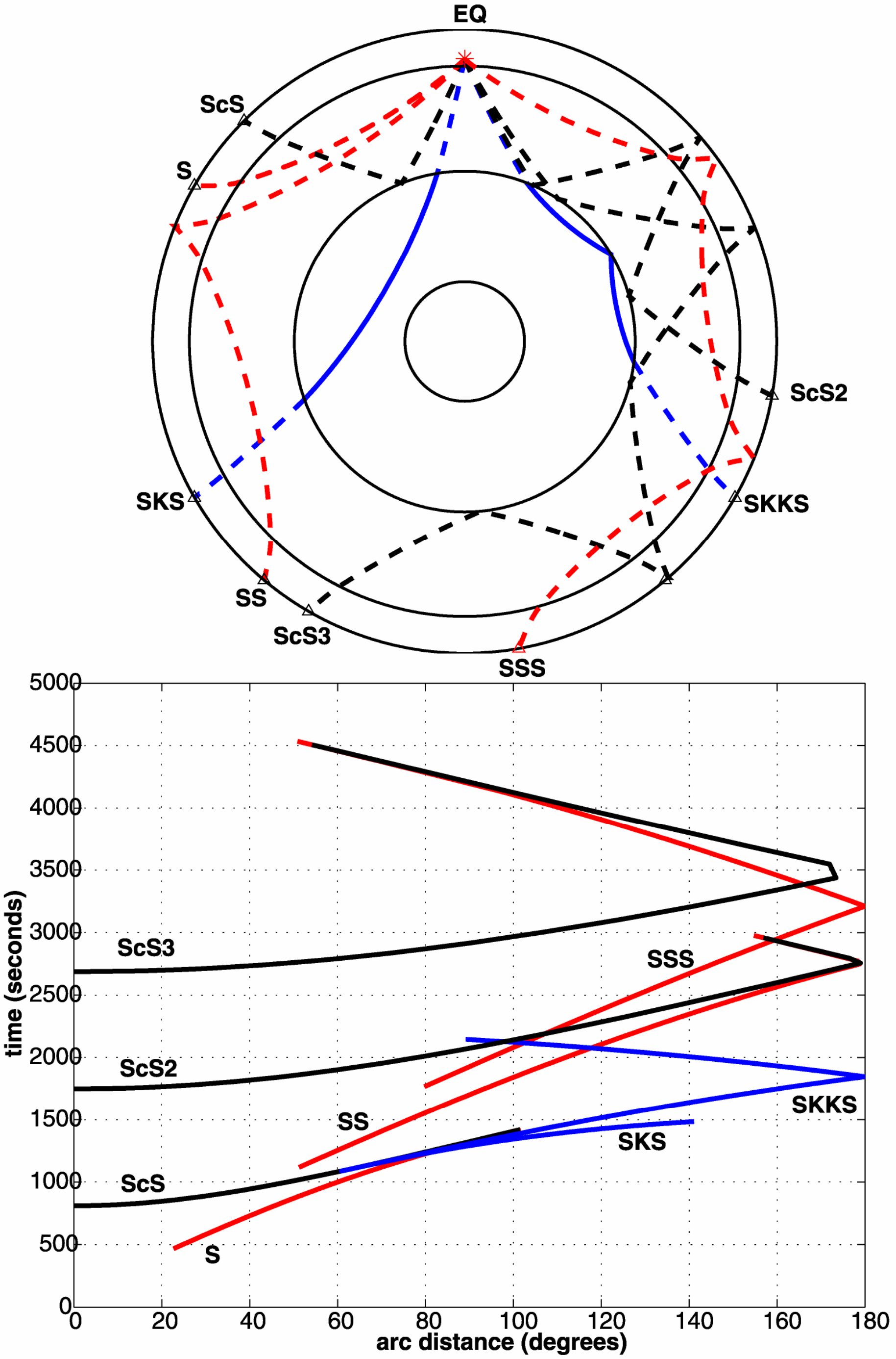

Figure 2.4 Ray paths (top) and travel times (bottom) for some of the teleseismic phases considered. These include direct *SH* waves (*S*), surface reflected multiples (i.e. *SS*) and waves converted to compressional (*P*) waves within the outer core (*SKS* and *SKKS*). Other phases including waves turning in the upper mantle and depth phases are not shown.

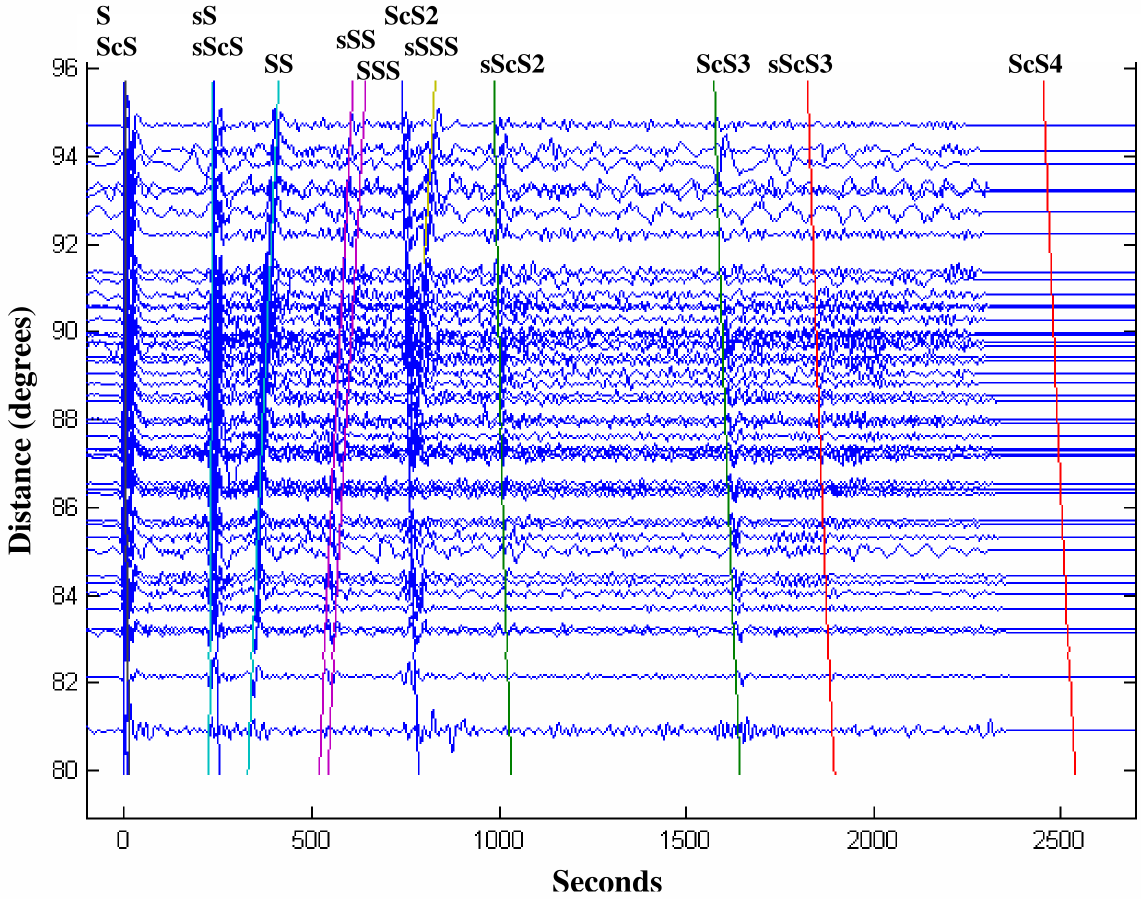

Figure 2.5 Data recorded at the Kaapvaal array in southern Africa (tangential component) after a 600-km deep earthquake occurred along the Peru-Bolivia border. The data are aligned with the *S* wave and the colored curves correspond to expected travel times based on the starting 1-D velocity model. Notice that many shear-wave multiples can easily be detected such as *SS* and *ScS3*. Measuring these multiples gives much better global coverage than simply using simpler phases such as *S* and *ScS*.

2.4 Travel time measurement

All deep earthquakes and mid-ocean ridge events occurring between April 20, 1997 and July 1, 1999 were examined (see Section 2.2). The data were initially decimated to 5 samples per second and rotated into radial and tangential components. The data were then band pass filtered to 0.01-0.07 Hz (14-100 second periods). Expected travel times for all possible measurable shear-wave phases were computed based upon a starting 1-D velocity model. The starting 1-D model consisted of the average TNA/SNA (Grand & Helmberger 1984) velocity model in the upper mantle and the PREM (Dziewonski & Anderson 1981) model in the lower mantle (Figure 2.6). Synthetic seismograms were computed using the WKBJ method (Chapman 1978) using the starting model. This synthetic seismogram technique is computationally efficient and, therefore, was used to generate synthetic waveforms for *S*, *SS*, *SKS* and *SKKS* phases for every event-receiver pair. The earthquake properties including event location, depth, origin time, focal mechanism and source duration were taken from the Harvard Centroid Moment Tensor (CMT) catalog (http://www.globalcmt.org/). The corresponding instrument response was convolved with the synthetic solution which was subsequently filtered the same as the data to allow for direct comparison with the seismogram.

A trapezoidal earthquake time function was determined based on the catalog's earthquake duration and trial-and-error by comparing the data and generated synthetics. For shallow earthquakes (such as mid-ocean ridge events), the earthquake duration and depth tradeoff due to the effects of the Earth's free surface. In these cases, I tried several time functions and source depths to determine the most likely set of properties by trial and error. These synthetic solutions were initially cross-correlated with the actual seismograms. Since the cross-correlation does not always perfectly align with the onset of the waveforms due to several factors including imperfect pulse widths, visual alignment in the time domain was used as needed (see Figure 2.7 for some examples). These time shifts (travel time residuals) are the difference between the predicted and actual travel time and act as the data to be inverted. Each measurement was given a numerical grade (integers 1-5) based on my confidence level (1 = *poor*, 5 = *excellent*) to form a basis for weighting the data in the inversion.

For earthquakes that had high signal-to-noise, I also generated full waveform synthetics using the reflectivity method (Fuchs & Muller 1971) considering only the tangential component of the seismogram (*SH* phases). The reflectivity method is a synthetic technique that generates full seismograms based on the principle of transmission and reflection recurrence relations for a layered Earth model. The reflectivity technique is computationally expensive. Therefore, reflectivity synthetics were computed only for earthquakes that generated numerous measurable complex phases (i.e. depth phases and additional surface-reflected multiples). The inputs were the same as those used to generate the WKBJ synthetics and the measurement process was very similar as well. To assure that the relative timing between the WKBJ and reflectivity synthetics was the same, I aligned the primary *SH* waveforms generated using each technique (either *S* or *SS*). I then directly compared the reflectivity synthetics to the tangential seismograms to identify potentially measurable phases. After identifying these phases and determining if there was interference with other phases, I simply time shifted the reflectivity synthetics until alignment with the data was achieved (see Figure 2.8 for example data and reflectivity synthetic). The residuals (time shifts) were stored along with phase identification tags within the corresponding structured array data files. Just as with the primary phases, each measurement was also given a numerical confidence grade (integers 1-5). Table 2.2 summarizes the measured travel time residuals and Figure 2.9 illustrates the sampling coverage at selected depths.

Table 2.2 Measured seismic phases

Phase ID	Added Measurements	Total Measurements
S	4,810	17,140
SS	5,122	13,668
SSS	538	2,341
SSSS	67	1,008
SSSSS	0	108
SSSSSS	0	1
sS	1,375	1,465
sSS	914	938
sSSS	70	70
sSSSS	8	8
ScS	919	2,006
ScS2	796	887
ScS3	119	202
sScS	277	277
sScS2	175	175
sScS3	2	2
SKS	2,120	4,049
SKKS	1,214	1,890
TOTAL	18,526	46,235

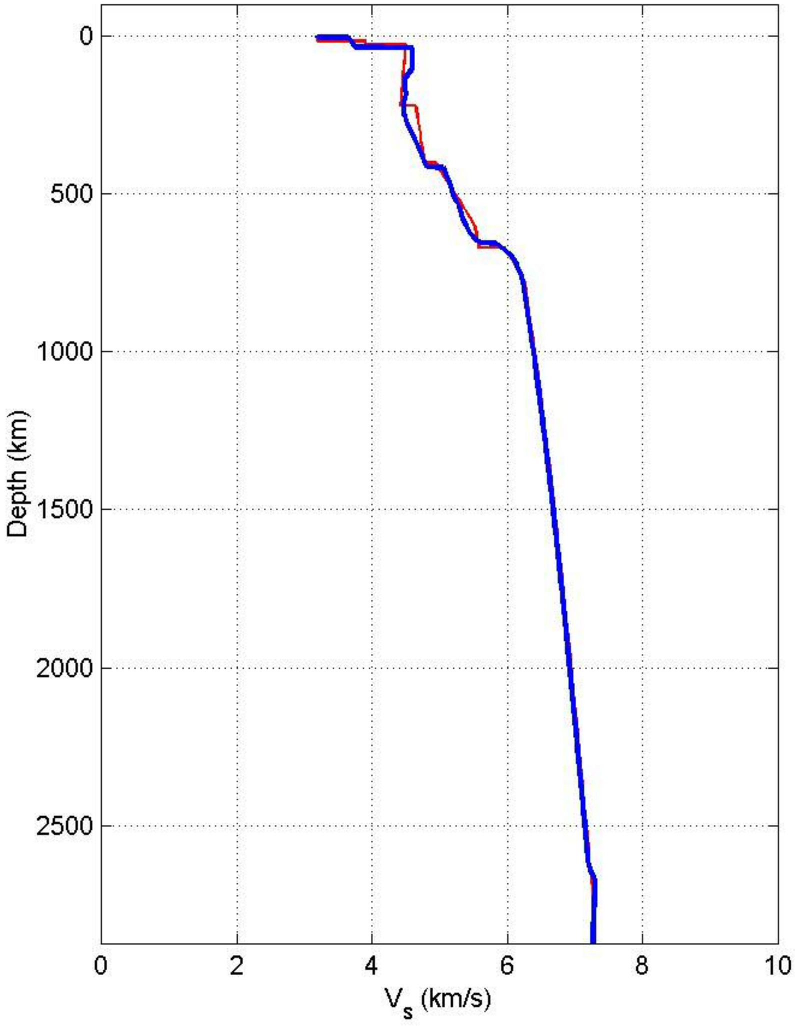

Figure 2.6 Starting shear-wave velocity model in the mantle (blue). The red curve is the PREM velocity model (Dziewonski & Anderson 1981). The blue curve is the same as PREM in the lower mantle and an average of TNA/SNA (Grand & Helmberger 1984).

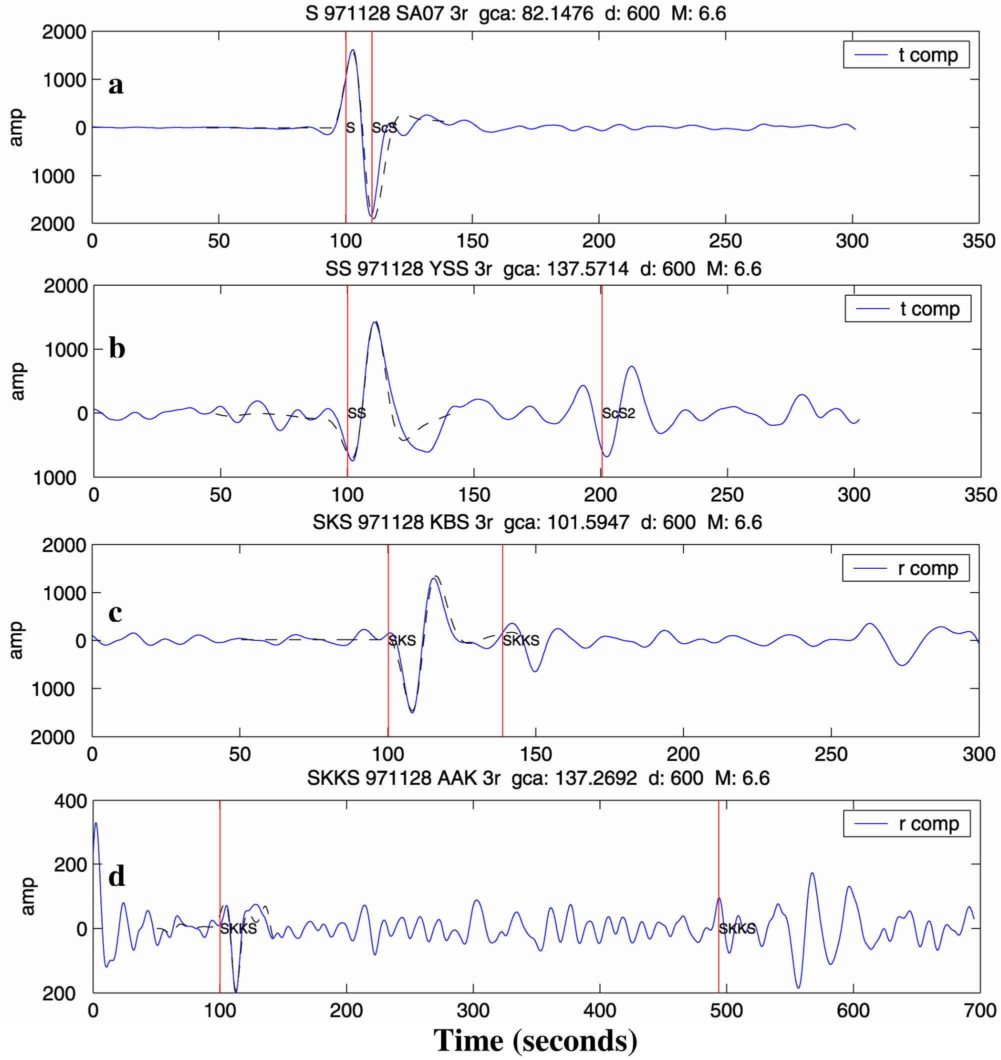

Figure 2.7 Example of WKBJ synthetic fits of *S*, *SS*, *SKS* and *SKKS* waveforms for a deep earthquake occurring beneath South America. (a) *S*-wave fit for South African station SA07. (b) *SS*-waveform fit for Russian station YSS. (c) *SKS* waveform fit for the Norwegian station KBS. (d) *SKKS* waveform fit for the Kyrgyzstan station AAK. The second *SKKS* arrival depicted here is the wrap-around phase (*SKKS* traveling >180°). (a) and (b) are the tangential components of the seismogram; (c) and (d) are the radial components.

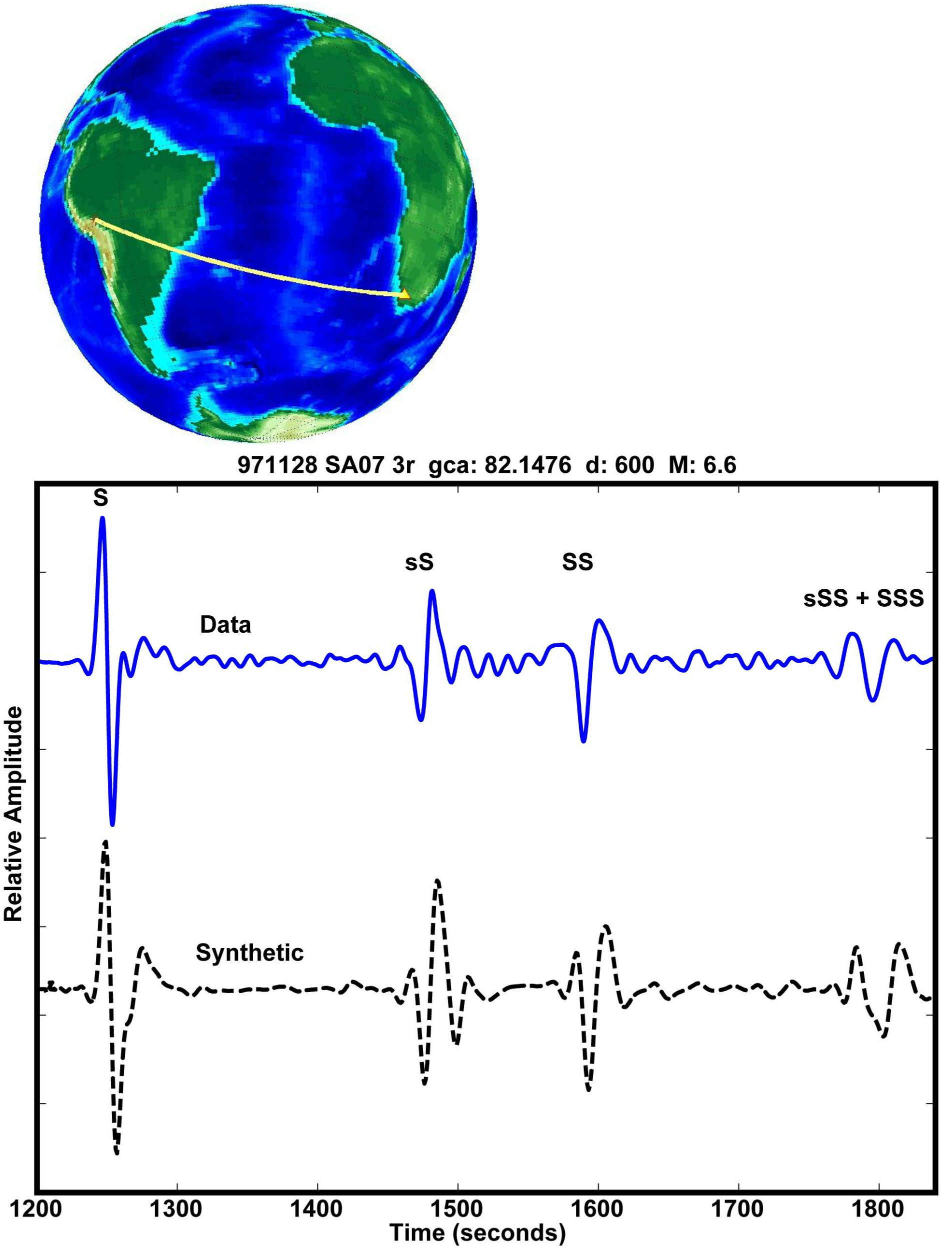

Figure 2.8 Example reflectivity synthetic comparison. The earthquake occurred 600 km beneath the Peru-Bolivia border and recorded at a station in the Kaapvaal array in South Africa. The reflectivity synthetics were simply shifted in time until a visual match was achieved for each detectable phase. The amount of shifting gives the travel time residual for that particular phase. The direct *S*, surface reflected *SS* and depth phase are easily measured. However, *sSS* and *SSS* interfere at this particular distance (82°).

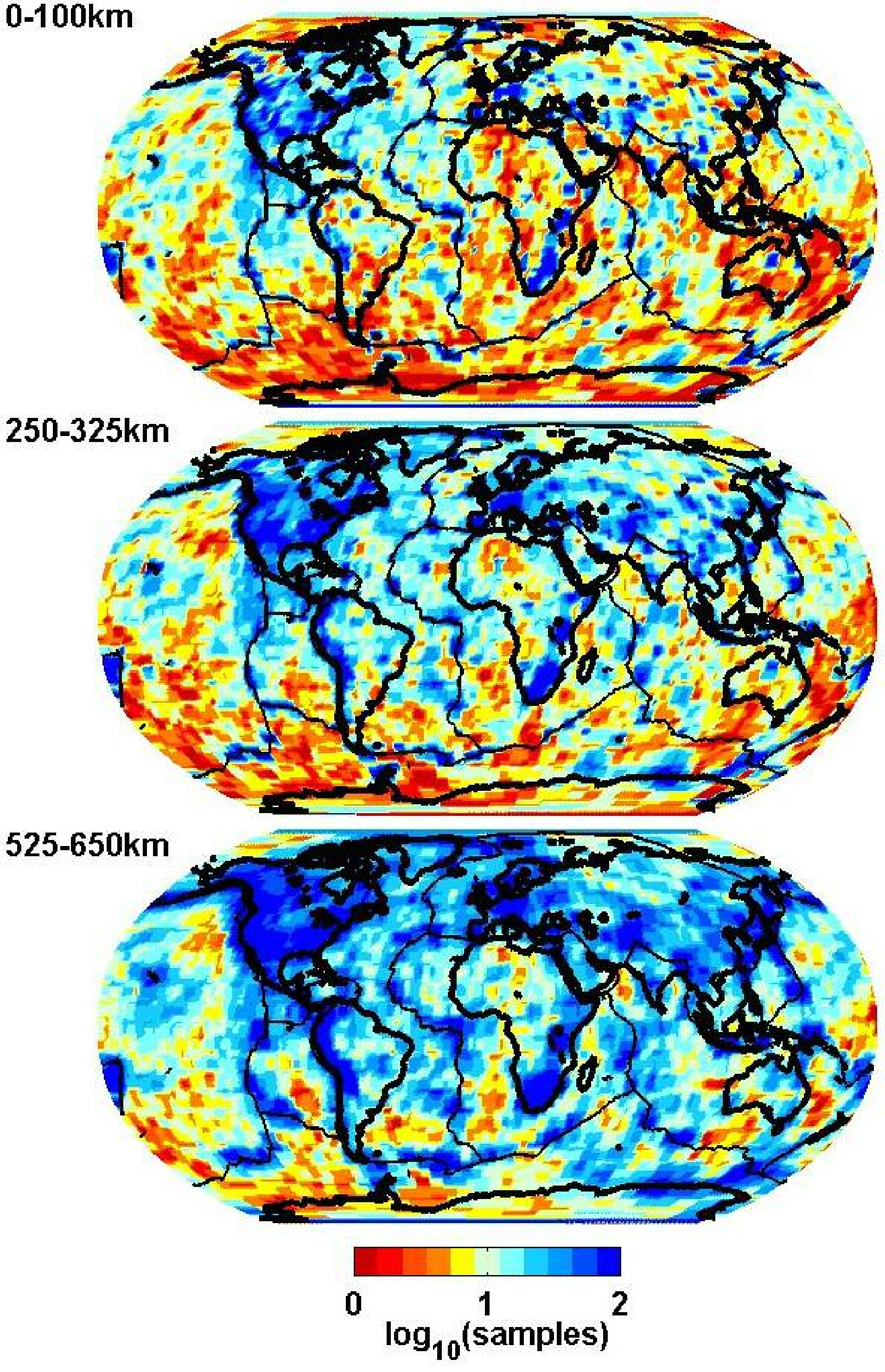

Figure 2.9 Shear-wave data sampling coverage at selected depth ranges. Notice the relatively poor sampling in the southern hemisphere and the coverage irregularity in the upper mantle. Coverage is more regular with depth due to ray paths spreading out from stations and earthquakes. **(continued on the next page)**

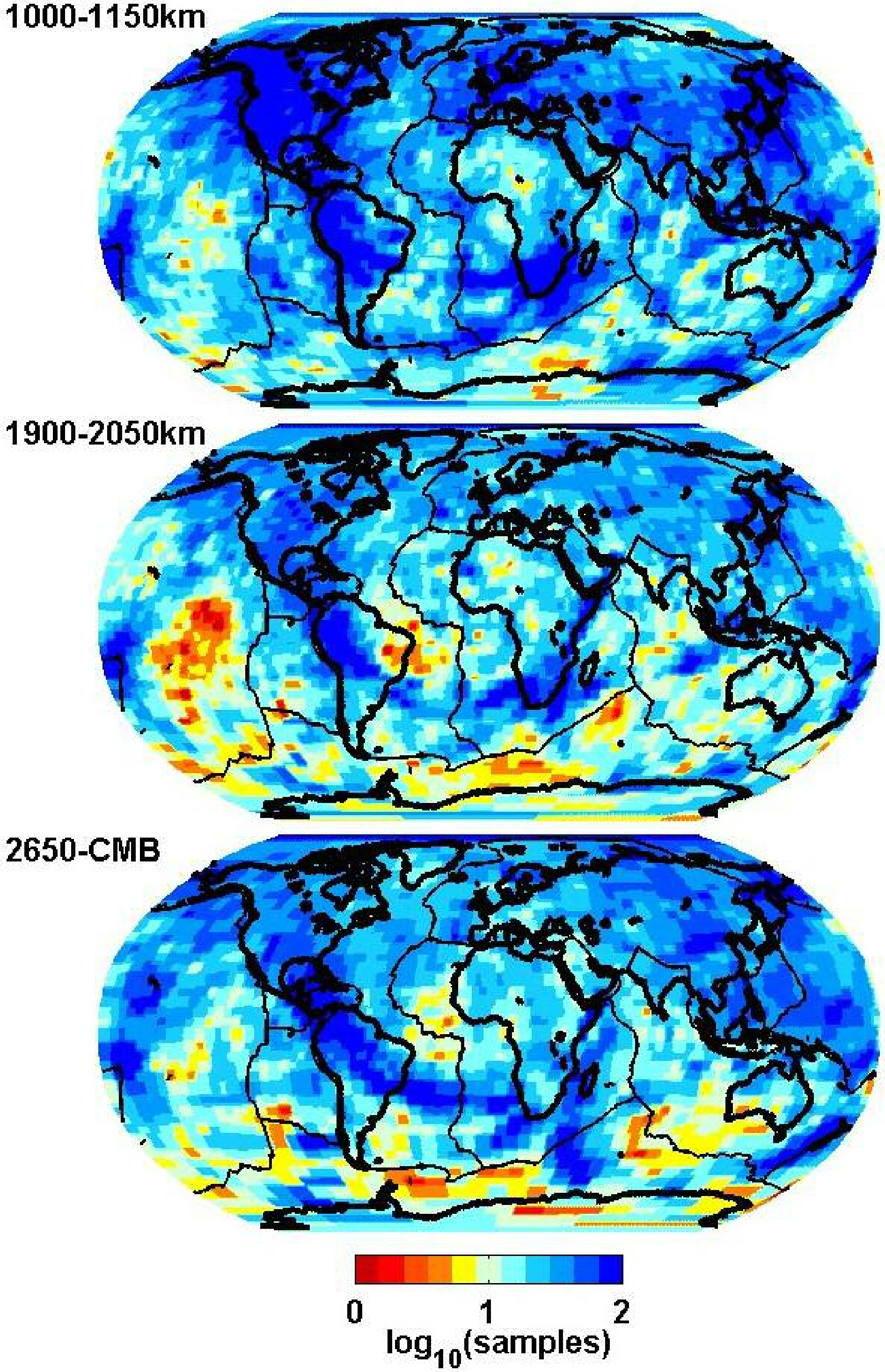

Figure 2.9 (continued) Coverage is most regular in the shallow and middle lower mantle since many measured waves turn within this depth range.

2.5 Travel time corrections

The predicted travel times were calculated assuming a spherically-symmetric Earth. Therefore, the data were corrected for the ellipticity of the Earth following *Dziewonski & Gilbert* (1976). In addition, all residuals contain signal from variations of crustal thickness, ice cap thickness and surface elevation. To remove these signals, I corrected the travel time residuals for variations of crustal thickness based on the global crust model provided by *Mooney et al.* (1998). Corrections for elevation were also applied based upon the ETOPO5 model developed by NOAA. To make these corrections we must consider crustal thicknesses and elevations near the source region, near any surface reflection points (bounce points) as well as the region near the recording instrument. A corrected travel time residual can be written in the general form:

$$r_{corrected} = r_{measured} + \delta t^{source} + \sum_{i=1}^{n} \delta t_i^{bounce} + \delta t^{station} \tag{2.6}$$

where *source*, *bounce* and *station* are the earthquake region, bounce point region and the recording station region respectively. The integer *n* is the number of surface reflections for the seismic phase considered. Each of the correction terms (e.g. δt^{source}) contain time corrections for regional elevation, crustal thickness, and ice layer thickness if any exists. The correction terms can be written in the general form:

$$\delta t = \delta t_{elevation} + \delta t_{thickness} + \delta t_{ice} = H\Delta\eta_{elevation} + T\Delta\eta_{thickness} + I\Delta\eta_{ice} \tag{2.7}$$

where *H*, *T* and *I* are the effective elevation, crustal thickness and ice layer thickness, respectively. The $\Delta\eta$ terms are the differential vertical slownesses:

$$\begin{aligned}
\Delta\eta_{elevation} &= \sqrt{\frac{1}{v_0^2} - p^2} \\
\Delta\eta_{thickness} &= \sqrt{\frac{1}{v_c^2} - p^2} - \sqrt{\frac{1}{v_m^2} - p^2} \\
\Delta\eta_{ice} &= \sqrt{\frac{1}{v_0^2} - p^2} - \sqrt{\frac{1}{v_{ice}^2} - p^2}
\end{aligned} \tag{2.8}$$

In Equation 2.8, *p* is the ray parameter, v_0 is the shallow crust velocity (3.2 km/s), v_c is the deep crustal velocity (3.7 km/s), v_m is the shallow mantle velocity (4.6 km/s), and v_{ice} is the shear-wave velocity of ice (1.9 km/s). The *H*, *T* and *I* terms near the source depend on the seismic phase considered, the earthquake depth and crustal thickness relative to the starting model thickness. Therefore, these terms must be determined on a case-by-case basis for all recorded travel time residuals (Figure 2.10). In many cases, these corrections are small compared to the amplitude of the residuals. However, in cases such as surface reflections under the ocean layer, these correction amplitudes could be larger than the recorded residual travel time. Using the variable definitions described in Figure 2.10, the terms near the seismic station are simply $H = Elev$ and $T = (35 - Th)$. These values are multiplied by a factor of two for bounce point corrections. The ice layer correction term (I) is simply the ice layer thickness near the source and station and doubled for bounce points.

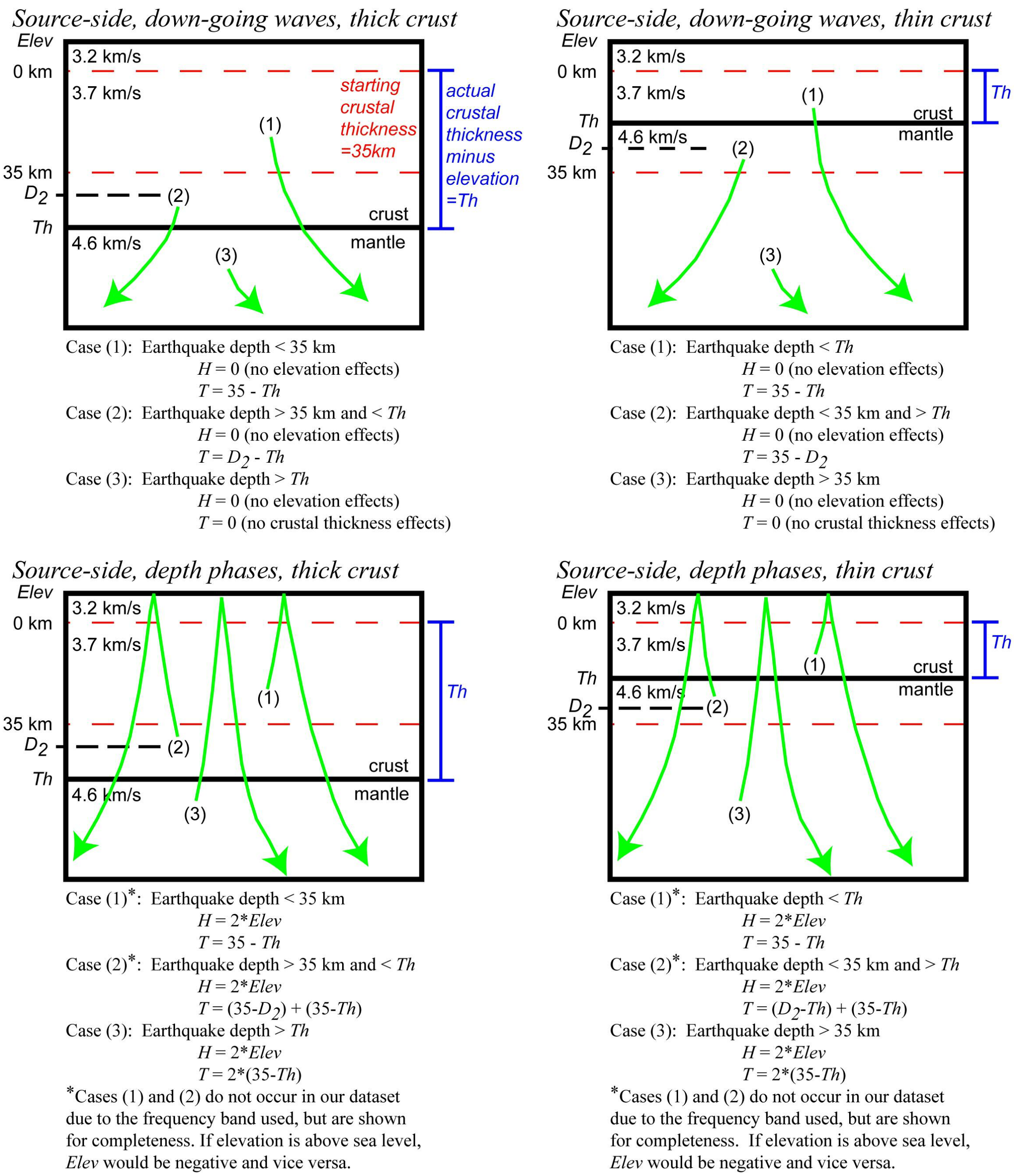

Source-side, down-going waves, thick crust

Case (1): Earthquake depth < 35 km
$H = 0$ (no elevation effects)
$T = 35 - Th$
Case (2): Earthquake depth > 35 km and < *Th*
$H = 0$ (no elevation effects)
$T = D_2 - Th$
Case (3): Earthquake depth > *Th*
$H = 0$ (no elevation effects)
$T = 0$ (no crustal thickness effects)

Source-side, down-going waves, thin crust

Case (1): Earthquake depth < *Th*
$H = 0$ (no elevation effects)
$T = 35 - Th$
Case (2): Earthquake depth < 35 km and > *Th*
$H = 0$ (no elevation effects)
$T = 35 - D_2$
Case (3): Earthquake depth > 35 km
$H = 0$ (no elevation effects)
$T = 0$ (no crustal thickness effects)

Source-side, depth phases, thick crust

Case (1)*: Earthquake depth < 35 km
$H = 2*Elev$
$T = 35 - Th$
Case (2)*: Earthquake depth > 35 km and < *Th*
$H = 2*Elev$
$T = (35-D_2) + (35-Th)$
Case (3): Earthquake depth > *Th*
$H = 2*Elev$
$T = 2*(35-Th)$
*Cases (1) and (2) do not occur in our dataset due to the frequency band used, but are shown for completeness. If elevation is above sea level, *Elev* would be negative and vice versa.

Source-side, depth phases, thin crust

Case (1)*: Earthquake depth < *Th*
$H = 2*Elev$
$T = 35 - Th$
Case (2)*: Earthquake depth < 35 km and > *Th*
$H = 2*Elev$
$T = (D_2-Th) + (35-Th)$
Case (3): Earthquake depth > 35 km
$H = 2*Elev$
$T = 2*(35-Th)$
*Cases (1) and (2) do not occur in our dataset due to the frequency band used, but are shown for completeness. If elevation is above sea level, *Elev* would be negative and vice versa.

Figure 2.10 Source-side correction term scenarios (see text).

2.6 Earthquake relocation

Slight mislocation of earthquake hypocenters may present a significant bias in the calculated residual travel times. Therefore, we must attempt to remove this bias prior to inverting for seismic structure by adjusting the location and origin time of each of the earthquakes considered. We begin with the initial event locations (determined by the Harvard CMT project) as well as the travel time residuals of an assortment of seismic phases recorded at globally-distributed stations. The general description of the forward model can be found in many texts including *Spakman & Nolet* (1988) and *Lay & Wallace* (1995), however a more complete description including weighting issues is provided in this section.

The forward problem consists of a combination of travel time corrections for relocating a hypocenter in origin time, depth, latitude and longitude. The total predicted change in travel time for a single phase due to a small perturbation of location can be written as:

$$dT^{P} = \frac{\partial T}{\partial t_o} dt_0 + \frac{\partial T}{\partial z} dz + \frac{\partial T}{\partial \theta} d\theta + \frac{\partial T}{\partial \phi} d\phi \qquad (2.9)$$

where dt_0 is the change in earthquake origin time (seconds), dz is the change in depth (km), $d\theta$ is the change in colatitude (radians), and $d\phi$ is the change in longitude of the hypocenter (radians). Since dT^{P} and dt_0 are directly related, the first derivative term simply becomes:

$$\frac{\partial T}{\partial t_0} = 1 \tag{2.10}$$

The travel time change with origin depth can be related to the vertical slowness, η in the following manner:

$$\left(\frac{\partial T}{\partial z}\right)_{down} = -\eta = -\frac{\cos i}{v(r)} = -\frac{\left(r^2 / v^2 - p^2\right)^{1/2}}{r} \tag{2.11}$$

where i is the angle of incidence near the source, r is radius to initial hypocenter, $v(r)$ is the shear-wave velocity near the source and p is spherical ray parameter defined by:

$$p = \frac{r \sin i}{v(r)} \tag{2.12}$$

The subscript, *down*, in Equation 2.11 denotes a down-going wave (such as *S* and *ScS*, etc.). Since the total ray path length is shortened with depth for a down-going wave, the predicted travel time will be lessened with increased depth. Therefore, a negative sign is used for this expression. However, for up-going waves (such as the depth phases *sS* and *sScS*), the total travel time increases with increasing source depth giving:

$$\left(\frac{\partial T}{\partial z}\right)_{up} = \frac{\left(r^2 / v^2 - p^2\right)^{1/2}}{r} \tag{2.13}$$

For a perturbation of colatitude by $d\theta$ radians, the earthquake hypocenter is adjusted by $rd\theta$ kilometers and the seismic ray path is lengthened according to:

$$dL = rd\theta \cos\varphi \sin i \tag{2.14}$$

where φ is the azimuth of the vector connecting the original hypocenter to the seismic station considered. Translating Equation 2.14 to differential travel time gives the relationship:

$$\frac{\partial T}{\partial \theta} = \frac{r \cos\varphi \sin i}{v(r)} = p \cos\varphi \tag{2.15}$$

where, again, $v(r)$ is the seismic velocity near the initial earthquake origin. The perturbation of travel time with a change in longitude is a similar expression with an adjustment with starting latitude:

$$\frac{\partial T}{\partial \phi} = -p \sin\varphi \sin\theta \tag{2.16}$$

These derivatives can be computed for each of the m phases originating from a single earthquake and collected into a sensitivity matrix:

$$\mathbf{D} = \begin{bmatrix} 1 & \left(\frac{\partial T}{\partial z}\right)_1 & \left(\frac{\partial T}{\partial \theta}\right)_1 & \left(\frac{\partial T}{\partial \phi}\right)_1 \\ \cdot & \cdot & \cdot & \cdot \\ \cdot & \cdot & \cdot & \cdot \\ 1 & \left(\frac{\partial T}{\partial z}\right)_m & \left(\frac{\partial T}{\partial \theta}\right)_m & \left(\frac{\partial T}{\partial \phi}\right)_m \end{bmatrix} \tag{2.17}$$

where each row is a set of derivatives for each computed travel time. The sign difference between the up- and down-going seismic phases on the depth derivative term should be kept in mind when generating **D** (Equations 2.11 versus 2.13). The differential timing and hypocenter vector, $\delta\mathbf{h}$, can be defined as the following:

$$\delta\mathbf{h} = \begin{bmatrix} dt_0 \\ dz \\ d\theta \\ d\phi \end{bmatrix} \tag{2.18}$$

We can now write the linear system:

$$\delta\vec{T}^P = \mathbf{D}\delta\mathbf{h} \tag{2.19}$$

The vector $\delta\vec{T}^{p}$ is the change in predicted travel time for each of the phases of interest with a small perturbation in origin time and location of the earthquake. The new origin time and position can be updated in terms of a truncated Taylor's series expansion:

$$\mathbf{h} = \mathbf{h}_0 + \delta\mathbf{h} \tag{2.20}$$

where $\mathbf{h}_0$ is the initial hypocenter origin. The predicted travel time can be updated in a similar manner:

$$\vec{T}^{p}(\mathbf{h}) = \vec{T}^{p}(\mathbf{h}_0) + \mathbf{D}\delta\mathbf{h} \tag{2.21}$$

We now need to express the affect that this predicted time will have on the calculated residual travel times. The calculated residuals can be expressed as the difference of time between the observed travel times and the predicted times:

$$\delta\vec{T}(\mathbf{h}_0) = \vec{T}^{o} - \vec{T}^{p}(\mathbf{h}_0) \tag{2.22}$$

where $\vec{T}^{o}$ is a vector of the observed travel times for an individual earthquake and $\vec{T}^{p}(\mathbf{h}_0)$ are the predicted travel times based on the initial earthquake location and origin time. Combining these last two equations, an expression for the updated residual travel time can be obtained:

$$\delta\vec{T}(\mathbf{h}) = \vec{T}^{o} - \vec{T}^{p}(\mathbf{h}) = \vec{T}^{o} - \left[\vec{T}^{p}(\mathbf{h}_0) + D\delta\mathbf{h}\right] = \delta\vec{T}(\mathbf{h}_0) - \mathbf{D}\delta\mathbf{h} \tag{2.23}$$

Assuming that the residual travel times are non-zero because of mislocation of the hypocenter, the earthquake origin time and location should be adjusted such that all travel time residuals are equal to zero ($\delta\vec{T}(\mathbf{h}) = \mathbf{0}$). This leads to the system of equations:

$$\delta\vec{T}(\mathbf{h}_0) = \mathbf{D}\delta\mathbf{h} \tag{2.24}$$

which can be solved for the differential hypocenter time and location $\delta\mathbf{h}$. Equation 2.24 is a linear approximation to a non-linear problem since **D** is a function of earthquake location. I found, however, only one iteration is necessary to achieve convergence with the data. In other words, the system can be treated as linear without iterative updates of the location and residual travel times. I chose to use a weighted and damped least squares approach to solve the system in Equation 2.24.

The objective function contains a weighted data error term as well as a damped and weighted model term:

$$\begin{aligned} \Phi &= E_w + \varepsilon^2 L_w \\ E_w &= (\delta\vec{T} - \mathbf{D}\delta\mathbf{h})^{\mathrm{T}} \mathbf{W}_d (\delta\vec{T} - \mathbf{D}\delta\mathbf{h}) \\ L_w &= (\delta\mathbf{h} - \delta\mathbf{h}_{prior})^{\mathrm{T}} \mathbf{W}_m (\delta\mathbf{h} - \delta\mathbf{h}_{prior}) \end{aligned} \tag{2.25}$$

E_w represents the weighted data error and L_w is the model length and ε is an arbitrary damping factor. $\mathbf{W}_d$ and $\mathbf{W}_m$ are data and model weighting matrices respectively, and $\delta\mathbf{h}_{prior}$ is the prior differential location. In this case, there is no previous differential location, and therefore we set $\delta\mathbf{h}_{prior} = \mathbf{0}$. The optimum value for $\delta\mathbf{h}$ is one such that the objective function is minimized. To find the minimum, a derivative is evaluated and set to zero:

$$\frac{\partial\Phi}{\partial(\delta\mathbf{h})} = \mathbf{0} = -\mathbf{D}^{\mathrm{T}}\mathbf{W}_d\delta\vec{T} + \left(\mathbf{D}^{\mathrm{T}}\mathbf{W}_d\mathbf{D} + \varepsilon^2\mathbf{W}_m\right)\delta\mathbf{h} \tag{2.26}$$

Equation 2.26 leads to a solution for earthquake relocation vector which can be solved directly after matrix inversion:

$$\delta\mathbf{h} = \left[\mathbf{D}^{\mathrm{T}}\mathbf{W}_d\mathbf{D} + \varepsilon^2\mathbf{W}_m\right]^{-1}\mathbf{D}^{\mathrm{T}}\mathbf{W}_d\delta\vec{T} \tag{2.27}$$

The data weighting matrix, $\mathbf{W}_d$, was constructed with a combination of the data grading weights and azimuthal weights to prevent possible directional bias. Recall that each of the recorded residuals was given a numeric grade (integers 1-5) based on my confidence of the particular fit to the synthetic data. Collectively, these confidence grades are represented by the vector $\mathbf{g}_w$.

In a lot of instances, the collection of residuals for a particular earthquake are from tight groupings of stations such as from the array of 50+ instruments in southern Africa and others. If recordings from all azimuths were weighted equally, the data from station groups would dominate the relocation and present bias in the solutions. To counteract this effect, the data were binned by 5° azimuthal and arc distance increments about the earthquakes and the total number of rays in each bin were determined (N_{bin}). An azimuthal weight of 1/ N_{bin} was given to each data point in the corresponding bins and collected into a vector $\mathbf{a}_w$.

In addition to the data confidence and azimuthal weighting, other types of data weights were applied. Residual travel times recorded for a single earthquake often have a large value range, especially for events producing multiple bouncing phases such as *SSSS* which could have residuals on the order of minutes rather than a few seconds. In such cases, the relocation would be biased to minimize the highest residuals while essentially ignoring phases with minimal travel time residuals. Therefore, two additional weighting factors were introduced: residual amplitude weighting ($\mathbf{t}_w$) and number of bounce points weighting ($\mathbf{b}_w$). The residual amplitude weighting assignments were as follows:

$$
\begin{aligned}
&0 \le |residual| < 3s \to t_w = 1\\
&3 \le |residual| < 6s \to t_w = 0.8\\
&6 \le |residual| < 9s \to t_w = 0.6\\
&9 \le |residual| < 12s \to t_w = 0.4\\
&12 \le |residual| < 15s \to t_w = 0.2\\
&|residual| > 15s \to t_w = 0
\end{aligned}
$$

The surface reflected phases (bouncing phases) are less reliable for relocating earthquakes since these phases are affected by strong near-surface heterogeneities at every bounce point thereby obscuring the signal associated with event mislocation. Therefore, the bounce point weighting ($\mathbf{b}_w$) was introduced and defined by 1/(number of bounces) so that *SS* waves would be weighted by 0.5, *SSS* would be weighted by 0.3 and so forth. The initial surface reflection associated with the depth phases (i.e. *sS* and *sSS* etc.) was not considered a bounce in this weighting scheme given the importance of these phases in constraining the depth of deep earthquakes.

The total data weights are the cumulative product of all of the described weighting terms and, therefore, the total data weight for the *i*-th data point can be determined as follows:

$$\mathbf{w}_i = \mathbf{g}_{w,i} \times \mathbf{a}_{w,i} \times \mathbf{t}_{w,i} \times \mathbf{b}_{w,i} \tag{2.28}$$

and the data weighting matrix can be constructed by placing the weighting values along the diagonal:

$$\mathbf{W}_d = diag(\mathbf{w}) \tag{2.29}$$

The model weighting matrix, $\mathbf{W}_m$, controls how much an earthquake can move from the initial position. Since $\delta\mathbf{h} = [dt_0 \quad dz \quad d\theta \quad d\phi]^{\mathrm{T}}$ contains a time term in seconds, a depth term in kilometers and surface position in radians, each parameter must have different weighting values so that they have an equal effect when measuring model length (see Equation 2.25). Similar to the data weighting matrix development, I chose to first define a 4-element weighting vector ($\mathbf{v}_w$). The third weighting term ($\mathbf{v}_{w,3}$) is associated with colatitude change in radians and was set to a value of 1. The 4th term (corresponding to change of longitude in radians), was scaled according to the source latitude since a particular latitude change is larger (in actual distance) than the same change in longitude. Therefore the weighting term for the longitude parameter was set to $\mathbf{v}_{w,4} = \mathbf{v}_{w,3}\sin\theta$ so that it would be allowed the same freedom to vary as the latitude term. The 2nd model parameter term is earthquake depth in kilometers and was set to $\mathbf{v}_{w,2} = \mathbf{v}_{w,3}/6371$ since 1 radian along the surface of the Earth is equal to 6371 kilometers (the radius of the Earth). This allows the dz term to vary by 6371 times the latitude change in radians. Note that without the calculation of depth phase travel times (i.e. *sS*, *sScS*, etc.), we do not have depth control since source depth trades off strongly with origin time. Therefore, for shallow events or deep events without depth phases, $\mathbf{v}_{w,2}$ was given an arbitrarily large value to prevent depth relocation. The 1st weighting term corresponds to the change in origin time and was set to $\mathbf{v}_{w,1} = \mathbf{v}_{w,3}/1000$ based on experimenting with several test cases. Placing these weights into the diagonal components of the model weighting matrix gives:

$$\mathbf{W}_m = diag(\mathbf{v}_w) = \begin{bmatrix} 1/1000 & 0 & 0 & 0 \\ 0 & 1/6371 & 0 & 0 \\ 0 & 0 & 1 & 0 \\ 0 & 0 & 0 & \sin\theta \end{bmatrix} \tag{2.30}$$

Up until this point, is has been presumed that the optimum earthquake location and origin time are such that the sum of the travel time residuals is equal to zero. We know that this may not be the true solution since all phases leaving a hypocenter could be either fast (such as from earthquakes originating in subduction zones) or slow (such as earthquakes originating at mid-ocean ridges). In tomographic inversion, we often don't know what the tradeoff should be, since the Earth's seismic structure is what we are trying to determine. One way to address this issue is to use an independently-derived 3-D seismic model and remove the predicted signals from the calculated residuals ($\delta\vec{T}$). An alternative approach is to account for the local tectonic regime by redefining the residuals in Equation 2.22:

$$\delta\vec{T}' = \delta\vec{T} - \kappa \tag{2.31}$$

where κ is the expected average residual due to local structure. For example, an event occurring within a subduction zone may be assigned a bias $\kappa = -1$ second since it is expected that all rays leaving the source are fast relative to the starting model. This procedure is used at specific stages of model development fully described in the following sections.

2.7 Forward model and parameterization

As described in Section 2.1, the general forward model can be expressed as $\mathbf{Lm} = \mathbf{r}$ which is a simple linear system of equations. **L** is the Fréchet kernel matrix (ray path lengths) and **r** is a vector containing all residual travel times (measurements). The vector **m** is the differential seismic slowness model to be determined. To develop the system of equations, the mantle was broken into 21 depth layers that range in thickness varying from 75 to 150 km plus an additional layer at the base of the mantle that is 240 km thick (roughly corresponding to the D'' layer). Each depth layer was broken into blocks that are *ca.* 275 km X 275 km in lateral dimension. The parameterized model also includes two depth layers in the outer core. The first core layer consists of the upper 200 km of the outer core and the final layer represents the remainder of the outer core (deeper than 200 km). In total, the mantle and outer core are represented by 24 depth layers and 99,148 parameterized blocks.

The **L** matrix is ill-conditioned since some blocks are heavily sampled by crossing ray paths (over determined) and other blocks are only lightly sampled (under determined) creating a mixed determined system of equations. Therefore, regularization is a necessity. Regularization includes both smoothing and damping parameters designed to find the smoothest solution that fits the data with the least amount of heterogeneity. To generate a smoothing operator, I designed custom block-by-block filters described in Figure 2.11. Each filter (1 per block) has 21 weighting factors acting to smooth the model in the lateral and vertical directions. The filters were combined into a matrix $\mathbf{S}_R$ (1 filter per row). Model damping can be achieved by a simple diagonal matrix (99,148 X 99,148 elements) containing the damping weights. However, given the highly irregular sampling coverage, I chose to develop a customized damping matrix that acts to dampen poorly sampled regions more than highly sampled regions in order to reduce variations in unconstrained model blocks. Taking the sum of all ray path lengths in each block, L_{sum}, I assigned damping values $d=100/\log_{10}[L_{sum}+10]$ for each model parameter. Although this style of damping is arbitrary, testing showed that regions with lesser sampling were reduced in amplitude without strongly affecting the data fit. The damping matrix will be denoted as $\mathbf{D}_R$ in the following discussion.

The system of equations described in Equation 2.5 can be expanded to include the smoothing and damping constraints:

$$\begin{bmatrix} \mathbf{L} \\ \lambda_S \mathbf{S}_R \\ \mathbf{D}_R \end{bmatrix} \mathbf{m} = \begin{bmatrix} \mathbf{r} \\ \mathbf{0} \\ \mathbf{0} \end{bmatrix} \tag{2.32}$$

Where **L**, **m** and **r** are the Fréchet kernel matrix, slowness model vector, and travel time residuals, respectively as in Equation 2.5. $\mathbf{S}_R$ and $\mathbf{D}_R$ are the smoothing and damping operators described in the text. The scalar value λ_S is the smoothing weight that, when increased, results in smoother solutions. Equation 2.32 describes the final forward model to be solved for **m** using the inversion scheme discussed in the following section.

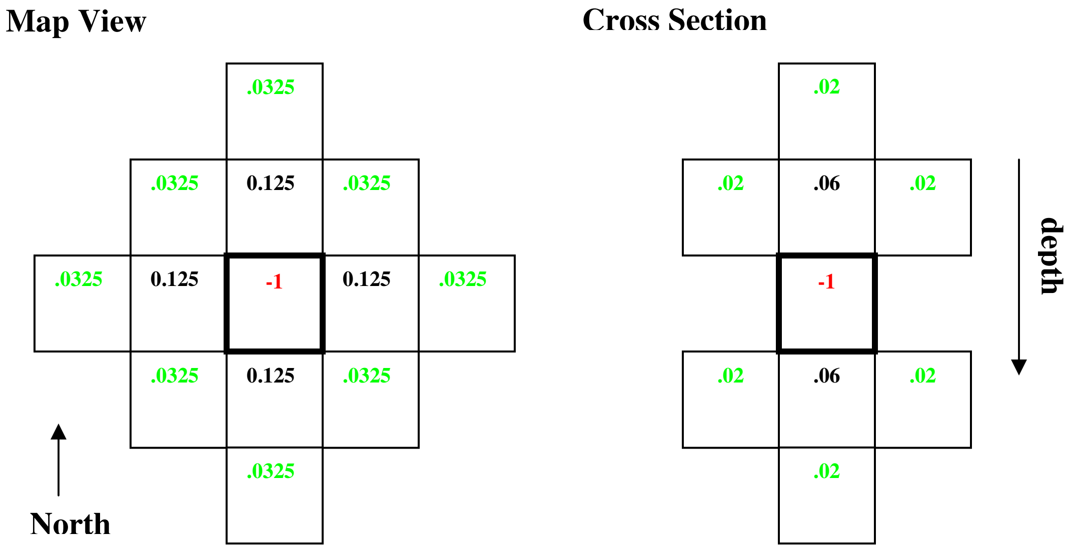

$$\sum_{i=1}^{21} weight_i = 0$$

Figure 2.11 Schematic illustration of the 21-point smoothing filter weights. On the left is a map view of the lateral filter weights about a central model block (red). The nearest neighboring block weights (black) are highest and drop by a factor of ~4 beyond the nearest neighbors (green). On the right side are the filtering weights in the vertical dimension. The nearest vertical blocks only contribute about ½ of the lateral blocks (black) and the adjacent block weights drop by a factor of 3 (green) providing for only light vertical smoothing relative to lateral smoothing.

2.8 Inversion process

The linear system of equations (Equation 2.32) can be solved for **m** using the iterative LSQR technique which is designed to efficiently deal with large, sparse systems of equations (Paige & Saunders 1982). The LSQR algorithm is very efficient and bypasses the need to calculate normal equations or directly invert a large and sparse matrix. Appendix A describes the iterative LSQR algorithm. However, rather than solving the linear system outright, we must consider other modeling issues. These issues include the fact that the velocity heterogeneity is far stronger in the shallow upper mantle than the deeper mantle. See *Megnin & Romanowicz* (2000) for a depth-dependent spectral heterogeneity map. The anomalous features in the upper mantle including the cratonic and mid-ocean ridge signatures could be smeared to deeper depths thus creating artifacts if the data are not properly modeled. In addition, the supposed optimum location and timing of the earthquakes depend on the heterogeneity model itself (a circular problem).

To address these issues, I solved for mantle heterogeneity in a stepwise fashion with subsequent earthquake relocations after each inversion step. The initial step was to relocate the earthquakes using the surface wave model developed by *Shapiro & Ritzwoller* (2002) as a proxy for shear-wave velocity heterogeneity in the upper 250 km of the mantle. If we define the surface wave model as $\mathbf{m}_{surf}$ and the corrected travel time residuals $\mathbf{r}_0$, we can calculate the reduced residuals by:

$$\mathbf{r}_0' = \mathbf{r}_0 - \mathbf{L}\mathbf{m}_{surf} \tag{2.33}$$

where $\mathbf{L}$ is the seismic ray path length matrix just as before. Essentially, $\mathbf{r}_0'$ is a vector of travel time residuals that have been "stripped" of the signal produced by the heterogeneity defined by the surface wave model ($\mathbf{L}\mathbf{m}_{surf}$). The earthquake relocation procedure was then performed on this reduced signal to minimize $\mathbf{r}_0'$.

Next, I solved for a velocity model assuming that all residual travel times were produced by heterogeneity in the upper 175 km (the first 2 model layers). This process is known as signal squeezing and is achieved by simply giving very high damping weights to the model parameters associated with the deeper layers. The earthquakes were then relocated (again) using the new model in a similar manner as the surface wave model. The exception is that a -0.5 second relocation bias (κ) was given to subduction earthquakes occurring deeper than 175 km. The purpose for this is that the new model is null below 175 km and we know that all seismic phases leaving a subduction zone should be fast since subducted slabs are presumably low temperature relative to ambient mantle (see Section 2.6 and Equation 2.31 for further explanation).

Using the newly-relocated residual travel times, the process was repeated considering an expanded depth range of 0 to 325 km. In this case, the model produced in the preceding step was used as a starting model (but not fixed) for the inversion scheme and the residuals were relocated with a -0.5 second bias (κ) for earthquakes occurring deeper than 325 km. This process was repeated for 0-650 km depth and the D'' layer (deepest mantle model layer) where independent studies have found significant heterogeneity (see Loper & Lay 1995; Lay *et al.* 1998; Helmberger *et al.* 2000; Ni & Helmberger 2001a,b). The final inversion steps allowed the entire mantle model space to vary followed by earthquake relocations until the inversion converged. See the flowchart in Figure 2.12 for a summary of the modeling steps.

In order to find an optimal level of smoothing, I performed the inversion process assuming a spectrum of λ_S values (smoothing weights). I then evaluated the tradeoff of data misfit with model complexity (roughness) using the standard L-curve analysis (e.g. Hansen 1992). This was done by first defining the travel time data misfit as the 2-norm of the data error vector:

$$E \equiv \left\| \mathbf{Lm} - \mathbf{r} \right\|_2 \tag{2.34}$$

where **r** is the crust and topography corrected travel time residuals also adjusted for the final earthquake locations and origin times. **L** is the seismic ray path length matrix and **m** is the final whole-mantle heterogeneity model. A relative measure of model complexity (sometimes called roughness) can be estimated by calculating the 2-norm of the regularized model solution:

$$C \equiv \left\| \mathbf{S}_R \mathbf{m} \right\|_2 \tag{2.35}$$

Comparison of these two measurements (*E* and *C*) produces a tradeoff curve that forms a corner in the region corresponding to the optimal smoothness parameter, λ_S (Figure 2.13). From the tradeoff curve, we find that the model generated using $\lambda_S = 1800$ is the optimum solution. The optimum slowness model provides for a 93.5% variance reduction fit to the travel time residuals. It should be noted that the LSQR inversion procedure is iterative. To determine the appropriate number of LSQR iterations, I performed the modeling procedure with a range of total inversion iterations. The actual number of iterations chosen followed a power of two pattern from 2 to 256 (i.e. 2,4,8,16,....,256). A total of 128 iterations was selected since further convergence was negligible beyond this number of iterations (Figure 2.13).

To examine the resolution of the model, single-layer synthetic heterogeneity models were generated. The test models consist of *ca.* 5 X 5 arc-degree blocks with alternating velocity perturbations of ±1%. This is similar to checkerboard resolution testing; however, the synthetic models are not perfect checkerboards due to the staggered nature of the model blocks. Taking the ray path lengths from the actual data set (**L**), synthetic travel time residuals were calculated assuming the synthetic heterogeneity model:

$$\mathbf{b}_{synthetic} = \mathbf{L}\mathbf{m}_{synthetic} \tag{2.36}$$

A velocity model was then found using the same inversion process used to generate the actual model. The synthetic and recovered models in selected depth layers are illustrated in Figure 2.14 and a complete set of resolution tests is presented in Appendix B. For each model layer, the input and output models were cross correlated and these coefficients are noted next to the synthetic model illustrations. In addition, the amplitude recovery levels, defined by the ratio of the RMS amplitudes of the input and output models, are similarly noted in the figures. The correlation coefficients range from 0.59 to 0.90 and are greater than ~0.70 for most depth layers. The amplitude recoveries range from 53 to 87% and are typically greater than 70% for the non-smoothed solutions and >60% when smoothing is incorporated. The most poorly resolved regions are generally in the southern hemisphere due to the sparseness of seismic stations there. This is most notable beneath the southern Pacific and Indian oceans from 175 to 525 km depth. The best resolved regions are beneath the Americas and most of Europe and Asia due to the relative high degree of sampling in these locations. These resolution tests give a sense of the portions of the actual model to trust and the level of detail to consider in particular regions. Figure 2.15 is a plot of the RMS amplitudes as a function of depth for each test case. The illustration gives a general sense of how signal might be smeared (or leaked) into other depth zones.

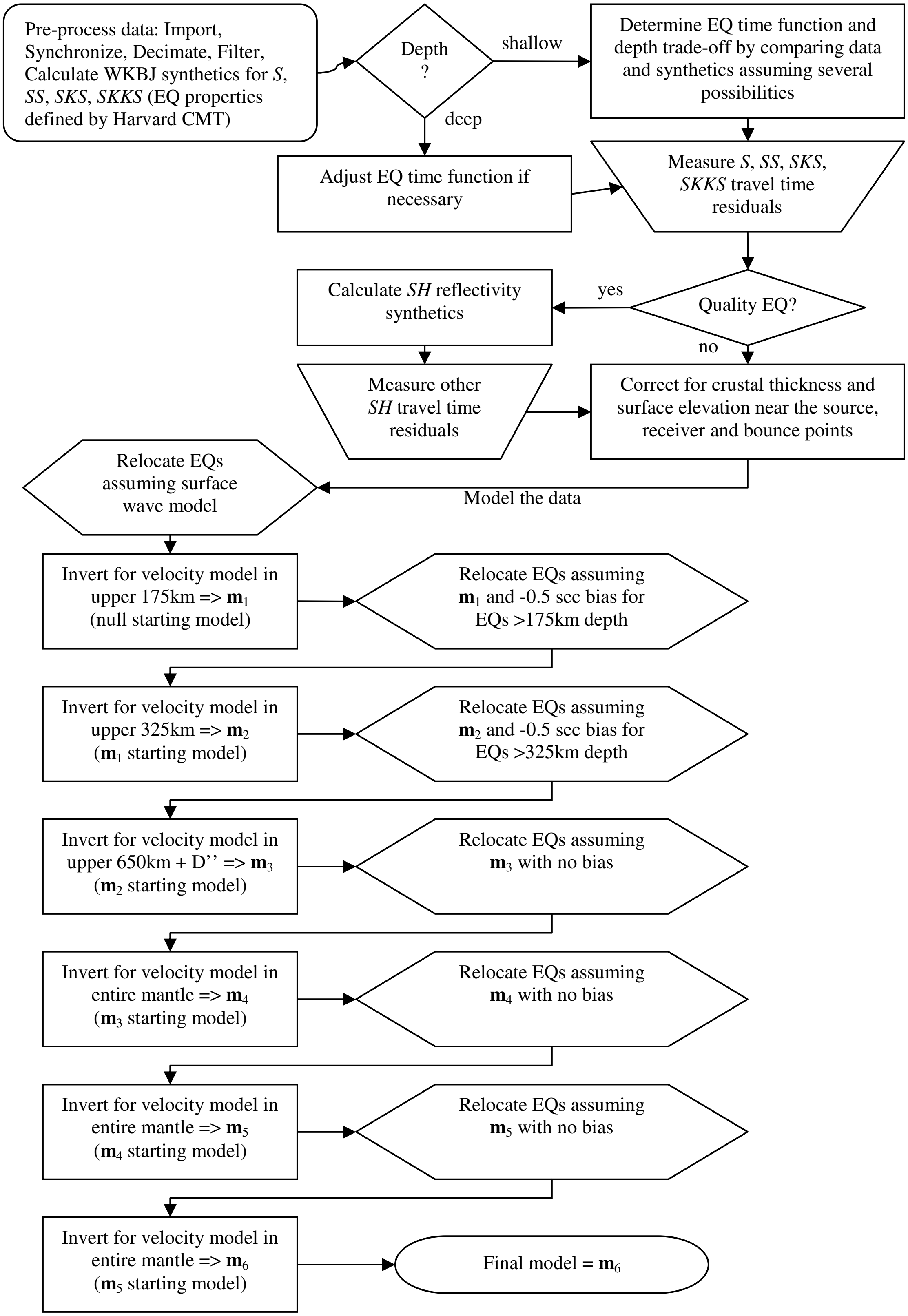

Figure 2.12 Data processing and modeling flowchart.

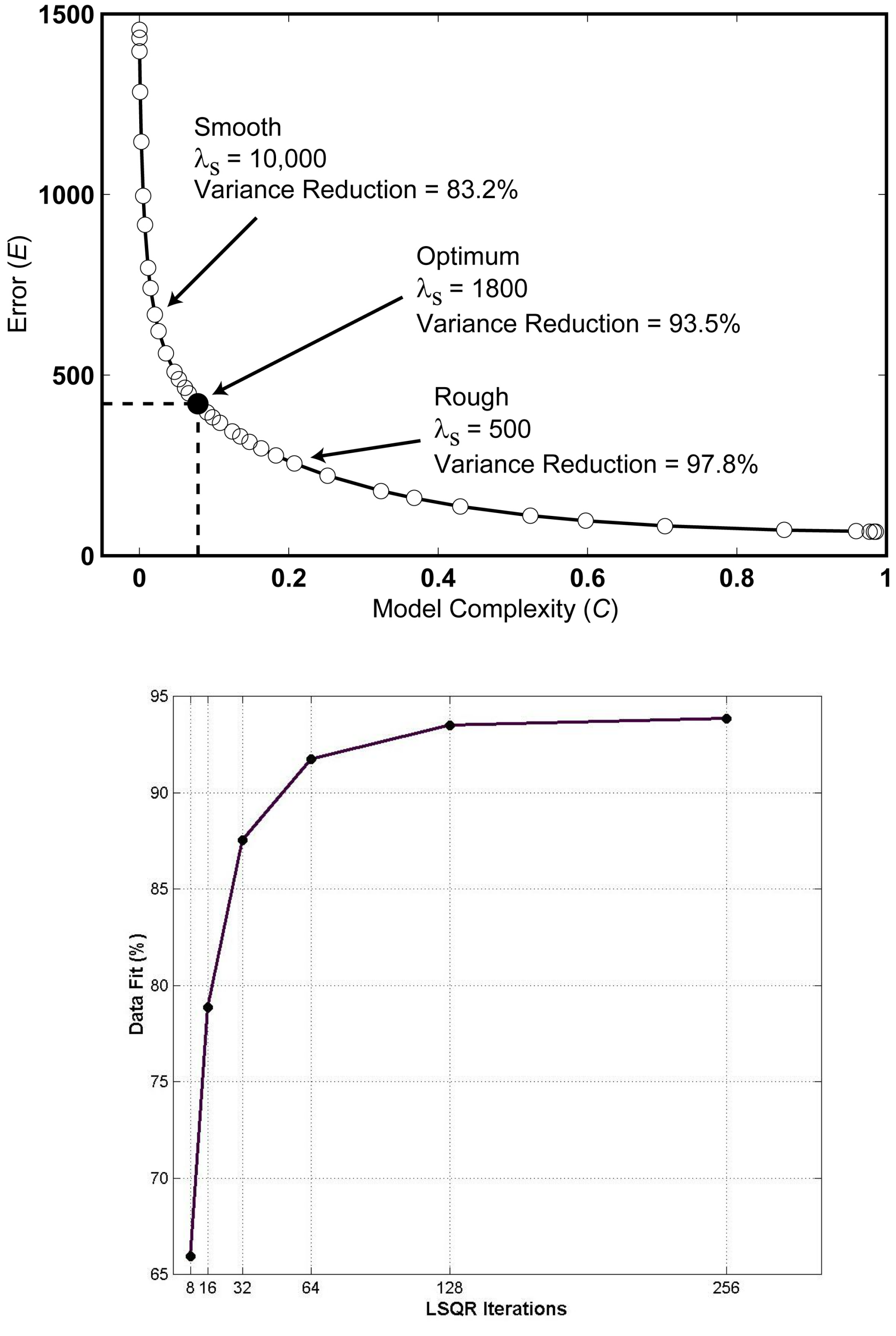

Figure 2.13 Model complexity (C) versus data error (E) for a range of smoothing weights (top panel). See text for definitions of C and E. The models corresponding to the "Smooth", "Optimum" and "Rough" points are illustrated in Appendix C. Variance reduction fit as a function of LSQR iterations (bottom panel). There are only small improvements in data fit beyond 128 iterations.

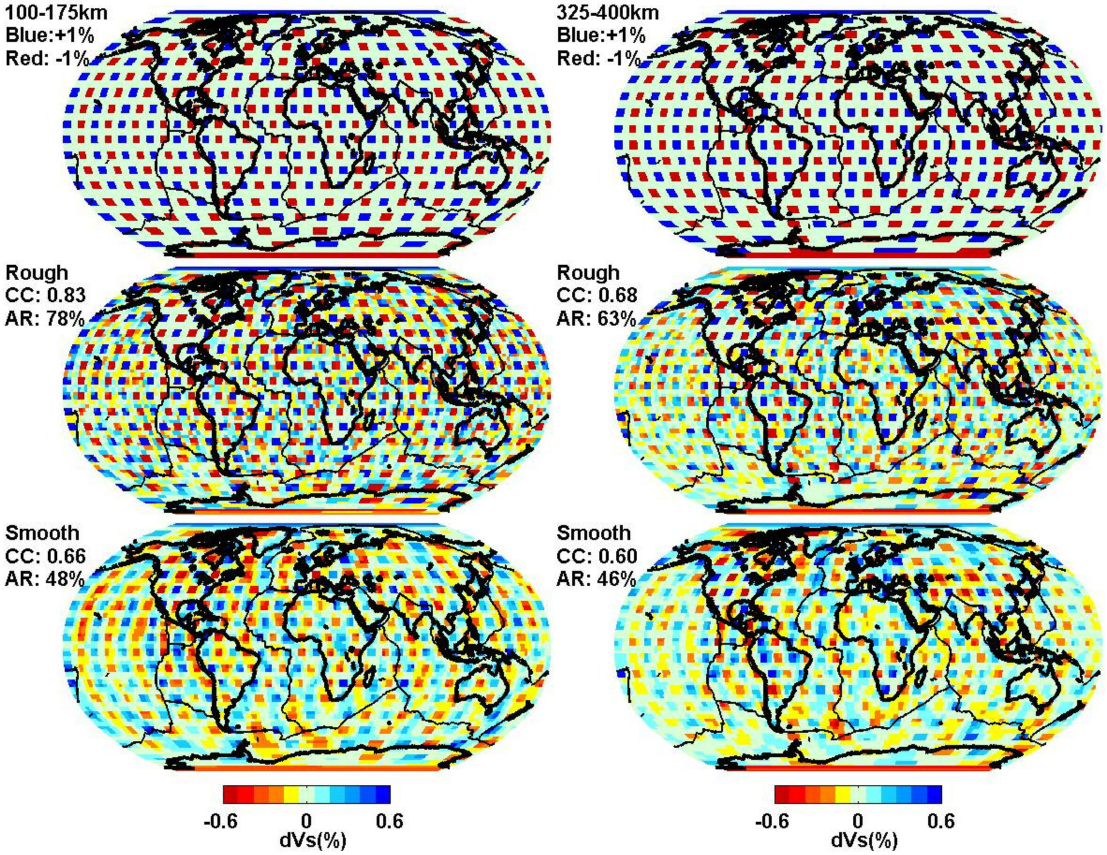

Figure 2.14 Resolution tests for two depth layers. The left column contains the synthetic model (top) and recovered models without smoothing constraints (middle) and with smoothing constraints (bottom) for the depth layer 100-175 km. The correlation between the synthetic and recovered models as well as the RMS amplitude recoveries are noted next to the models (“CC” and “AR” respectively). The right column is similar for the depth layer 325-400 km. See Appendix B for the complete set of resolution tests. **(continued on the next page)**

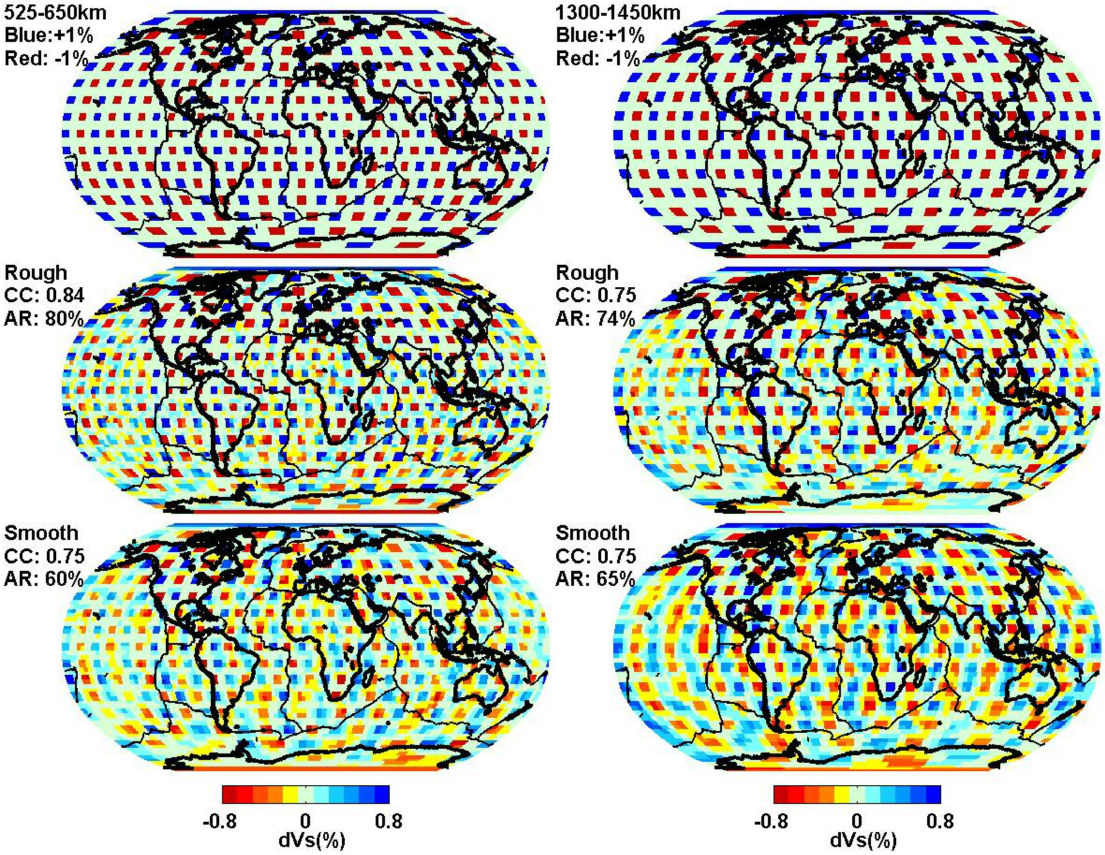

Figure 2.14 (continued) The left column contains the synthetic model (top) and recovered models without smoothing constraints (middle) and with smoothing constraints (bottom) for the depth layer 525-650 km. The right column is similar for the depth layer 1300-1450 km.

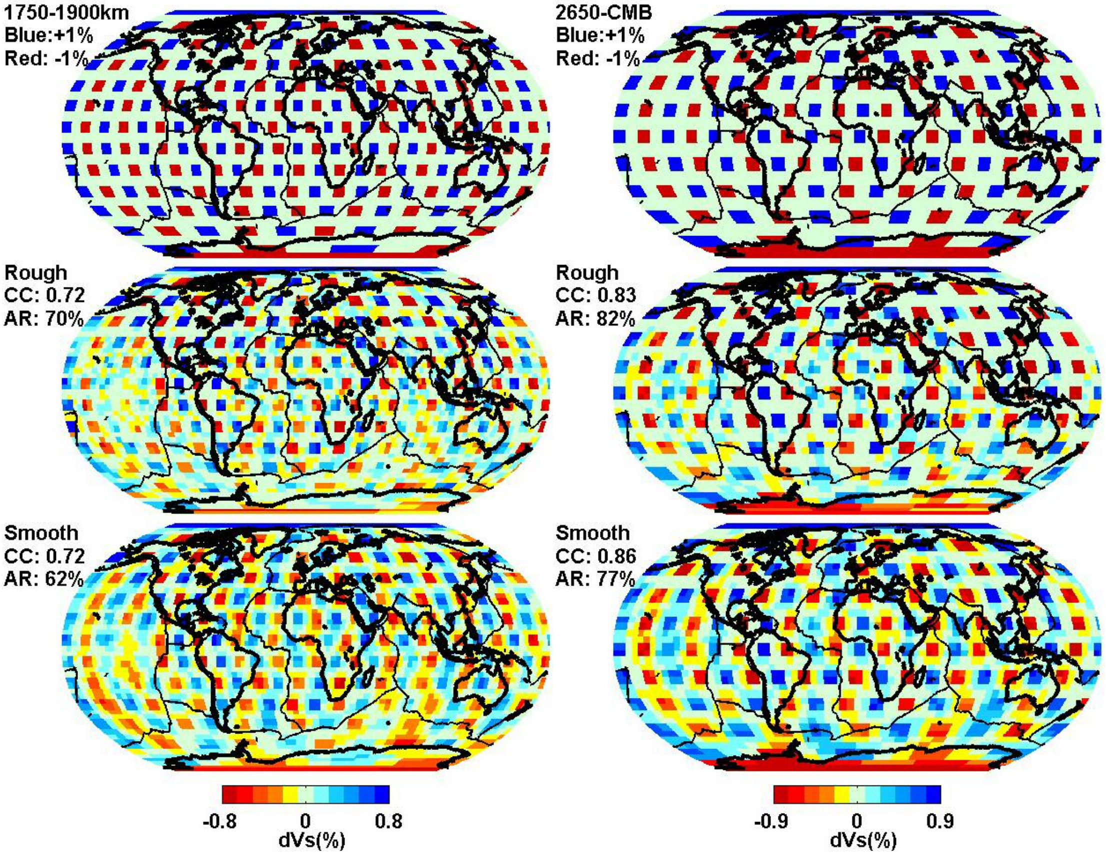

Figure 2.14 (continued) The left column contains the synthetic model (top) and recovered models without smoothing constraints (middle) and with smoothing constraints (bottom) for the depth layer 1750-1900 km. The right column is similar for the D'' layer (2650 km to the CMB).

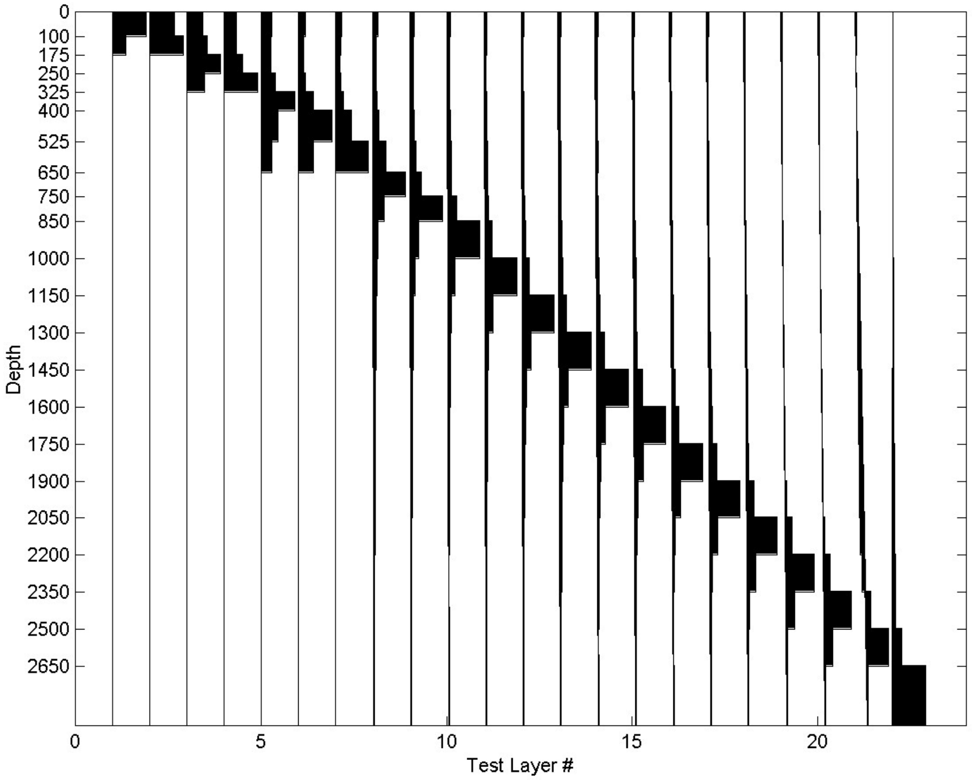

Figure 2.15 RMS velocities within each depth layer for each of the synthetic tests. This gives a general view of how signal may be vertically distributed in the actual model. For example, placing anomalies only within the top layer (layer #1) results in some heterogeneity leaking into the layer below as determined by the inversion procedure. However, the iterative inversion procedure prevents further leakage into deeper layers. The amplitude distribution for test layer #5 reveals significant leakage above and below which may account for some of the apparent deep extensions of the cratonic roots as well as other features including the East African Rift Zone.

2.9 Results and conclusions

Selected depth slices of the optimum model are displayed in Figure 2.16 and the complete model is displayed in Appendix C. In the shallow upper mantle (0 to 250 km depth), the model is highly correlated to tectonic provinces. Specifically, the velocity heterogeneity is dominated by fast (blue) anomalies beneath continental cratons. Beneath some continents, the cratonic signatures appear to extend to ~400 km depth (such as beneath Australia, Africa, and limited parts of eastern Europe/western Russia). These deeper signatures beneath the continents may be indicating a downward conductive cooling effect of the overlying cratons or may be products of vertical streaking due to the ray path geometries. It should also be noted that the fast anomalies ~400 km beneath Australia lie within a region with very limited seismic control based on the resolution tests (see Figure 2.14 and Appendix B). Therefore, the actual depth extent of the cratonic signatures beneath Australia is unconstrained by our data.

Aside from the fast anomalies associated with cratonic roots, slow (red) regions corresponding to mid-oceanic ridges are clearly visible in the upper 175 km of the mantle. These signatures are most notable along the East Pacific Rise in the eastern Pacific Ocean which is marked by velocity reductions in excess of 6%. This divergent boundary is also the fastest current spreading center on Earth. Overall, there is a direct correlation of seafloor age with seismic velocity suggesting that the velocity heterogeneity is directly mapping the temperature of the oceanic lithosphere. Another shallow mantle low-velocity feature is located within the East African Rift Zone (EARZ) in Ethiopia and Kenya. The rift is marked by a mostly north-south trending low-velocity lineation that is detected throughout the entire vertical span of the upper mantle (down to ~650 km depth). Because of the vertical nature of many of the ray paths, it is possible that the deep upper mantle heterogeneities in the EARZ are artifacts due to smearing of the strong velocity heterogeneity from shallower depths. In addition to the strong velocity heterogeneity near the surface, there exists a collection of large-scale low-velocity structures in the lower mantle beneath much of the African continent. These deep mantle anomalies could potentially be smeared upward into the upper mantle thereby further obscuring the actual velocity heterogeneity associated with the EARZ.

Near the base of the upper mantle (400-650 km depth), the most prominent features are high-velocity anomalies along the western Pacific subduction zones. These anomalous regions are marked by a ~2% velocity increase most notable beneath Japan, Korea and the Philippines but observable around the entire western half of the Ring of Fire. Another notable high-velocity feature in the same depth range is a zone beneath the southern tip of the South American continent. This anomalous feature extends beneath the Scotia arc region which is also an active subduction zone. These fast anomalies beneath the western Pacific Ocean and South America most likely represent subducted slabs atop the upper-lower mantle boundary. It is unclear whether the upper-lower mantle boundary permanently hinders slabs from penetrating into the lower mantle. This remains an unresolved fundamental issue and more discussion on this topic can be found in Chapter 3.

In the upper/middle of the lower mantle, two types of anomalous features are observed. First, a very slow (red) zone is detected beneath the southern African continent. This feature (marked by ~2% velocity reduction) is an upward extension of a broad and very slow anomaly lying near the base of the mantle known as the African superplume. This upward extension may be indicative of vertical flow through the mantle which may be responsible for the uplift of the southern African continent (Lithgow-Bertelloni & Silver 1998; Gurnis *et al*. 2000). There is more discussion and analysis of this important feature in Chapter 4.

Also at mid-mantle depths, there are linear high-velocity structures beneath the Americas and India most notable between 1000 and 1750 km depths. The fast zones beneath eastern North America are vertically-oriented sheets that correlate well with the expected locations of the subducted Farallon slab which subducted beneath western North America during the Cretaceous period (Grand 1994; Grand *et al*. 1997). Note that the resolution tests demonstrate that this feature lies within a highly resolvable zone (Figure 2.14 and Appendix B). Similarly, the fast anomaly centered deep beneath India has been associated with the consumed Tethys slab (Grand *et al*. 1997; van der Hilst *et al*. 1997). The subduction of the Tethys slab occurred during the closing of the Tethys Sea in the same general time period that the Farallon slab was presumably consumed. The Tethys anomaly appears more dispersed than the Farallon anomaly possibly owing to the lower degree of resolution beneath India rather than differences in the subduction process between the two areas. Similar mid-mantle features are not detected beneath other subduction zones including along the north-western Pacific Ocean where the fast anomalies only persist down to the base of the upper mantle.

Near the base of the mantle, very large-scale low-velocity anomalies centered beneath the central Pacific Ocean and the southern African continent dominate the heterogeneity. These features are commonly referred to as the Pacific and African superplumes, respectively. The superplume anomalies are known to possess complex seismic characteristics (e.g. Ritsema *et al*. 1998, 1999; Ishii & Tromp 1999; Masters *et al*. 2000; Ni *et al*. 2002, 2005; Ni & Helmberger 2003a,b). In particular, studies have concluded that the center of the structures may in fact be denser than the surrounding mantle contradicting what is expected assuming seismic anomalies are due to variations in temperature. In addition, it is believed that portions of these structures have very sharp edges clearly indicating at least a partial chemical origin. Therefore, these structures have been deemed thermochemical plumes and numerical flow models with an intrinsically-dense basal layer have supported this argument (Tackley 2002; McNamara & Zhong 2005).

The zones outside of the superplumes are generally fast and correspond to regions where subduction has occurred over the past 100 million years. This observation was noted by *Richards & Engebretson* (1992) and is fully supported by the model produced in the current study. The implication is that subducted slabs eventually penetrate the entire mantle and eventually pile on the core-mantle boundary indicating whole-mantle flow without permanent flow boundaries. It has therefore been argued that the shape and locations of the superplume structures could be primarily a product of past subduction processes acting to sweep dense material into piles (McNamara & Zhong 2005; Quéré & Forte 2006). There is more discussion on these issues in the following chapters.

In conclusion, a number of features important to the dynamics and evolution of the Earth have been imaged in my new tomographic model. These include subducted slabs that are hindered at the upper-lower mantle boundary indicating a boundary to flow, but it is unclear if hindrance is temporary or permanent. Features that suggest that the slabs eventually penetrate into the lower mantle have also been detected including the Farallon and Tethys slabs. If the interpretations are correct, this would imply that the complete slab hindrance along the western Pacific subduction zones is a temporary situation. In addition, the heterogeneity at the base of the mantle strongly supports the idea that slabs eventually do penetrate the entire length of the mantle and pile upon the core-mantle boundary. This subduction process may sweep intrinsically-dense material into piles known as the superplume structures which may be linked to some hotspots observed at the surface (Thorne *et al*. 2004). However, the connection of hotspots to the proposed superplume piles has not been fully established. The following chapters are focused on addressing these issues more completely by including several geodynamic observations.

100-175km

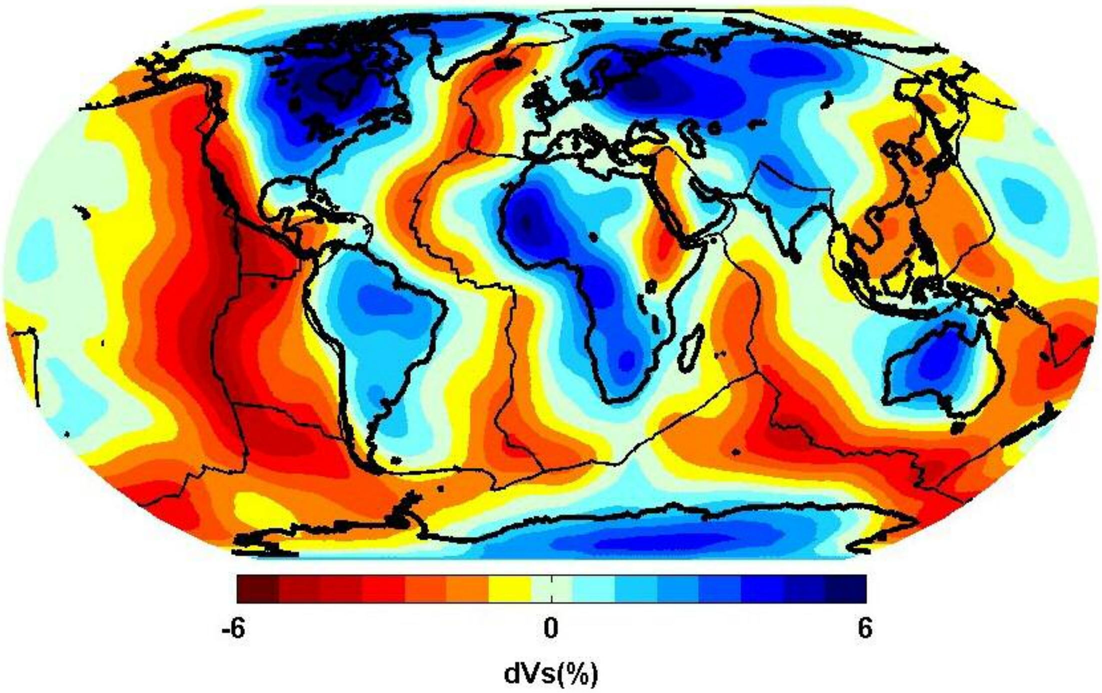

325-400km

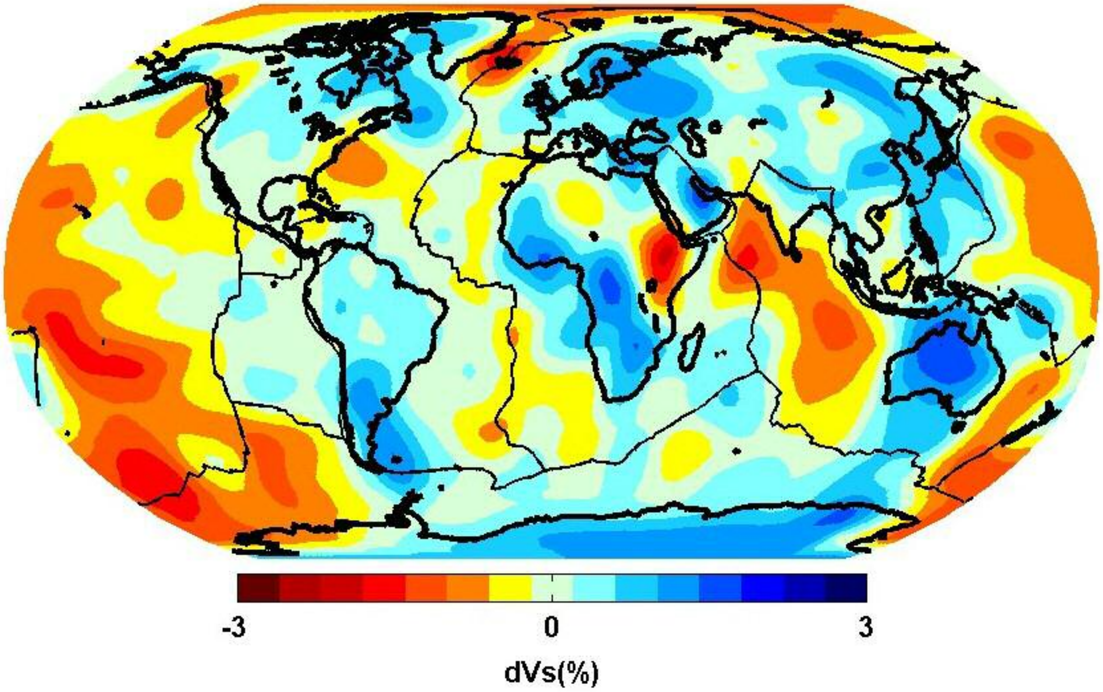

Figure 2.16 The final shear-wave velocity model at selected depths. See text for discussion and Appendix C for the complete model. **(continued on the next page)**

525-650km

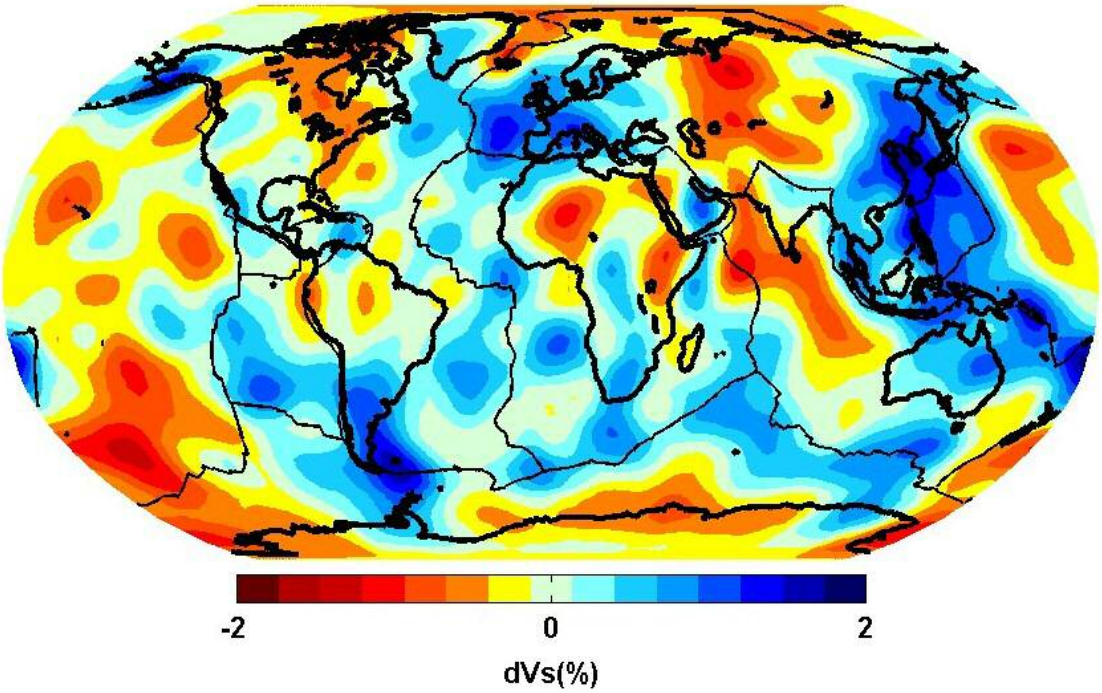

1300-1450km

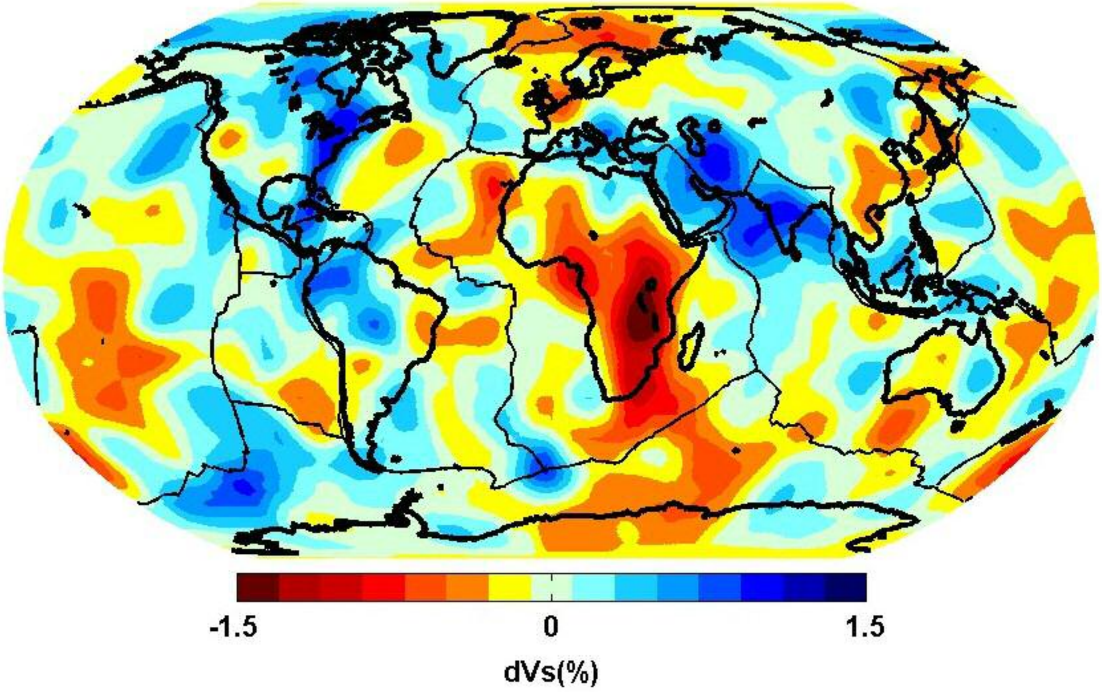

Figure 2.16 (continued)

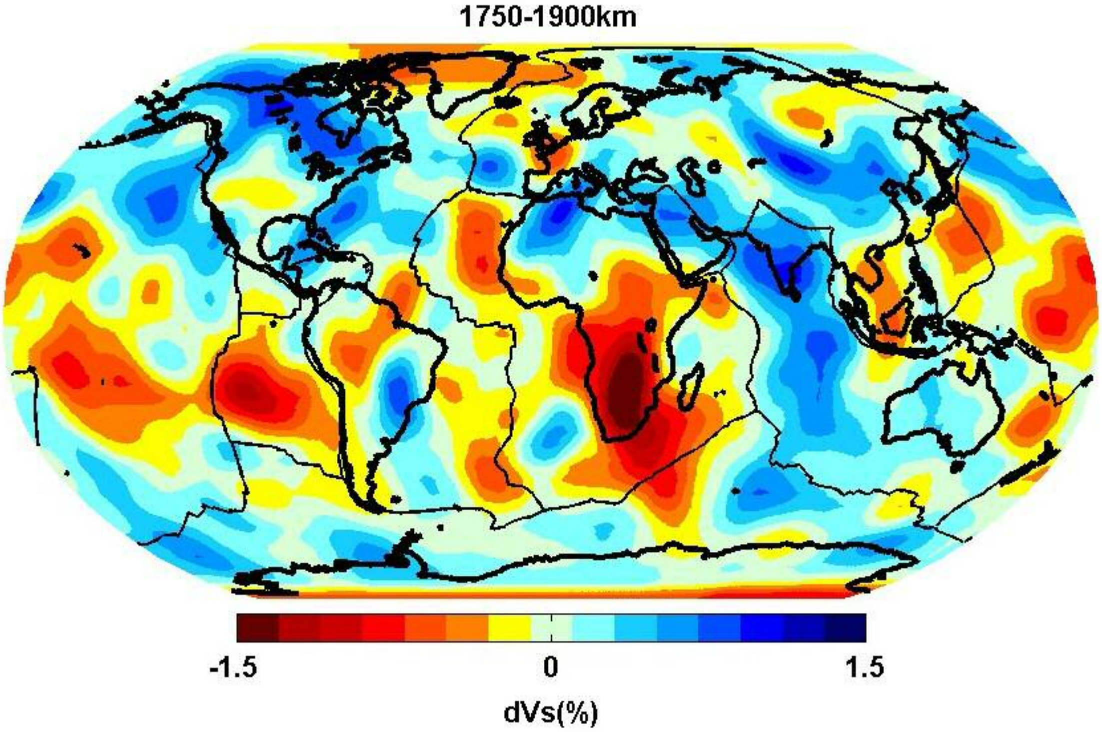

1750-1900km

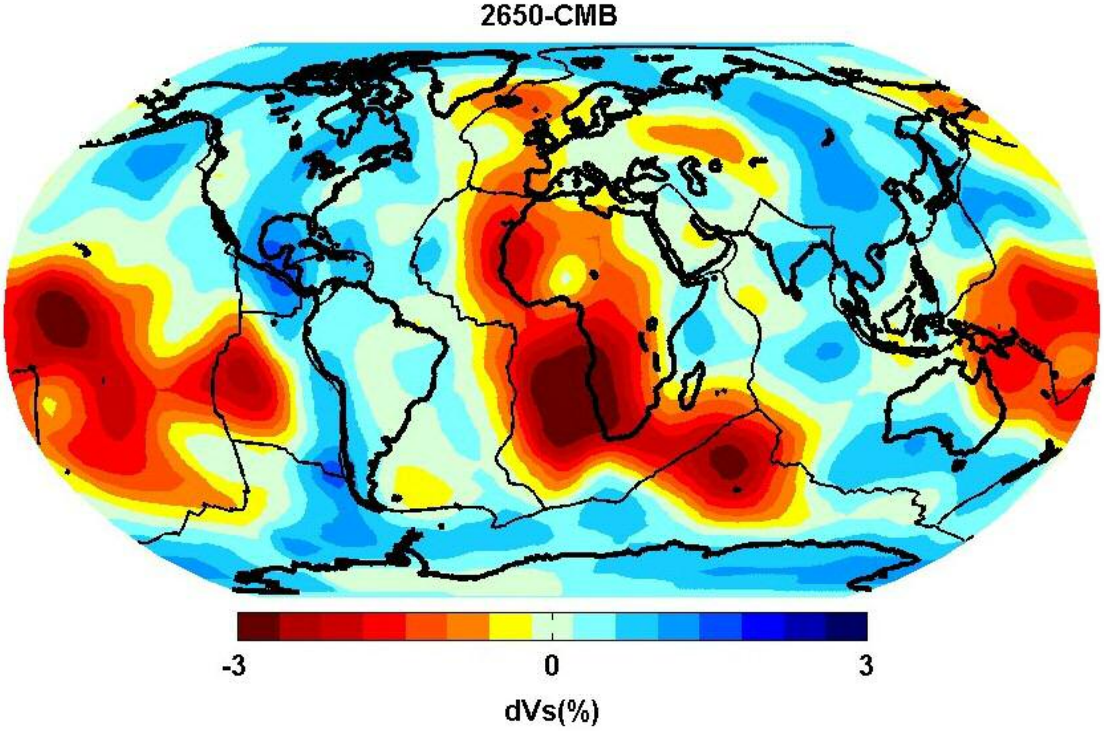

2650-CMB

Figure 2.16 (continued)

2.10 References

Aki, K., A. Christofferson & E.S. Husebye (1977), Determination of the three-dimensional seismic structure of the lithosphere, *J. Geophys. Res.*, *82*, 277-296.

Chapman, C.H. (1978), A new method for computing synthetic seismograms, *Geophys. J. R. Astron. Soc.*, *54*, 481-518.

Dziewonski, A.M. & F. Gilbert (1976), The effect of small, aspherical perturbations on travel times and a re-examination of the corrections for ellipticity, *Geophys. J. R. Astron. Soc. 44*, 7-17.

Dziewonski, A.M. & D.L. Anderson (1981), Preliminary reference Earth model, *Phys. Earth Planet. Inter.*, *25*, 297-356.

Fuchs, K. & G. Muller (1971), Computation of synthetic seismograms with the reflectivity method and comparison with observations, *Geophys. J. R. Astron. Soc. 23*, 417-433.

Grand, S.P. & D.V. Helmberger (1984), Upper mantle shear structure of North America, *Geophys. J. R. Astron. Soc*. 76, 399-438.

Grand, S.P. (1994), Mantle shear structure beneath the Americas and surrounding oceans, *J. Geophys. Res.*, *99*, 11591-11621.

Grand, S.P., R.D. Van der Hilst & S. Widiyantoro (1997), Global seismic tomography: a snapshot of convection in the Earth, *GSA Today*, *7*, 1-7.

Grand, S.P. (2002), Mantle shear-wave tomography and the fate of subducted slabs, *Phil. Trans. R. Soc. Lond. A*, *360*(1800), 2475-2491.

Gu, Y.J., A.M. Dziewonski, W. Su & G. Ekstrom (2001), Models of the mantle shear velocity and discontinuities in the pattern of lateral heterogeneities, *J. Geophys. Res.*, *106*, 11169-11199.

Gurnis, M., J.X. Mitrovica, J. Ritsema & H.J. Van Heijst (2000), Constraining mantle density structure using geological evidence of surface uplift rates: The case of the African Superplume, *Geochem. Geophys. Geosys.*, *1*(7), doi: 1999GC000035.

Hansen, P.C. (1992), Analysis of discrete ill-posed problems by means of the L-curve, *SIAM Rev.*, *34*, 561-580.

Helmberger, D.V., S. Ni, L. Wen & J. Ritsema (2000), Seismic evidence for ultralow-velocity zones beneath Africa and eastern Atlantic, *J. Geophys. Res.*, *105*, 23865-23878.

Ishii, M. & J. Tromp (1999), Normal-mode and free-air gravity constraints on lateral variations in velocity and density of Earth’s mantle, *Science*, *285*(5431), 1231-1236.

Ishii, M. & J. Tromp (2004), Constraining large-scale mantle heterogeneity using mantle and inner-core sensitive normal modes, *Phys. Earth Planet. Inter.*, *146*(1-2), 113-124.

Karason, H. & R.D. van der Hilst (2000), Constraints on mantle convection from seismic tomography, in: M.R. Richards, M.R. Gordon, R.D. van der Hilst (Eds.), The History and Dynamics of Global Plate Motion, AGU, Washington, DC, pp. 277-288.

Kennett, B.L.N. & A. Gorbatov (2004), Seismic heterogeneity in the mantle—strong shear wave signature of slabs from joint tomography, *Phys. Earth Planet. Inter.*, *146*, 87-100.

Lay, T. & T. C. Wallace (1995), “Modern Global Seismology”, Academic Press, San Diego, 521pp.

Lithgow-Bertelloni, C. & P.G. Silver (1998), Dynamic topography, plate driving forces and the African superswell, *Nature*, *395*(6699), 269-272.

Loper, D.E. & T. Lay (1995), The core-mantle boundary region, *J. Geophys. Res.*, *100*, 6397-6420.

Masters, G., G. Laske, H. Bolton & A.M. Dziewonski (2000), The relative behavior of shear velocity, bulk sound speed, and compressional velocity in the mantle: implications for chemical and thermal structure, *in Earth’s Deep Interior: Mineral Physics and Tomography from the Atomic to the Global Scale*, edited by S.-I. Karato et al., pp. 63-87, AGU, Washington, DC.

McNamara, A.K. & S. Zhong (2005), Thermochemical structures beneath Africa and the Pacific Ocean, *Nature*, *437*(7062), 1136-1139.

Megnin, C. & B. Romanowicz (2000), The three-dimensional shear velocity structure of the mantle from the inversion of body, surface and higher-mode waveforms}, *Geophys. J. Int.*, *143*, 709-728.

Montelli, R., G. Nolet, F.A. Dahlen, G. Masters, R.E. Engdahl & S.H. Hung (2004), Finite-frequency tomography reveals a variety of plumes in the mantle, *Science*, *303*, 338-343.

Mooney, W.D., G. Laske & G. Masters (1998), CRUST 5.1: a global crustal model at 5 x 5 degrees, *J. Geophys. Res. Solid Earth*, *103*(B1), 727-747.

Ni, S. & D.V. Helmberger (2001a), Horizontal transition from fast to slow structures at the core-mantle boundary; South Atlantic, *Earth Planet. Sci. Lett.*, *187*, 301-310.

Ni, S. & D.V. Helmberger (2001b), Probing an ultra-low velocity zone at the core mantle boundary with P and S waves, *Geophys. Res. Lett.*, *28*, 2345-2348.

Ni, S.D., E. Tan, M. Gurnis & D.V. Helmberger (2002), Sharp sides to the African superplume, *Science*, *296*(5574), 1850-1852.

Ni, S.D. & D.V. Helmberger (2003a), Ridge-like lower mantle structure beneath South Africa, *J. Geophys. Res. Solid Earth*, *108*(B2), doi:10.1029/2001JB001545.

Ni, S.D. & D.V. Helmberger (2003b), Seismological constraints on the South African superplume; could be the oldest distinct structure on Earth, *Earth Planet. Sci. Lett.*, *206*(1-2), 119-131.

Ni, S.D., D.V. Helmberger & J. Tromp (2005), Three-dimensional structure of the African superplume from waveform modeling, *Geophys. J. Int.*, *161*, 283-294.

Paige, C.C. & M.A. Saunders (1982), LSQR: an algorithm for sparse linear equations and sparse least squares, *ACM Transactions on Mathematical Software*, *8*, 43-71.

Panning, M. & B. Romanowicz (2004), Inferences on flow at the base of Earth's mantle based on seismic anisotropy, *Science*, *303*(5656), 351-353.

Quéré, S. & A.M. Forte (2006), Influence of past and present-day plate motions on spherical models of mantle convection: implications for mantle plumes and hotspots, *Geophys. J. Int.*, *165*, 1041-1057.

Richards, M.A. & D.C. Engebretson (1992), Large-scale mantle convection and the history of subduction, *Nature 355*, 437-440.

Ritsema, J., H.J. van Heijst & J.H. Woodhouse (1999), Complex shear wave velocity structure imaged beneath Africa and Iceland, *Science 286,* 1925-1928.

Ritsema, J., S. Ni, D.V. Helmberger & H.P. Crotwell (1998), Evidence for strong shear velocity reductions and velocity gradient in the lower mantle beneath Africa, *Geophys. Res. Lett.*, *25*(23), 4245-4248.

Ritsema, J., H.J. Van Heijst & J.H. Woodhouse (1999), Complex shear wave velocity structure imaged beneath Africa and Iceland, *Science*, *286*(5446) 1925-1928.

Robertson, G.S & J.H. Woodhouse (1996), Ratio of relative S to P velocity heterogeneity in the lower mantle, *J. Geophys. Res*., *101*, 20041-20052.

Shapiro, N.M. & M.H. Ritzwoller (2002), Monte-Carlo inversion for a global shear-velocity model of the crust and upper mantle, *Geophys. J. Int.*, *151*, 88-105.

Spakman, W. & G. Nolet (1988), Imaging algorithms, accuracy and resolution in delay time tomography, in "Mathematical Geophysics" (eds. Vlaar, Nolet, Wortel and Cloetingh), *D. Reidel Publishing Company*, pp. 155-187.

Su, W. & A.M. Dziewonski (1997), Simultaneous inversion for 3-D variations in shear and bulk velocity in the mantle, *Phys. Earth Planet. Inter.*, *100*(1-4), 135-156.

Tackley, P.J. (2002), Strong heterogeneity caused by deep mantle layering, *Geochem. Geophys. Geosys.*, *3*, doi: 10.1029/2001GC000167.

Thorne, M.S., E.J. Garnero & S.P. Grand (2004), Geographic correlation between hot spots and deep mantle lateral shear-wave velocity gradients, *Phys. Earth. Planet. Int.*, *146*, 47-63.

Van der Hilst, R.D., S. Widiyantoro & E.R. Engdahl (1997), Evidence for deep mantle circulation from global tomography, *Nature*, *386*, 578-584.

Zhao, D. (2001), Seismic structure and origin of hotspots and mantle plumes, *Earth Planet. Sci. Lett. 192*, 251-265.

Chapter 3

Constraining Mantle Flow with Seismic and Geodynamic Data

3.1 Abstract

Understanding the style of convective flow occurring in the mantle is essential to understand the thermal and chemical evolution of Earth's interior as well as the forces driving plate tectonics. Models of mantle convection based on three-dimensional (3-D) seismic tomographic reconstructions have the potential to provide the most direct constraints on mantle flow. Seismic imaging of deep Earth structure has made great advances in recent years; however it has not been possible to reach a consensus on the nature of convection in the mantle. Models of mantle flow based on tomography results have yielded variable conclusions largely because of the inherent non-uniqueness and differing degrees of resolution of seismic tomography models as well as the difficulty in determining flow directly from seismic images. Here we address this difficulty by simultaneously inverting global seismic and convection-related data sets. The seismic data consist of globally distributed shear body wave travel times including multi-bounce S-waves, shallow-turning triplicated phases, as well as core reflections and phases traversing the core (SKS and SKKS). Convection-related datasets include global free air gravity, tectonic plate divergence, and excess ellipticity of the core-mantle boundary. In addition, the convection-related constraint on dynamic surface topography is estimated on the basis of a recent global model of

crustal heterogeneity. These convection-related observables are related to mantle density anomalies through instantaneous mantle flow calculations and linked to the seismic data via optimized density-velocity scaling relationships. Simultaneous inversion allows us to test various mantle flow hypotheses directly against the combined seismic and convection data sets, rather than considering flow predictions based solely on a seismically-derived 3-D mantle model. In this study, we test four different mantle flow hypotheses, including whole-mantle flow and models with impenetrable flow boundaries at depths of 670 km, 1200 km, and 1800 km. This hypothesis testing shows that the combined global seismic and geodynamic data sets are best reconciled when a whole-mantle flow scenario is considered. Convection models with restrictive flow boundaries within the lower mantle provide distinctly poorer fits to these combined data sets providing evidence that the mantle flows without permanent hindrance at the boundaries considered.

3.2 Introduction

The simplest hypothesized mode of convection is the whole-mantle scenario where the entire mantle convects as a single layer with continuous vertical mass and heat transport from the core-mantle boundary (CMB) to the surface. The whole-mantle flow scenario does not exclude the presence of phase transitions and viscosity stratification, which can affect the amplitude and pattern of flow, but, it does exclude global chemical discontinuities, which act as impermeable flow horizons within the mantle. Seismic tomographic images of 3-D mantle structure have often been invoked as primary evidence supporting whole-mantle flow because of the association of fast seismic anomalies in the lower mantle with recently subducted slabs (Grand *et al*. 1997; Masters *et al*. 2000). Furthermore, the correlation of high-velocity zones at the base of the mantle with regions of ancient subduction suggests that plates may descend across the entire mantle and form slab graveyards near the CMB demonstrating unrestricted flow over long time scales (Richards & Engebretson 1992).

An alternative to whole-mantle flow is layered-flow where it is assumed that mantle flow is segregated by an internal boundary across which vertical flow is prohibited. This style of convection implies a mantle that is chemically and thermally stratified at the boundary. The strongest arguments favoring layered convection have been mainly based on geochemical considerations. See *Hofmann* (1997) and *Tackley* (2000) for reviews. Purely numerical simulations of phase-change modulated thermal convection have also indicated that if the Clapeyron slope of the phase change near 670 km depth is sufficiently negative, a layered style of convection would eventually develop without the need for pure chemical stratification (Machetel & Weber 1991; Tackley *et al.*1994; Solheim & Peltier 1994).

Direct evidence for layered convection from seismic tomography and seismicity mainly rests on observations that, in some regions, subducted tectonic plates appear to be flattened or perhaps halted near 670 km depth. This suggests that the depth region around the base of the upper mantle transition zone acts as a convective flow boundary prohibiting subducting slabs from entering the lower mantle (Zhou & Clayton 1990). It has thus been proposed that an alternative explanation for the correlation between the surface location of subduction zones and fast seismic anomalies in the lower mantle is thermal coupling across the flow boundary acting to cool the region just below subducted slabs (Čižková *et al*. 1999). In addition, there are concerns that the apparent extensions of seismically-imaged slabs into the lower mantle are merely artifacts produced by sampling and processing problems within tomographic techniques thereby discounting the existence of coherent anomalous features in some regions of the lower mantle (Hamilton 2002).

Alternatives to strict layering between the upper- and lower-mantle have allowed for a partial flow boundary where mass transport is reduced but not entirely inhibited near 670 km depth (Thoraval & Machetel 1995; Le Stunff & Ricard 1997; Čadek & Fleitout 1999, 2003). Some of these studies have concluded that mass transfer across the 670 km discontinuity must be reduced by a factor of about 3 in order to match the long-wavelength geoid observations (Čadek & Fleitout 1999, 2003). Such results have been obtained, however, in the context of mantle flow models in which the plate velocities are imposed a-priori rather than predicted on the basis of the driving buoyancy forces in the mantle (Ricard & Vigny 1989; Forte & Peltier 1991). The latter approach will be employed in the flow modeling presented below.

Although layered convection models have mostly assumed a flow boundary at 670 km depth (either partial or strict), other boundaries to flow have also been proposed in recent work. Seismic reflection horizons have been detected in some regions of the lower mantle and they have been invoked as evidence for a flow boundary at those depths (Kawakatsu & Niu 1994; Niu & Kawakatsu 1997). Furthermore, it has been suggested that a flow boundary must exist near 920 km depth in order to simultaneously explain Earth's long-wavelength gravity field and dynamic surface topography (Wen & Anderson 1997). Further support for such a flow boundary has been based on interpretations of tomography models which suggest that subducted slabs eventually penetrate below 670 km depth but are hindered near 1000 km depth (Fukao *et al*. 2001). Other studies have concluded that the lower ~1000 km of the mantle is chemically-distinct based on a combination of geochemical and seismic considerations (Kellogg et al. 1999; Van der Hilst & Karason 1999; Trampert et al. 2004). This implies the possible presence of significant barrier to vertical convective flow which may be located in the depth interval of 1600 to 1800 km.

The controversy surrounding the nature of convective flow in the Earth's mantle is due to several factors. In spite of the apparently increasing agreement among tomography models (Romanowicz 2003), there still exist large enough differences to allow for varying interpretations of mantle flow. In this regard, it is important to recognize that seismic tomography models only provide a snapshot of the present-day 3-D mantle structure and, by themselves, provide no direct information on convective flow in the mantle. Mapping the flow in the mantle requires the introduction of dynamic models that interpret the seismic anomalies in terms of density anomalies which are the driving force of mantle flow. Such mantle flow models are subject to uncertainties arising from imperfect or insufficient mineral physical data required to derive a scaling relation between seismic and density anomalies (Karato & Karki 2001; Cammarano *et al*. 2003). Another fundamental uncertainty with using tomography models to infer mantle flow is that the viscosity of the mantle must be known. Mantle viscosity is still uncertain but there has been progress through integrated analyses (Mitrovica & Forte 1997; Panasyuk & Hager 2000; Mitrovica &

Forte 2004). Hypothesis testing based on the simultaneous inversion of combined seismic and geodynamic data sets (Forte *et al*. 1994; Forte & Woodward 1997) allows us to effectively counter these uncertainties inherent in modeling mantle flow with any single seismic tomography model. In this paper, we test four end-member mantle-flow hypotheses: whole-mantle flow and layered flow with boundaries at 670 km, 1200 km and 1800 km depth, respectively. For each flow scenario, we derive optimum radial seismic velocity-to-density scalings and radial viscosity models by carrying out inversions of a large and diverse array of convection-related surface data and post-glacial rebound data. The objective is to directly test the plausibility of each end-member flow hypothesis against the combined seismic and geodynamic data sets and provide constraints on the nature of convective flow in the mantle. We do not directly consider hybrid flow scenarios, but rather attempt to simultaneously reconcile the seismic and geodynamic data with the simplest possible flow scenarios without a free parameter limiting mass transport at the boundaries considered.

3.3 Characterizing 3-D mantle structure

Seismic waves traversing the Earth's interior provide the most direct constraint on mantle structure and tomographic imaging has made great strides due to increased amounts of available data and development of techniques (Grand *et al*. 1997; Van der Hilst *et al*. 1997; Masters *et al*. 2000; Romanowicz 2003; Ritsema *et al*. 1999; Karason & Van der Hilst 2000; Megnin & Romanowicz 2000; Gu *et al*. 2001; Zhao 2001; Grand 2002). However, determination of mantle flow from tomographic images is limited since the overall shape, depth extent, sharpness and intensity of the heterogeneous features are not absolutely resolved in any given tomographic model. This is due to multiple factors including variations in the type of data used, approximations in modeling techniques and, perhaps most importantly, the non-uniqueness of the problem due to insufficient data sampling. The addition of more data to these analyses provides stricter constraints on mantle structure and continually reduces these affects.

For this study, we use a shear-wave tomography model produced with the general methodology presented in Chapter 2. However, it should be noted that the seismic data set used in this chapter precedes that used in the final model presented in Chapter 2. In addition, the velocity model used here is rougher than the “optimum” model as determined in Chapter 2; thus the level of fit to the dataset is slightly higher. This shear-wave tomography model (TX2005) provides a 95.7% variance reduction to the residual travel time data and it serves as a starting model for the joint inversions of the combined seismic-geodynamic data sets. Selected maps of the TX2005 shear-wave velocity model are shown in Figure 3.1. For clarity, the mean velocity perturbation was removed and velocity scales vary with each depth. There are several dynamically-significant features observed in the shear-wave velocity model. Specifically, within the transition zone, fast anomalies associated with western Pacific subduction zone are most prominent (Figure 3.1c). These features are not present in the lower mantle suggesting that the subducted slabs are stagnant in the upper mantle. However, fast zones in the mid-mantle beneath the Americas and Eurasia may be attributed to recently subducted slabs well below the upper-lower mantle boundary. In addition, slow regions corresponding to the East African Rift zone can be seen in

Figure 3.1d which may be physically connected to the African superplume in the deeper mid-mantle (Figure 3.1e,f). Another large-scale feature is a broad slow anomaly beneath the Pacific Ocean in the deep mantle that has no clear connection to the surface (Figure 3.1g,h). Collectively, these features provide hints about the style of flow occurring in the mantle. However, the velocity model does not provide for a perfect understanding of mantle dynamics requiring the need for constraints directly dependent on the style of flow.

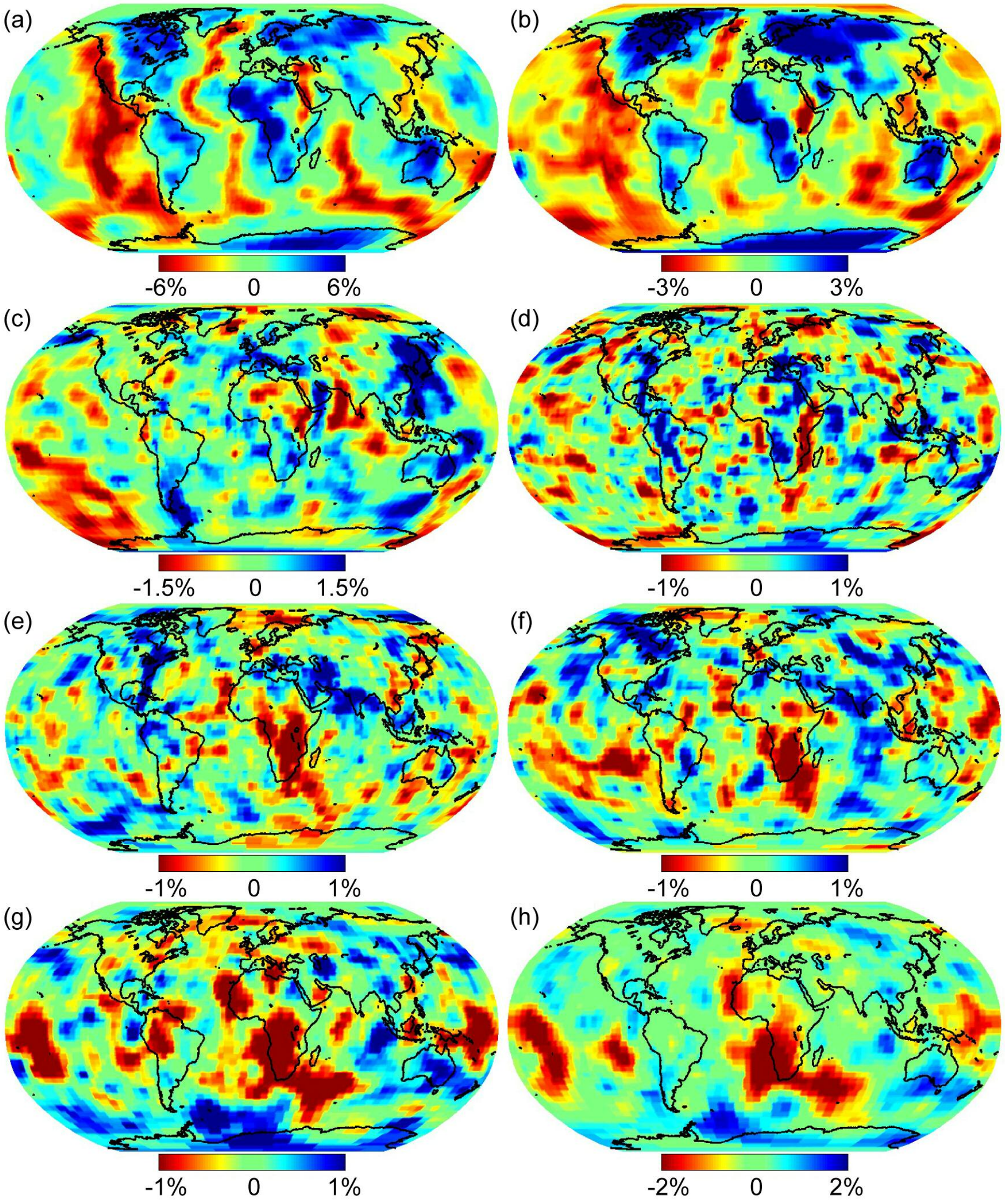

Figure 3.1 Shear-wave tomography model TX2005. (a) 0-100 km; (b) 175-250 km; (c) 425-525 km; (d) 850-1000 km; (e) 1300-1450 km; (f) 1750-1900 km; (g) 2200-2350; and (h) 2500-2650 km. The model is derived solely from the body wave seismic data and provides a 95.7% variance reduction to our travel time residual data. Note that the means are removed and velocity scales are adjusted for each depth range.

3.4 Mantle flow constraints from geodynamic data

A successful model of mantle flow must be capable of reproducing a wide array of convection-related surface observations. We employ a diverse array of global geodynamic observables, which include: surface gravity, surface topography, tectonic plate motions and CMB topography. Each of these data sets provides independent constraints on 3-D mantle heterogeneity and flow. In addition, they provide a sampling of mantle structure that is independent of that supplied by global seismic data. In this study, we employ satellite-derived free-air gravity anomalies from the GEM-T2 geopotential model (Marsh *et al*. 1990), crust-corrected dynamic surface topography (Forte & Perry 2000) and the horizontal divergence of the tectonic plate velocities from the NUVEL-1 model (DeMets *et al*. 1990), expressed in terms of spherical harmonic basis functions up to harmonic degree l=16. The most robust and accurate constraint on CMB topography is the excess ellipticity of this boundary, which has been determined by analyses of free-core nutation (Herring *et al*. 2002). This excess ellipticity is represented by a single zonal harmonic of degree l=2 and corresponds to 400 meters of excess flattening of the CMB (Mathews *et al*. 2002) that is presumably flow-induced. The least robust constraint, owing to the uncertainties in crustal heterogeneity (Perry *et al*. 2002), is the estimate of crust-corrected dynamic topography. In this study we employ the CRUST2.0 model (Bassin *et al*. 2000) to estimate the crustal isostatic correction required to recover the dynamic surface topography.

The geodynamic surface observables are linearly related to mantle density perturbations by theoretical, wavelength-dependent kernel functions that represent the viscous flow response of the mantle to internal density loads (Richards & Hager 1984; Ricard *et al*. 1984; Forte & Peltier 1987). We calculate the geodynamic kernels using a viscous flow theory for a compressible, gravitationally consistent mantle on which the tectonic plate motions are dynamically coupled to the underlying mantle flow (Forte & Peltier 1991; Forte 2000). The form of the geodynamic kernels depends on the viscosity structure of the mantle and on whether there are any internal flow-boundaries present. We determined geodynamic kernels for the four different flow scenarios we wish to test, namely whole-mantle flow and strictly layered flow with internal boundaries at 670 km, 1200 km, and 1800 km depth, respectively. Selected harmonic degrees of these kernel functions are plotted in Figure 3.2 and it can be seen that there are significant sensitivity variations from one flow scenario to the next.

The reference seismic tomography model TX2005 was used to derive an optimal scaling between seismic shear velocity anomalies and mantle density anomalies and the optimal viscosity distribution in the mantle. For each of the four flow scenarios, the geodynamic data were inverted using an iterative, Occam inversion (Constable *et al*. 1987) in which the shear velocity-to-density scaling ($d[\ln\rho]/d[\ln V_S]$) and viscosity are allowed to vary only with depth. The Occam inversions for viscosity also employ a suite of post-glacial rebound observations (Mitrovica *et al*. 2000) in addition to the convection-related data discussed above. The details of the Occam inversion procedure are fully described in *Mitrovica & Forte* (2004). Figure 3.3 shows the resulting profiles for the viscosity and velocity-density scaling which provide the best fit to the geodynamic data for the flow hypotheses we test. The most evident feature in the viscosity profiles is the strong, 3-order magnitude increase in viscosity from the base of the lithosphere to the deep lower mantle. These profiles are also characterized by a thin low-viscosity layer near 670 km depth (except for the flow scenario with a boundary at 670 km) and a viscosity peak in the mid-mantle region which varies in depth depending on the assumed flow boundary location. The origin of the low-viscosity layer at 670 km depth may perhaps be explained in terms of the rheological effect of the endothermic spinel-post-spinel phase transition at this depth (Panasyuk & Hager 2000; Panasyuk & Hager 1998). The $d[\ln\rho]/d[\ln V_S]$ profiles also exhibit significant variations from one flow scenario to the next. In particular, the model with a flow boundary near 670 km depth requires a significant reduction in velocity-density scaling, characterized by near-zero and negative values, in the middle of the lower mantle.

As noted above, the viscous flow theory we employ is based on the assumption that mantle viscosity varies with depth only. It is expected, however, that the effective viscosity in the mantle can also vary laterally, owing to the strong temperature-dependence of the microphysical processes which control the creep of mantle rocks (Karato & Wu 1993). It is therefore important to address the question of possible bias or error incurred by the neglect of such lateral viscosity variations. It is possible to estimate this bias with more complex flow models, which explicitly include the dynamical effects of large-amplitude, global-scale viscosity heterogeneity (Forte & Peltier 1994; Forte & Mitrovica 2001; Moucha *et al*. 2004). The presence of lateral viscosity variations which span three orders of magnitude throughout the mantle can be shown to perturb the predicted gravity and topography fields by about

20-25%, compared to flow models which have only a depth-dependent viscosity (Forte & Mitrovica 2001; Moucha *et al*. 2004). These perturbations are not likely to change the conclusions of this study, although they may change the resultant models and data fits to a small degree.

If we calculate the geodynamic surface observables for the four flow scenarios, in each case using the TX2005 tomography model, we find that the whole-mantle flow assumption yields a fit to the geodynamic data which is distinctly better than the three layered-flow scenarios. The data variance reductions calculated using the starting seismic model are listed in Table 3.1 (in parentheses). It can be seen from Table 3.1 that even for the whole-mantle flow case, there is still a significant misfit to the geodynamic observables. The misfit to the free-air gravity anomalies is always much greater than that obtained for the non-hydrostatic geoid since the amplitude spectra of these two fields differ significantly (Forte *et al*. 1994). The difficulty in fitting the gravity anomalies is greatly amplified by the requirement that the flow models must also deliver simultaneous fits to the other geodynamic observables (plate motions, topography). It is therefore important to determine whether the current misfits are due to errors in the seismic model or to errors in the hypotheses tested. It is also critical to determine whether incomplete seismic resolution leads to an artificial bias that favors the whole-mantle flow assumption.

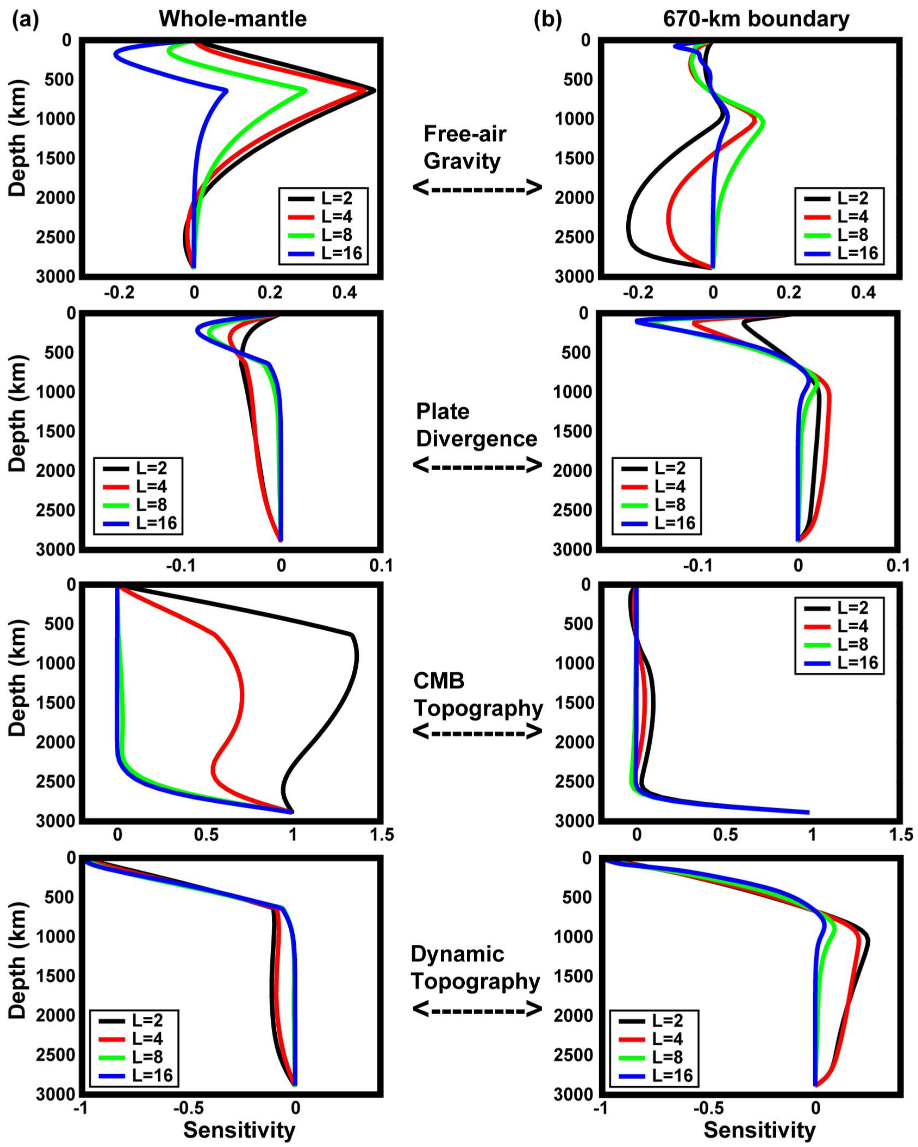

Figure 3.2 Geodynamic depth-dependent sensitivity kernels for spherical harmonic degrees: $l = 2$, 4, 8, and 16. (a) Free-air gravity (top left), plate divergence (top right), surface dynamic topography (bottom left), and CMB topography (bottom right) sensitivity kernels for the whole-mantle flow case. (b) Same as in (a) for the 670 km flow boundary case. Notice that all kernels for the 670 km boundary case have zero crossings at 670 km depth. This is due to isostatic compensation of density loads by the deformation of the boundary producing no surface signal. The other layered cases (1200 and 1800 km) exhibit similar zero crossings at their respective depths (not shown). Note that these kernels represent the free-slip boundary conditions for tectonic plate coupling (Forte & Peltier 1994). See Chapter 5 for a more complete set of geodynamic kernels for both the free-slip and no-slip boundary conditions for the whole-mantle flow case.

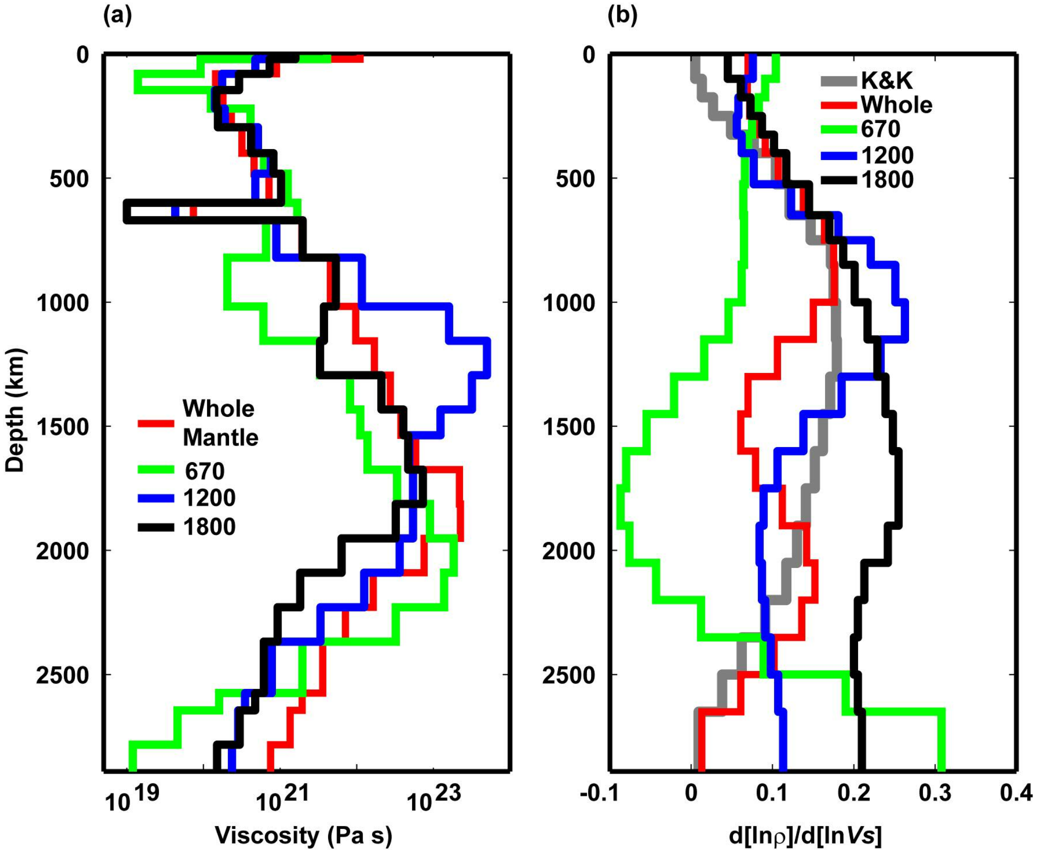

Figure 3.3 Radially-symmetric viscosity and velocity-to-density scaling ($d[\ln\rho]/d[\ln V_S]$) profiles for each of the considered flow scenarios. These profiles are calculated from Occam-style inversions of glacial isostatic adjustment and other geodynamic constraints described in the text. (a) Viscosity profiles for whole-mantle flow and flow boundaries at 670, 1200 and 1800 km depths. These profiles generally exhibit viscosity increase with depth to the mid-mantle region and subsequent drop-off with depth to the CMB. The profiles are similar in the upper 1000 km excluding the solution with a boundary at 670 km. In this case, the low-viscosity notch near 670 km is non-existent and a new notch is formed near the surface (see text for discussion). (b) Velocity-to-density scaling relationships are represented as $d[\ln\rho]/d[\ln V_S]$ for each of the flow scenarios. For comparison, the 'K&K' curve represents predicted scaling relationships that consider dominance of thermal affects. The other relationships are Occam-style solutions coupled to the corresponding viscosity profile. The assumption of flow bounded at 670 km depth requires a scaling profile that dramatically diverges from a purely thermal relationship between shear wave velocity and density. In particular, a broad low-scaling zone (even negative) centered at ~1800 km is observed. This suggests that velocity perturbations are nearly unrelated or negatively correlated to density perturbations in this depth zone when a flow boundary at 670 km is considered.

Table 3.1 Statistics of joint models providing 95% seismic data fit (λ=0.8)

Flow Type	Free-air gravity[a] (%)	Plate divergence[b] (%)	Dynamic topography[c] (%)	CMB excess ellipticity[d] (km)
Whole-mantle	92 (45)	87 (39)	63 (52)	0.4
670 km	67 (22)	94 (56)	56 (30)	0.4
1200 km	75 (26)	83 (44)	38 (40)	0.4
1800 km	51 (21)	77 (39)	39 (31)	0.4

Percentages are variance reduction fits to spherical harmonic components. Values in parentheses are fits calulated using the seismically-derived starting model (TX2005) for the given flow type.

[a] Satellite-derived free-air gravity anomalies from the GEM-T2 geopotential model (degrees 2-16) (Marsh et al. 1990).

[b] Horizontal divergence of the tectonic plate velocities from the NUVEL-1 model (degrees 1-16) (DeMets et al. 1990).

[c] Crust-corrected dynamic surface topography estimate (degrees 1-16) (Forte & Perry 2000).

[d] Excess ellipticity is represented by a single zonal harmonic of degree l=2 and corresponds to 400 meters of excess flattening of the CMB (Mathews *et al*. 2002).

3.5 Integrated seismic-geodynamic solutions

The crucial question about seismic resolution of mantle heterogeneity and the resulting uncertainty concerning the mode of flow in the mantle can be most effectively addressed by directly testing different flow hypotheses against combined seismic and geodynamic data sets. Such testing is carried out by performing simultaneous inversions of the global seismic and geodynamic data (Forte *et al.* 1994; Forte & Woodward 1997). The procedure essentially involves combining the geodynamic and seismic data constraints into a single set of linear equations, which is subsequently solved to determine the shear velocity heterogeneity in the mantle for each flow scenario. The convection data are modelled with the geodynamic kernels appropriate for each flow scenario and in each case we impose a connection between perturbations of density and shear velocity by using the associated profile of $d[\ln\rho]/d[\ln V_S]$ (Figure 3.3b). In this analysis, we wish to find a differential shear-wave slowness model, $\mathbf{m}$, that satisfies the following relation:

$$\begin{bmatrix} \mathbf{L} \\ \lambda \mathbf{G}_f \\ \mu \mathbf{c}_f \end{bmatrix} \mathbf{m} = \begin{bmatrix} \mathbf{r} \\ \lambda \mathbf{s} \\ \mu e \end{bmatrix} \tag{3.1}$$

where **L** and **r** are the seismic ray length matrix and the vector of travel time residuals, respectively. $\mathbf{G}_f$ is a matrix of viscosity-dependent geodynamic kernels for a given flow scenario (subscript *f*) where each row represents the sensitivities of a particular spherical harmonic degree and order to a specific convection data type including free air gravity, horizontal plate divergence, and surface dynamic topography. Each value in $\mathbf{G}_f$ assumes the appropriate density-velocity conversions discussed above. The vector $\mathbf{s}$ represents spherical harmonic coefficients corresponding to the convection-related observables. The row vector $\mathbf{c}_f$ and scalar value e represent the l=2 zonal spherical harmonic sensitivity and known solution for the excess CMB ellipticity, respectively.

Each of the geodynamic data fields in Equation 3.1 were normalized by their corresponding estimated standard error. These theoretical errors are estimated, as in *Panasyuk & Hager* (2000), on the basis of differences in geodynamic predictions derived from a suite of previous tomography-based flow models. The resulting geodynamic data norms, as a percentage of the seismic data norm ($\|\mathbf{r}\|$), were maintained at 13, 16, and 9% for the free-air gravity, plate motions, and dynamic topography, respectively. The scalar values λ and μ in Equation 3.1 are weights applied to the geodynamic variables in the inversion to increase their relative weight (and corresponding data norms) compared to the seismic constraints. For example, when λ=1, the geodynamic data norms are equivalent to the previously mentioned relative values. These norms are simply boosted or diminished in the inversion depending on the chosen value of λ. Damping and smoothing constraints are omitted from Equation 3.1 for simplicity but are included in the inversion.

For each flow case, we inverted for a large suite of joint models using the iterative LSQR technique (Paige & Saunders 1982). The system in Equations 3.1 was solved using several geodynamic weighting values (λ). Increasing this weight drives the resulting 3-D mantle models to be less dependent on the seismic constraints and consequently places greater importance on the geodynamic data. The CMB ellipticity constraint is strongly enforced and is matched to very high degrees by amplifying μ appropriately when the geodynamic data are introduced in the tomographic inversion ($\lambda > 0$). We find that there exists no single, optimal value for the geodynamic weight λ, and we therefore present a suite of solutions obtained with a range of scalar weights ($0 \leq \lambda \leq 3$, Figure 3.4). The purely seismic 3-D mantle model ($\lambda = 0$) provides a relatively poor match to the geodynamic data (< 60% variance reduction for all cases and datasets). As we introduce the geodynamic constraints into the inversion ($\lambda > 0$), we find that the geodynamic data fits can be improved dramatically with some adjustment to the starting model. It is also evident that as λ increases, the decline in variance reduction to the seismic data is minimal for the whole-mantle flow case. We find that satisfying the seismic data is most difficult for the three layered flow models as we impose increasing dependence on the geodynamic constraints. For $\lambda > 0.8$, the fit to the seismic data falls below ~95% variance reduction and the layered flow cases begin to show a clear degradation in fits to the seismic data. For this reason, we treat $\lambda = 0.8$ as a key level to evaluate the different flow scenarios. Table 3.1 provides a statistical summary of the data fits for the joint-inversion models that provide a 95% variance reduction of the seismic travel time residuals.

Looking beyond $\lambda = 1$, we find that excellent fits to the geodynamic data can be obtained for the whole-mantle flow hypothesis (approaching 100% for the gravity and plate motions; and 80-90% for the surface dynamic topography), while maintaining

>92% variance reduction to the seismic data. This high degree of reconciliation of the data is achieved with the optimal, Occam-inferred profile of $d[\ln\rho]/d[\ln V_S]$. Note also that the whole-mantle $d[\ln\rho]/d[\ln V_S]$ scaling is similar to a predicted density scaling assuming a dominance of thermal affects in the lower mantle (Karato & Karki 2001) (Figure 3.3b, “K&K” curve). The K&K density-velocity scaling curve is derived for lower mantle conditions considering anharmonic and anelastic effects due to a thermal origin. For illustration purposes, the K&K curve is extrapolated towards zero from the lower mantle to the Earth’s surface in Figure 3.3b. The similarity of the optimized scaling relationship to the theoretical curve suggests that the whole-mantle flow hypothesis, where thermal contributions to density and seismic anomalies are dominant, provides a model of 3-D mantle structure that is consistent with both seismic and geodynamic data.

The worst data fits are obtained for models with flow boundaries at 1200 km and 1800 km depth. This is best verified by evaluating the degradation of variance reduction of the seismic constraints with increasing λ without a dramatic improvement to the geodynamic fits. It is difficult to justify the existence of a flow boundary at the mid-mantle depths considered in the present work since we cannot simultaneously reconcile the data easily with deep-mantle boundaries. Nevertheless, this result does not exclude partial flow boundaries, nor does it exclude multiple boundaries to flow. Inspection of the variance reduction curves shows that the model with a flow boundary at 670 km depth provides only marginally worse fits to the data than the whole-mantle flow model. However, this case requires unusual velocity-density scaling in the middle of the lower mantle characterized by negative values of

$d[\ln\rho]/d[\ln V_S]$ in the depth range 1300 km to 2200 km. Such anomalous values for the density-velocity scaling are not consistent with mineral physics estimates for thermally-controlled variations in the mantle's density field. Negative scaling factors may perhaps be explained in terms of chemical heterogeneity and would imply dominance of chemical contributions to the density field in deeper regions of the mantle (Trampert *et al*. 2004). This would likely mean that thermal convection is not a significant factor in the evolution of the lower mantle which, in our estimation, is unlikely. The current study supports this view since invoking whole-mantle flow with thermally-controlled density variations provides a better match to all data considered. This is most evident from evaluation of the data fit trade-off curves plotted in Figure 3.4, particularly the difficulty in matching the free-air gravity observations and seismic constraints simultaneously when a flow boundary at 670 km is invoked (Figure 3.4a,b). On the other hand, we note that the good fits to the seismic and geodynamic data provided by the whole-mantle flow model require a thin, low-viscosity layer above 670 km depth. This layer may act to partially decouple the flow fields above and below the upper-lower mantle boundary, and, therefore mimic a partial boundary to flow near the 670 km discontinuity.

From Figure 3.4 ($\lambda = 0$) and Table 3.1, it is clear that the purely seismically-derived tomography model does not satisfy the geodynamic constraints to a high degree. However, these data can be matched well with mostly subtle adjustments to the seismically-derived model while maintaining a 95% variance reduction to the seismic constraints (see Figures 3.5-7 for model comparisons). Different mantle flow assumptions affect the model in various ways; however, the primary difference between the seismically-derived model and joint models comes in the form of intensity variations of the anomalous features. This effect is most evident within the large African slow anomaly which is demonstrated in the cross sections in Figures 3.5-7. The western Pacific subduction zone fast region also shows variable intensity near the base of the upper mantle which can be easily recognized for the whole-mantle case in Figure 3.5. In addition, features in the middle of the lower mantle remain intact with only slight intensity and mean variations (Figure 3.6). The most dramatic variations can be observed near the base of the mantle (Figure 3.7) especially beneath the mid-Pacific and Indian oceans where our seismic constraints are weakest (see Figure 3.8 for the seismic data coverage).

The inference of significant changes in mantle heterogeneity in regions of weakest seismic sampling clearly arises from the additional resolving power of the geodynamic data. All joint models include the same seismic data sets and hence the same seismic null space, therefore this will not affect the results of our hypothesis testing. Indeed, the whole point of hypothesis testing is not to consider the detailed structure in any given tomography model but rather to consider the final fit to the data.

The RMS amplitude profiles for the seismic and joint models are plotted in Figure 3.9. In general, all joint models are amplified relative to the starting seismic model. Specifically, all joint models have increased RMS amplitudes in the lower half of the mantle. And, with the exception of the 670 km case, all models exhibit increased amplitudes within the upper mantle transition zone primarily corresponding to subducted slab anomalies (400-650 km model depth range). This is not surprising given that our seismically-derived tomography model is a minimum length solution. It can be seen in Figure 3.9a that in the whole-mantle case, heterogeneity is squeezed away from ~1500 km depth (upward toward the transition zone and downward toward the deep mantle). This characteristic is simply mimicking the sinuous density scaling curve for the whole-mantle case (see Figure 3.3b). The RMS amplitude profile for the 670 km case reveals an amplification maximum in the depth range ~1500-2300 km which corresponds to the region where we find negative density scaling relations for this case (Figure 3.3b). The RMS amplification characteristics of the joint models are reasonable when compared to other recent tomography models (Romanowicz 2003) and are primarily demonstrating the minimum-amplitude nature of our starting seismic model. It is also evident that the optimized density scaling profiles contain correction factors acting to amplify the seismic model by varying degrees (depending on depth and style of flow). Separation of these quantities from the true density-to-velocity conversion is not a primary concern in the current study but will be a focus of future research.

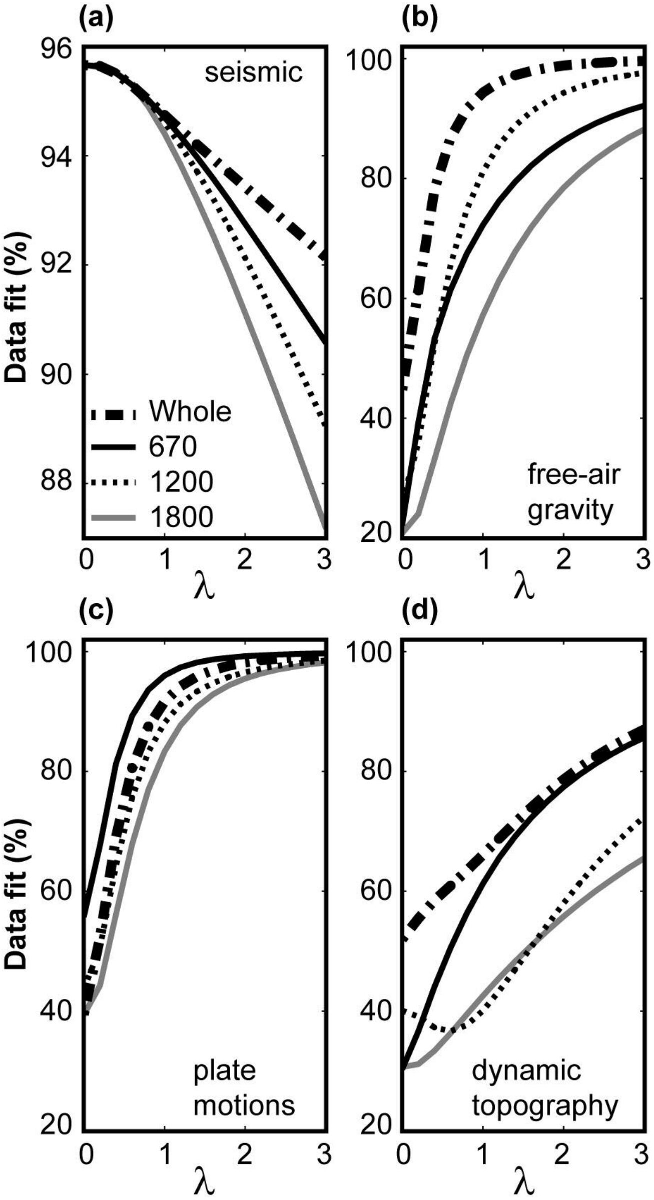

Figure 3.4 Joint model variance reductions to the seismic and geodynamic data. Each curve represents a suite of solutions plotted against a scalar multiplier (λ) that acts as a weight to the geodynamic constraints. The data fits for the seismically-derived model (TX2005, this study) correspond to values at $\lambda=0$. The curves in (a) are seismic data fits as a function of λ demonstrating the effect of forcing the solution to satisfy the geodynamic data for each flow case. The seismic fit decays least rapidly with λ when whole-mantle flow is assumed while deep flow boundaries supply the fastest decay. The curves in (b-d) are variance reduction to the free-air gravity field, horizontal plate motions and dynamic topography. The free-air gravity field and dynamic topography are best matched for the whole-mantle case while maintaining the best fit to the seismic constraints.

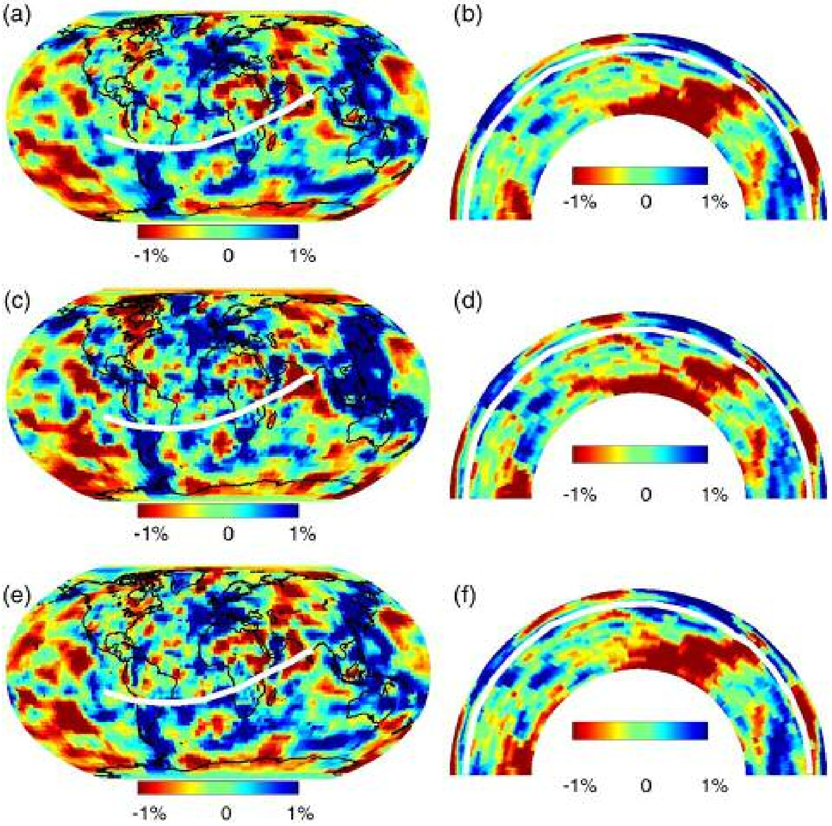

Figure 3.5 Comparisons of the TX2005 shear wave velocity model (a, b) and joint seismic-geodynamic tomographic models assuming whole-mantle flow (c, d) and a flow boundary at 670 km depth (e, f). The maps (left column) are the depth range 525-650 km and the cross sections (right column) are generally west to east as indicated by the great circle paths on the maps. The great circle path line is the same line indicated at 650 km depth in the cross sections. All models are represented as percent velocity perturbation from a 1-D model with a range of ±1%. The seismically-derived model provides a 95.7% variance reduction to the seismic data and each of the joint models provide a 95% fit (λ=0.8, see Table 3.1 for other statistics). It can be seen that most of adjustment from the seismic model is in the intensity of the anomalies particularly along the western Pacific subduction zones at 650 km depth (blue, fast) and in the African superplume feature at greater depths (red, slow).

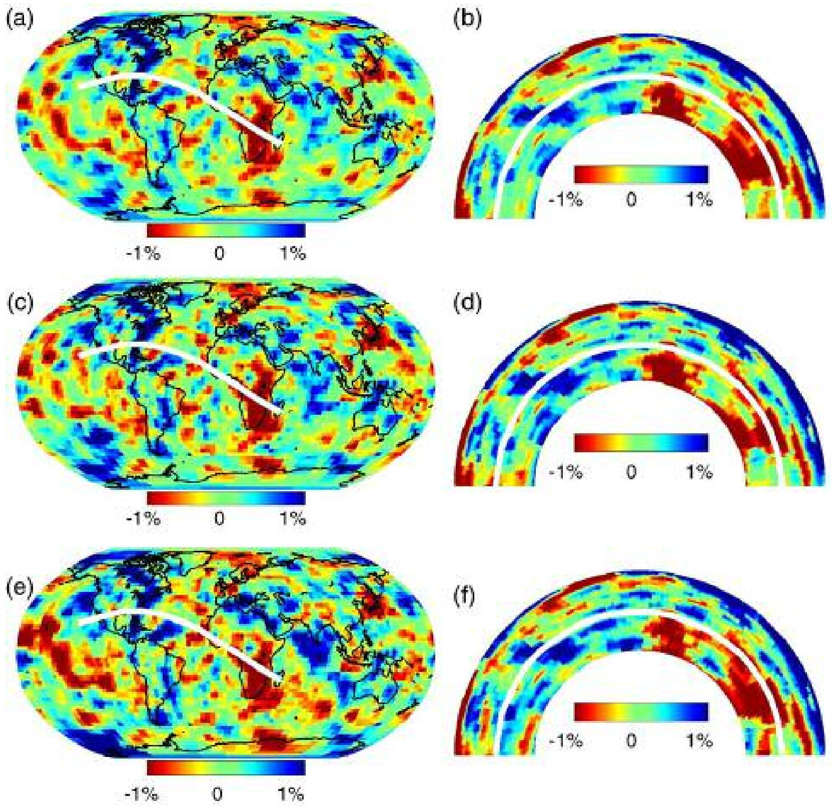

Figure 3.6 Tomographic model comparisons of the seismic model (a, b), whole-mantle joint model (c, d) and flow boundary at 670 km case (e, f). See Figure 3.5 for further explanation. The maps (left column) correspond to 1450-1600 km depth range. The cross sections (right column) cut across the fast Farallon anomaly in the mid-mantle beneath North America and the slow African anomalies in the deepest mantle.

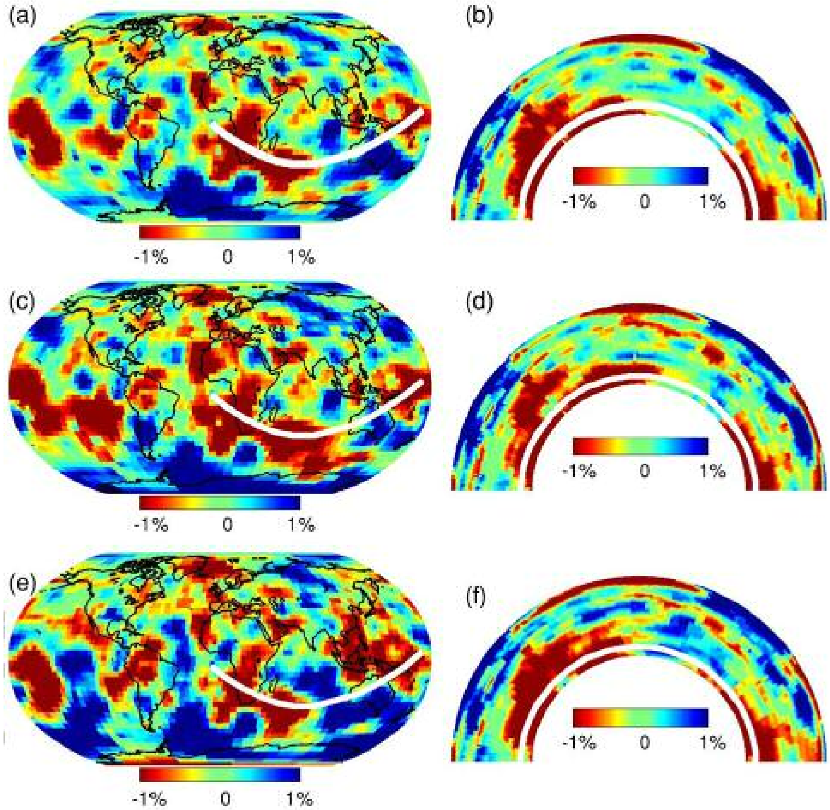

Figure 3.7 Tomographic model comparisons of the seismic model (a, b), whole-mantle joint model (c, d) and flow boundary at 670 km case (e, f). See Figure 3.5 for further explanation. The maps (left column) correspond to 2350-2500 km depth range. The cross sections (right column) cut across the broad African superplume feature and the low-velocity zone at the base of the mantle beneath the Pacific Ocean.

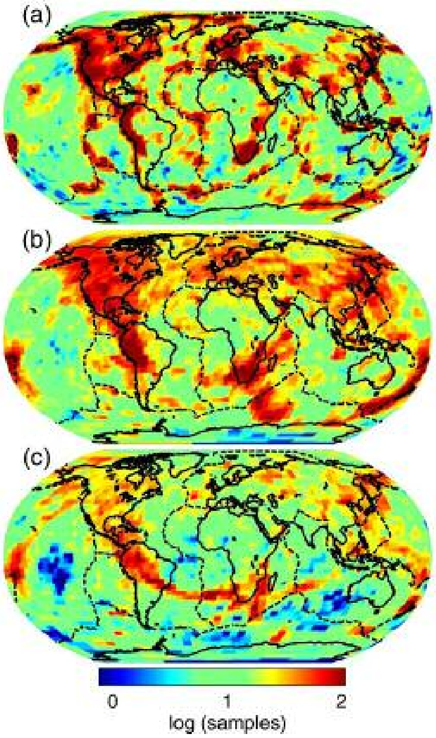

Figure 3.8 Seismic data coverage maps presented as $\log_{10}$(# of samples) for the same model depths presented in Figures 3.5-7. These depths are (a) 525-650 km; (b) 1450-1600 km; and (c) 2350-2500 km. The blue shades represent poorly sampled regions, light green represents moderate sampling, and red shades represent highly sampled regions. Our current constraints provide fairly even coverage beneath the ocean basins at the shallower depths (a,b), but there are some data-poor regions at greater depths beneath parts of the Pacific and Indian Ocean basins (c). It is in these data-poor regions where we see the more significant adjustments to the starting seismic model (e.g. compare Figure 3.7 to Figure 3.8c).

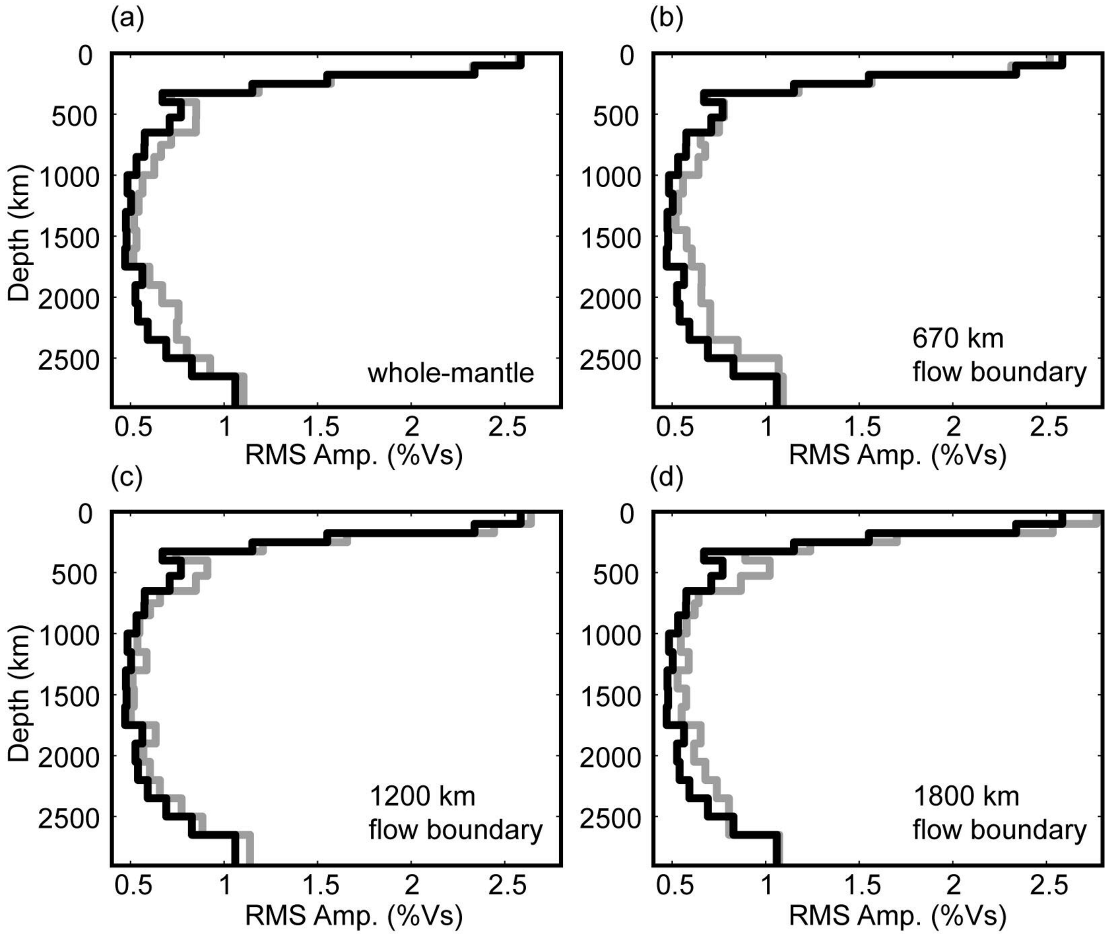

Figure 3.9 RMS amplitude profiles of joint models providing 95% match to the seismic data (obtained with a weighting value λ=0.8). The black curves correspond to the RMS amplitude of the percent shear wave velocity perturbations for the starting seismic model (TX2005). The gray curves correspond to RMS amplitudes of the joint solutions for (a) the whole-mantle case, (b) a flow boundary at 670 km depth, (c) a boundary at 1200 km depth, and (d) a boundary at 1800 km depth. All joint models are amplified in the lower mantle relative to the starting seismic model by varying degrees. With the exception of the 670 km boundary case, all joint models show increased RMS amplitudes within the upper mantle transition zone (~400-650 km).

3.6 Conclusions and discussion

The testing of different mantle-flow hypotheses by jointly inverting global seismic and geodynamic datasets has yielded new 3-D mantle models that can provide excellent fits to all data considered. This can be achieved with generally mild adjustments to a shear-wave tomography model derived solely with seismic data. The whole-mantle flow hypothesis provides the best reconciliation of the combined seismic and geodynamic constraints on 3-D mantle structure. Specifically, 92% of the free-air gravity field (degrees 2-16) and 87% of the observed horizontal divergence of the plate motions can be accounted for, while matching 63% of the estimated dynamic surface topography (degrees 1-16). These fields are matched while simultaneously satisfying CMB flattening estimates of 400 m as well as 95% fit to our seismic constraints when we invoke the whole-mantle flow scenario. If we allow a small decrease in the fit to the seismic constraints, the geodynamic data can be explained to even higher degrees as demonstrated by our trade-off curves plotted in Figure 3.4. For instance, if we reduce the seismic variance reduction to 92%, we find that >95% of the free-air gravity and plate divergence can be explained, as well as >80% of the estimated dynamic surface topography.

Layered-flow models with internal chemical boundaries that block vertical flow in the mantle provide significantly poorer matches to the data and they are characterized, in some cases, by implausible velocity-density scaling relations. These results are based on an analysis of end-member flow scenarios and they do not rule out the existence of 'leaky' modes of flow in which internal (for example, phase-change) boundaries act to only partially inhibit vertical mass transport. Nor has this analysis ruled out more complex boundaries. However, we have shown that whole-mantle flow provides the best fit to seismic and geodynamic data while using the most plausible mineral physics parameters. Simple chemical boundaries located at 1200 and 1800 km depths are clearly not justified in our analysis given the disagreement between the seismic and geodynamic constraints. Only marginally worse data fits are found for the case with a flow boundary at 670 km depth. However, in order to attain reasonable reconciliation of the data for this style of flow, unusual mineral physics parameters (density-to-velocity scaling values) are required in the middle of the lower mantle. To assess this requirement, we coupled the mineral physical estimates for thermal density scaling (Karato & Karki 2001) plotted in Figure 3.3b ("K&K") with the 670 km flow-boundary case and found extreme disagreements amongst the datasets after inversion. Specifically, we matched the seismic constraints to 92% and found only ~30% match to both the free-air gravity and observed plate motions. In this case, the dynamic topography estimates were clearly unsatisfied by the model (34% variance increase). On the other hand, coupling the "K&K" density scaling profile to the whole-mantle flow scenario yielded similar data matches to those presented in Figure 3.4 clearly demonstrating that these two styles of flow require entirely different families of density scaling relationships.

An important implication of the preferred 3-D mantle model derived on the basis of the whole-mantle flow hypothesis is the occurrence of radial layering. This is evident in geographically-localized vertical flow field calculations. We have carried out a 20°×20° equal-area sampling of the mantle to determine those locations in which the predicted mantle flow goes through a strong vertical-flow minimum below 400 km depth. We find that more than 25% of the samples display this radial flow minimum (solid black lines in Figure 3.10). In contrast, the standard mean vertical flow diagnostic, namely the RMS horizontal average of the vertical flow rates (dashed-dotted red line in Figure 3.10), displays little or no indication of a vertical flow minimum below 400 km depth. This result shows that the preferred "whole-mantle" flow model actually yields significant partially-layering of vertical flow between 500 km and 1200 km depth. This outcome is entirely consistent with observations of subducted slabs hindered near or above about 1000 km depth with regionally variability (Fukao *et al*. 2001).

For each flow scenario we tested, we find that the variance reduction to the seismic data invariably decreases with increased weighting to the geodynamic constraints (i.e. increasing λ values). If the resultant joint models are constrained to have generally the same roughness as the starting model, we are forced to mismatch the seismic constraints to varying degrees in order to gain improved matches to the geodynamic constraints. This result is not surprising given that we optimize a-priori the free parameters (density scaling and viscosity structure) for each flow scenario using a previously derived seismic model with smoothing and damping parameters derived independent from the geodynamic constraints. In addition, there are other possible causes for the residual and rather modest level of disagreement between the seismic-geodynamic constraints. Firstly, the starting seismic model (TX2005) was generated by a multi-step process whereby partial solutions were found and optimum earthquake locations (including origin times) were subsequently established at each iteration in the inversion. Therefore, the starting seismic model absorbed travel time adjustments that are not recovered in the joint inversion process. Secondly, our modeling assumes simple radially-dependent 1-D density-velocity scaling and viscosity structure. It is likely that particular regions of the Earth have significant 3-D variations in both of these variables. This is probably particularly significant near the surface when considering sub-cratonic versus sub-oceanic lithosphere as well as partial melting near mid-ocean ridges. Some researchers have concluded that 3-D rheological variations in the upper portion of the Earth have significant impacts on the geodynamic data fields considered in this study (Čadek & Fleitout 1999). However, recent studies have shown a rather small impact of global-scale lateral viscosity variations on tomography-based predictions of geodynamic observables (Moucha *et al*. 2004, 2005).

Regardless of the true extent to which lateral heterogeneity in density-velocity scaling and viscosity affect the geodynamic data, such lateral variations will yield some disagreement between the seismic and geodynamic data when the latter are treated in the context of a purely 1-D parameterization of these parameters. In this regard, it is noteworthy that we are able to successfully reconcile the joint seismic and geodynamic constraints on mantle structure using a simplified whole-mantle flow model which assumes 1-D viscosity and density scaling profiles. This suggests that lateral variations in these model parameters will be difficult to constrain and more work is required to address this challenge. In spite of the limitations of the work presented here, we have shown that robust testing of alternative mantle flow hypotheses will require the simultaneous consideration of both seismic and geodynamic datasets in order to discriminate between varying styles of mantle flow.

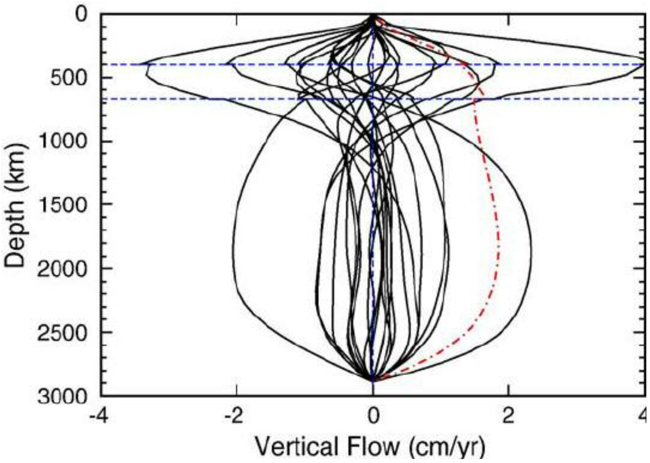

Figure 3.10 Geographically localized vertical flow minima obtained from the whole-mantle-flow joint tomography model. The solid black lines show local geographical profiles of predicted vertical flow in the mantle – extracted from a 20˚×20˚ equal-area sampling – in which the vertical flow passes through a strong minimum below 400 km depth. Most vertical-flow minima are located in the depth interval between 500 and 1200 km. The dash-dotted red line shows the RMS horizontally-averaged amplitude of the predicted vertical flow field. The two dashed horizontal blue lines identify the locations of the 400 km and 670 km seismic discontinuities.

3.7 References

Bassin, C., G. Laske & G. Masters (2000), The current limits of resolution for surface wave tomography in North America, EOS Trans AGU 81(48) 897.

Čadek, O., L. & Fleitout (1999), A global geoid model with imposed plate velocities and partial layering, *J. Geophys. Res. 104*, 29055-29075.

Čadek, O., L. & Fleitout (2003), Effect of lateral viscosity variations in the top 300 km on the geoid and dynamic topography, *Geophys. J. Int. 152*, 566-580.

Cammarano, F., S. Goes, P. Vacher & D. Giardini (2003), Inferring upper-mantle temperatures from seismic velocities, *Phys. Earth Planet. Inter.*, *138*(3-4), 197-222.

Čižková, H. O. Čadek, A.P. Van den Berg & N.J. Vlaar (1999), Can lower mantle slab-like seismic anomalies be explained by thermal coupling between the upper and lower mantles?, *Geophys. Res. Lett. 26*, 1501-1504.

Constable, S.C. R.L. Parker & C.G. Constable (1987), Occam’s inversion; a practical algorithm for generating smooth models from electromagnetic sounding data, *Geophys. 52*, 289-300.

DeMets, C.R., Gordon, R.G., Argus, D.F. & S. Stein (1990), Current plate motions, *Geophys. J. Int.*, *101*(2), 425-478.

Forte, A.M. & W.R. Peltier (1987), Plate tectonics and aspherical Earth structure; the importance of poloidal-toroidal coupling, *J. Geophys. Res. 92*, 3645-3679.

Forte, A.M. & W.R. Peltier (1991), Viscous flow models of global geophysical observables; 1, Forward problems, *J. Geophys. Res. 96*, 20131-20159.

Forte, A.M. & W.R. Peltier (1994), The kinematics and dynamics of poloidal-toroidal coupling in mantle flow; the importance of surface plates and lateral viscosity variations, *Adv. Geophys. 36*, 1-119.

Forte, A.M., R.L. Woodward & A.M. Dziewonski (1994), Joint inversions of seismic and geodynamic data for models of three-dimensional mantle heterogeneity, *J. Geophys. Res. 99*, 21857-21877.

Forte, A.M. & R.L. Woodward (1997), Seismic-geodynamic constraints on three-dimensional structure, vertical flow, and heat transfer in the mantle, *J. Geophys. Res. 102*, 17981-17994.

Forte, A.M. (2000), Seismic-geodynamic constraints on mantle flow: implications for layered convection, mantle viscosity, and seismic anisotropy in the deep mantle, *in Earth's Deep Interior: Mineral Physics and Tomography from the Atomic to the Global Scale*, edited by S.-I. Karato et al., pp. 3-36, AGU, Washington, DC.

Forte, A.M. & H.K.C. Perry (2000), Geodynamic evidence for a chemically depleted continental tectosphere, *Science*, *290*, 1940-1944.

Forte, A.M. & J.X. Mitrovica (2001), Deep-mantle high-viscosity flow and thermochemical structure inferred from seismic and geodynamic data, *Nature*, *410*(6832), 1049-1056.

Fukao, Y., S. Widiyantoro, M. Obayashi (2001), Stagnant slabs in the upper mantle transition region, *Rev. Geophys. 39*, 291-323.

Grand, S.P., R.D. Van der Hilst & S. Widiyantoro (1997), Global seismic tomography: a snapshot of convection in the Earth, *GSA Today*, *7*, 1-7.

Grand, S.P. (2002), Mantle shear-wave tomography and the fate of subducted slabs, *Phil. Trans. R. Soc. Lond. A*, *360*(1800), 2475-2491.

Gu, Y.J., A.M. Dziewonski, W. Su & G. Ekstrom (2001), Models of the mantle shear velocity and discontinuities in the pattern of lateral heterogeneities, *J. Geophys. Res.*, *106*, 11169-11199.

Hamilton, W.B. (2002), The closed upper-mantle circulation of plate tectonics, in S. Stein, J.T. Freymueller (Eds.), Plate Boundary Zones, AGU, Washington, DC, pp. 359-410.

Herring, T.A., P.M. Mathews & B.A. Buffett (2002), Modeling of nutation-precession; very long baseline interferometry results, *J. Geophys. Res. Solid Earth*, *107*(B4), doi: 10.1029/2001JB000165.

Hofmann, A.W. (1997), Mantle geochemistry: the message from oceanic volcanism, *Nature 385*, 219-229.

Karason, H. & R.D. van der Hilst (2000), Constraints on mantle convection from seismic tomography, in: M.R. Richards, M.R. Gordon, R.D. van der Hilst (Eds.), The History and Dynamics of Global Plate Motion, AGU, Washington, DC, pp. 277-288.

Karato, S.-I. & P. Wu (1993), Rheology of the upper mantle; a synthesis, *Science 260*, 771-778.

Karato, S.I. & B.B. Karki (2001), Origin of lateral variation of seismic wave velocities and density in the deep mantle, *J. Geophys. Res. Solid Earth*, *106*(B10), 21771-21783.

Kawakatsu, H. & F. Niu (1994), Seismic evidence for 920-km discontinuity in the mantle, *Nature 371*, 301-305.

Kellogg, L.H., B.H. Hager & R.D. Van der Hilst (1999), Compositional stratification in the deep mantle, *Science*, *283*(5409), 1181-1184.

Le Stunff, Y. & Y. Ricard (1997), Partial advection of equidensity surfaces: A solution for the dynamic topography problem? *J. Geophys. Res. 102*, 24655-24667.

Marsh, J.G., *et al*. (1990), The GEM-T2 gravitational model, *J. Geophys. Res. Solid Earth*, *95*(13), 22043-22071.

Masters, G., G. Laske, H. Bolton & A.M. Dziewonski (2000), The relative behavior of shear velocity, bulk sound speed, and compressional velocity in the mantle: implications for chemical and thermal structure, *in Earth's Deep Interior: Mineral Physics and Tomography from the Atomic to the Global Scale*, edited by S.-I. Karato et al., pp. 63-87, AGU, Washington, DC.

Machetel, P. & P. Weber (1991), Intermittent layered convection in a model mantle with and endothermic phase change at 670 km, *Nature 350*, 55-57.

Mathews, P.M., T.A. Herring & B.A. Buffett (2002), Modeling of nutation and precession: new nutation series for nonrigid Earth and insights into the Earth's interior, *J. Geophys. Res. Solid Earth*, *107*(B4), doi: 10.1029/2001JB000390.

Megnin, C. & B. Romanowicz (2000), The three-dimensional shear velocity structure of the mantle from the inversion of body, surface and higher-mode waveforms}, *Geophys. J. Int.*, *143*, 709-728.

Mitrovica, J.X. & A.M. Forte (1997), Radial profile of mantle viscosity; results from the joint inversion of convection and postglacial rebound observables, *J. Geophys. Res. 102*, 2751-2769.

Mitrovica, J.X., A.M. Forte & M. Simons (2000), A reappraisal of postglacial decay times from Richmond Gulf and James Bay, Canada, *Geophys. J. Inter. 142*, 783-800.

Mitrovica, J.X. & A.M. Forte (2004), A new inference of mantle viscosity based upon joint inversion of convection and glacial isostatic adjustment data, *Earth Planet. Sci. Lett.*, *225*(1-2), 177-189.

Moucha, R., A.M. Forte, J.X. Mitrovica & A.L. Daradich (2004), Geodynamic implications of convection-related surface observables: the role of lateral variations in mantle rheology, *Eos Trans. AGU 85*, T11E-1325.

Moucha, R., A.M. Forte, J.X. Mitrovica & A.L. Daradich (2005), Geodynamic implications of lateral variations in mantle rheology on convection related observables and inferred viscosity models, *Geophys. J. Inter*. submitted.

Niu, F., H. Kawakatsu (1997), Depth variation of the midmantle seismic discontinuity, *Geophys. Res. Lett. 24*, 429-432.

Paige, C.C. & M.A. Saunders (1982), LSQR: an algorithm for sparse linear equations and sparse least squares, *ACM Transactions on Mathematical Software*, *8*, 43-71.

Panasyuk, S.V. & B.H. Hager (1998), A model of transformational superplasticity in the upper mantle, *Geophys. J. Inter. 133,* 741-755.

Panasyuk, S.V. & B.H. Hager (2000), Inversion for mantle viscosity profiles constrained by dynamic topography and the geoid, and their estimated errors, *Geophys. J. Int. 143*, 821-836.

Perry, H.K.C., D.W.S. Eaton & A.M. Forte (2002), LITH5.0: A revised crustal model for Canada based on Lithoprobe results, *Geophys. J. Int. 150*, 285-294.

Ricard, Y., L. Fleitout & C. Froidevaux (1984), Geoid heights and lithospheric stresses for a dynamic Earth, Ann. *Geophys. 2*, 267-286.

Ricard, Y. & C. Vigny (1989), Mantle dynamics with induced plate tectonics, *J. Geophys. Res. 94*, 17543-17559.

Richards, M.A. & B.H. Hager (1984), Geoid anomalies in a dynamic earth, *J. Geophys. Res. Solid Earth*, *89*(B7), 5987-6002.

Richards, M.A. & D.C. Engebretson (1992), Large-scale mantle convection and the history of subduction, *Nature 355*, 437-440.

Ritsema, J., H.J. Van Heijst & J.H. Woodhouse (1999), Complex shear wave velocity structure imaged beneath Africa and Iceland, *Science*, *286*(5446) 1925-1928.

Romanowicz, B. (2003) Global mantle tomography: progress status in the last 10 years, *Ann. Rev. Earth Plan. 31*, 303-328.

Solheim, L.P. & W.R. Peltier (1994), Avalanche effects in phase transition modulated thermal convection: a model of Earth's mantle, *J. Geophys. Res. 99*, 6997-7018.

Tackley, P.J., D.J. Stevenson, G.A. Glatzmaier & G. Schubert (1994), Effects of multiple phase transitions in a three-dimensional spherical model of convection in Earth's mantle, *J. Geophys. Res. 99*, 15877-15901.

Tackley, P.J. (2000), Mantle convection and plate tectonics: toward an integrated physical and chemical theory, *Science 288*, 2002-2007.

Thoraval, C. & P. Machetel (1995), Locally layered convection inferred from dynamic models of the Earth's mantle, *Nature 375*, 777-780.

Trampert, J., F. Deschamps, J. Resovsky & D. Yuen (2004), Probabilistic tomography maps chemical heterogeneities throughout the lower mantle, *Science*, *306*(5697), 853-856.

Van der Hilst, R.D., S. Widiyantoro & E.R. Engdahl (1997), Evidence for deep mantle circulation from global tomography, *Nature*, *386*, 578-584.

Van der Hilst, R.D. & H. Kárason (1999), Compositional heterogeneity in the bottom 1000 kilometers of the Earth's mantle: Toward a hybrid convection model, *Science*, *283*, 1885-1888.

Wen, L. & D.L. Anderson (1997), Layered mantle convection: a model for geoid and topography, Earth Planet. *Sci. Lett. 146,* 367-377.

Zhao, D. (2001), Seismic structure and origin of hotspots and mantle plumes, *Earth Planet. Sci. Lett. 192*, 251-265.

Zhou, H. & R.W. Clayton (1990), P and S wave travel-time inversions for subducting slab under the island arcs of the northwest Pacific, *J. Geophys. Res. 95*, 6829-6851.

Chapter 4

Thermochemical Structure and Dynamics of the African Superplume

4.1 Abstract

We present a new three-dimensional (3-D) model of the thermochemical structure of the African superplume region obtained from simultaneous inversion of global seismic and convection-related data. Convection-related observations include the global free-air gravity field, tectonic plate motions, dynamic surface topography and the excess ellipticity of the core-mantle boundary. A 3-D image of the chemically-induced density perturbations provides direct evidence that intrinsically-dense material is entrained within the superplume and concentrated into a rounded structure ~1000 km above the core-mantle boundary. The thermally-induced density perturbations are greater in magnitude than the chemically-induced implying overall positive buoyancy throughout the superplume. The observed morphology and density signatures are consistent with a thermochemical plume that has risen from a compositionally-distinct ‘pile’ at the base of the mantle and may be currently deforming under the influence of its intrinsic negative chemical buoyancy.

4.2 Introduction

The African ‘superplume’ is a large-scale structure near the base of the mantle centered beneath South Africa that exhibits complex seismic characteristics (Ritsema *et al*. 1998, 1999; Ishii & Tromp 1999; Masters *et al*. 2000; Ni *et al*. 2002, 2005; Ni & Helmberger 2003a,b). The superplume is most notably characterized by slow shear (*S*) wave speeds as discussed in Chapter 2. Detailed waveform analyses have revealed that the superplume possesses a ridge-like morphology and abrupt wave speed reductions near its boundaries (Ni *et al*. 2002; Ni & Helmberger 2003). Slow seismic wave speeds may indicate high temperatures (Karato 1993); however, the morphology and abrupt velocity jumps associated with the structure cannot be easily attributed to temperature variations alone implying a potential chemical origin. This hypothesized chemical component could have considerable consequences for the dynamics of the mantle and, therefore, has led to numerical models and scaled experiments with compositional variations (Thompson & Tackley 1998; Kellogg *et al*. 1999; Ni *et al*. 2002; Tackley 2002; Davaille *et al*. 2003; McNamara & Zhong 2005; Tan & Gurnis 2005).

Integrated approaches considering both seismic and geodynamic constraints are necessary to provide insight on the relative chemical and thermal contributions to mantle heterogeneity (e.g. Forte 2000; Forte & Mitrovica 2001; Trampert *et al*. 2004; Simmons *et al*. 2006). The integrated tomographic study described in Chapter 3 concluded that mantle models that are consistent with both geodynamic and seismic constraints could be found while assuming a dominance of thermal effects on mantle heterogeneity. The models found were reasonable in that, relative to a purely seismically-derived model, no significant increase in model roughness was required to explain the combined observations. However, no attempt was made to model the chemical contributions to the mantle's density field. We have thus expanded on this approach of simultaneously inverting multiple geophysical constraints including those directly sensitive to density perturbations to explore the structure of the African superplume in detail.

4.3 Thermal contributions to mantle heterogeneity

As described in Chapter 3, the integrated approach involves linearly relating seismic velocity structure ($\mathbf{m}$) to our seismic observations ($\mathbf{r}$) as well as the geodynamic observations ($\mathbf{s}$). The geodynamic observations are represented as spherical harmonics up to degree 16 and are linearly related to density perturbations via viscous flow theory calculations (Richards & Hager 1984) assuming whole-mantle flow. The simplified forward model setup can be represented as follows:

$$\begin{bmatrix} \mathbf{L} \\ \mathbf{G}\left(R_{\rho/s}\right) \end{bmatrix} \mathbf{m} = \begin{bmatrix} \mathbf{r} \\ \mathbf{s} \end{bmatrix} \tag{4.1}$$

where we wish to solve for the seismic heterogeneity model ($\mathbf{m}$, slowness perturbations) using iterative inversion techniques. In this relationship, **L** is the seismic sensitivity matrix (ray path lengths) and **G** is the viscous flow response matrix based on the radially-symmetric viscosity profile developed in (Mitrovica & Forte 2004). The geodynamic sensitivity matrix is now dependent upon the scaling between seismic velocity heterogeneity and density perturbations ($R_{\rho/s}$). This relationship is defined as the ratio of relative density (ρ) to shear wave velocity (V_S) heterogeneity by:

$$R_{\rho/s} = d\left[\ln\rho\right]/\,d\left[\ln V_S\right]. \tag{4.2}$$

We tested a wide range of radially-symmetric scaling profiles derived from recent mineral physics estimates based on the assumption of thermally-dominated heterogeneity in the mantle (Karato & Karki 2001; Cammarano *et al*. 2003). The thermal velocity-density relationship ($R_{\rho/s}^{thermal}$) that yielded the most successful fit to the combined dataset after joint inversion was selected (Figure 4.1). The mantle heterogeneity model $\mathbf{m}^{thermal}$ corresponding to the $R_{\rho/s}^{thermal}$ profile provides an equivalent level of match to the shear-wave seismic data as the purely seismically-derived model. In addition, the jointly-derived model is consistent with the geodynamic constraints; with the exception of dynamic surface topography which is less well fit (Table 4.1).

Given the likelihood that continental shield roots are chemically- and thermally-distinct relative to the mantle beneath ocean basins (Jordan 1981), we defined the Archean/Proterozoic shield regions (Mooney *et al*. 1998) in the model parameter space and solved for individual 1-D profiles for the shield ($R_{\rho/s}^{shield}$) and ambient mantle domains ($R_{\rho/s}^{ambient}$) within the upper 250 km (Figure 4.1). Treating these chemically-distinct mantle domains independently yields an increased fit to the estimated dynamic surface topography (Table 4.1). Incorporating this simplified, regionalized representation of shallow lateral variations in the density-velocity scaling into the joint inversion also provides for a high degree of reconciliation of all other geodynamic data fields demonstrating the dominance of thermal variations to heterogeneity below ~250 km.

Translating the resultant velocity structure into thermally-induced density perturbations in the lower mantle can be achieved with the relationship:

$$\left(\delta\rho / \rho\right)^{thermal} = R_{\rho/s}^{thermal}\left(\delta V_s / V_s\right) \tag{4.3}$$

as per our forward model assumptions. One of the most prominent features of this new joint model (Figure 4.2) is the African superplume consisting of a low-velocity (low-density) zone at the base of the mantle with a tilted upward extension into the mid-mantle similar to previous seismic models (e.g. Ritsema *et al*. 1999; Ni *et al*. 2002). The deepest part of the structure covers a vast area beneath most of the African continent and has a northwest-southeast trending ridge-like structure extending into the southwest Indian Ocean. This joint solution is generally in accord with previous detailed seismic studies of the region (Wen 2001; Ni & Helmberger 2003a,b). In addition to the broad basal structure, a low-velocity upward extension directly beneath South Africa reaches distances of ~1500 km above the CMB and displays a quasi-bulbous morphology that may be interpreted as a large plume head that has risen from the basal structure.

Table 4.1 Data fits for joint seismic-geodynamic models

Density/Velocity conversion (R)	Seismic (%)	Free-air gravity (%)	Plate divergence (%)	Dynamic topography (%)	CMB excess ellipticity (km)
simple 1-D	95.8	78	80	44	0.4
1-D with shields	95.8	80	80	64	0.4
3-D	95.8	90	94	76	0.4

Percentages are variance reduction fits to the seismic travel time residual data and spherical harmonic components of the geodynamic data fields (up to degree 16). For comparison, the starting model derived solely with the seismic constraints matches the seismic data equally well (95.8%).

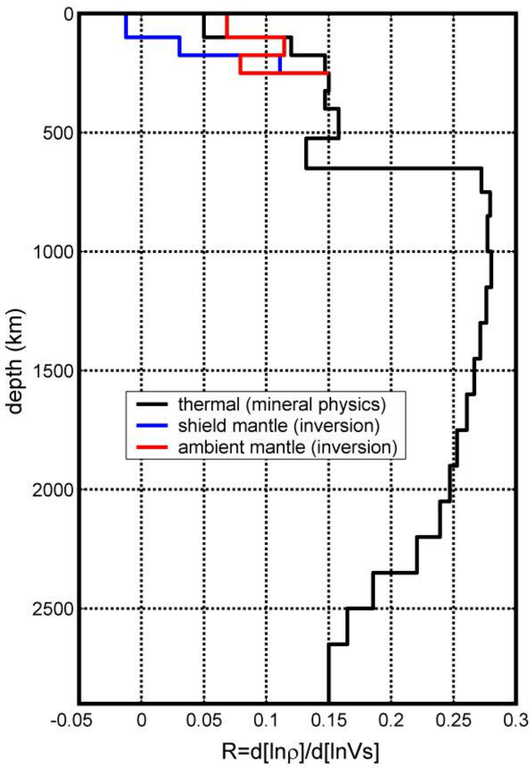

Figure 4.1 Relationship between shear-wave velocity and density perturbations presented in terms of $R_{\rho/s} = d[\ln\rho]/d[\ln V_S]$. The black line corresponds to values obtained from recent mineral physics estimates for thermal contributions (see text). The blue and red curves are inversion results for mantle corresponding to shield and ambient mantle domains in the upper 250 km.

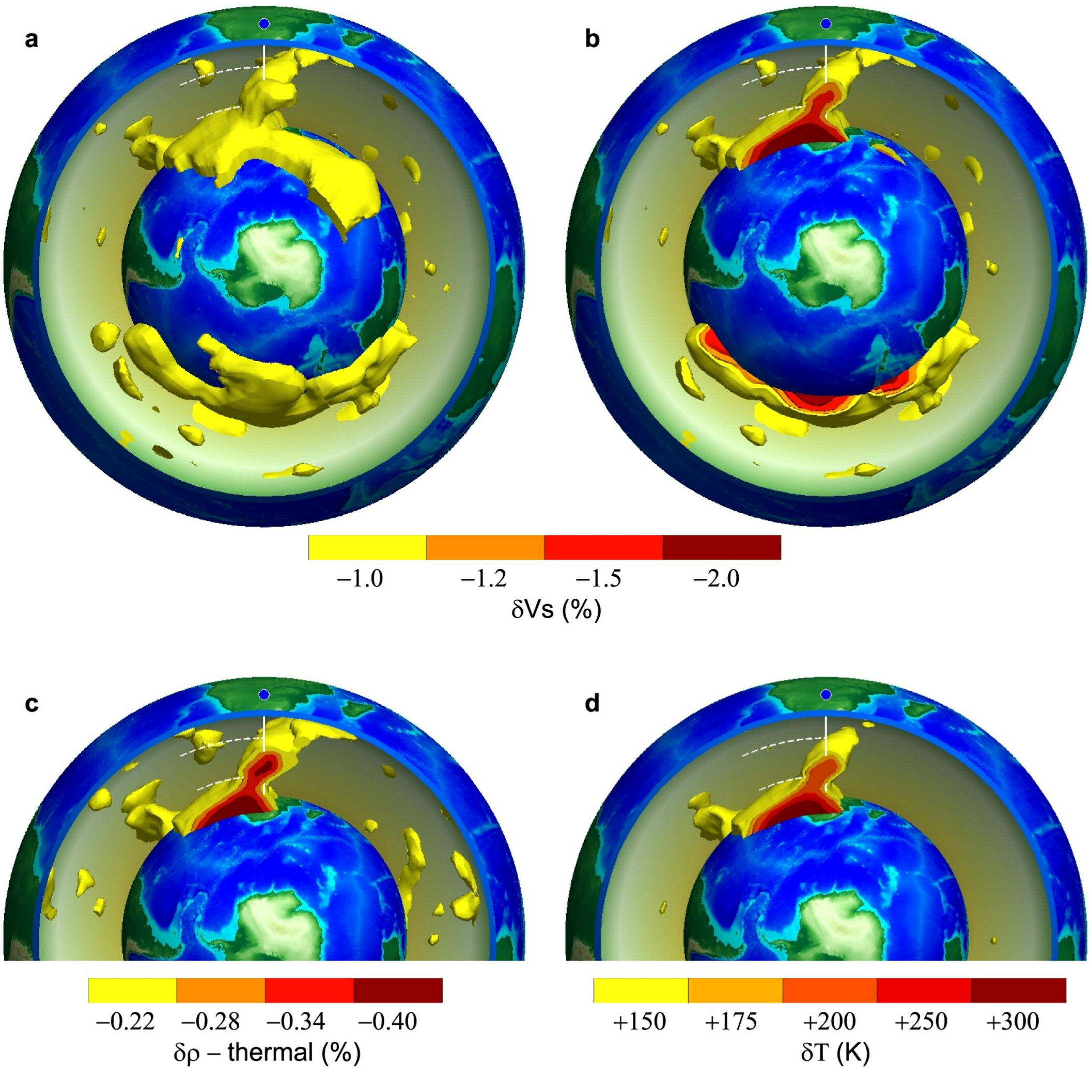

Figure 4.2 Isocontours of the velocity, thermally-induced density, and temperature fields within the African superplume region. The Earth is sliced open and surface topography is projected onto the CMB for perspective. The white vertical line is for spatial reference and intersects the southern African continent at 25ºS latitude and 25ºE longitude. The dashed lines correspond to 1000 and 2000 km depths. (**a**) Shear-wave velocity perturbation field determined by simultaneous inversion of seismic and geodynamic data. (**b**) Internal view of the shear-wave perturbation field. (**c**) Internal view of the thermally-induced density field found by converting the velocity field with the velocity-density relationship in Fig. 1. (**d**) Temperature variations derived using recent estimates of the coefficient of thermal expansion (Karki *et al.* 2001) and the thermally-induced density field. For display purposes, model values south of 55ºS and above 700 km depth are excluded.

4.4 Chemical contributions to mantle heterogeneity

The thermal modeling results suggest that density perturbations in the mantle are primarily due to lateral temperature variations. However, there still exist significant residual misfits to the dynamic topography, free-air gravity and plate motion observations. This suggests the presence of residual density anomalies that cannot be directly attributed to variations in temperature. Therefore, compositional heterogeneity in the mantle may be an important contributor to the overall density field. In order to account for the combined thermal and chemical density field, we allow the density-velocity scaling $R_{\rho/s}$ to vary laterally, thus creating a fully 3-D relationship between density and shear wave velocity ($R_{\rho/s}^{3D}$). Any significant deviations from the optimal 1-D thermal relationship ($R_{\rho/s}^{thermal}$) can be considered a departure from an isochemical mantle and therefore represents lateral compositional variations.

A 3-D density-velocity relationship including both thermal and chemical contributions, $R_{\rho/s}^{3D}$, must satisfy the following forward model:

$$\mathbf{G}\left(\mathbf{m}^{thermal}\right)R_{\rho/s}^{3D} = \mathbf{s}\,. \qquad (4.4)$$

Rather than finding a new seismic model, we fixed the seismic model to that obtained by joint inversion of seismic and geodynamic data considering only thermal contributions discussed above ($\mathbf{m}^{thermal}$, Figure 4.2) and inverted for $R_{\rho/s}^{3D}$. It should be noted that where seismic constraints are lacking, there should be no significant deviation from the 1-D density-velocity scaling relationship since the joint inversion will attempt to satisfy the geodynamic constraints while assuming only thermal variations. The resultant total (thermal + chemical) density perturbation field becomes:

$$\left(\delta\rho / \rho\right)^{total} = R_{\rho/s}^{3D}\left(\delta V_s / V_s\right). \tag{4.5}$$

This acquired total density field provides an excellent fit to the employed geodynamic constraints (Table 4.1).

The compositional contributions to mantle density heterogeneity are estimated as the residual field obtained by removing the thermal density anomalies from the total density field:

$$\left(\delta\rho / \rho\right)^{chemical} = \left(\delta\rho / \rho\right)^{total} - \left(\delta\rho / \rho\right)^{thermal}. \tag{4.6}$$

These chemically-induced density anomalies are characterized by amplitudes that are very small relative to the thermal density field throughout the majority of the lower mantle. The only exception to this generality is the African superplume region where we detect significant chemically-induced density heterogeneity (Figure 4.3). Specifically, we find that the African superplume structure requires a positive chemical density anomaly (particularly at mid-mantle depths) that opposes the thermally-induced density anomalies. These characteristics are not found anywhere else in the mid-mantle making this a globally unique feature based on our models. The highest concentration of intrinsically-dense material is detected at about 1000 km above the CMB where we also observe large negative thermal density anomalies and, therefore, higher than average temperature. This positive density component is lower in amplitude than the thermal component and it effectively reduces the total buoyancy of the superplume, although the structure remains positively buoyant throughout.

The fluid dynamical impact of the effective chemical contribution to the density field can be quantified using the buoyancy ratio:

$$B = \left|\delta\rho^{chemical} / \delta\rho^{thermal}\right| . \tag{4.7}$$

Within the African superplume, we find buoyancy ratios within the range 0.3-0.6 with a general increase with distance above the base of the mantle (Figure 4.4). Buoyancy ratio mapping also reveals that the mid-mantle extension of the superplume (~1800 km depth) may be succumbing to the positive chemical density component and folding eastward, demonstrating a significant loss of positive buoyancy near this depth range and possible stagnation of parts of the upwelling. The high-density chemical component may gradually overcome the thermally-induced buoyancy and ultimately cause collapse of the structure towards the CMB.

When 3-D density-velocity scaling is introduced, significant improvement in fit to the dynamic surface topography is obtained (Table 4.1). This improvement is mainly due to inference of compositional heterogeneity in the shallow mantle, especially in the subcontinental tectosphere (e.g., Forte & Perry 2000). However, it is possible that the acquired shallow mantle heterogeneity affects the outcome of the mid-mantle heterogeneity and thereby dynamic topography could be an indirect contributor to the superplume density heterogeneity. To test this, we performed the entire inversion process by excluding dynamic topography as a constraint and found only slight variations in the mid-mantle heterogeneity models (Figure 4.5). Therefore the dynamic topography constraint is not a primary contributor to the compositional densities detected in the mid-mantle superplume structure.

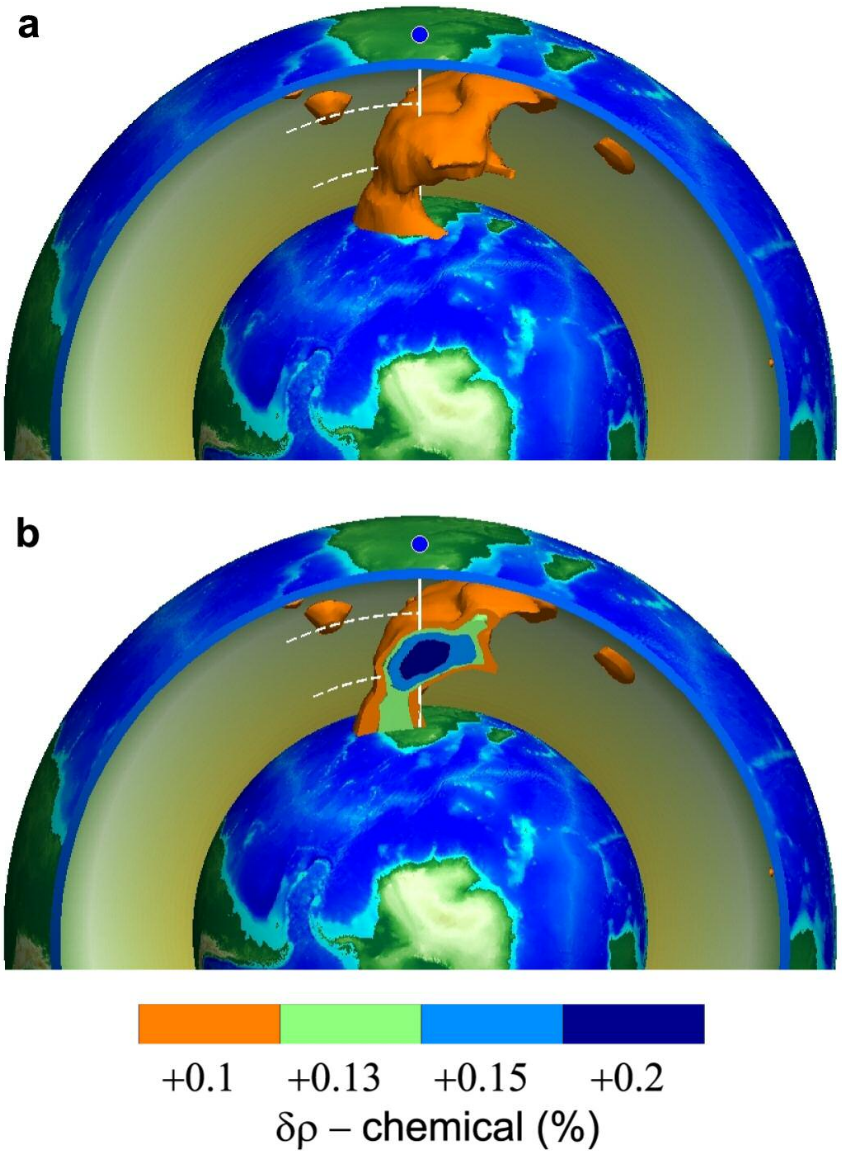

Figure 4.3 Positive chemically-induced density determined by allowing for a fully 3-D density-velocity relationship ($R_{\rho/s}^{3D}$). (**a**) View of the African superplume region exhibiting a plume-like morphology with a large-volume rounded structure centered at ~1800 km depth directly beneath the southern African continent. (**b**) View of the internal domain of the positive chemical density field.

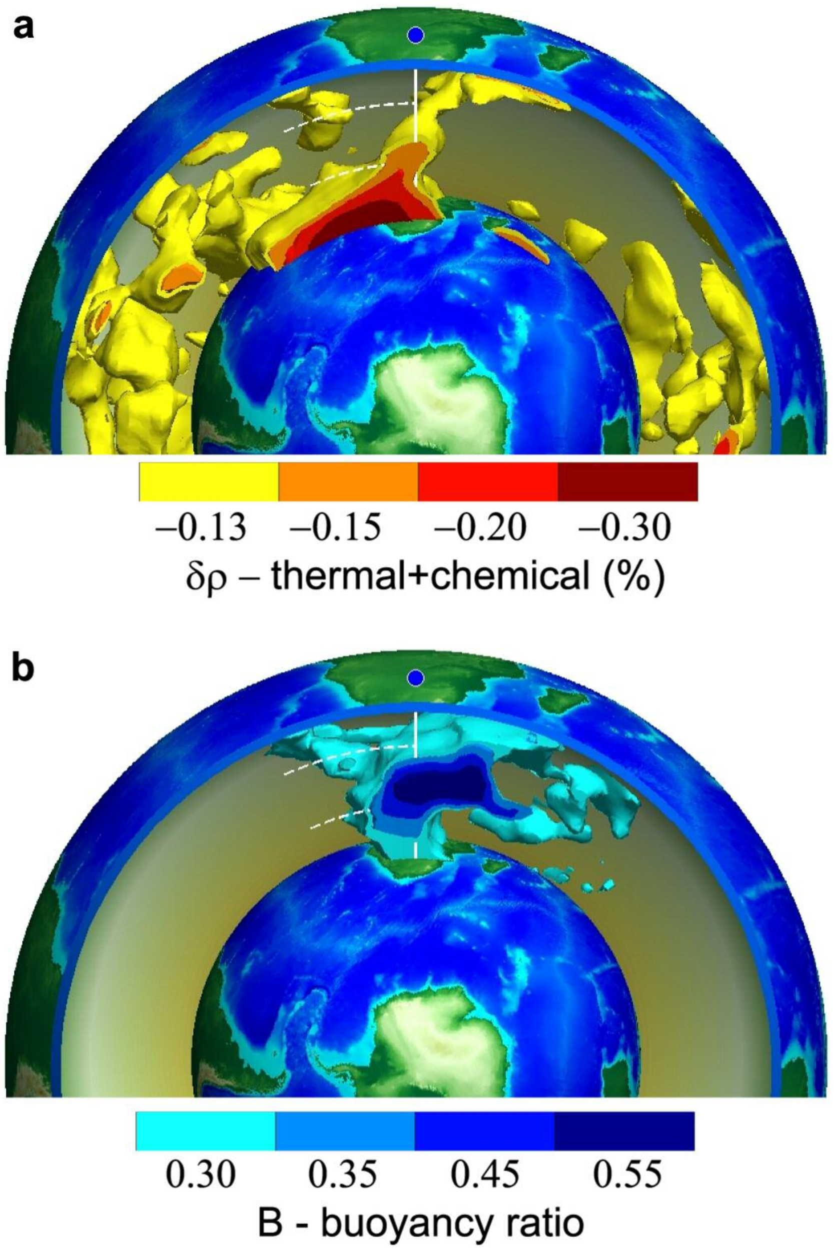

Figure 4.4 Total density perturbation field and buoyancy ratio $B = \left|\delta\rho^{chemical} / \delta\rho^{thermal}\right|$ within the African superplume region. (**a**) Summation of the thermally- and chemically-induced density fields yields negative density (positive buoyancy) of the superplume structure. (**b**) The buoyancy ratio field reveals that the superplume buoyancy is strongly reduced by the positive-density chemical component near 1800 km depth. The superplume structure appears to bend eastward within the same region as a response to buoyancy deficiency.

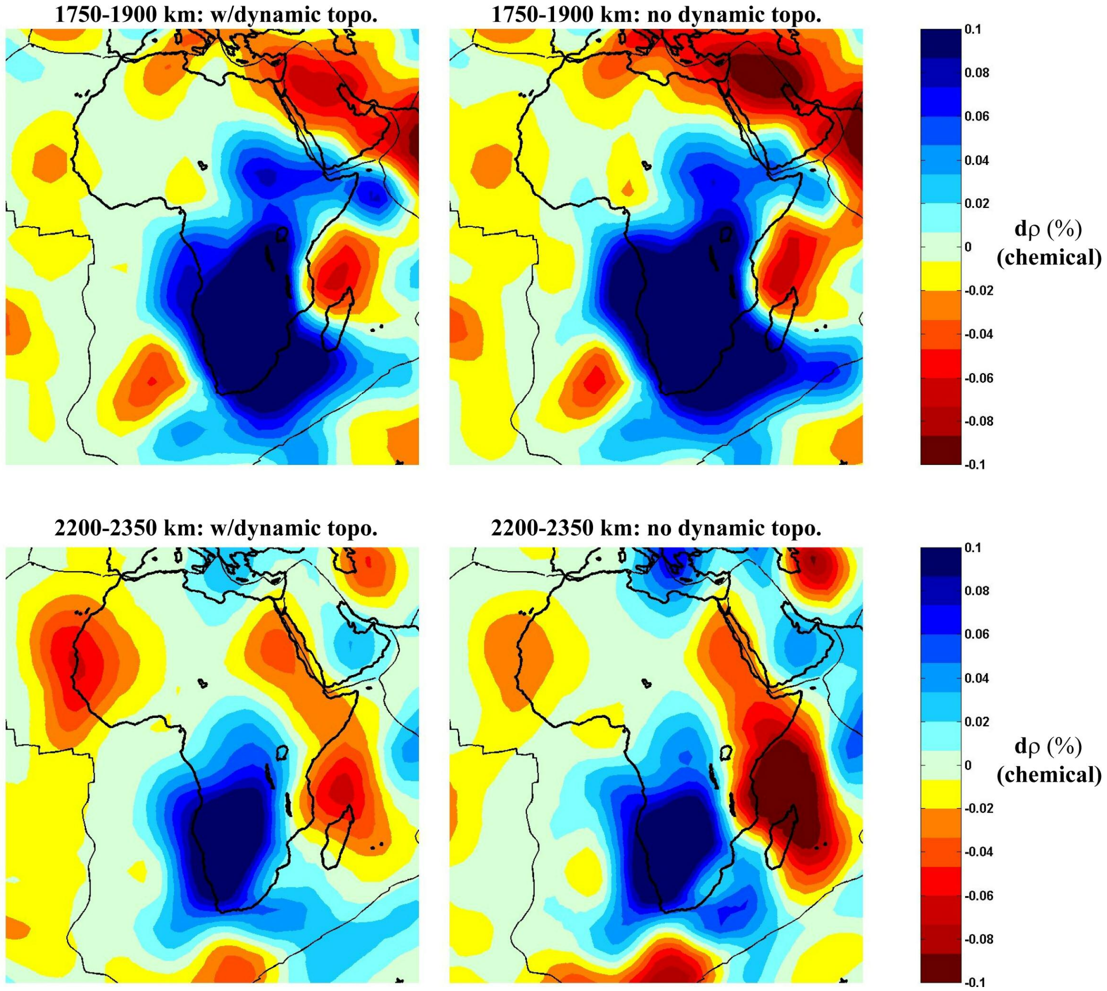

Figure 4.5 The effect of dynamic topography on the resulting compositional density anomalies. The top row is the compositional density models at 1750-1900 km depth for the case including dynamic topography (left) and without dynamic topography as a constraint (right). The bottom row is similar except for the depth range 2200-2350. At these depths, the dynamic topography has little effect on the outcome.

4.5 Conclusions

Our results indicate that the African superplume is an active, buoyant upwelling consistent with the uplift of the African continent (Lithgow-Bertelloni & Silver 1998) and previous mantle flow studies (Gurnis *et al*. 2000; Forte & Mitrovica 2001). Active upwelling from the base of the mantle beneath Africa is also supported by study of seismic anisotropy demonstrating an onset of vertical flow in this same region (Panning & Romanowicz 2004). The morphology of the base of the superplume region is found to be ridge-like with steeply dipping sides based on our joint inversion solutions. Deep mantle ridge-shaped structures, such as the one observed extending into the Indian Ocean, are indicative of compositional variability at the base of the mantle and have been mimicked successfully by numerical flow models with an intrinsically-dense basal layer (Tackley 2002; McNamara & Zhong 2005). The shape and locations of observed ridge structures in the deep mantle could be primarily a product of past subduction processes acting to sweep dense material into these linear ridge-like piles (McNamara & Zhong 2005; Quéré & Forte 2006).

A large-scale buoyant upwelling rising well above the basal structure is observed directly beneath South Africa. This feature is plume-like and rises at least 1500km above the CMB. Significant positive chemical density signatures that tend to oppose the thermally-induced density anomaly are found within the upwelling. This substantial chemical density anomaly is not found elsewhere in our global model making this a unique feature in Earth's mid-mantle region. Without sufficient seismic resolution in the region, the compositional effects would not be detected since the joint inversion procedure assuming only thermal contributions (1-D scaling model) would nullify any disagreement between the seismic and geodynamic datasets. It may be that the lack of seismic resolution in other mid-mantle regions (such as beneath the Pacific Ocean) prevents the detection of additional significant compositional anomalies.

The density characteristics and morphology of the rounded mid-mantle structure beneath Africa are indicative of an actively rising thermochemical plume that has entrained intrinsically-dense material from a pile at the base of the mantle similar to numerical simulations (e.g. Ni *et al*. 2002; Tackley 2002). Additionally, the observed tilting and asymmetry of the upward flow are possibly the response to large-scale ambient flow and the relative motion of the African plate (Ni *et al*. 2002). Sweeping of compositionally-distinct mantle material into discontinuous piles coupled with large-scale plumes actively rising from the piles provides a plausible framework for the heterogeneity and dynamics of the African superplume region. An alternative view is that this structure is a manifestation of a ‘doming’ event where a heated dense layer (discontinuous in this case) ascends and descends through the mantle in a cyclic manner (Davaille *et al*. 2003). A potential problem with each of these scenarios is the small amplitude of the intrinsic chemical density we find in the basal layers. These small amplitudes could be the result of the lessened sensitivity of the geodynamic observables or the underestimation of the thermal density contribution in the basal layers. Future application of the general methodology presented here in conjunction with numerical and physical modeling will help to unravel the source of the intrinsically-dense material observed in the African superplume. Future investigations should include lateral, temperature-dependent viscosity variations in the forward model assumptions and determine its influence on mantle density heterogeneity in and around the superplume structures.

4.6 References

Cammarano, F., S. Goes, P. Vacher & D. Giardini (2003), Inferring upper-mantle temperatures from seismic velocities, *Phys. Earth Planet. Inter.*, *138*(3-4), 197-222.

Davaille, A., M. Le Bars & C. Carbonne (2003), Thermal convection in a heterogeneous mantle, *C. R. Geoscience*, *335*(1), 141-156.

Forte, A.M. (2000), Seismic-geodynamic constraints on mantle flow: implications for layered convection, mantle viscosity, and seismic anisotropy in the deep mantle, *in Earth's Deep Interior: Mineral Physics and Tomography from the Atomic to the Global Scale*, edited by S.-I. Karato et al., pp. 3-36, AGU, Washington, DC.

Forte, A.M. & H.K.C. Perry (2000), Geodynamic evidence for a chemically depleted continental tectosphere, *Science*, *290*, 1940-1944.

Forte, A.M. & J.X. Mitrovica (2001), Deep-mantle high-viscosity flow and thermochemical structure inferred from seismic and geodynamic data, *Nature*, *410*(6832), 1049-1056.

Gurnis, M., J.X. Mitrovica, J. Ritsema & H.J. Van Heijst (2000), Constraining mantle density structure using geological evidence of surface uplift rates: The case of the African Superplume, *Geochem. Geophys. Geosys.*, *1*(7), doi: 1999GC000035.

Ishii, M. & J. Tromp (1999), Normal-mode and free-air gravity constraints on lateral variations in velocity and density of Earth's mantle, *Science*, *285*(5431), 1,231-1,236.Jordan, T.H. (1981), Continents as a chemical boundary layer, *Phil. Trans. Roy. Soc. London A*, *301*(1461), 359-373.

Jordan, T.H. (1981), Continents as a chemical boundary layer, *Phil. Trans. Roy. Soc. London A*, *301*(1461), 359-373.

Karato, S.I. (1993), Importance of anelasticity in the interpretation of seismic tomography, *Geophys. Res. Lett.*, *20*, 1623-1626.

Karato, S.I. & B.B. Karki (2001), Origin of lateral variation of seismic wave velocities and density in the deep mantle, *J. Geophys. Res. Solid Earth*, *106*(B10), 21771-21783.

Kellogg, L.H., B.H. Hager & R.D. Van der Hilst (1999), Compositional stratification in the deep mantle, *Science*, *283*(5409), 1181-1184.

Lithgow-Bertelloni, C. & P.G. Silver (1998), Dynamic topography, plate driving forces and the African superswell, *Nature*, *395*(6699), 269-272.

Masters, G., G. Laske, H. Bolton & A.M. Dziewonski (2000), The relative behavior of shear velocity, bulk sound speed, and compressional velocity in the mantle: implications for chemical and thermal structure, *in Earth's Deep Interior: Mineral Physics and Tomography from the Atomic to the Global Scale*, edited by S.-I. Karato et al., pp. 63-87, AGU, Washington, DC.

McNamara, A.K. & S. Zhong (2005), Thermochemical structures beneath Africa and the Pacific Ocean, *Nature*, *437*(7062), 1136-1139.

Mitrovica, J.X. & A.M. Forte (2004), A new inference of mantle viscosity based upon joint inversion of convection and glacial isostatic adjustment data, *Earth Planet. Sci. Lett.*, *225*(1-2), 177-189.

Mooney, W.D., G. Laske & G. Masters (1998), CRUST 5.1: a global crustal model at 5 x 5 degrees, *J. Geophys. Res. Solid Earth*, *103*(B1), 727-747.

Ni, S.D., E. Tan, M. Gurnis & D.V. Helmberger (2002), Sharp sides to the African superplume, *Science*, *296*(5574), 1850-1852.

Ni, S.D. & D.V. Helmberger (2003a), Ridge-like lower mantle structure beneath South Africa, *J. Geophys. Res. Solid Earth*, *108*(B2), doi:10.1029/2001JB001545.

Ni, S.D. & D.V. Helmberger (2003b), Seismological constraints on the South African superplume; could be the oldest distinct structure on Earth, *Earth Planet. Sci. Lett.*, *206*(1-2), 119-131.

Ni, S.D., D.V. Helmberger & J. Tromp (2005), Three-dimensional structure of the African superplume from waveform modeling, *Geophys. J. Int.*, *161*, 283-294.

Panning, M. & B. Romanowicz (2004), Inferences on flow at the base of Earth's mantle based on seismic anisotropy, *Science*, *303*(5656), 351-353.

Quéré, S. & A.M. Forte (2006), Influence of past and present-day plate motions on spherical models of mantle convection: implications for mantle plumes and hotspots, *Geophys. J. Int.*, *165*, 1041-1057.

Richards, M.A. & B.H. Hager (1984), Geoid anomalies in a dynamic earth, *J. Geophys. Res. Solid Earth*, *89*(B7), 5987-6002.

Ritsema, J., S. Ni, D.V. Helmberger & H.P. Crotwell (1998), Evidence for strong shear velocity reductions and velocity gradient in the lower mantle beneath Africa, *Geophys. Res. Lett.*, *25*(23), 4245-4248.

Ritsema, J., H.J. Van Heijst & J.H. Woodhouse (1999), Complex shear wave velocity structure imaged beneath Africa and Iceland, *Science*, *286*(5446) 1925-1928.

Simmons, N.A., A.M. Forte & S.P. Grand (2006), Constraining mantle flow with seismic and geodynamic data: A joint approach, *Earth Planet. Sci. Lett.*, *246*(1-2), 109-124.

Tackley, P.J. (2002), Strong heterogeneity caused by deep mantle layering, *Geochem. Geophys. Geosys.*, *3*, doi: 10.1029/2001GC000167.

Tan, E., & M. Gurnis (2005), Metastable superplumes and mantle compressibility, *Geophys. Res. Lett.*, *32*, doi: 10.1029/2005GL024190.

Thompson, P.F. & P.J. Tackley (1998), Generation of mega-plumes from the core-mantle boundary in a compressible mantle with temperature-dependent viscosity, *Geophys. Res. Lett.*, *25*(11), 1999-2002.

Trampert, J., F. Deschamps, J. Resovsky & D. Yuen (2004), Probabilistic tomography maps chemical heterogeneities throughout the lower mantle, *Science*, *306*(5697), 853-856.

Wen, L.X. (2001), Seismic evidence for a rapidly varying compositional anomaly at the base of the Earth's mantle beneath the Indian Ocean, *Earth Planet. Sci. Lett.*, *194*(1-2), 83-95.

Chapter 5

Thermal versus Compositional Heterogeneity in the Mantle

5.1 Abstract

The synthesis of seismic and geodynamic data requires mineral physical parameters linking seismic velocity to density perturbations in the Earth's mantle. These parameters are dependent upon several factors including chemical composition, anelasticity of mantle material, mineralogy, and ambient mantle temperature. Therefore, there is a wide range of possible density-velocity conversion factors ($R_{\rho/s} = d[\ln\rho]/d[\ln V_S]$) even when only considering thermal effects in an isochemical mantle. We test the validity of several depth-dependent conversion profiles assuming that all mantle heterogeneity (seismic velocity and density) is generated by lateral variations in temperature. The tests are conducted by simultaneously inverting shear wave travel time data and a diverse suite of geodynamic constraints interpreted with viscous flow response kernels. The geodynamic constraints are represented by spherical harmonics (up to degree 16) and consist of the global free-air gravity field, tectonic plate divergences, dynamic surface topography and the excess ellipticity of the core-mantle boundary. The optimum 1-D thermal $R_{\rho/s}$ profile is compatible with all data excluding dynamic surface topography which is most sensitive to shallow upper mantle compositional variability and non-linear behavior of the thermal $R_{\rho/s}$ relationship. To directly account for

these effects, we estimated 1st-order correction factors to the ambient $R_{\rho/s}$ profile within the cratonic roots and ambient upper mantle independently. These correction factors (defined as $d\left[R_{\rho/s}\right]/\,d\left[\ln Vs\right]$) are highly negative within the cratons signifying considerable compositional buoyancy that counteracts the thermal effects resulting in near-neutral buoyancy. Within the ambient upper mantle, the correction factors are positive and consistent with the expected non-linear behavior of the thermal $R_{\rho/s}$ relationship. The gravity field and dynamic surface topography are shown to be significantly more consistent with each other when applying these corrections to a 1-D $R_{\rho/s}$ relationship. Inversion for a 3-D $R_{\rho/s}$ relationship reveals secondary effects including additional compositional variation within the cratonic roots and the deep-mantle 'superplume' structures. Although compositional effects are found, we estimate the relative contributions of the thermally- and compositionally-induced densities and conclude that thermal effects dominate heterogeneity throughout the non-cratonic mantle.

5.2 Introduction

As discussed in previous chapters, seismic waves are our most direct probe of the Earth and tomographic images have provided evidence of significant heterogeneity in the mantle (e.g. Robertson & Woodhouse 1996; Grand *et al.* 1997; Su & Dziewonski 1997; van der Hilst *et al.* 1997; Ritsema *et al.* 1999; Karason & van der Hilst 2000; Masters *et al.* 2000; Megnin & Romanowicz 2000; Gu *et al.* 2001; Zhao 2001). These mantle heterogeneities can clearly be seen in the new 3-D shear-wave tomography model developed in Chapter 2. The complete model is illustrated in Appendix B and is summarized in Figure 5.1. This model will subsequently be referred to as “TX2007”. Tomographic images, however, do not directly tell us the composition or the density perturbations that drive mantle convection. A simplistic view is that low seismic velocities are due to elevated temperatures which would imply thermally-expanded low-density material and vice versa (Karato 1993). Given such a scenario, seismically fast zones would be cold and sinking while slow zones would be positively buoyant and, therefore, slowly rising through the mantle. The results from Chapter 3 suggest that, to first order, this situation may be correct; however, numerous recent studies combining a variety of constraints including shear (*S*) waves, compressional waves (*P*), normal modes and geodynamic inferences have revealed that variations in temperature do not entirely account for heterogeneous features especially in the Earth’s deep mantle (e.g. Robertson & Woodhouse 1996; Su & Dziewonski 1997; Ishii & Tromp 1999, 2004; Masters *et al*. 2000; Forte & Mitrovica 2001; Saltzer *et al*. 2001; Trampert *et al*. 2004).

In particular, seismic tomography investigations have found that bulk sound and shear wave anomalies significantly vary in character in certain regions of the deep mantle which most likely violates the assertion that mantle heterogeneity is of purely thermal origin (Robertson & Woodhouse 1996; Su & Dziewonski 1997; Masters *et al*. 2000; Saltzer *et al*. 2001). Additionally, long-wavelength tomographic studies including normal mode splitting functions have concluded that some seismically-imaged anomalies are not correlated with density perturbations and may in fact be negatively correlated in limited regions (Ishii & Tromp 1999, 2004; Trampert *et al*.

2004). Moreover, a rapid decrease of vertical correlation of mantle anomalies and a change in the relative behavior of bulk sound and shear wave heterogeneities are found to occur in the lower ~1000 km of the mantle (van der Hilst & Karason, 1999). These observations provide evidence that compositional variations are not necessarily isolated to specific regions and may be ubiquitous in the deepest mantle. Collectively, these seismic studies have made a strong case for the existence of significant compositional heterogeneity in the mantle. However, a remaining issue concerns whether the primary contributor to observed mantle heterogeneity are thermal variations or if these contributions are overshadowed by the proposed strong compositional variations.

The density perturbation field and the relative contribution of thermal and compositional effects to seismic anomalies are difficult to estimate when considering seismic information alone. However, combining seismic body waves and a variety of flow-related geodynamic constraints into single joint tomographic inversions has the potential to detect detailed density perturbations in the mantle (Forte *et al*. 1994; Forte & Woodward 1997; Forte 2000; Simmons *et al*. 2006, 2007). In Chapter 3, we tested whole- versus layered-mantle flow scenarios and concluded that whole-mantle flow is favored since seismic as well as a diverse set of flow-induced geodynamic constraints could be mostly accounted for in this case. Additionally, this study found that a positive correlation of shear wave velocity and density perturbations throughout the lower mantle provides for an optimal solution which favors the dominance of thermal effects on heterogeneity throughout the vast majority of the mantle. It should be noted that this result conflicts with recent long-wavelength solutions where this correlation was found to be weak (or non-existent) in the deep mantle (e.g. Trampert *et al*. 2004) supporting the need for further investigation.

In our previous work (Chapter 3; Simmons *et al.*, 2006), mineral physics derived parameters that relate seismic velocity to density (i.e. $R_{\rho/s} = d[\ln\rho] / d[\ln V_S]$) were not considered since these values are not well-constrained and full exploration of these parameters was not the primary goal of the investigation. However, the determined optimal values of $R_{\rho/s}$ were found to be within the range of recent estimates derived from mineral physics studies when whole-mantle flow was assumed (Karato & Karki 2001; Cammarano *et al*. 2003). In this chapter, we directly employ a large range of radially-symmetric profiles of $R_{\rho/s}$ where density perturbations are assumed to be purely thermally-induced in both the upper mantle (Cammarano *et al.* 2003) and lower mantle (Karato & Karki 2001) rather than assuming an independent optimal solution. These values are integrated within the framework of simultaneous inversions of shear body wave constraints and flow-induced geodynamic observables. As in the preceding chapters, these observables include the global free-air gravity field, dynamic surface topography, horizontal divergences of tectonic plates and the excess ellipticity of the core-mantle boundary (CMB). The overall objective is to identify the mineral physics parameters most capable of explaining the integrated dataset and to explore the assertion that mantle heterogeneity is primarily an effect of thermal variations in more detail. Consequently, we generate a new jointly-derived model of mantle shear wave velocity and our best estimate of thermally-induced density heterogeneities. By establishing a thermal density model, we then estimate the compositional contributions to the total density field by solving for a 3-D density-velocity scaling relationship in the mantle required to fully satisfy all considered data.

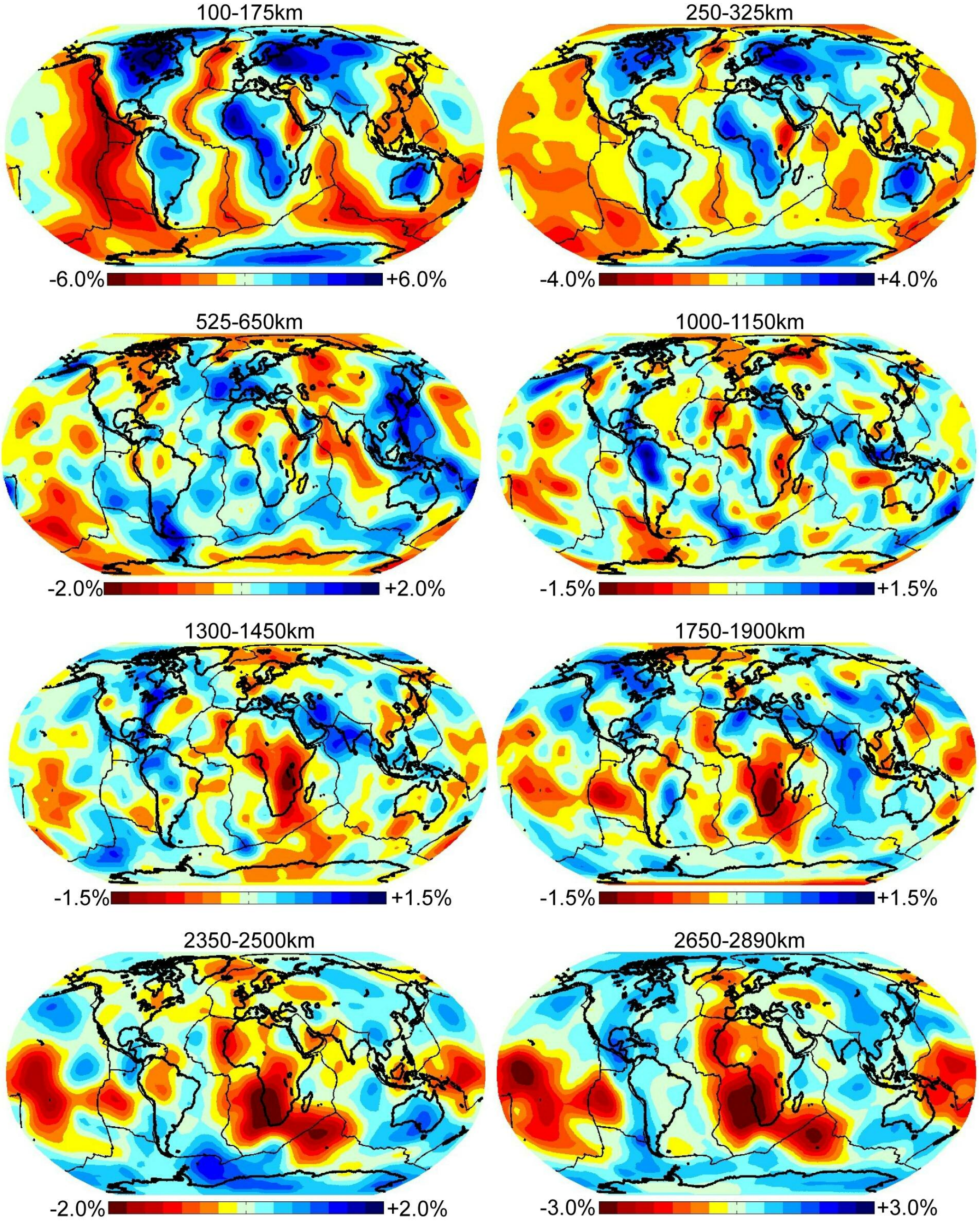

Figure 5.1 Shear wave velocity model TX2007. All values are in terms of percent velocity perturbation relative to a radially-symmetric model described in the text. In the shallow depths (100-325km), the model closely mimics known geologic features including cratonic roots (fast = blue) and mid-ocean ridges (slow = red). Possible subducted slab material is visible near the base of the upper mantle (525-650km) and the mid-mantle where the proposed Farallon slab resides (>1000km depth). The most prominent features in the deep mantle are the large-scale slow regions corresponding to the superplume structures beneath the African continent and Pacific Ocean.

5.3 Combined seismic-geodynamic system

It has been shown in previous studies that mantle heterogeneity models derived solely from seismic constraints are not capable of satisfying the degrees 1-16 geodynamic data fields appreciably; however considering these data sets simultaneously results in mantle models far more consistent with all considered observations (Chapter 3; Simmons *et al*. 2006). We have thus taken a similar approach of integrating a diverse suite of flow-induced geodynamic observables (described in Chapter 3) with the seismic data into a single linear system and inverting for seismic velocity and density heterogeneity at the same time.

The combined linear seismic-geodynamic system described in Chapters 3-4 can be expanded to include weighting factors and regularization:

$$\begin{bmatrix} \mathbf{L} \\ \lambda_G \mathbf{G}\left(R_{\rho/s}\right) \\ \lambda_{CMB} \mathbf{c}\left(R_{\rho/s}\right) \\ \lambda_R \mathbf{R} \end{bmatrix} \mathbf{m} = \begin{bmatrix} \mathbf{r} \\ \lambda_G \mathbf{s} \\ \lambda_{CMB} e \\ \mathbf{0} \end{bmatrix} \tag{5.1}$$

where, again, we solve for the seismic slowness perturbations represented by **m** using the LSQR inversion technique (Paige & Saunders 1982). In this integrated system of equations, **G** is a full matrix ($861 \times 99{,}148 \approx 85\text{M}$ elements) of viscous flow sensitivity kernels where each row represents a specific spherical harmonic component of the free-air gravity, plate divergence and dynamic topography constraints (Figure 5.2). The column vector **s** represents the spherical harmonic coefficients of the observations represented in **G** normalized by their corresponding estimated standard error. The row vector **c** is the viscous flow response sensitivity function for the $l = 2$ zonal harmonic of the excess ellipticity of the CMB (e). Since the viscous flow sensitivity kernels are directly related to density perturbations rather than seismic structure, we must also incorporate a linear relationship between density perturbations (ρ) and shear wave velocity (V_S). In Equation 5.1, the density-velocity relationship is identified by $R_{\rho/s}$ which, again, is the depth-dependent ratio of density to velocity heterogeneity defined by:

$$R_{\rho/s} = d\left[\ln\rho\right] / \, d\left[\ln V_S\right]. \tag{5.2}$$

At some mantle depths, the possible $R_{\rho/s}$ values range by a factor of 2 even when considering thermal contributions alone (Karato & Karki 2001; Cammarano *et al.* 2003). Therefore we evaluated several radially-symmetric $R_{\rho/s}$ profiles recently derived from mineral physics.

Since the integrated linear system contains sensitivity kernels that vary in amplitude, a spectrum of weighting values must also be considered. The scalar value λ_G is a variable incorporated to control the weighting of the geodynamic observations relative to the seismic constraints. A higher value of λ_G forces the solution to match the geodynamic constraints to higher degrees and, therefore, diminishes the control of the seismic constraints on the resulting heterogeneity model (and vice versa). Similarly, amplification of the scalar value λ_{CMB} strengthens the control of the excess CMB ellipticity constraint on the resulting solution. For every computed solution, we forced the CMB constraint to be fully matched by using appropriately large values of λ_{CMB}.

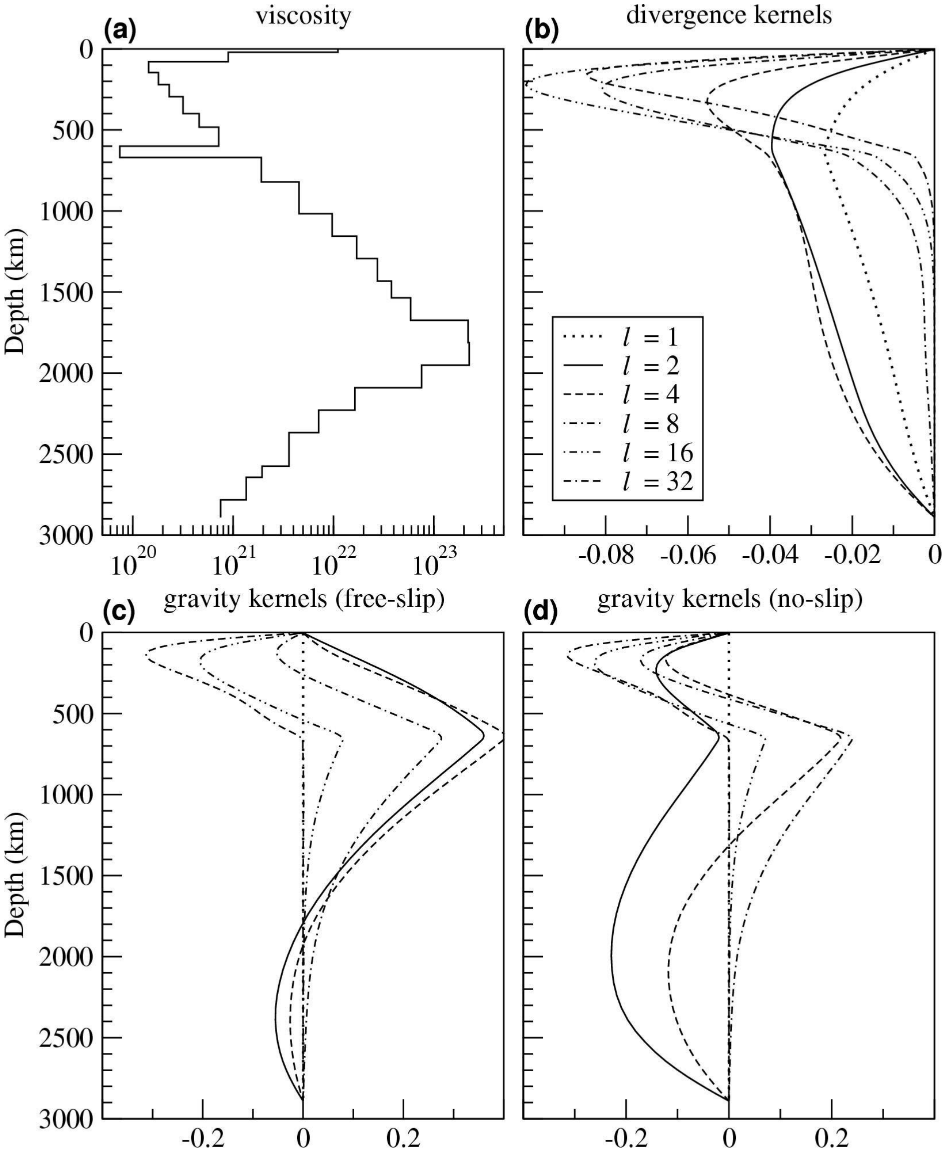

Figure 5.2 Radially-symmetric viscosity profile and associated geodynamic sensitivity kernels. (a) Viscosity profile from *Mitrovica & Forte* (2004). (b) Tectonic plate divergence kernels. (c) Free-air gravity kernels for the free-slip tectonic plate boundary condition. (d) Free-air gravity kernels for the no-slip boundary condition. See *Forte & Peltier* (1994) for further description of the dynamic coupling of the plate motions. **(continued on the next page)**

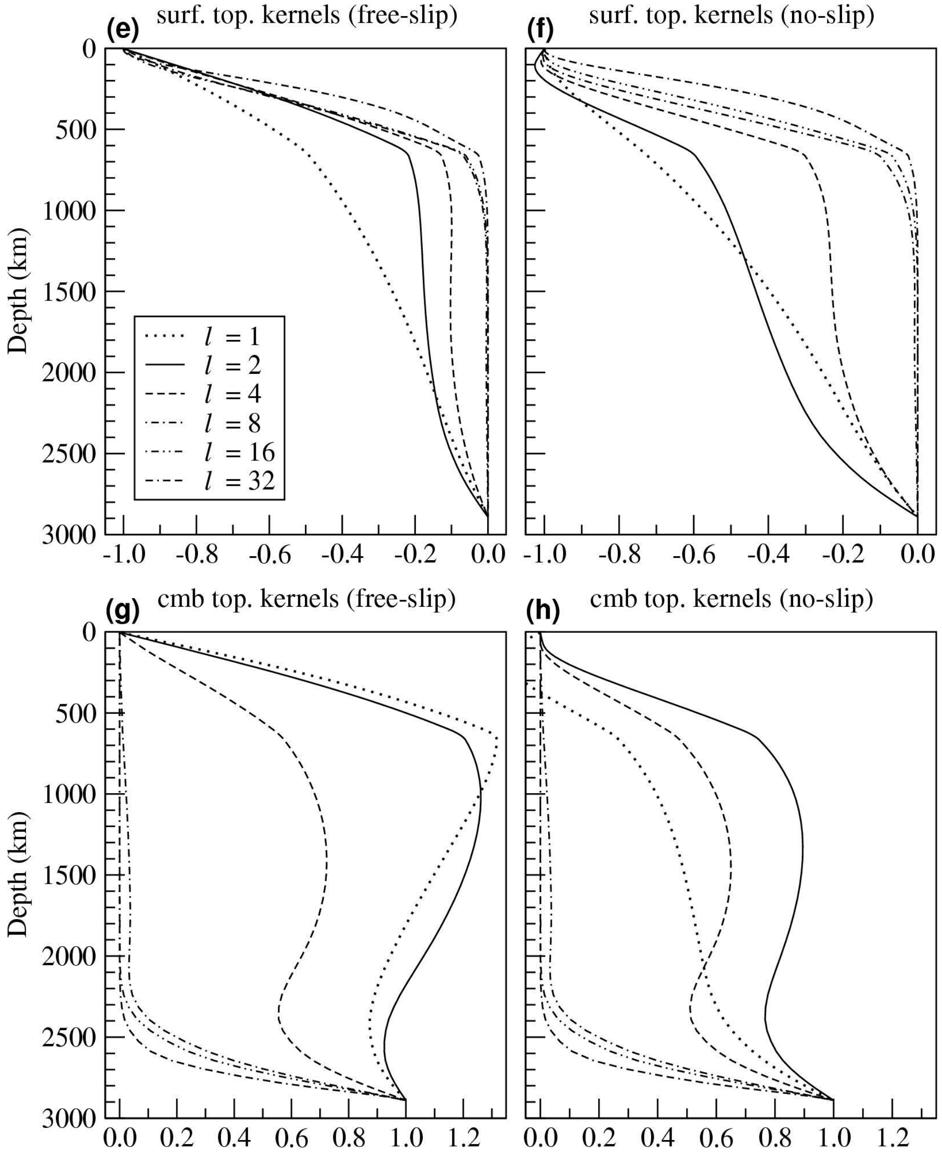

Figure 5.2 (continued) Dynamic surface topography sensitivity kernels for the free-slip boundary conditions (e) and no-slip boundary conditions (f). The CMB topography kernels are similarly shown (g, h).

5.4 Density-velocity conversion

We evaluate three possible depth-dependent density-velocity conversion profiles in the upper mantle ($R_{\rho/s}^{UM}$) from a recent mineral physics study by *Cammarano et al.* (2003). Similarly, we consider six possible conversion profiles in the lower mantle ($R_{\rho/s}^{LM}$) from the work of *Karato & Karki* (2001). The upper and lower mantle cases are considered independently, generating $3 \times 6 = 18$ possible combined profiles. For clarity of further discussion, we will adopt a nomenclature for the density-velocity scaling models. Upper mantle models will be identified by UM# (e.g. UM2) and lower mantle models be further identified by LM# (e.g. LM5). Combined upper-lower mantle scaling profiles will therefore be identified as UM#.LM# (e.g. UM2.LM5).

The selected upper mantle $R_{\rho/s}^{UM}$ profiles are taken from the work of *Cammarano et al.* (2003) and represent the total range of uncertainty based on the compilation of mineral physics parameters considering anelastic and anharmonic effects of thermally-varying, pyrolitic mantle calculated along the 1300°C adiabat (Figure 5.3). These values are averaged over our parameterized depth ranges (1 value per layer) and extrapolated to the surface layer (upper 100km) where no values were estimated. Model UM1 corresponds to the lowest amplitude scaling model, UM2 is a mid-range estimate and UM3 corresponds to the highest amplitude model within the estimated range of uncertainty. It should be noted that these values do not consider compositional effects or the expected non-linear effects primarily associated with the temperature dependence of shear wave attenuation which are known to be significant in the upper mantle (Cammarano *et al*. 2003).

For the lower mantle, we selected a range of independent $R_{\rho/s}^{LM}$ profiles from the work of *Karato & Karki* (2001) (Figure 5.3). Similar to the upper mantle cases, we average values over our depth parameterization and extrapolated into the D'' region. These values represent anelastic and anharmonic effects for thermally-varying perovskite calculated for a variety of shear wave attenuation (Q_S) models (Romanowicz & Durek 2000) and a non-dimensional parameter proportional to the activation energy of attenuation (g). Specifically, we consider three possible shear wave attenuation models (*Q1*, *Q2* and *Q3*) and two possible activation energies (g) equal to 10 and 20 providing six possible lower mantle cases to be considered (Table 5.1). Each model assumes a singular Anderson-Grüneisen parameter, Γ, for perovskite equal to 6. See *Karato & Karki* (2001) for further description of the input parameter definitions and Q_S model profiles. It should be noted that there is expected to be significant depth variation of the $R_{\rho/s}$ values for all possible upper and lower mantle cases which can clearly be observed in Figure 5.3. It is therefore improper to assume that all velocity heterogeneities can be scaled to density using a single value for either the upper or lower mantle. This is true even if compositional effects to mantle heterogeneity are ignored.

Table 5.1 Lower mantle density-velocity conversion profile parameters ($R_{\rho/s}$)

Model ID	*Q* model ID	Dimensionless Attenuation activation parameter, *g*
LM1	Q2	20
LM2	Q3	20
LM3	Q1	20
LM4	Q2	10
LM5	Q3	10
LM6	Q1	10

Each model assumes a Anderson-Grüneisen parameter for perovskite equal to 6. See Karato & Karki (2001) for Q models and other details.

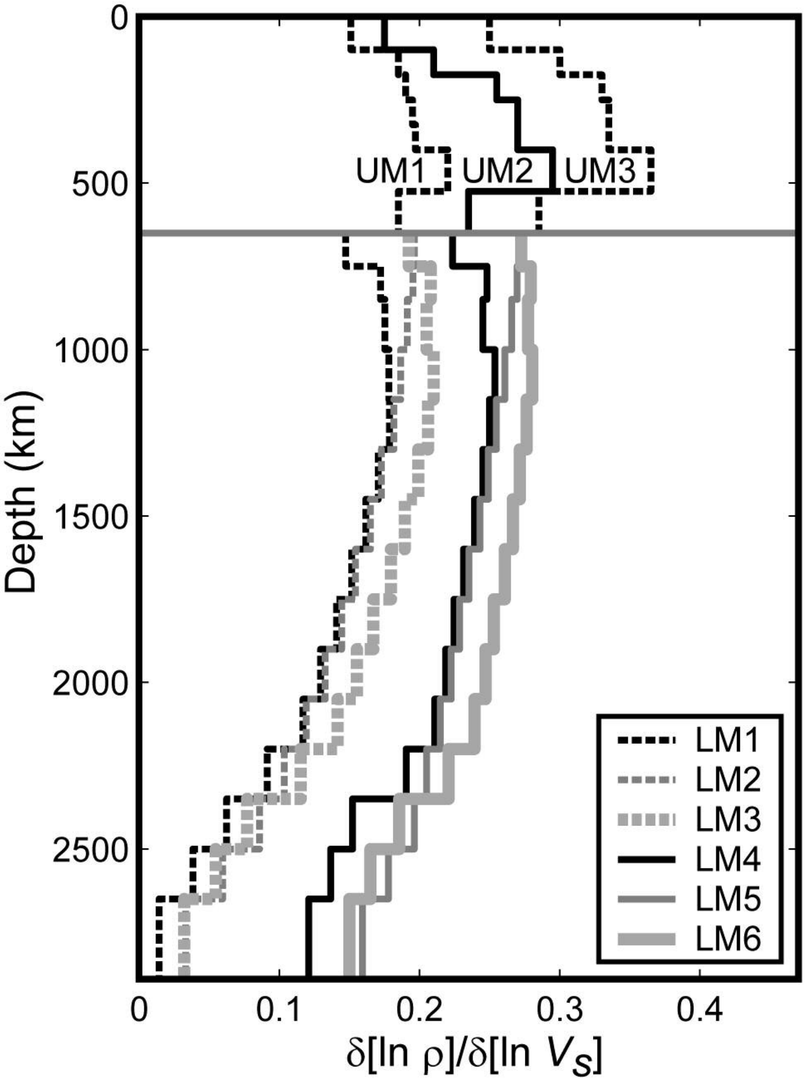

Figure 5.3 Mineral physical density-velocity conversion profiles considered in this study for the purpose of simultaneous inversion of seismic and geodynamic constraints. Each upper mantle profile (UM#) considers anelastic and anharmonic effects of thermally-varying pyrolitic material calculated along the1300°C adiabat (Cammarano *et al*. 2003). These upper mantle models represent the full range of uncertainty of Q_S and composition. The lower mantle models (LM#) represent anelastic and anharmonic effects for thermally-varying mantle (Karato & Karki 2001). See Table 5.1 for description of the parameters used for each LM profile. The upper and lower mantle models were considered independently providing 18 possible combined profiles.

5.5 Applying radially-symmetric $R_{\rho/s}$ models

Simple velocity-to-density scaling of a mantle model derived solely from seismic constraints does not provide for satisfactory reconciliation of the geodynamic constraints as previously pointed out in Chapter 3 (Simmons *et al*. 2006). However, minor adjustments to the amplitude of the anomalies and slight reconfigurations of the seismic structures via simultaneous inversions allow for much higher degrees of reconciliation of the geodynamic observations. To further strengthen this point, we scaled the TX2007 velocity model derived in Chapter 2 by each of the 18 scaling models described in the previous section ($R_{\rho/s}$). The best scaling model was found to be UM1.LM1 (the lowest amplitude density case) which provided the highest variance reduction fit to the geodynamic constraints. These variance reduction fits are: 1% for the gravity field; 48% for the horizontal plate divergence field; -44% for the dynamic surface topography; and an excess CMB ellipticity corresponding to 444m (the observation is 400m). If we perform the joint inversion assuming the same scaling profile (UM1.LM1), we find much better fits to the observations: 60%, 95% and -16% of the gravity, plate divergence and dynamic topography fields, respectively. This is achieved while satisfying the observed CMB ellipticity perfectly and matching the seismic data almost equally well as TX2007 without increased model complexity (*C*) as defined by Equation 2.34. Although there is still a significant misfit, the simultaneous inversion finds heterogeneity models that are distinctly more consistent with all data fields considered. This evaluation shows that in order to properly discriminate amongst $R_{\rho/s}$ profiles, we must perform simultaneous inversions considering both seismic and geodynamic constraints so that the solutions are not biased by the employed seismic model. Also, if we generate models with unlimited complexity, all constraints could be fully satisfied using a wide range of scaling profiles ($R_{\rho/s}$) providing no clear discrimination. Consequently, we must also consider the resulting model complexity (*C*) and how this measure trades off with seismic and geodynamic data fits for each case. The approach described in this section is, therefore, to find mantle heterogeneity models that match our seismic constraints equally well for each of the 18 profiles for a spectrum of model complexity estimates.

In terms of the linear forward model described in Equation 5.1, the approach entails finding the values for the geodynamic and regularization weighting parameters (λ_G and λ_R, respectively) that allow for an equivalent fit to the employed seismic observations. The initial steps in this procedure were to select a scaling profile ($R_{\rho/s}$), a fixed regularization weight (λ_R) and a first guess of the geodynamic weighting parameter, λ_G. Given these inputs, we then solved the system in Equation 5.1 for the seismic slowness perturbation model (**m**) and calculated the variance reduction fit to the seismic constraints. A simple optimization script was used to adjust the value of λ_G and iterate the inversion process until the resulting model matched the seismic data to the desired level. We chose to match the seismic data to 93.2% which is reasonably close to the starting seismic model match (93.5%). After convergence, we assigned a new regularization weight (λ_R) and repeated the optimization procedure and, thus, generated tradeoff curves of geodynamic data fit with model complexity.

This process requires the ability to solve the large-scale system of equations many times over (~1000 inversions). The combined system includes the geodynamic sensitivity matrix which is a full system of ~85 million elements (~700 Mbytes) as well as a ~99% sparse set of equations (seismic Fréchet kernels and regularization matrix). To augment these mixed matrices in MATLAB, either the sparse system must be converted to full (not tenable) or the full system must be converted to sparse which is extremely inefficient. With this in mind, I developed a modified LSQR inversion algorithm in the MATLAB environment that can solve sparse sets of equations as well as a full set of equations simultaneously without converting to either storage system. This modified algorithm also allows for a functional form of $R_{\rho/s}$ rather than directly embedding this relationship into the geodynamic sensitivity kernel matrix. Therefore, the density-velocity scaling is applied within the inversion scheme rather than explicitly generating multiple geodynamic sensitivity kernel matrices. The modified LSQR algorithm and the MATLAB script are outlined in Appendix A. With this algorithm, we are able to solve the integrated seismic-geodynamic system in less than 30 minutes on a standard Unix workstation allowing for a multitude of model runs and a comprehensive evaluation of the input parameters.

Geodynamic data matches for each of the 18 velocity-density profiles are plotted in Figure 5.4. The variance reduction fits are plotted as a function of the relative density model complexity defined by the ratio:

$$C_R \equiv \frac{\left\| \mathbf{R}\left(\mathrm{d}ln\bar{\rho}\right)^{joint} \right\|_2}{\left\| \mathbf{R}\left(\mathrm{d}ln\bar{\rho}\right)^{seismic} \right\|_2} \tag{5.3}$$

where **R** is a regularization matrix. The vector $\left(\mathrm{d}ln\bar{\rho}\right)^{joint}$ is the density perturbation field determined by joint inversion and $\left(\mathrm{d}ln\bar{\rho}\right)^{seismic}$ is the density field found by scaling the purely seismically-derived velocity model (TX2007) by the corresponding $R_{\rho/s}$ profile. Two fundamental observations can be made from the tradeoff curves (Figure 5.4). Firstly, the upper mantle models UM2 and UM3 are incapable of satisfying the employed geodynamic constraints with model complexity levels similar to the starting model ($C_R \approx 1$). Most notably, we find that particularly complex models are required to explain the dynamic topography data when applying models UM2-3. Regardless of the lower mantle scaling model assumed, it is evident that the upper mantle model UM1 is preferred over the higher amplitude scaling profiles UM2-3. The second fundamental observation is that, while there is a clear discrimination amongst upper mantle scaling models, the lower mantle models (LM1-6) show relatively minor variance reduction deviations providing a lower degree of discriminatory power. The primary reasons for this result are the low-amplitude nature of the seismic perturbations in the middle of the lower mantle (therefore small density perturbations) and generally decreasing geodynamic sensitivity with depth (see Chapter 3). Additionally, the seismic constraints allow for significant amplitude variations of the seismic model in the deepest mantle while maintaining a similar level of fit to the seismic data (Figure 5.5). This relative lack of amplitude control in the deepest mantle reduces the effect of increased $R_{\rho/s}^{LM}$ values thereby making discrimination more difficult than the upper mantle scaling.

Although lower mantle heterogeneity accounts for only a fraction of the total geodynamic observations, we are still able to differentiate amongst lower mantle scaling models with closer inspection. Figure 5.6 is a detailed view of the tradeoff between geodynamic data match and model complexity for the cases UM1.LM1-6. It can be concluded from Figure 5.6 that the plate motion and dynamic topography data fields are fit to very similar levels for each of the lower mantle scaling models and, therefore, provide insignificant discriminatory power. This result is not surprising given that these fields are most sensitive to uppermost mantle heterogeneity (<250 km depth). However, significant deviations of variance reduction fit to the gravity field are observed amongst the $R_{\rho/s}^{LM}$ models owing to the relatively higher sensitivity of the gravity field to deep mantle heterogeneity (Figure 5.6). Specifically, there is >10% range in variance reduction fit to the free-air gravity field when considering heterogeneity models with a level of complexity similar to the seismically-derived model ($C_R \approx 1$) and it is observed that the high-amplitude $R_{\rho/s}^{LM}$ models (LM4-6) consistently provide higher degrees of fit to the global free-air gravity field.

In order to determine if the variance reduction fits simply reflect the ability to match the low-degree harmonics, we calculated the degree-dependent cross correlation of the observed and predicted geodynamic data fields for heterogeneity models with equivalent complexity ($C_R = 1$) (Figure 5.7). It is observed that the low degree components of the gravity field are best matched and the correlation generally decreases with increasing harmonic degree in all cases. It is also evident that components beyond harmonic degree 13 are poorly matched in all cases most likely owing to the low power of the gravity field at these higher degrees (Marsh *et al.* 1990). We find that each of the harmonic degree components of the free-air gravity field are best matched by joint heterogeneity models generated using the high-amplitude scaling models (LM4-6) while the low-amplitude scaling models (LM1-3) consistently provide for poorer correlations to each harmonic component of the gravity field. Therefore, the level of data fit is not merely reflecting the ability to match the low-degree harmonics while ignoring the high-degree harmonics. Based on these observations, we conclude that the higher amplitude $R_{\rho/s}^{LM}$ scaling profiles (LM4-6) are preferred over the lower amplitude models (LM1-3). Additionally, mineralogical changes across the 660-km discontinuity should provide for an abrupt and significant increase of the $R_{\rho/s}$ factor across upper-lower mantle boundary (see Cammarano *et al.* 2003). The high-amplitude $R_{\rho/s}^{LM}$ models are required to remain consistent with these mineral physics constraints providing an additional argument for selecting lower mantle models LM4-6 rather than the low-amplitude models. However, it is difficult to discriminate within the subset of high-amplitude scaling models (LM4-6) since there is no clear preference in terms of fit to the employed geodynamic observations. Since the absolute highest amplitude $R_{\rho/s}^{LM}$ models (LM5-6) provide no significant improvement to the geodynamic data fits relative to LM4, we selected LM4 as our preferred 1-D lower mantle thermal scaling profile. Therefore, our preferred combined 1-D thermal scaling profile is UM1.LM4 (Figure 5.8) and will further be referred to by $R_{\rho/s}^{ambient}$.

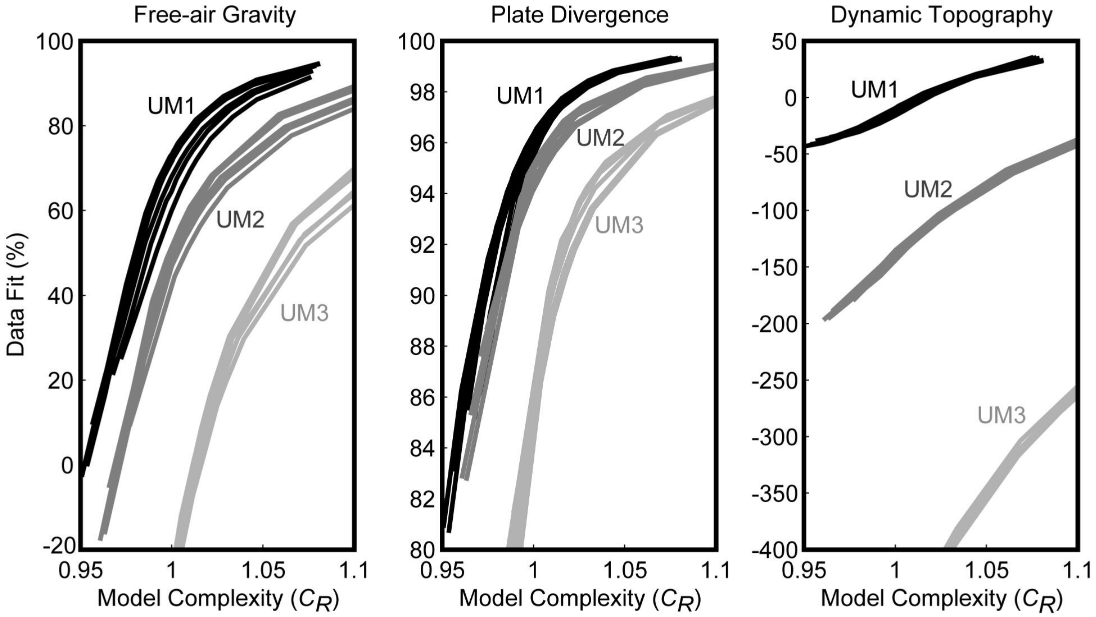

Figure 5.4 Geodynamic data fit tradeoffs with model complexity for heterogeneity models satisfying the seismic constraints to level of 93.2% variance reduction. Each curve corresponds to a suite of jointly-derived heterogeneity models assuming a specific thermal density-velocity scaling profile. The curves are grouped according to the upper mantle $R_{\rho/s}$ profile used (black = UM1.LM1-6; dark gray = UM2.LM1-6; light gray = UM3.LM1-6). Note that model complexity ratio C_R = 1 corresponds to a model complexity level equivalent to the TX2007 seismic model (see text for definition). It is clear that upper mantle model UM1 is most capable of satisfying the combined dataset. Note that all models fully satisfy the current constraints on excess CMB ellipticity (not shown).

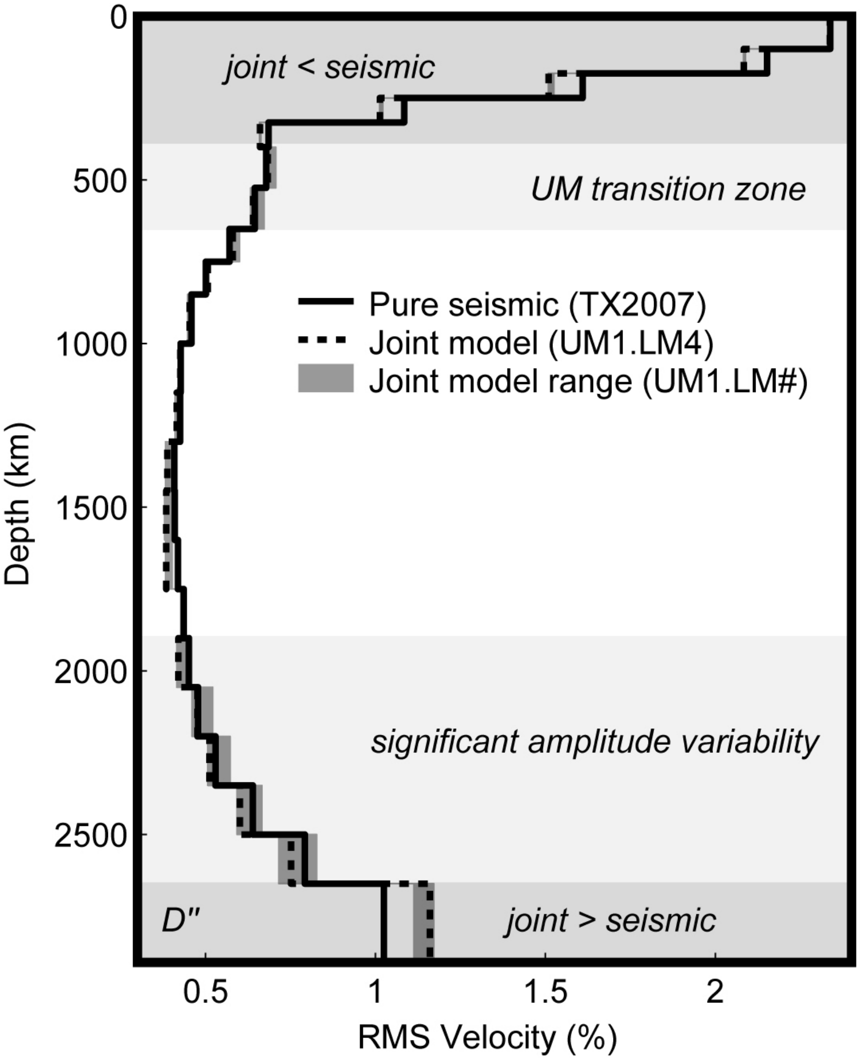

Figure 5.5 Root-mean-squared (RMS) amplitude profiles for the pure seismic model (TX2007) and joint models considering seismic and geodynamic constraints simultaneously. Upper mantle amplitudes tend to reduce when geodynamic constraints are included in the inversion. Amplitudes in the lower ~1000 km of the mantle vary significantly depending on the lower mantle $R_{\rho/s}$ applied. Typically, the lower amplitude scaling models (LM1-3) increase the amplitudes in the deepest mantle whereas the higher amplitude models (LM4-6) decrease the amplitudes. All scaling models tend to increase the amplitudes in the D'' region which means that heterogeneity is pushed towards the deepest mantle by the simultaneous inversion.

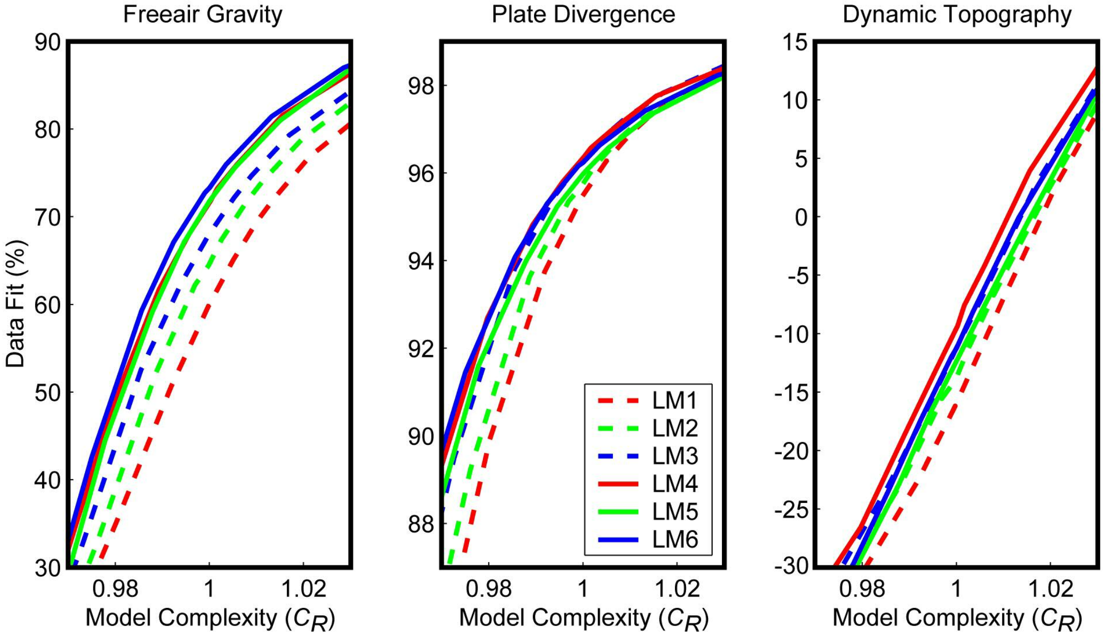

Figure 5.6 Geodynamic data fit tradeoffs with joint heterogeneity model complexity for each of the lower mantle density-velocity scaling profiles (LM1-6). The same upper mantle scaling profile (UM1) was assumed in all cases and each model satisfies the seismic data equally well (93.2%). The higher amplitude models (LM4-6) reconcile the combined dataset better than the lower amplitude cases (LM1-3).

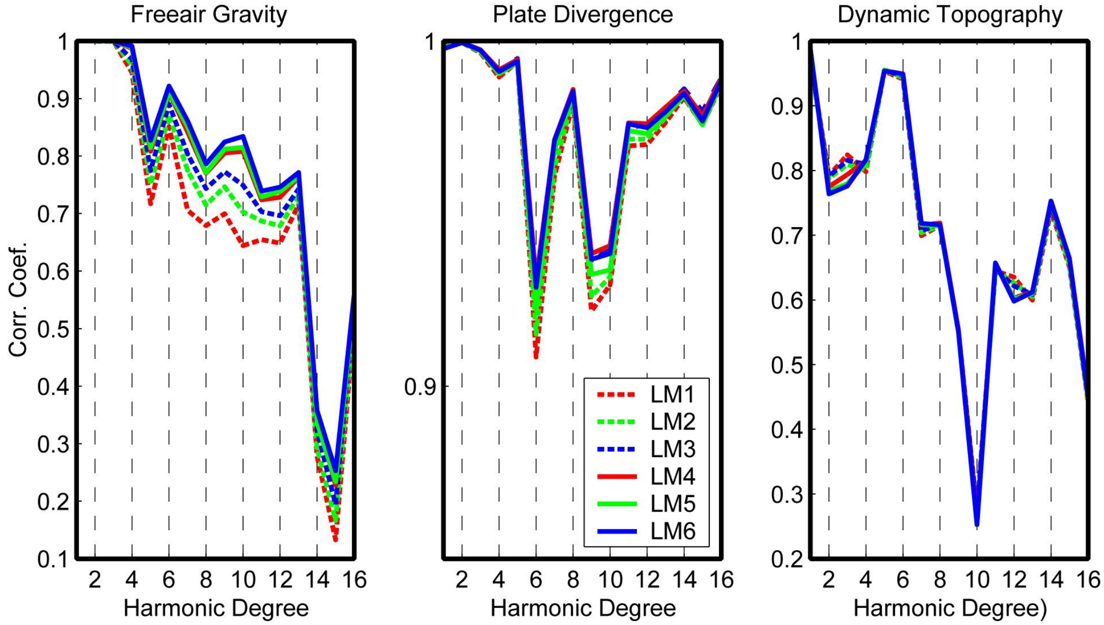

Figure 5.7 Cross correlation of the observed and predicted geodynamic harmonic components for equally complex jointly-derived heterogeneity models ($C_R = 1$). All harmonic components of the free-air gravity and tectonic plate divergence fields are best correlated when assuming the high amplitude scaling models (LM4-6).

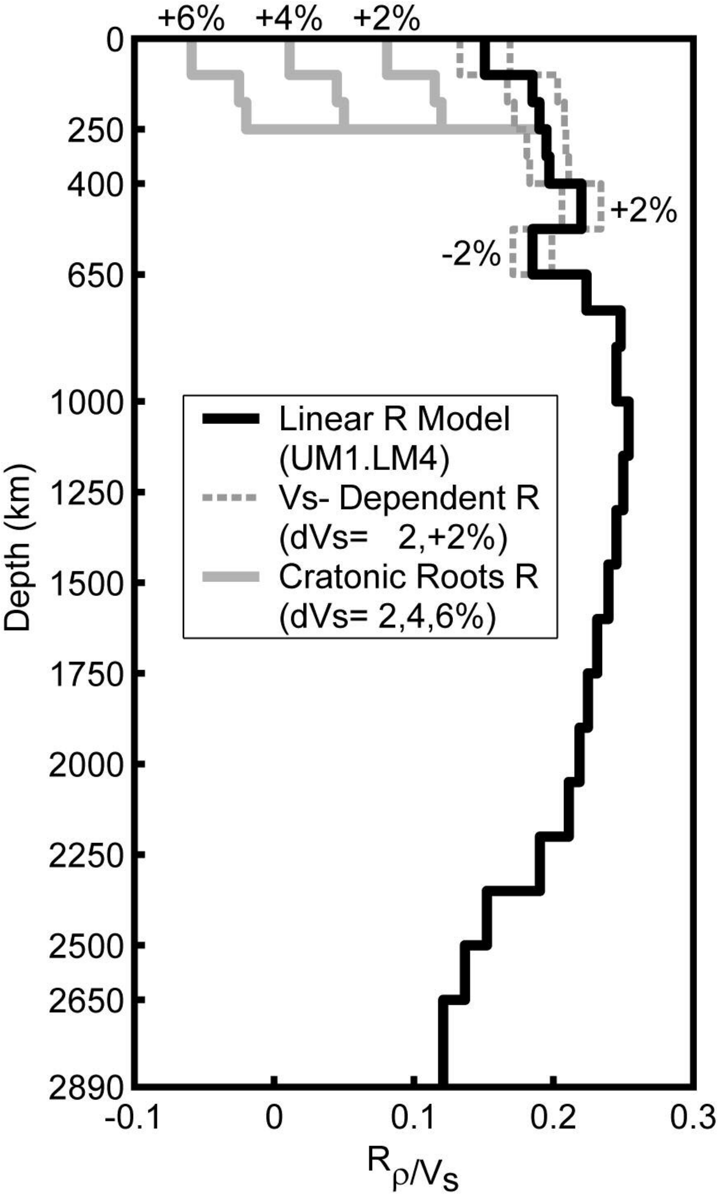

Figure 5.8 Best combined ambient thermal scaling profile (black) and corrected profiles for selected velocity perturbation levels. The corrected scaling factors within the cratonic roots are dramatically lower amplitude than the ambient profile and are negative in the extremely fast shallow mantle portions of the cratonic roots (solid gray lines). This results in overall near-neutral buoyancy of the cratonic roots. The determined correction factors for the non-linear behavior of the thermal scaling relationship result in slightly reduced density-velocity scaling in slow zones and vice versa (dashed gray lines).

5.6 Shallow-mantle scaling corrections

The surface dynamic topography data field is poorly matched when assuming the simple radially-symmetric $R_{\rho/s}^{ambient}$ model (Table 5.2). It is known that dynamic topography is most sensitive to the density variations in the shallowest upper mantle where significant compositional heterogeneity as well as non-linear behavior of the thermal density-velocity scaling is expected (Cammarano *et al*. 2003). Previous studies have concluded that the cratonic roots are nearly neutrally-buoyant contradicting what the thermal density-velocity conversion would predict (Jordan 1978, 1981; O'Reilly *et al*. 2001). Therefore, lower (sometimes negative) $R_{\rho/s}$ values are required within the cratonic roots in order to better match the dynamic surface topography clearly contradicting what is expected in purely thermally-varying upper mantle material (Forte *et al*. 2007; Simmons *et al*. 2007; Chapter 4). Additionally, the thermal $R_{\rho/s}$ values within the ambient (non-cratonic) upper mantle are non-linear in that they are expected to decrease significantly in high-temperature regions and increase in low-temperature regions (Cammarano *et al*. 2003). This effect results in different thermal density anomaly magnitudes in hot and cold zones even if the velocity anomalies are equal in magnitude (but opposite in sign). The first-order non-linear and compositional effects on $R_{\rho/s}^{ambient}$ can be estimated by correcting the scaling factors on the basis of background velocity structure within the ambient upper mantle and cratonic regimes:

$$R_{\rho/s}^{corrected} = R_{\rho/s}^{ambient} + \left(\frac{d\left[R_{\rho/s}\right]}{d\left[\ln V_S\right]}\right)\left(\frac{\delta V_S}{V_S}\right) \tag{5.4}$$

where the derivative $d\left[R_{\rho/s}\right]/\,d\left[\ln Vs\right]$ adjusts the background $R_{\rho/s}$ according to the underlying velocity model obtained by joint inversion ($\delta V_S\,/\,V_S$) assuming the radially-symmetric $R_{\rho/s}^{ambient}$ model. A total of three derivatives were found by directly testing all reasonable values within three independently defined mantle regimes:

1) cratonic roots (0-250 km)
2) non-cratonic shallow mantle (0-250 km)
3) deep upper mantle (250-650 km)

We defined the cratonic roots using the surface locations of Archean/Proterozoic shield regions in the CRUST5.1 model (Mooney *et al.* 1998) and delineating with depth (down to 250 km) according to the jointly-derived velocity structure. The obtained correction factors are listed in Table 5.3 and the effects are illustrated in Figure 5.8 for some selected velocity perturbations. Within the cratonic roots, $d\left[R_{\rho/s}\right]/\,d\left[\ln Vs\right]$ is highly negative and results in overall negative scaling factors in regions with very high velocities (greater than ~4% velocity increase in the upper 100 km). In the non-cratonic (presumably thermally-controlled) upper mantle, the $d\left[R_{\rho/s}\right]/\,d\left[\ln Vs\right]$ values were found to be positive and relatively small compared to the cratonic correction (Table 5.3). These positive values result in a decrease of $R_{\rho/s}^{ambient}$ in low-velocity zones and an increase in high-velocity zones which is generally consistent with the expected non-linear behavior of $R_{\rho/s}$ within the upper mantle (Cammarano *et al*. 2003). Adopting the corrected density-velocity scaling ($R_{\rho/s}^{corrected}$) and re-performing the joint inversion process produces a mantle heterogeneity model that fits the estimated dynamic topography to much higher levels than the simple 1-D scaling model ($R_{\rho/s}^{ambient}$) (Table 5.2). The observed degree of improvement (~50%) far exceeds previous treatment where velocity-dependence of $R_{\rho/s}$ within the cratonic roots was not considered (e.g. Simmons *et al*. 2007; Chapter 4).

Table 5.2 Heterogeneity model properties

		Data fits					
Model type	ρ-V_s conversion model	Seismic (%)	Free-air gravity[a] (%)	Plate divergence[b] (%)	Dynamic topography[c] (%)	CMB ellipticity[d] (km)	Model complexity (C_R) [e]
TX2007	UM1.LM4	93.5	-46	32	-80	1.3	1.0
Joint	UM1.LM4	93.2	71	96	-9	0.4	1.0
Joint	Corrected[f]	93.2	75	98	41	0.4	1.0
Joint	3D	93.2	92	99	82	0.4	1.0

Percentages are variance reduction fits to spherical harmonic components.

[a] Satellite-derived free-air gravity anomalies from the GEM-T2 geopotential model (Marsh et al. 1990) (degrees 2-16).

[b] Horizontal divergence of the tectonic plate velocities from the NUVEL-1 model (De Mets et al. 1999) (degrees 1-16).

[c] Crust-corrected dynamic surface topography estimate (Forte & Perry 2000) (degrees 1-16).

[d] Excess ellipticity is represented by a single zonal harmonic of degree l=2 and corresponds to 400 meters of excess ellipticity of the CMB (Mathews et al. 2002).

[e] Complexity (i.e. roughness) is represented by the density model complexity ratio (C_R) (see text).

[f] Includes velocity-dependent corrections for ambient and cratonic upper mantle (see text).

Table 5.3 Preferred thermal ($R_{\rho/s}$) and corrections.

Depth Range (km)	$R_{\rho/s}$	1st-order Thermal Correction: $d[R_{\rho/s}]/d[\ln_s]$	1st-order Craton Correction: $d[R_{\rho/s}]/d[\ln V_s]$
0-100	0.151	0.9	-3.5
100-175	0.185	0.9	-3.5
175-250	0.190	0.9	-3.5
250-325	0.195	0.7	0
325-400	0.197	0.7	0
400-525	0.220	0.7	0
525-650	0.185	0.7	0
650-750	0.224	0	0
750-850	0.248	0	0
850-1000	0.245	0	0
1000-1150	0.254	0	0
1150-1300	0.250	0	0
1300-1450	0.245	0	0
1450-1600	0.239	0	0
1600-1750	0.231	0	0
1750-1900	0.225	0	0
1900-2050	0.219	0	0
2050-2200	0.211	0	0
2200-2350	0.190	0	0
2350-2500	0.152	0	0
2350-2650	0.137	0	0

5.7 Thermal vs. non-thermal mantle density

As noted in the previous section, $R_{\rho/s}^{corrected}$ represents the scaling relationship including 1st-order corrections for the non-linear thermal effects as well as the compositional effects of the cratonic roots. Incorporating the estimated non-linear thermal corrections throughout the upper mantle and ignoring the compositional effects of the cratonic roots, we can define a purely thermal relationship:

$$R_{\rho/s}^{thermal} = R_{\rho/s}^{ambient} + \left(\frac{d\left[R_{\rho/s}\right]}{d\left[\ln V_S\right]} \right)^{thermal} \left(\frac{\delta V_S}{V_S} \right) \tag{5.5}$$

where $R_{\rho/s}^{ambient}$ is the simple 1-D scaling model (UM1.LM4), $\left(d\left[R_{\rho/s}\right] / d\left[lnVs\right]\right)^{thermal}$ are the upper mantle thermal correction derivatives (Table 5.3), and ($\delta V_S / V_S$) is the jointly-derived velocity model generated assuming $R_{\rho/s}^{ambient}$. Using this density-velocity scaling model and the jointly-derived velocity model, we can estimate the thermally-induced density perturbations in the mantle:

$$\left(\frac{\delta\rho}{\rho} \right)^{thermal} = R_{\rho/s}^{thermal} \left(\frac{\delta V_S}{V_S} \right) \tag{5.6}$$

In addition, we can approximate the necessary temperature fluctuations required to generate the density anomalies:

$$\delta T = -\frac{1}{\alpha(r)}\left(\frac{\delta\rho}{\rho}\right)^{thermal} \tag{5.7}$$

where $\alpha(r)$ is the depth-dependent coefficient of thermal expansion. We assumed $\alpha = 3\times10^{-5}K^{-1}$ at the surface linearly decreasing to $\alpha = 2.5\times10^{-5}K^{-1}$ at the base of the upper mantle and reported high-pressure estimates in the lower mantle (Chopelas & Boehler 1992). Figures 5.9-11 display our thermal density model and corresponding temperature variations for selected depths.

It is evident that we can satisfy the degree 16 geodynamic data to fairly reasonable levels assuming that all mantle heterogeneity outside of the cratonic roots are generated by lateral variations in temperature (Table 5.2). However, there are certainly still substantial misfits to the ascribed geodynamic constraints implying that the thermal hypothesis is not completely satisfactory. Some of the likely sources of the misfit to the geodynamic constraints are the existence of additional compositional heterogeneity, partial melting and higher order non-linear behavior of the $R_{\rho/s}^{thermal}$ profile in the shallowest mantle (Cammarano *et al*. 2003). None of these complications are directly considered in the previous model development; therefore, additional steps are required to address these possibilities.

In the context of our generalized modeling approach, we can account for 'non-thermal' heterogeneity by solving for a fully three-dimensional $R_{\rho/s}$ relationship that translates seismic velocity to density considering all possible sources including thermal and compositional contributions. A three-dimensional (3D) density-velocity scaling relationship, $R_{\rho/s}^{3D}$, can be established by solving the forward model (expanded version of Equation 4.4):

$$\begin{bmatrix} \lambda_G \mathbf{G}\left(\mathbf{m}^{joint}\right) \\ \lambda_{CMB} \mathbf{c}\left(\mathbf{m}^{joint}\right) \\ \lambda_R \mathbf{R} \end{bmatrix} R_{\rho/s}^{3D} = \begin{bmatrix} \lambda_G \mathbf{s} \\ \lambda_{CMB} e \\ \mathbf{0} \end{bmatrix} \tag{5.8}$$

where $\mathbf{m}^{joint}$ is the seismic slowness model obtained by joint inversion assuming the $R_{\rho/s}^{corrected}$ density-velocity relationship. This linear system is similar to the system described in Equation 5.1. However, rather than solving for a seismic model, we solve for a density-velocity scaling field while assuming a fixed seismic model. The process is similar to the 2nd step of a non-linear inversion where both the scaling relationship and seismic models are unknown. The fundamental difference is that we accept the seismic model obtained by the thermal joint inversion process as the final shear wave velocity model. After solving the linear system, we can then estimate the *total* density perturbation field:

$$\left(\frac{\delta\rho}{\rho}\right)^{total} = R_{\rho/s}^{3D}\left(\frac{\delta V_S}{V_S}\right) \tag{5.9}$$

It is clear from the above relationship that a departure of $R_{\rho/s}^{3D}$ from the thermal density-velocity conversion ($R_{\rho/s}^{thermal}$) represents effects not directly accounted for by the assumed thermal relationship. Therefore, these scaling model deviations are a product of variations of composition and possibly higher order non-linear behavior of the thermal density-velocity relationship.

We can reveal density contributions from ‘non-thermal’ sources (including variability of mantle composition) through removal of the thermally-induced densities from the total density perturbation field:

$$\left(\frac{\delta\rho}{\rho}\right)^{non-thermal} = \left(\frac{\delta\rho}{\rho}\right)^{total} - \left(\frac{\delta\rho}{\rho}\right)^{thermal} \tag{5.10}$$

Linear combination of the thermal *and* non-thermal density fields allows for nearly complete reconciliation of the geodynamic observations (Table 5.2). Selected depths of the calculated residual density field model are displayed in Figures 5.9-11. The most notable residual densities observed in the shallow mantle (0-250 km) are the negative density signatures associated with the roots of the continental cratons (Figure 5.9c). These negative residual densities oppose the thermal densities making the cratonic roots nearly neutrally-buoyant on average (compare to Figure 5.9a). This result is consistent with studies of the sub-continental lithosphere where a balance of the thermal and chemical buoyancy is thought to occur (Jordan 1978, 1981). Also in accord with the results of this study, analysis of mantle xenoliths suggests that the compositional buoyancy associated with cratonic roots could persist to depths exceeding 200 km (O’Reilly *et al*. 2001).

Also within the shallow upper mantle, a secondary residual density anomaly is found beneath the eastern Pacific Ocean extending from Antarctica to Alaska. The reduction of the density-velocity scaling factor within this structure is likely a product of higher order non-linear behavior of the $R_{\rho/s}$ relationship which is not directly accounted for by $R_{\rho/s}^{thermal}$. Relatively minor residual densities are found in the base of the upper mantle (Figure 5.9d) as well as the upper portion of the lower mantle (down to ~1000 km depth). However, a high residual density is observed beneath the East African Rift zone that persists over a vast depth range (Figure 5.10c,d). It is difficult to interpret the cause of this particular anomaly since it is unclear if partial melting could occur at these great depths and/or whether this feature is connected to the deeper mantle structures beneath the African continent.

In the middle of the lower mantle, we find few zones with residual density anomalies comparable in magnitude to the estimated thermal density field. However, we do detect a significant high-density (positive) residual component beneath the southern tip of the African continent that extends from the base of the mantle well into the mid-mantle (Figures 5.11-12). This density signature correlates with the location of the well-known African 'superplume' structure. A multitude of studies (including Chapter 4) have provided evidence that this structure is compositionally-distinct relative to the surrounding mantle and has therefore been deemed a large-scale thermochemical plume (e.g. Ritsema *et al*. 1998, 1999; Ishii and Tromp 1999; Masters *et al*. 2000; Ni *et al*. 2002, 2005; Ni and Helmberger 2003a,b; Simmons *et al*. 2007). Our results indicate that the high-density compositional component acts to decrease the overall buoyancy of the superplume structure and may have significant dynamic consequences (Simmons *et al*. 2007). However, it should be noted that the amplitude of the compositional density component is less than the thermal component; therefore, the feature remains buoyant and is actively rising through the mantle. See Chapter 4 for a detailed image and further discussion of the African superplume structure.

In the basal layer of our model space (corresponding to the D'' region), we find more significant compositional density signatures than found within the shallower mid-mantle depths (Figure 5.12d). Specifically, we find that the region surrounding the compositionally-dense core of the African superplume possesses an opposite compositional signature. In particular, the linear structure extending from the southern tip of the African continent into the Indian Ocean possesses positive compositional buoyancy as well as positive thermal buoyancy. Therefore, the compositional component acts to increase the total buoyancy of this structure. Other studies have concluded that this region is likely compositionally distinct (Wen 2001) in line with our conclusions. Similar to the features observed beneath Africa, we find a high-density signature within the central domain of the Pacific superplume structure opposing the thermal buoyancy. We also detect an opposite (low-density) compositional signature encasing the central portion of the Pacific superplume. Also paralleling the African superplume region, a low-density compositional blob beneath the East Pacific Rise extends toward the high-density domain in the central part of the structure in a ridge-like fashion. This peculiar combination of features beneath the

Pacific Ocean is analogous to the structures observed beneath the African continent and Indian Ocean suggesting that the anomalous regions have a similar origin.

Using a variety of data and arguments, some recent studies have concluded that the lower ~1000 km of the mantle possesses a significant degree of compositional heterogeneity (e.g. van der Hilst & Karason 1999; Ishii & Tromp 1999, 2004; Masters *et al*. 2000; Trampert *et al*. 2004). Moreover, evidence suggests that the compositional heterogeneity may in fact outweigh the thermal signature of the features providing either a null correlation or anti-correlation of seismic velocity and density. Conversely, our simultaneous inversions indicate that multiple geodynamic observations can be matched to high levels assuming a positive correlation of density and velocity. This implies that lateral fluctuations in temperature are the principal source of mantle heterogeneity outside of the cratonic roots. Although it is evident that temperature variations dominate, some compositional heterogeneity is required to completely satisfy the geodynamic observations. However, we find that the compositional component of the density field is secondary to the thermally-induced density signatures throughout the lower mantle (Figure 5.13).

To examine this result further, we performed the density-velocity scaling inversion to find $R_{\rho/s}^{\mathrm{3D}}$ assuming that the starting seismic model (TX2007) represents the "true" shear wave velocity structure. In other words, we did not allow for reorganization of seismic heterogeneity via joint inversion including the geodynamic observations. Similar to the previous calculations, the total density field was then determined:

$$\left(\frac{\delta\rho}{\rho}\right)^{total} = R^{3\mathrm{D}}_{\rho/s}\left(\frac{\delta V_S}{V_S}\right)^{\mathrm{TX2007}} \tag{5.11}$$

Utilizing the pre-determined thermal scaling relationship, $R^{thermal}_{\rho/s}$, the thermal and non-thermal components can be separated for this case just as in the previous case. The RMS profiles of these density components are plotted in Figure 5.13 for comparison. It is evident that if we assume that the purely seismically-derived velocity model can be directly mapped into thermal density variations, a significant compositional component is required in the lower ~1000 km of the mantle to satisfy the geodynamic observations. Moreover, the compositional effects dominate the density signal in the two lowest layers of our model space (>2500 km depth) in this case. The calculated density fields within the D'' region are displayed in Figure 5.12 for comparison. Without performing simultaneous inversion of seismic and geodynamic observations, the central portions of the superplume structures (African and Pacific) possess higher-than-average *total* density signifying anti-correlation with seismic velocity in these regions. In contrast, our joint modeling results show that reorganization of seismic structure via simultaneous inversion eliminates the requirement for dominating compositional effects in deepest mantle with our combined dataset.

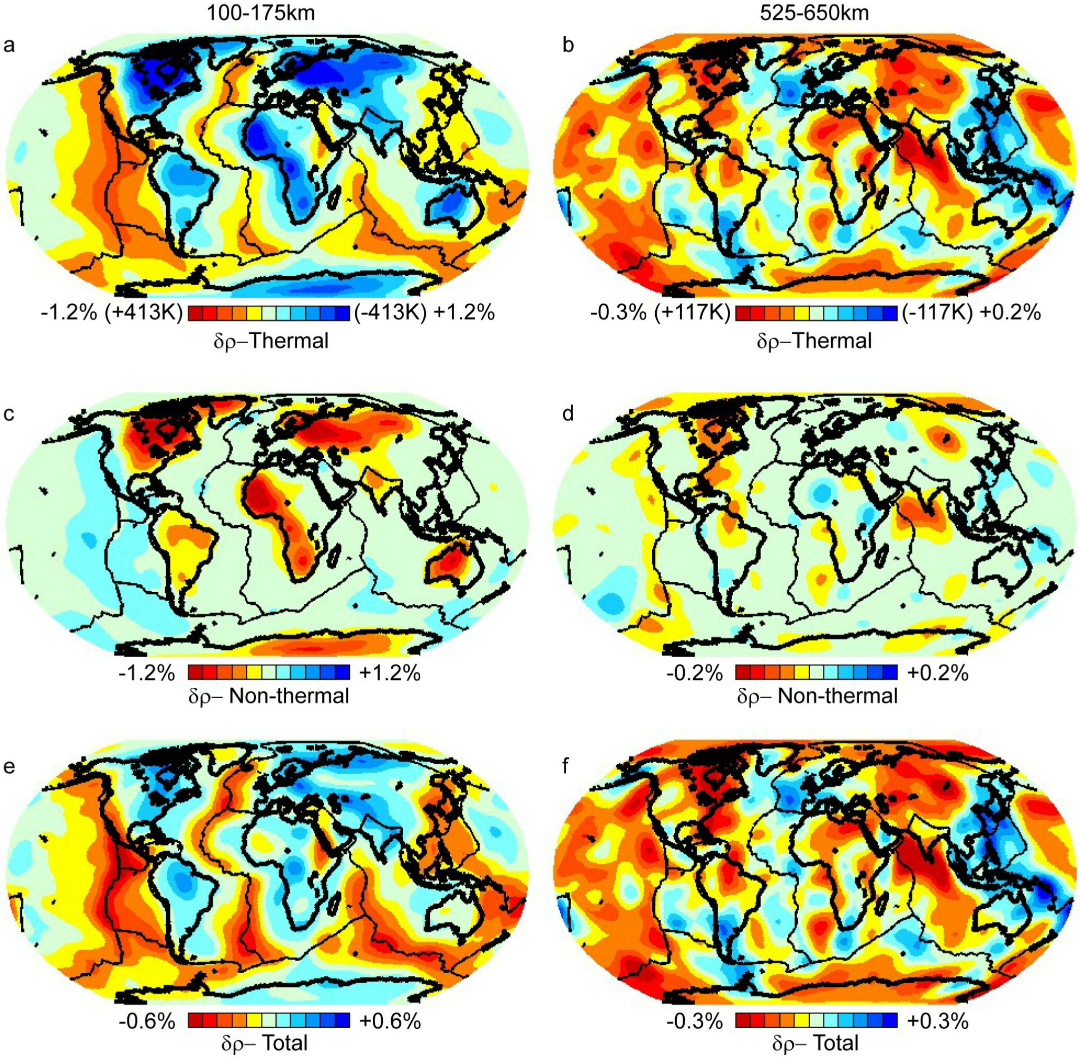

Figure 5.9 Thermal, non-thermal and total density fields at 100-175 km depth (left column) and 525-650 km depth (right column).

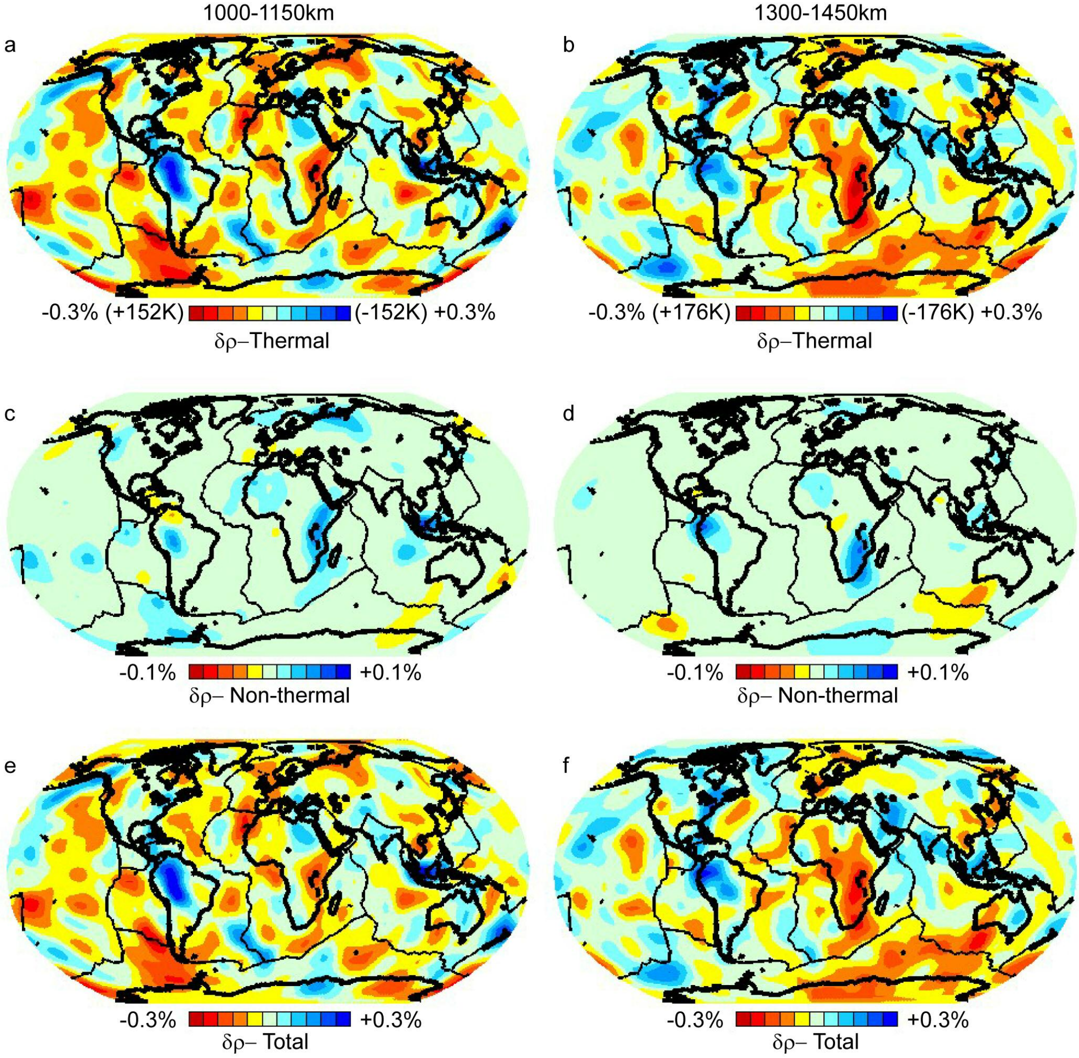

Figure 5.10 Thermal, non-thermal and total density fields at 1000-1150 km depth (left column) and 1300-1450 km depth (right column).

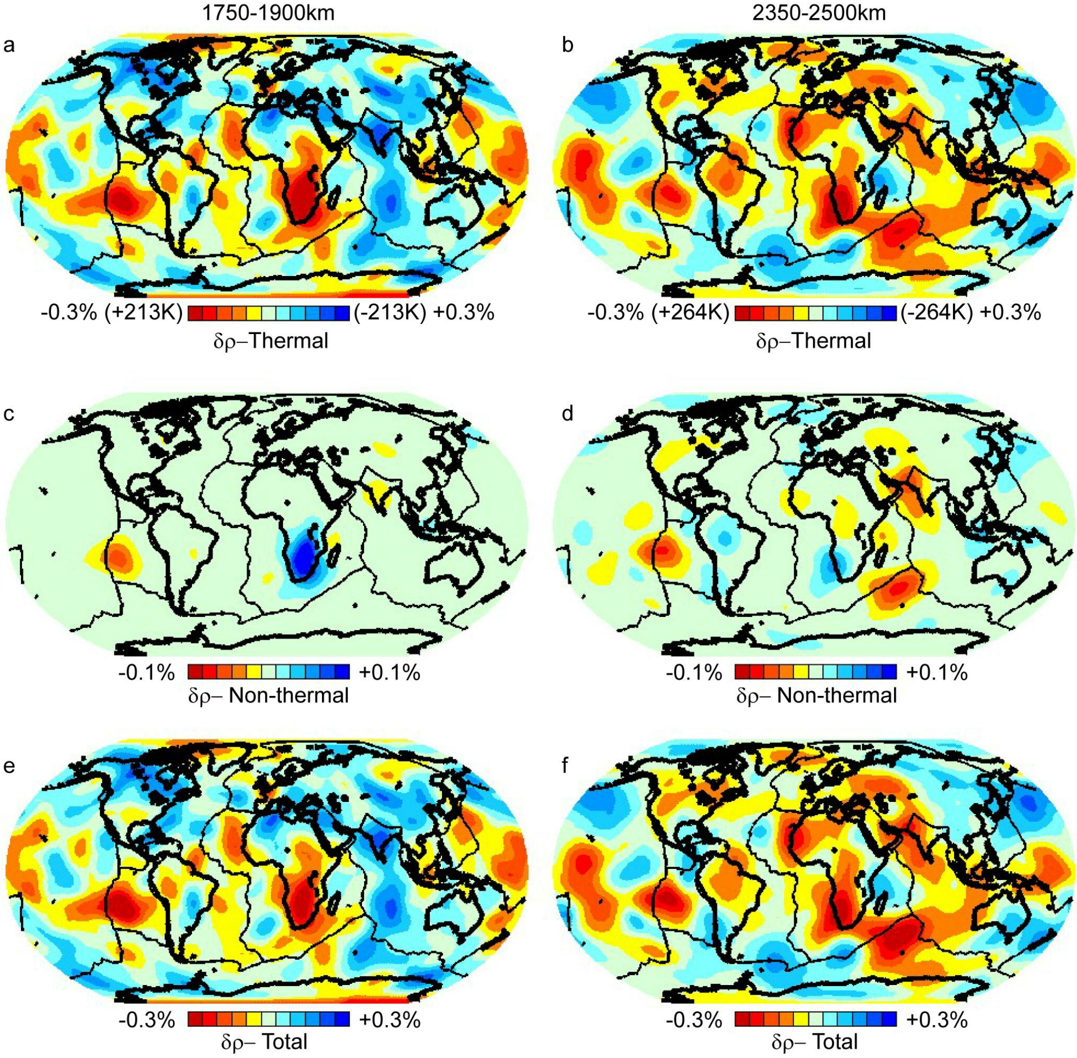

Figure 5.11 Thermal, non-thermal and total density fields at 1750-1900 km depth (left column) and 2350-2500 km depth (right column).

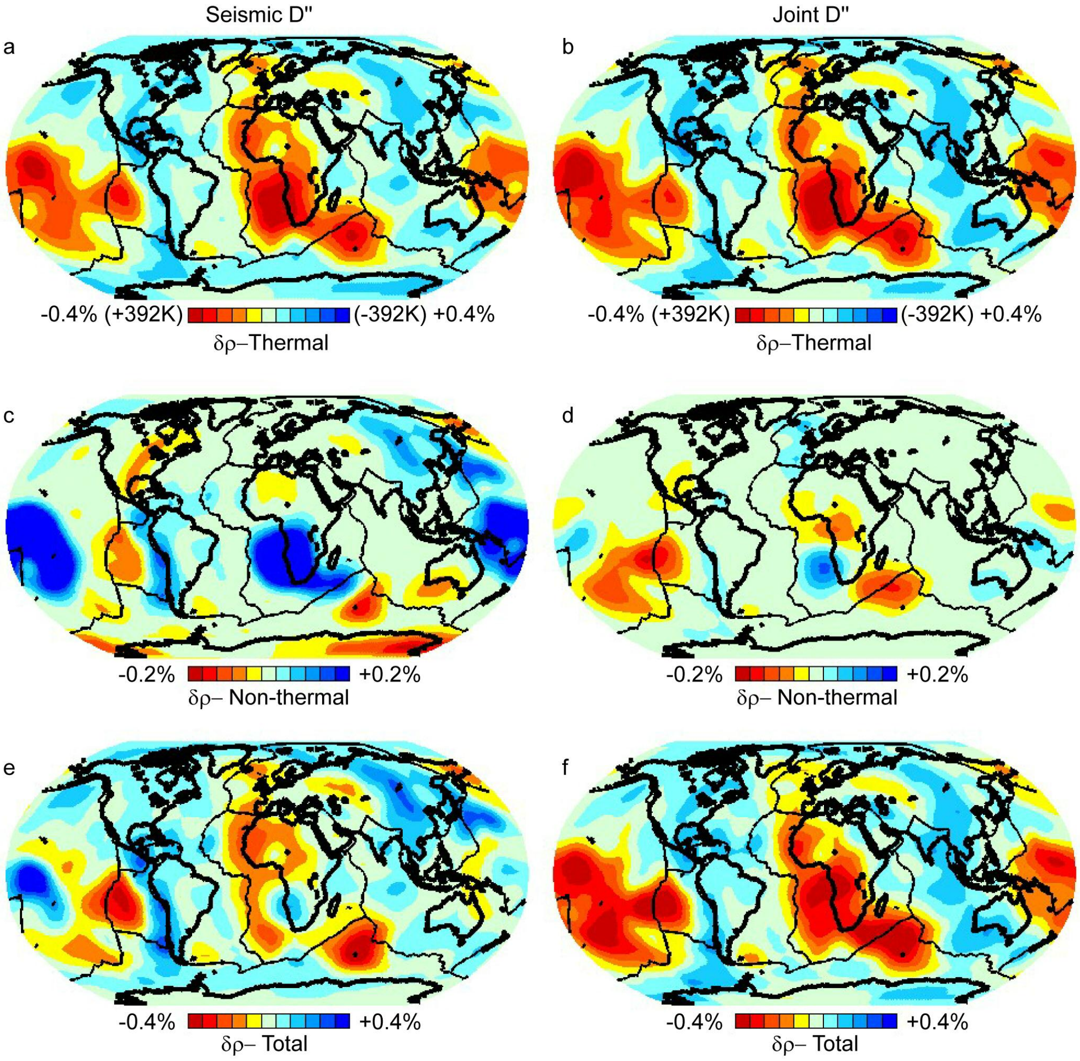

Figure 5.12 Thermal, compositional, and total density fields in the D'' region for two cases. Joint inversion with a thermal density-velocity relationship succeeded by inversion for a 3D density-velocity relationship yields negative density (positive buoyancy) throughout the African and Pacific superplume structures (right column). However, if no joint inversion for shear wave velocity is performed, the central portions of the superplume structures become denser than the surrounding mantle suggesting an anti-correlation of seismic velocity and density (left column). Joint inversion for seismic velocity tends to reduce the low-velocity heterogeneity above D'' lessening the need for a dense feature at the base to counteract the buoyancy of the shallower anomalies.

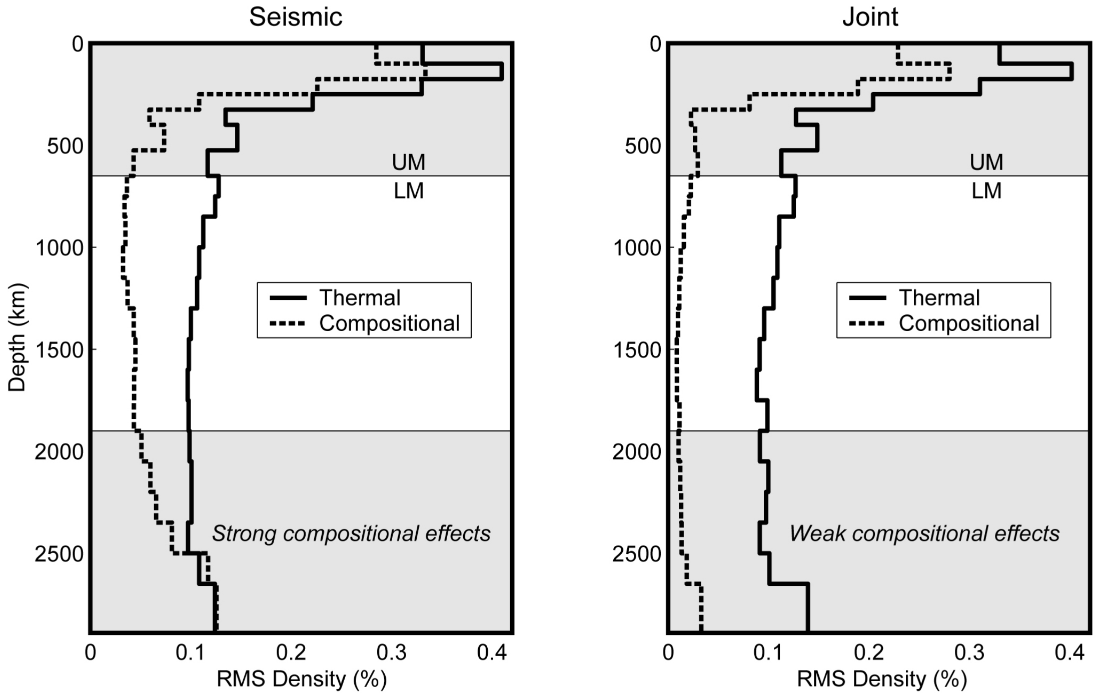

Figure 5.13 Relative contributions of thermal and non-thermal effects to the mantle density field. Joint inversion of seismic and geodynamic constraints assuming that all heterogeneity is thermally-induced followed by 3D density-velocity scaling inversion yields thermal densities larger than the residual contributions throughout the lower mantle (right column). The alternative case (left column) assumes that the seismic model represents thermal effects (convert TX2007 with UM1.LM4 density-velocity relationship and invert for a 3D scaling model). In this case, compositional contributions become very strong in the lower ~1000 km of the mantle and perhaps dominate the density field below ~2500 km depth. This result shows that joint inversion removes bias in the model produced solely with our seismic constraints allowing for a positive correlation of seismic velocity and density perturbations throughout the mantle (the thermal hypothesis). The 'true' compositional contribution is likely between these two extremes, but it is not necessary to have null correlations or anti-correlations of shear wave velocity and density in the deepest mantle to find heterogeneity models consistent with our seismic and geodynamic inferences.

5.8 Conclusions

We have investigated a wide range of possible $R_{\rho/s}$ profiles taken from recent mineral physics studies focused on the effects of temperature on mantle material in the upper mantle (Cammarano *et al*. 2003) and lower mantle (Karato & Karki 2001). Through simultaneous inversion of seismic data and a diverse suite of geodynamic constraints, we have found the radially-symmetric thermal $R_{\rho/s}$ relationship most capable of satisfying the seismic and geodynamic observations (Figure 5.8). In addition, we have found 1st-order velocity-dependent corrections to $R_{\rho/s}$ which account for the non-linear behavior of the thermal $R_{\rho/s}$ relationship in the upper mantle and compositional effects of the Fe-depleted cratonic roots (Forte & Perry 2000). This corrected $R_{\rho/s}$ relationship allows for high levels of reconciliation of the combined dataset implying that the dominant cause of mantle heterogeneity outside of the cratonic roots is lateral variations in temperature. Solving for a 3-D $R_{\rho/s}$ relationship reveals secondary contributions to the mantle density field including additional compositional effects and higher order non-linear thermal effects.

The reorganization of purely seismically-derived heterogeneity via simultaneous inversion greatly decreases the requirement for compositional components to explain the combined seismic-geodynamic dataset. In effect, joint inversion reduces the bias of the seismic data on the resulting heterogeneity model allowing for positive correlation of velocity and density throughout the non-cratonic mantle. We have demonstrated this effect by inverting for a 3-D scaling relationship using our seismically-derived model (TX2007) as the established velocity model. This method results in features that are negatively correlated (low-velocity = high-density) including the central portions of the African and Pacific superplume structures similar to previous studies (e.g. Ishii & Tromp 1999). Moreover, we find that without joint inversion, compositional influence on heterogeneity is increased throughout the lower ~1000 km of the mantle (Figure 5.13) and dominates in the deepest mantle. If instead, we use an unbiased jointly-determined velocity model, the overall buoyancy of the superplume structures is reduced but *not* reversed and heterogeneity is only weakly influenced by compositional variations throughout the majority of the lower mantle. Therefore, scaling a purely seismically-derived velocity model by some quantity is not necessarily the best method to obtain density heterogeneity.

Additionally, our modeling process inherently attempts to minimize compositional effects by first assuming that all heterogeneity is generated by variations in temperature. Therefore it is likely that our mantle heterogeneity model provides minimal estimates of compositional influence and does not exclude the possibility that anti-correlation of velocity and density exists in some regions of the lower mantle. Also, these results do not imply that chemical variations are insignificant to the dynamics and evolution of the mantle as we have recently pointed out in a detailed study of the African superplume region (Simmons *et al*. 2007; Chapter 4).

5.9 References

Cammarano, F., S. Goes, P. Vacher & D. Giardini (2003), Inferring upper-mantle temperatures from seismic velocities, *Phys. Earth Planet. Inter.*, *138*(3-4), 197-222.

Chopelas, A. & R. Boehler (1992), Thermal expansivity in the lower mantle, *Geophys. Res. Lett.*, *19*, 1983-1986.

DeMets, C.R., Gordon, R.G., Argus, D.F. & S. Stein (1990). Current plate motions, *Geophys. J. Int.*, *101*(2), 425-478.

Forte, A.M. & W.R. Peltier (1994), The kinematics and dynamics of poloidal-toroidal coupling in mantle flow; the importance of surface plates and lateral viscosity variations, *Adv. Geophys. 36*, 1-119.

Forte, A.M., R.L. Woodward & A.M. Dziewonski (1994), Joint inversions of seismic and geodynamic data for models of three-dimensional mantle heterogeneity, *J. Geophys. Res. 99*, 21857-21877.

Forte, A.M. & R.L. Woodward (1997), Seismic-geodynamic constraints on three-dimensional structure, vertical flow, and heat transfer in the mantle, *J. Geophys. Res. 102*, 17981-17994.

Forte, A.M. (2000), Seismic-geodynamic constraints on mantle flow: implications for layered convection, mantle viscosity, and seismic anisotropy in the deep mantle, *in Earth's Deep Interior: Mineral Physics and Tomography from the Atomic to the Global Scale*, edited by S.-I. Karato et al., pp. 3-36, AGU, Washington, DC.

Forte, A.M. & H.K.C. Perry (2000), Geodynamic evidence for a chemically depleted continental tectosphere, *Science*, *290*, 1940-1944.

Forte, A.M. & J.X. Mitrovica (2001), Deep-mantle high-viscosity flow and thermochemical structure inferred from seismic and geodynamic data, *Nature*, *410*(6832), 1049-1056.

Forte, A.M., J.X. Mitrovica, R. Moucha, N.A. Simmons & S.P. Grand (2007), Descent of the ancient Farallon slab drives localized mantle flow below the New Madrid seismic zone, *Geophys. Res. Lett.*, *34*, doi: 10.1029/2006GL027895.

Grand, S.P., R.D. Van der Hilst & S. Widiyantoro(1997), Global seismic tomography: a snapshot of convection in the Earth, *GSA Today*, *7*, 1-7.

Gu, Y.J., A.M. Dziewonski, W. Su & G. Ekstrom (2001), Models of the mantle shear velocity and discontinuities in the pattern of lateral heterogeneities, *J. Geophys. Res.*, *106*, 11169-11199.

Ishii, M. & J. Tromp (1999), Normal-mode and free-air gravity constraints on lateral variations in velocity and density of Earth's mantle, *Science*, *285*(5431), 1231-1236.

Ishii, M. & J. Tromp (2004), Constraining large-scale mantle heterogeneity using mantle and inner-core sensitive normal modes, *Phys. Earth Planet. Inter.*, *146*(1-2), 113-124.

Jordan, T.H. (1978), Composition and development of the continental tectosphere, *Nature*, *274*, 544-548.

Jordan, T.H. (1981), Continents as a chemical boundary layer, *Phil. Trans. Roy. Soc. London A*, *301*(1461), 359-373.

Karason, H. & R.D. van der Hilst (2000), Constraints on mantle convection from seismic tomography, in: M.R. Richards, M.R. Gordon, R.D. van der Hilst (Eds.), The History and Dynamics of Global Plate Motion, AGU, Washington, DC, pp. 277-288.

Karato, S.I. (1993), Importance of anelasticity in the interpretation of seismic tomography, *Geophys. Res. Lett.*, *20*, 1623-1626.

Karato, S.I. & B.B. Karki (2001), Origin of lateral variation of seismic wave velocities and density in the deep mantle, *J. Geophys. Res. Solid Earth*, *106*(B10), 21771-21783.

Marsh, J.G., *et al*. (1990), The GEM-T2 gravitational model, *J. Geophys. Res. Solid Earth*, *95*(13), 22043-22071.

Masters, G., G. Laske, H. Bolton & A.M. Dziewonski (2000), The relative behavior of shear velocity, bulk sound speed, and compressional velocity in the mantle: implications for chemical and thermal structure, *in Earth's Deep Interior: Mineral Physics and Tomography from the Atomic to the Global Scale*, edited by S.-I. Karato et al., pp. 63-87, AGU, Washington, DC.

Mathews, P.M., T.A. Herring & B.A. Buffett (2002), Modeling of nutation and precession: new nutation series for nonrigid Earth and insights into the Earth's interior, *J. Geophys. Res. Solid Earth*, *107*(B4), doi: 10.1029/2001JB000390.

Megnin, C. & B. Romanowicz (2000), The three-dimensional shear velocity structure of the mantle from the inversion of body, surface and higher-mode waveforms}, *Geophys. J. Int.*, *143*, 709-728.

Mitrovica, J.X. & A.M. Forte (2004), A new inference of mantle viscosity based upon joint inversion of convection and glacial isostatic adjustment data, *Earth Planet. Sci. Lett.*, *225*(1-2), 177-189.

Mooney, W.D., G. Laske & G. Masters (1998), CRUST 5.1: a global crustal model at 5 x 5 degrees, *J. Geophys. Res. Solid Earth*, *103*(B1), 727-747.

Ni, S.D., E. Tan, M. Gurnis & D.V. Helmberger (2002), Sharp sides to the African superplume, *Science*, *296*(5574), 1850-1852.

Ni, S.D. & D.V. Helmberger (2003a), Ridge-like lower mantle structure beneath South Africa, *J. Geophys. Res. Solid Earth*, *108*(B2), doi:10.1029/2001JB001545.

Ni, S.D. & D.V. Helmberger (2003b), Seismological constraints on the South African superplume; could be the oldest distinct structure on Earth, *Earth Planet. Sci. Lett.*, *206*(1-2), 119-131.

Ni, S.D., D.V. Helmberger & J. Tromp (2005), Three-dimensional structure of the African superplume from waveform modeling, *Geophys. J. Int.*, *161*, 283-294.

O'Reilly, S.Y., W.L. Griffin, Y.H. Proudjom & P. Morgan (2001), Are lithospheres forever? Tracking changes in subcontinental lithospheric mantle through time, *GSA Today*, *11*, 4-10.

Paige, C.C. & M.A. Saunders (1982), LSQR: an algorithm for sparse linear equations and sparse least squares, *ACM Transactions on Mathematical Software*, *8*, 43-71.

Ritsema, J., S. Ni, D.V. Helmberger & H.P. Crotwell (1998), Evidence for strong shear velocity reductions and velocity gradient in the lower mantle beneath Africa, *Geophys. Res. Lett.*, *25*(23), 4245-4248.

Ritsema, J., H.J. Van Heijst & J.H. Woodhouse (1999), Complex shear wave velocity structure imaged beneath Africa and Iceland, *Science*, *286*(5446) 1925-1928.

Robertson, G.S. & J.H. Woodhouse (1996), Ratio of relative S to P velocity heterogeneity in the lower mantle, *J. Geophys. Res.*, *101*, 20041-20052.

Romanowicz, B. & J. Durek (2000), Seismological constraints on attenuation in the earth: a review, *Geophys. Monogr.*, *117*, 61-80.

Saltzer, R.L., R.D.Van der Hilst & H. Kárason (2001), Comparing P and S wave heterogeneity in the mantle, *Geophys. Res. Lett.*, *28*(7) 1335-1338.

Simmons, N.A., A.M. Forte & S.P. Grand (2006), Constraining mantle flow with seismic and geodynamic data: A joint approach, *Earth Planet. Sci. Lett.*, *246*(1-2), 109-124.

Simmons, N.A., A.M. Forte & S.P. Grand (2007), Thermochemical structure and dynamics of the African superplume, *Geophys. Res. Lett. 34*(2), L02301, doi: 10.1029/2006GL028009.

Su, W. & A.M. Dziewonski (1997), Simultaneous inversion for 3-D variations in shear and bulk velocity in the mantle, *Phys. Earth Planet. Inter.*, *100*(1-4), 135-156.

Trampert, J., F. Deschamps, J. Resovsky & D. Yuen (2004), Probabilistic tomography maps chemical heterogeneities throughout the lower mantle, *Science*, *306*(5697), 853-856.

Van der Hilst, R.D., S. Widiyantoro & E.R. Engdahl (1997), Evidence for deep mantle circulation from global tomography, *Nature*, *386*, 578-584.

Van der Hilst, R.D. & H. Kárason (1999), Compositional heterogeneity in the bottom 1000 kilometers of the Earth’s mantle: Toward a hybrid convection model, *Science*, *283*, 1885-1888.

Wen, L.X. (2001), Seismic evidence for a rapidly varying compositional anomaly at the base of the Earth’s mantle beneath the Indian Ocean, *Earth Planet. Sci. Lett.*, *194*(1-2), 83-95.

Zhao, D. (2001), Seismic structure and origin of hotspots and mantle plumes, *Earth Planet. Sci. Lett. 192*, 251-265.

Appendix A

LSQR Algorithm with Sparse-Full Modifications

Here I outline the LSQR algorithm originally developed by *Paige & Saunders* (1982). The LSQR algorithm is an iterative inversion method that is designed to deal with large, sparse systems of equations efficiently. The method is analytically equivalent to the conjugate gradient method but has been shown to be more numerically reliable. I have also included modifications of the algorithm that allow for simultaneous inversion of sparse and full systems of equations without directly combining the systems by matrix augmentation. In addition the modifications include scaling relationships that relate one system to the other (i.e. density-velocity conversion factors) without directly embedding these factors into the linear system. The primary motivation for modifying the algorithm is that, in MATLAB, in order to combine a sparse and full system by matrix augmentation means that either the resulting system must be full OR sparse (not both).

In our specific case, this means that if we augment a highly sparse seismic sensitivity kernel matrix with a full geodynamic sensitivity kernel matrix that we would have to store the combined system as a full matrix which would require ~4Gbytes of RAM storage (not tenable on standard UNIX workstations). Alternatively, we could treat the full geodynamic sensitivity kernel matrix as a sparse system by storing pointer indices along with the matrix values. Although this treatment would be feasible, it would still require about 2 times the storage needed to store the original full matrix. Also, specific to our case, the geodynamic sensitivity kernels (full matrix) must be scaled by the density-velocity conversion ratios denoted as *R* in the following equations. Considering the linear system $\mathbf{A}x = b$, the basic algorithm (left column) and modifications (right column) are as follows:

Step 1 – Initialize variables

$x_0 =$ starting model

$\beta_1 = \|b - Ax_o\|_2$ *Modify:* $\beta_1 = \left\| \begin{matrix} b_{full} - A_{full}x_o \\ b_{sparse} - A_{sparse}x_o \end{matrix} \right\|_2$

where $\mathbf{A}_{full}$ and b_{full} correspond to the full part of the combined system (geodynamic sensitivity matrix and data in our case). $\mathbf{A}_{sparse}$ and b_{sparse} correspond to the sparse part of the combined system (seismic sensitivity matrix and data in our case).

$u_1 = \dfrac{b - \mathbf{A}x_o}{\beta_1}$ *Modify:* $u_1^{full} = \dfrac{b_{full} - \mathbf{A}_{full}x_0'}{\beta_1}$

where $x_{0,k}' = x_{0,k}R_k$ ($k = 1,2,3...n$). Effectively, this is a point-by-point multiplication of the model with the conversion factors contained within the vector *R* with *n* elements (i.e. density-to-velocity scaling)

$$u_1^{sparse} = \frac{b_{sparse} - \mathbf{A}_{sparse}x_0}{\beta_1}$$

$$u_1 = \begin{bmatrix} u_1^{full} \\ u_1^{sparse} \end{bmatrix}$$

$\alpha_1 = \left\|\mathbf{A}^T u_1\right\|_2$ *Modify:* $\alpha_1 = \left\|\mathbf{A}^T_{full} u_1^{full} + \mathbf{A}^T_{sparse} u_1^{sparse}\right\|_2$

$v_1 = \dfrac{\mathbf{A}^T u_1}{\alpha_1}$ *Modify:* $v_{1,k}^{full} = \left(\dfrac{\mathbf{A}^T_{full} u_1^{full}}{\alpha_1}\right)_k R_k$

$\bar{\phi}_1 = \beta_1$ *Modify:* None required

$\bar{\rho}_1 = \alpha_1$ *Modify:* None required

$w_1 = v_1$ *Modify:* None required

Step 2 – Repeat steps 3-5 until convergence

Step 3 – Update variables

$\beta_{i+1} = \left\|\mathbf{A} v_i - \alpha_i u_i\right\|_2$ *Modify:* $\beta_{i+1} = \left\|\begin{matrix} \mathbf{A}_{full} v_i' - \alpha_i u_i^{full} \\ \mathbf{A}_{sparse} v_i - \alpha_i u_i^{sparse} \end{matrix}\right\|_2$

where $v_i' = v_{i,k} R_k$ ($k = 1,2,3\ldots n$)

Again, this is point-by-point multiplication of the model with the conversion factors contained within the vector *R* with *n* elements.

$u_{i+1} = \dfrac{\mathbf{A} v_i - \alpha_i u_i}{\beta_{i+1}}$ *Modify:* $u_{i+1} = \dfrac{1}{\beta_{i+1}} \begin{bmatrix} \mathbf{A}_{full} v_i' - \alpha_i u_i^{full} \\ \mathbf{A}_{sparse} v_i - \alpha_i u_i^{sparse} \end{bmatrix}$

$\alpha_{i+1} = \left\|\mathbf{A}^T u_{i+1} - \beta_{i+1} v_i\right\|_2$ *Modify:* $t_k = \left(\mathbf{A}^T_{full} u_{i+1}^{full}\right)_k R_k$ (point-by-point scaling)

$$\alpha_{i+1} = \left\|\left(t - \beta_{i+1} v_i^{full}\right) + \left(\mathbf{A}^T_{sparse} u_{i+1}^{sparse} - \beta_{i+1} v_i^{sparse}\right)\right\|_2$$

$v_{i+1} = \dfrac{\mathbf{A}^T u_{i+1} - \beta_{i+1} v_i}{\alpha_{i+1}}$ *Modify:* $v_{i+1}^{full} = \dfrac{t - \beta_{i+1} v_i^{full}}{\alpha_{i+1}}$

$\rho_i = \sqrt{\bar{\rho}_i^2 + \beta_{i+1}^2}$ *Modify:* None required

$c_i = \dfrac{\bar{\rho}_i}{\rho_i}$ *Modify:* None required

$s_i = \dfrac{\beta_{i+1}}{\rho_i}$ *Modify:* None required

$\theta_{i+1} = s_i \alpha_{i+1}$ *Modify:* None required

$\bar{\rho}_{i+1} = -c_i \alpha_{i+1}$ *Modify:* None required

$\phi_i = c_i \bar{\phi}_i$ *Modify:* None required

$\bar{\phi}_{i+1} = s_i \bar{\phi}_i$ *Modify:* None required

Step 4 – Update model

$x_i = x_{i-1} + \dfrac{\phi_i}{\rho_i} w_i$ *Modify:* None required

$w_{i+1} = v_{i+1} - \dfrac{\theta_{i+1}}{\rho_i} w_i$ *Modify:* None required

Step 5 – Test for convergence and return to Step 3 if necessary

MATLAB script:

```matlab
function [x,flag,relres,iter,resvec,res,xall]=
t_lsqr_sparse_scale(Afull,bfull,Aspar,bspar,tol,maxit,x0,suffix,sc);
%Original MATLAB LSQR algorithm with modifications to
%  implicitly solve for the sparse and full portions of
%  the linear system.  Modifications also scale the full
%  system based on the vector "sc" which should have the
%  same dimensions as the output model.  This is
%  equivalent to multiplying each row of the "Afull"
%  matrix by the factors in "sc" point-by-point to linearly
%  relate the two datasets.
%
%INPUTS:
%Afull, bfull:    Full part of the system Ax=b
%Aspar, bspar:    Sparse part of the system Ax=b
%tol:             Relative tolerance (can be empty [])
%maxit:           Maximum number of iterations
%x0:              Starting model
%suffix:          Output name suffix
%sc:              Scaling factors applied to the full part of the
system
%
%OUTPUTS:   [may simply be [x]=t_lsqr_sparse_scale(...)]
%x:               Computed model
%flag: 0 LSQR converged to the desired tolerance TOL
%              within MAXIT iterations.
%     1 LSQR iterated MAXIT times but did not converge.
%     2 preconditioner M was ill-conditioned.
%     3 LSQR stagnated (two consecutive iterates were the same).
%     4 one of the scalar quantities calculated during LSQR became
%       too small or too large to continue computing.
```

```
%relres:    Relative residual
%iter:      Number if iterations
%resvec:    Vector of relative residuals at each iteration
%res:       The final actual residual (Ax-b)
%xall:      Matrix of models at each power of 2 iteration
%           (iterations 2,4,8,16,...)

[mfull,nfull] = size(Afull);
[mspar,nspar] = size(Aspar);
m=mfull+mspar;
n=nfull;

% Assign default values to unspecified parameters
if nargin < 5 | isempty(tol)
    tol = 1e-6;
end
if nargin < 6 | isempty(maxit)
    maxit = min([m,n,20]);
end
n2b = norm([bfull(:);bspar(:)]);  % Norm of rhs vector, b
if nargin<7 | isempty(x0)
    x0=zeros(n,1);
end
x=x0;
% Set up for the method
flag = 1;
xmin = x;                          % Iterate which has minimal 
residual so far
imin = 0;                          % Iteration at which xmin was 
computed
tolb = tol * n2b;                  % Relative tolerance

disp(['Calculating u=b-Ax'])
%%u = b - A * x;
ufull=bfull-Afull*(x.*sc);
uspar=bspar-Aspar*x;
u=[ufull;uspar];
disp(['Done'])

beta = norm(u);
normr = beta;                      % Norm of residual
if (normr <= tolb)                 % Initial guess is a good enough 
solution
    flag = 0;
    relres = normr / n2b;
    iter = 0;
    resvec = normr;
    return
end
ufull = ufull / beta;
uspar = uspar / beta;
u=[ufull;uspar];
c = 1;
s = 0;
phibar = beta;
```

```
d = zeros(n,1);
%%v = A' * u;
vfull = (Afull' * ufull).*sc;
vspar = Aspar' * uspar;
v = vfull + vspar;

alpha = norm(v);
vfull = vfull / alpha;
vspar = vspar / alpha;
v = [vfull+vspar];

resvec = zeros(maxit+1,1);         % Preallocate vector for norm of
residuals
resvec(1) = normr;                 % resvec(1) = norm(b-A*x0)
normrmin = normr;                  % Norm of residual from xmin
stag = 0;                          % stagnation of the method
% loop over maxit iterations (unless convergence or failure)
for i = 1 : maxit
   disp(['Iteration: ' int2str(i)])
   zfull = vfull;
   zspar = vspar;
   z = v;
   %%u = A * z - alpha * u;
   ufull = Afull * (z.*sc) - alpha * ufull;
   uspar = Aspar * z - alpha * uspar;
   u=[ufull;uspar];

   beta = norm(u);
   %%u = u / beta;
   ufull = ufull / beta;
   uspar = uspar / beta;
   u=[ufull;uspar];

   thet = - s * alpha;
   rhot = c * alpha;
   rho = sqrt(rhot^2 + beta^2);
   c = rhot / rho;
   s = - beta / rho;
   phi = c * phibar;
   if (phi == 0)                  % stagnation of the method
       stag = 1;
   end
   phibar = s * phibar;
   d = (z - thet * d) / rho;

   % Check for stagnation of the method
   if (stag == 0)
        stagtest = zeros(n,1);
        ind = (x ~= 0);
        stagtest(ind) = d(ind) ./ x(ind);
        stagtest(~ind & d ~= 0) = Inf;
        if norm(stagtest,inf) < eps
            stag = 1;
        end
    end
```

```
    if normr <= tolb                 % check for convergence
        flag = 0;
        iter = i;
        break
    end

    if stag == 1
        flag = 3;
        break
    end

    if normr < normrmin             % update minimal norm quantities
        normrmin = normr;
        xmin = x;
        imin = i;
    end

    x = x + phi * d;

    modvar(i)=std(x)^2;
    modmean(i)=mean(x);
    %%res=A*x-b;
    resfull=Afull*(x.*sc)-bfull;
    resspar=Aspar*x-bspar;
    res=[resfull;resspar];

    resvar(i)=std(res)^2;
    resmean(i)=mean(res);
    iternums=sort([2.^[0:20]+1 maxit]);
    if nargout==7 & any(iternums==i)%save all models
        ii=find(iternums==i);
       xalliter(ii)=iternums(ii);
       xall(:,ii)=x(:);
    end
    normr = abs(s) * normr;
    resvec(i+1) = normr;
    %%vt = A' * u;
    vtfull = (Afull' * ufull).*sc;
    vtspar = Aspar' * uspar;
    vt=vtfull+vtspar;

    %%v = vt - beta * v;
    vfull = vtfull - beta*vfull;
    vspar = vtspar - beta*vspar;
    v=vfull+vspar;

    alpha = norm(v);
    %%v = v / alpha;
    vfull = vfull / alpha;
    vspar = vspar / alpha;
    v=[vfull+vspar];

end                                % for i = 1 : maxit
% returned solution is first with minimal residual
if flag == 0
```

```
    relres = normr / n2b;
else
    x = xmin;
    iter = imin;
    relres = normrmin / n2b;
end
% truncate the zeros from resvec
if flag <= 1 | flag == 3
    resvec = resvec(1:i+1);
else
    resvec = resvec(1:i);
end

 %output
 if nargin==8 & nargout==6
      save(['LSQR.out.' suffix'.mat'],...
         'x','flag','relres','iter','resvec',...
         'res','modvar','resvar','modmean','resmean')
 elseif nargin==8 & nargout==7
      save(['LSQR.out.' suffix '.mat'],'x','flag','relres',...
         'iter','resvec','res','modvar','resvar',...
         'modmean','resmean','xall','xalliter')
 end
```

Appendix B

Seismic Resolution Tests

Resolution testing was performed by generating single-layer synthetic heterogeneity models and attempting to recover them by inversion. The test models consist of *ca*. 5 X 5 arc-degree blocks with alternating velocity perturbations of ±1%. This is similar to checkerboard resolution testing; however, the synthetic models are not perfect checkerboards due the staggered nature of the model parameters. A velocity model was found using the same inversion process used to generate the actual model with and without smoothing constraints (see Chapter 2). For each depth, the synthetic and recovered models were cross correlated and these coefficients are noted next to the model figures. The amplitude recovery levels, defined by the ratio of the RMS amplitudes of the input and output model, are similarly noted next to the images.

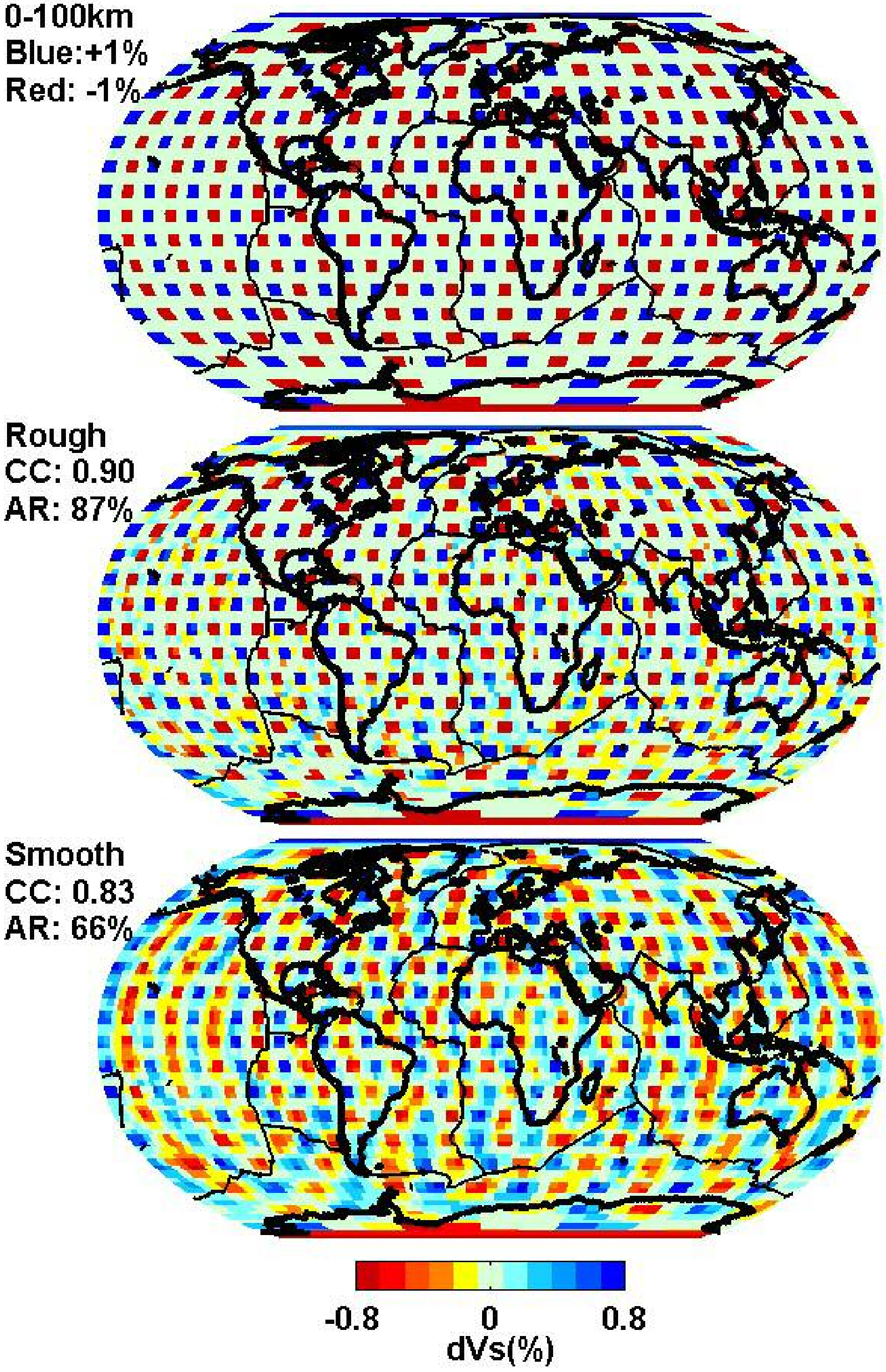

Figure B1 Synthetic (top) and recovered models with and without smoothing.

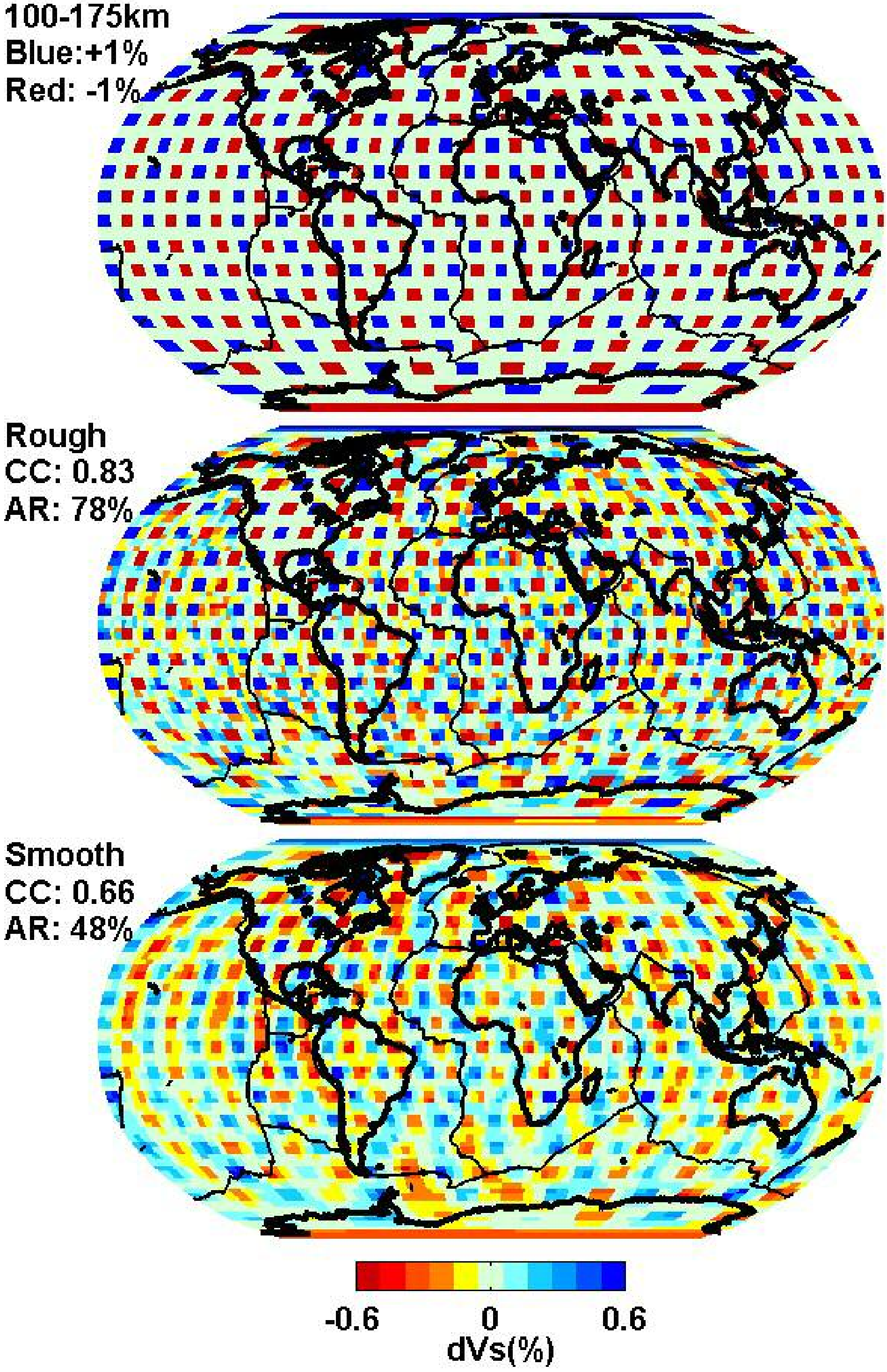

Figure B1 (continued)

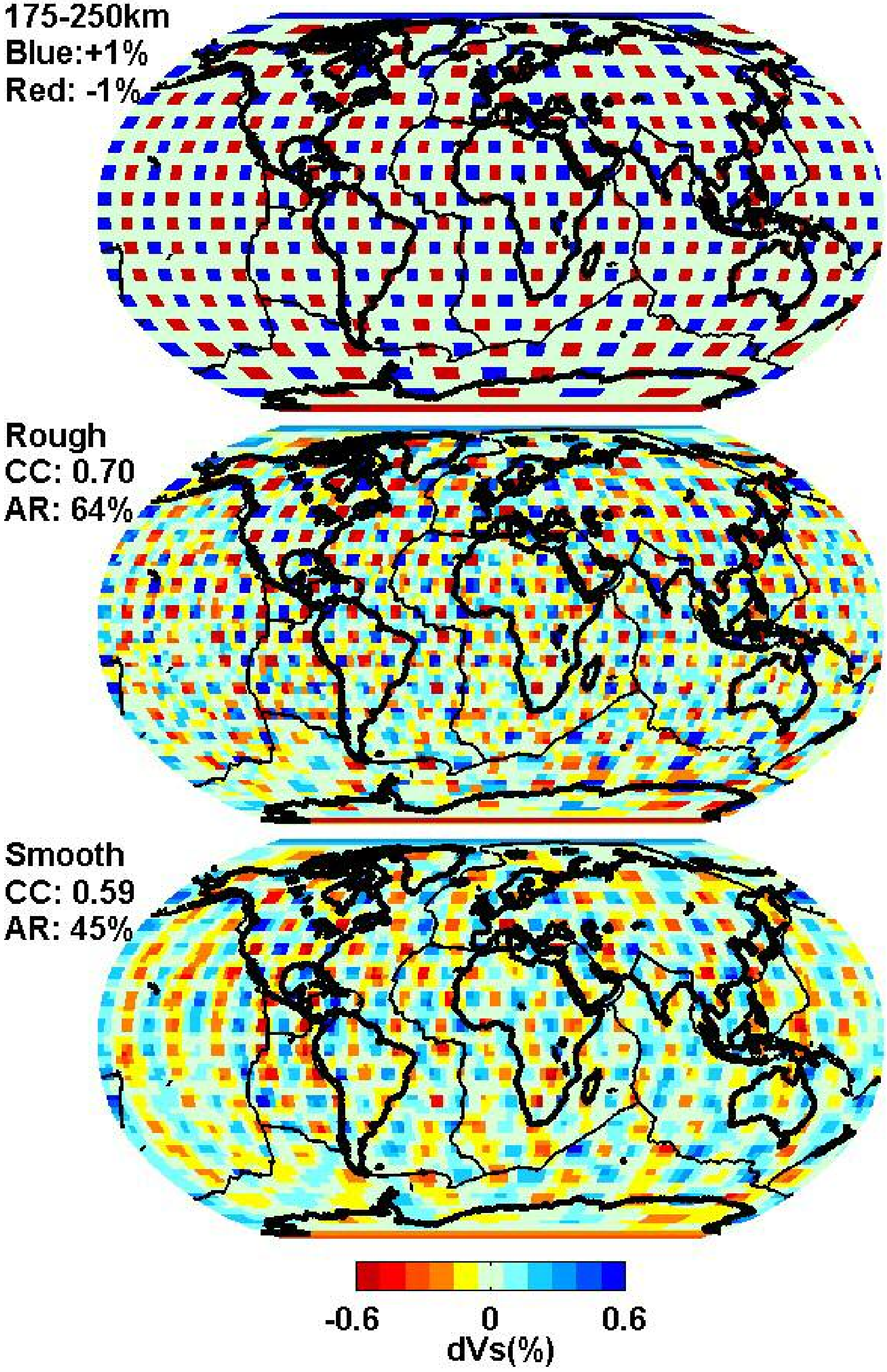

Figure B1 (continued)

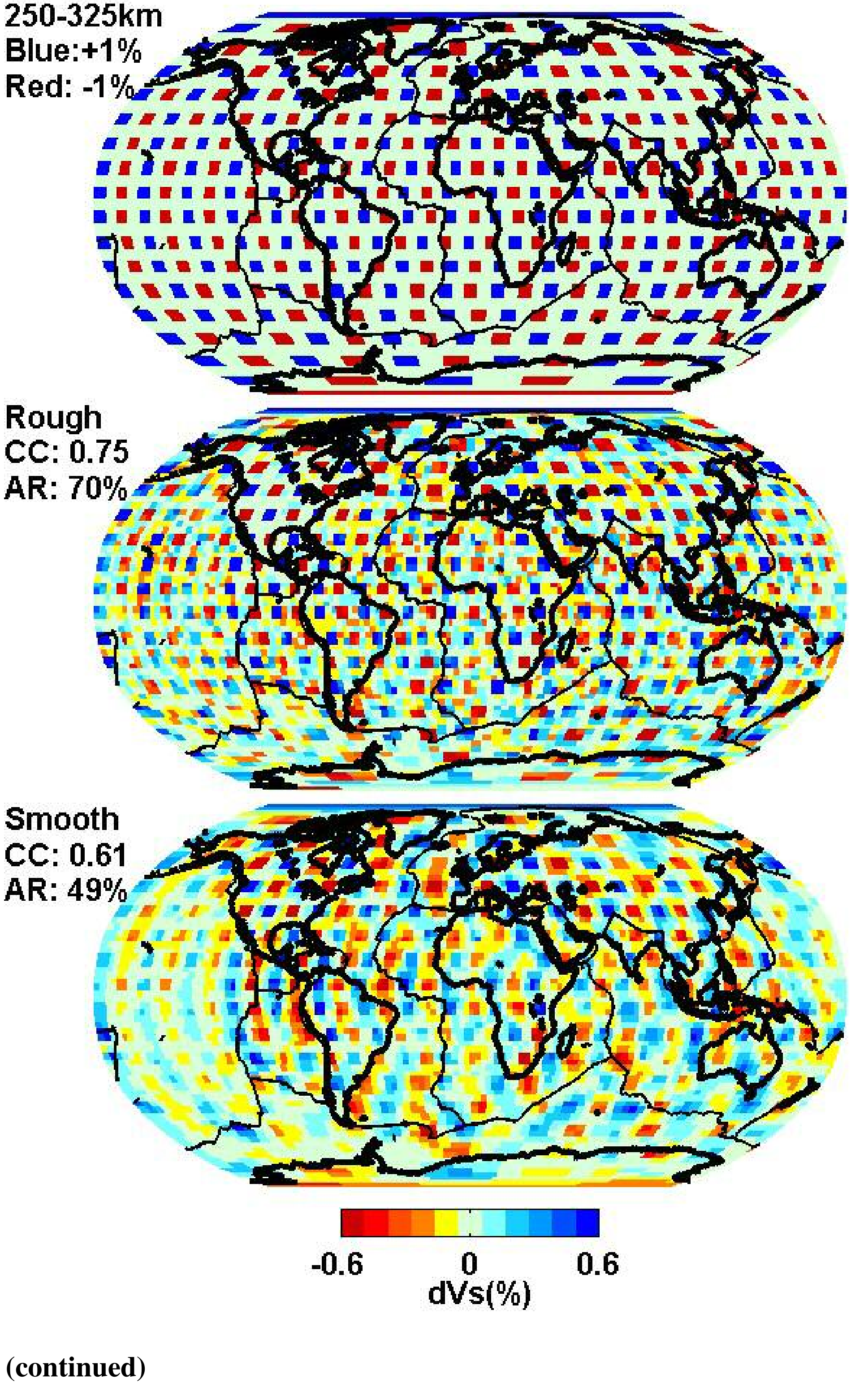

Figure B1 (continued)

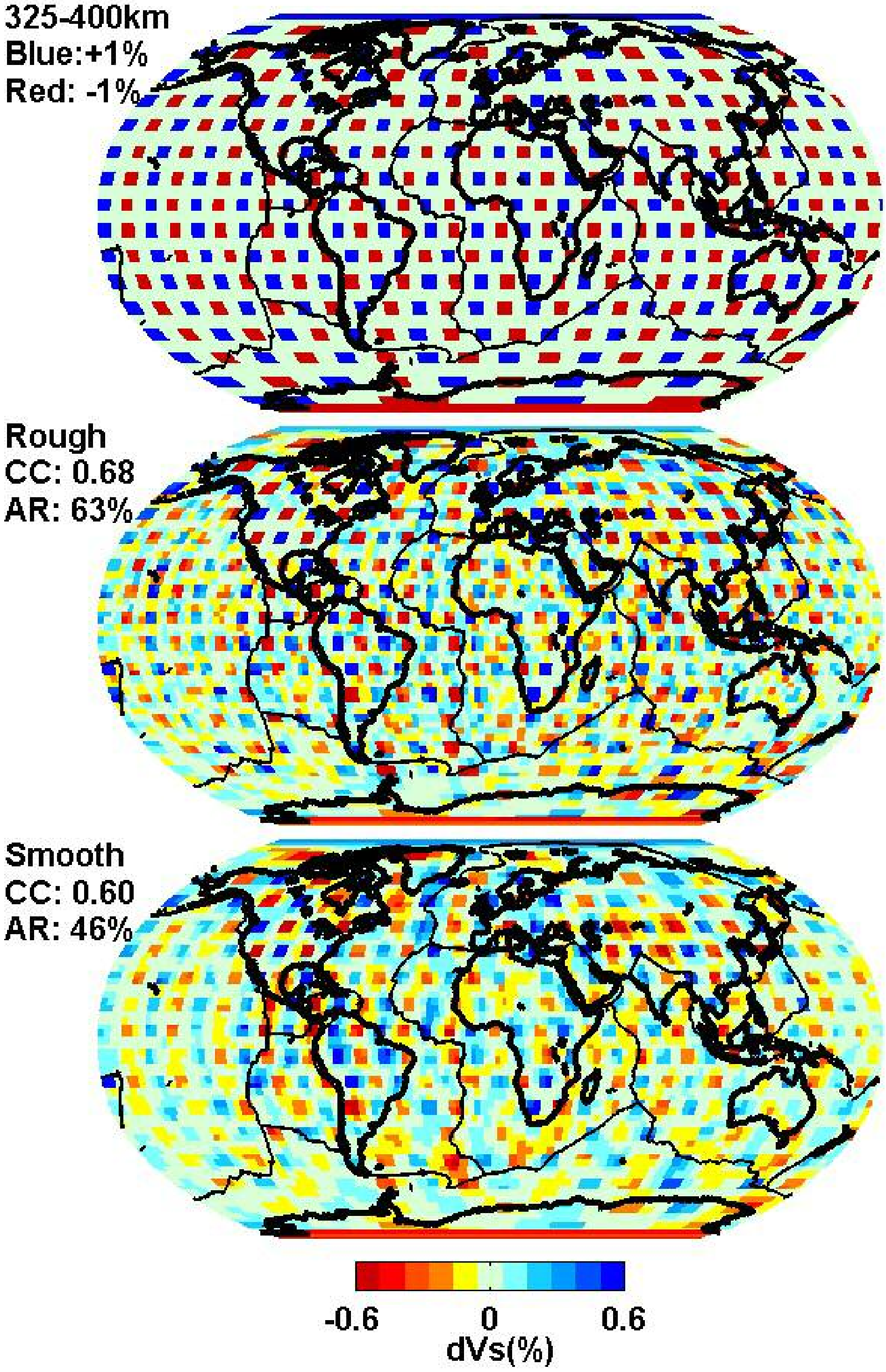

Figure B1 (continued)

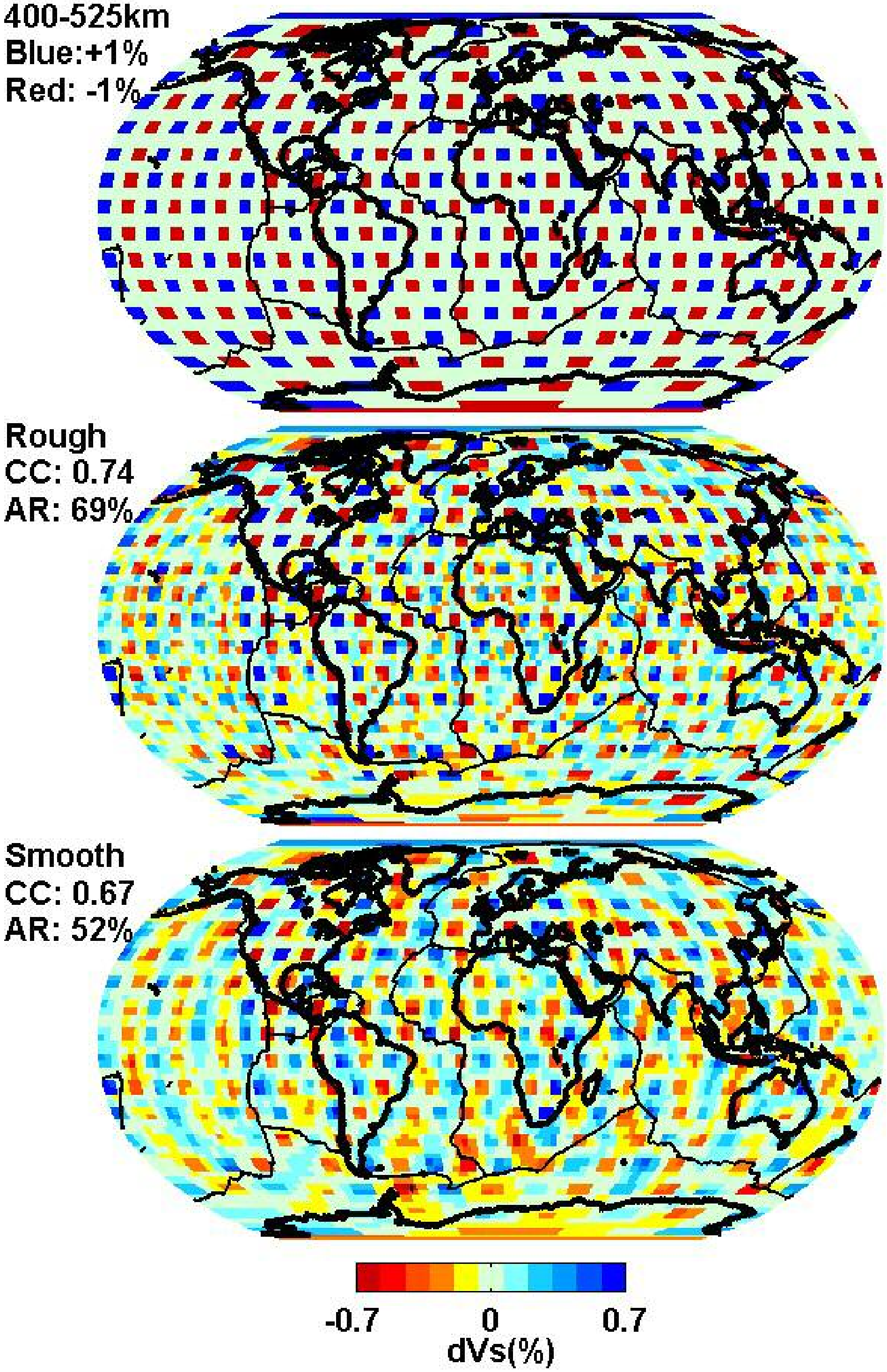

Figure B1 (continued)

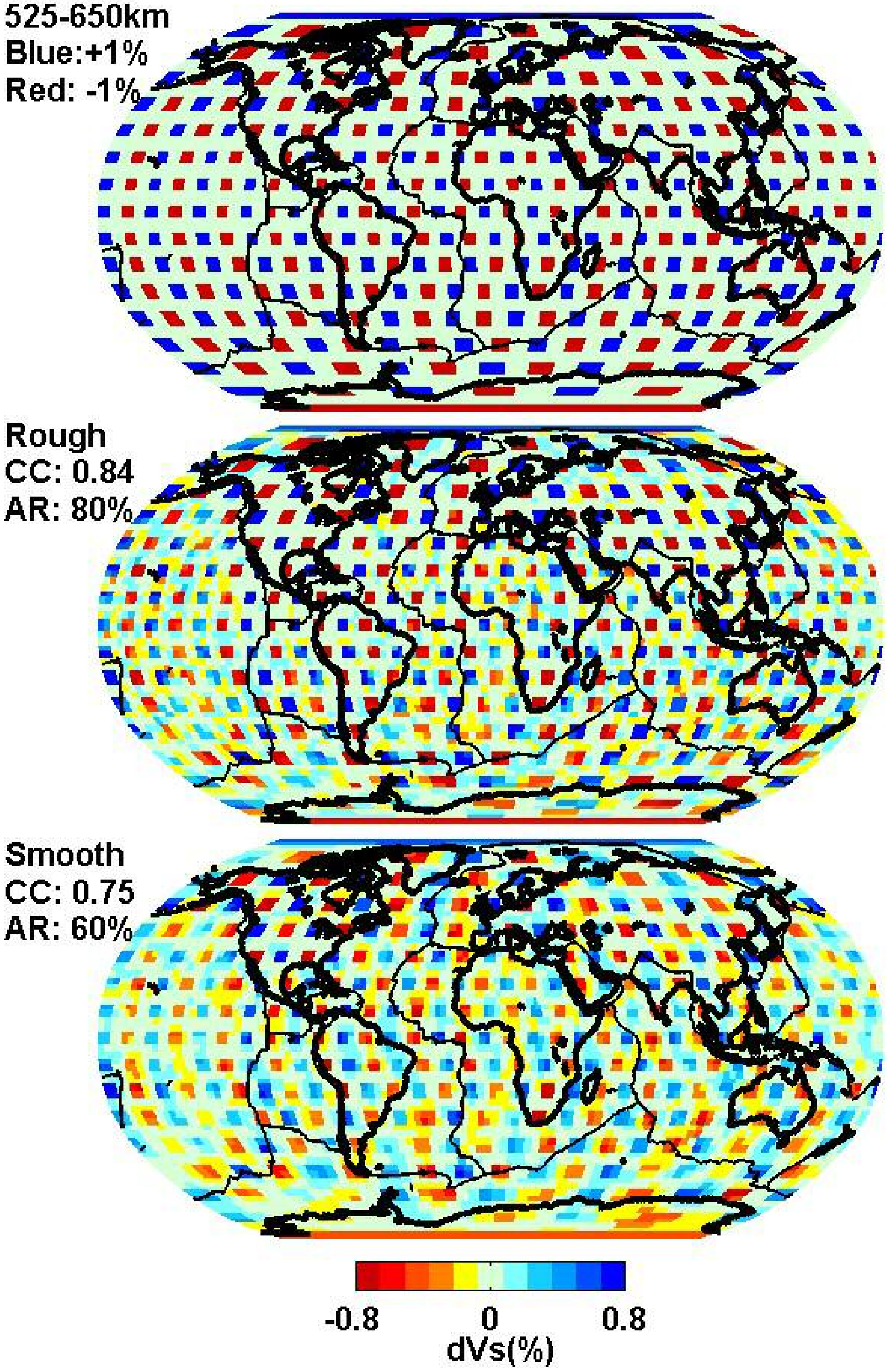

Figure B1 (continued)

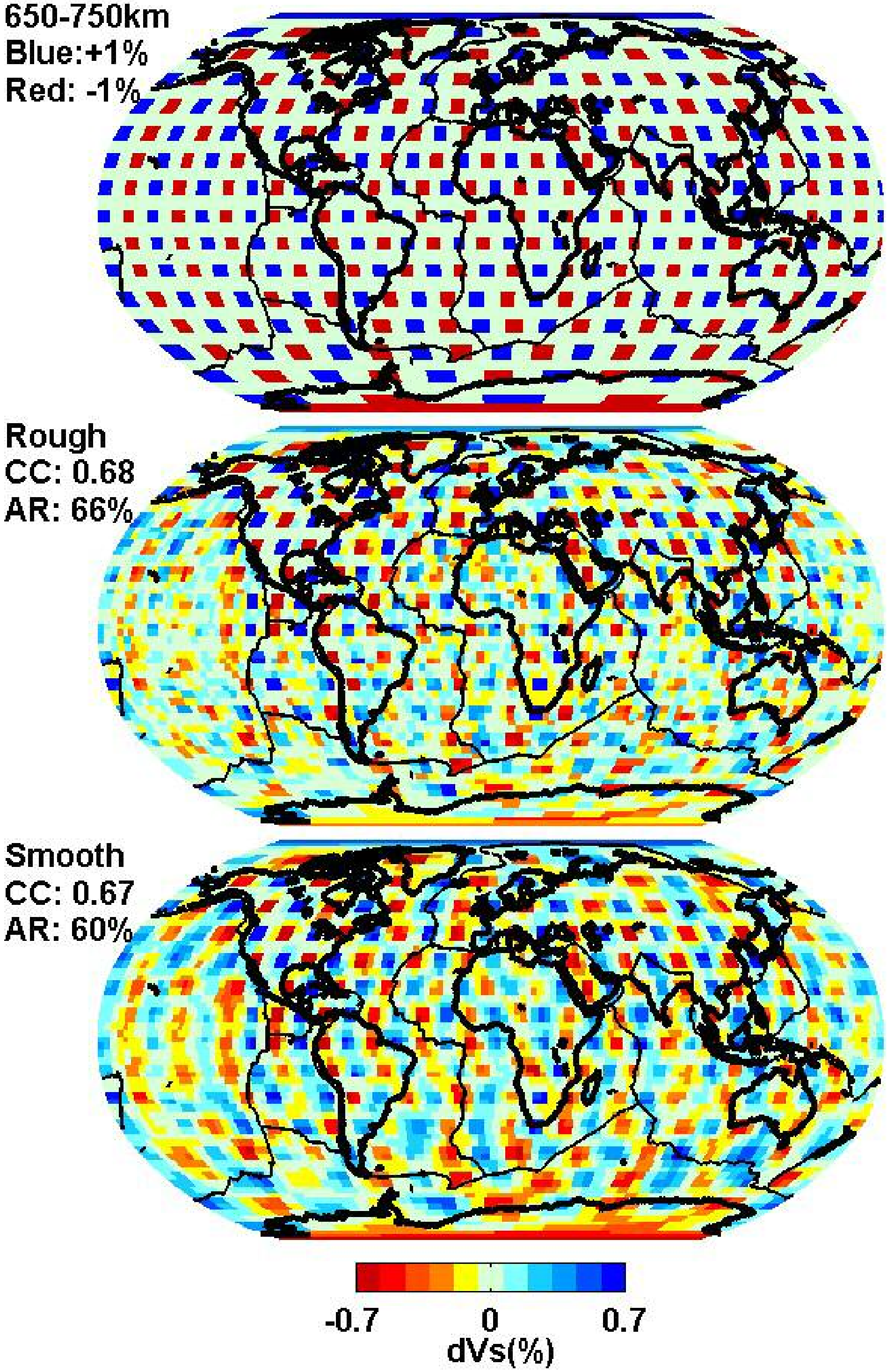

Figure B1 (continued)

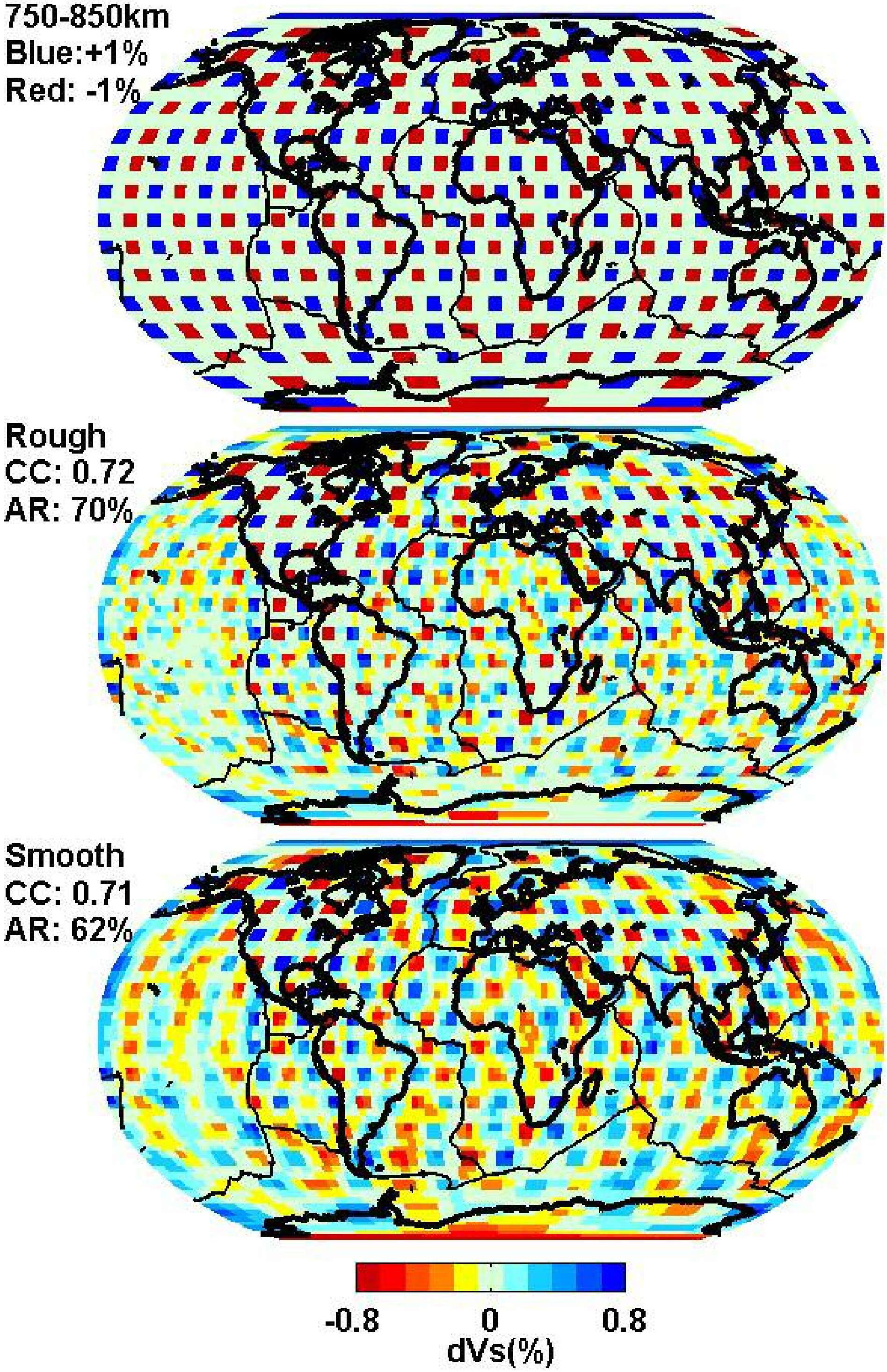

Figure B1 (continued)

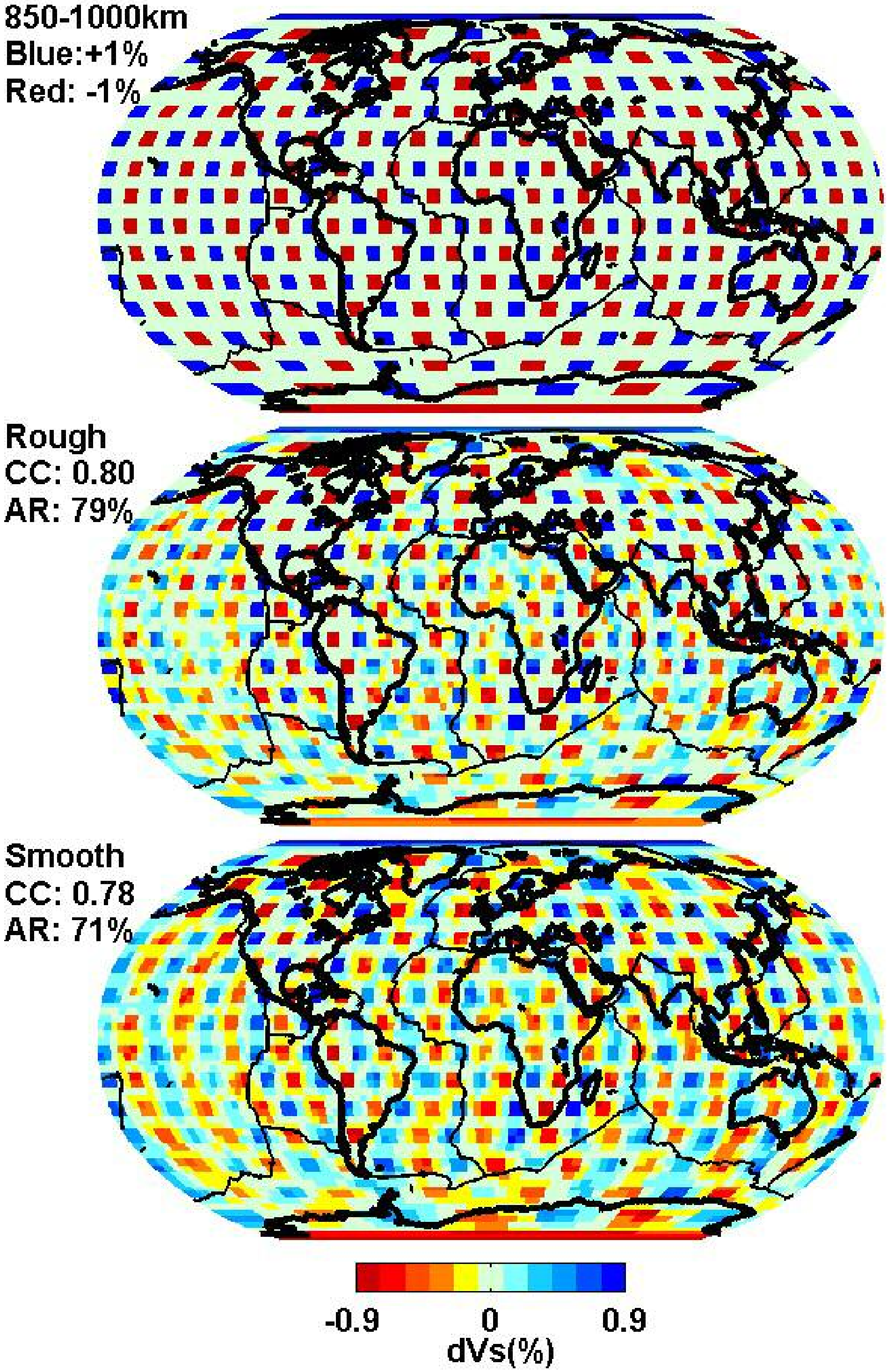

Figure B1 (continued)

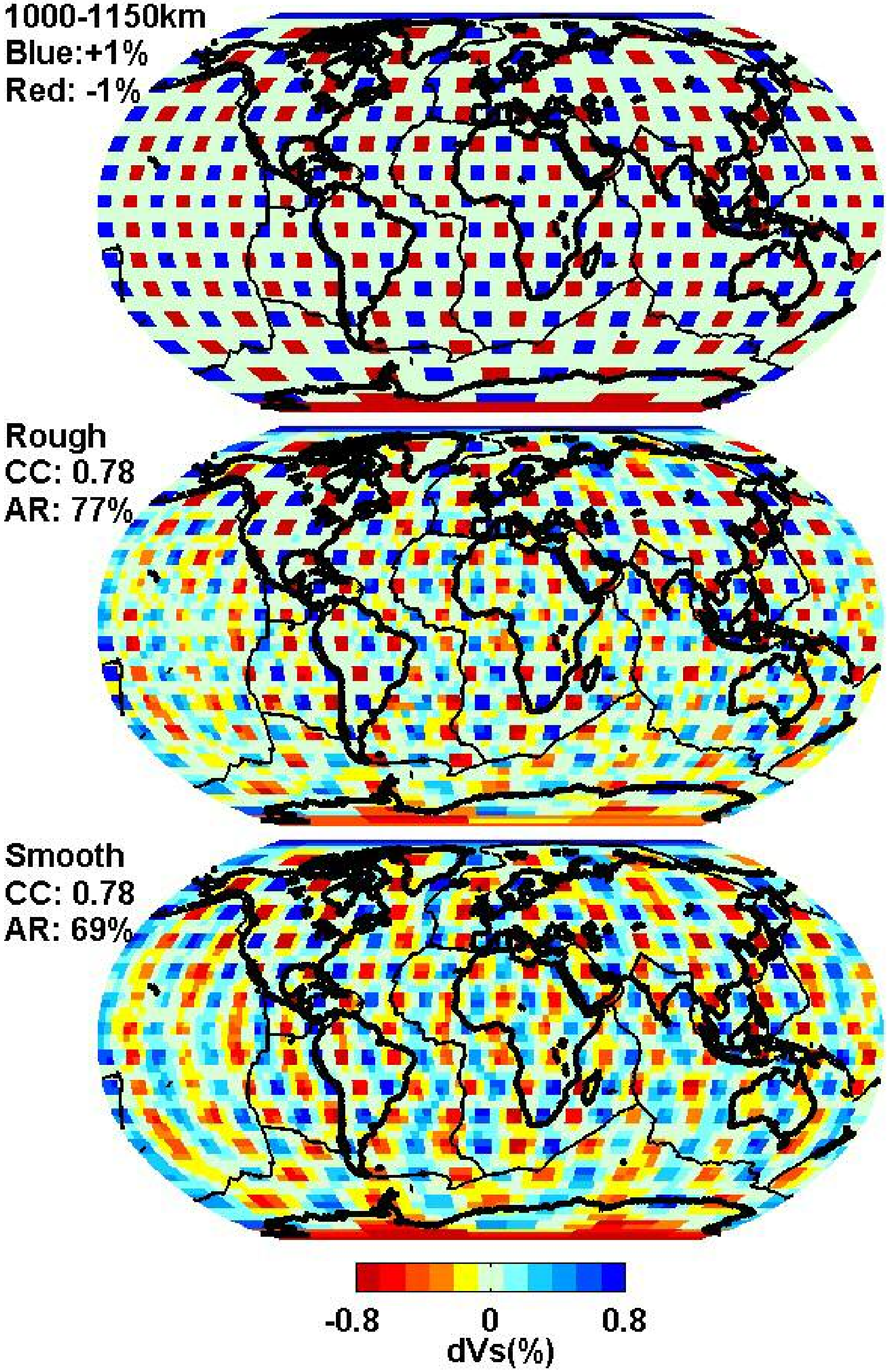

Figure B1 (continued)

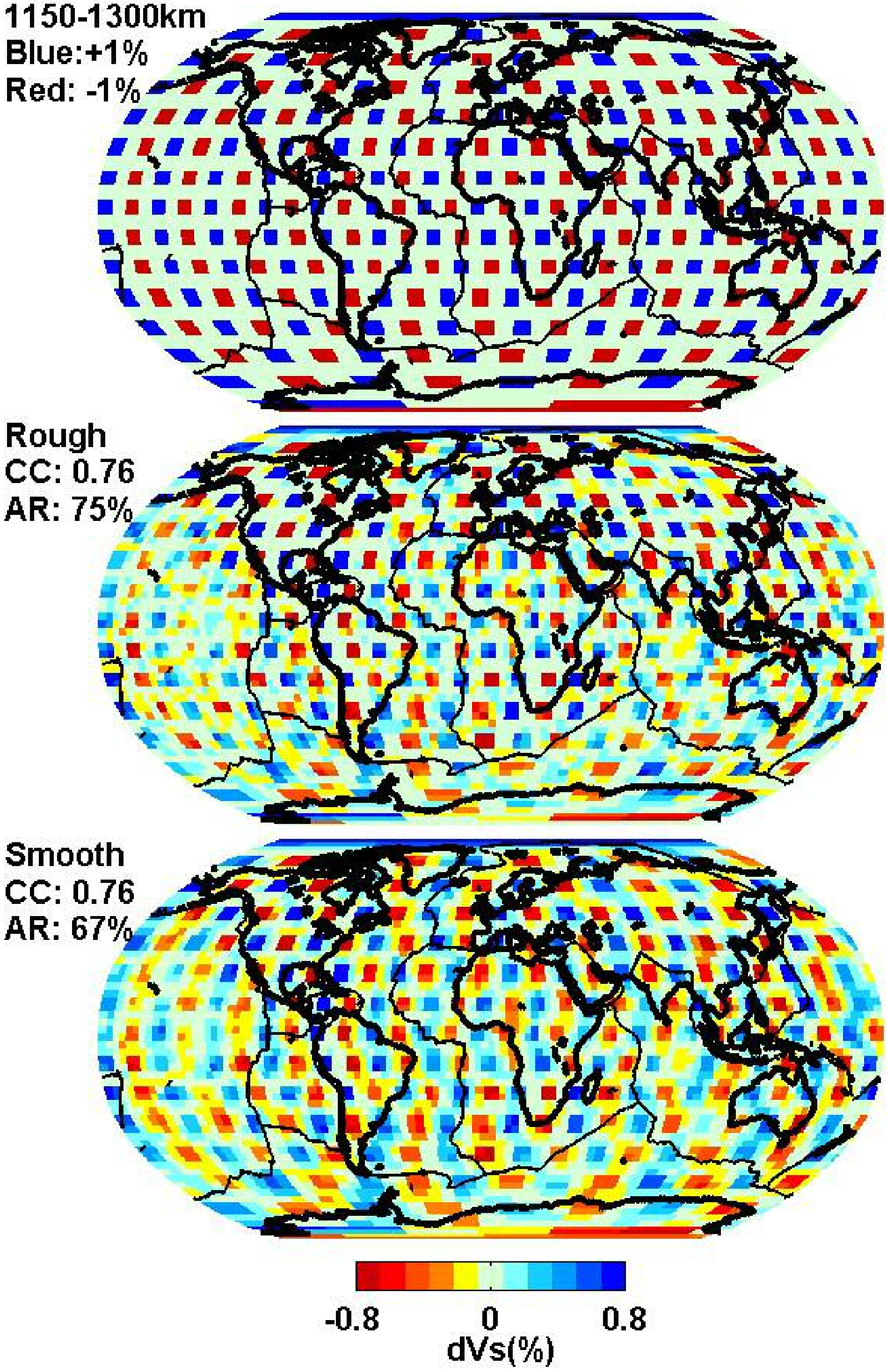

Figure B1 (continued)

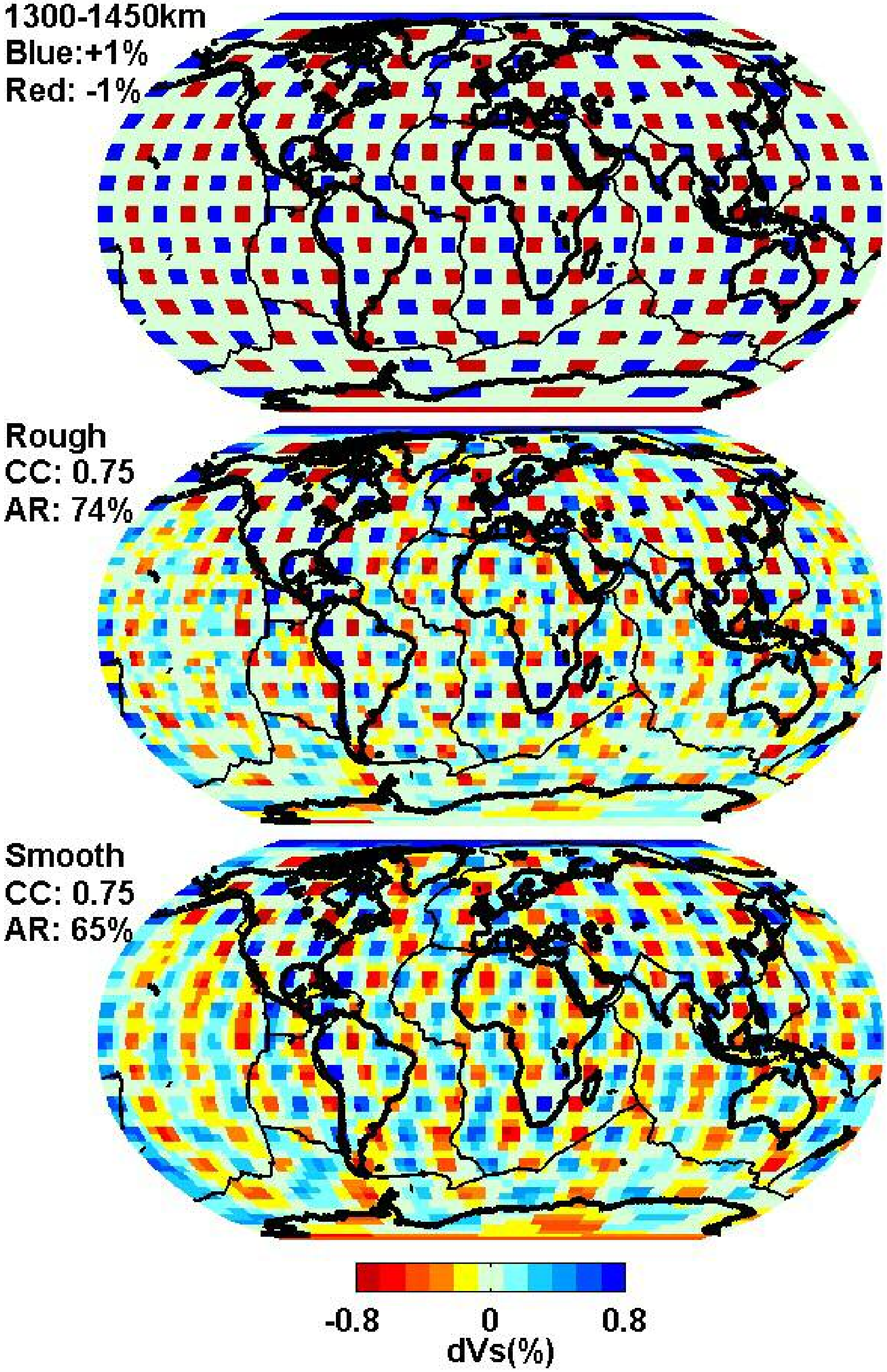

Figure B1 (continued)

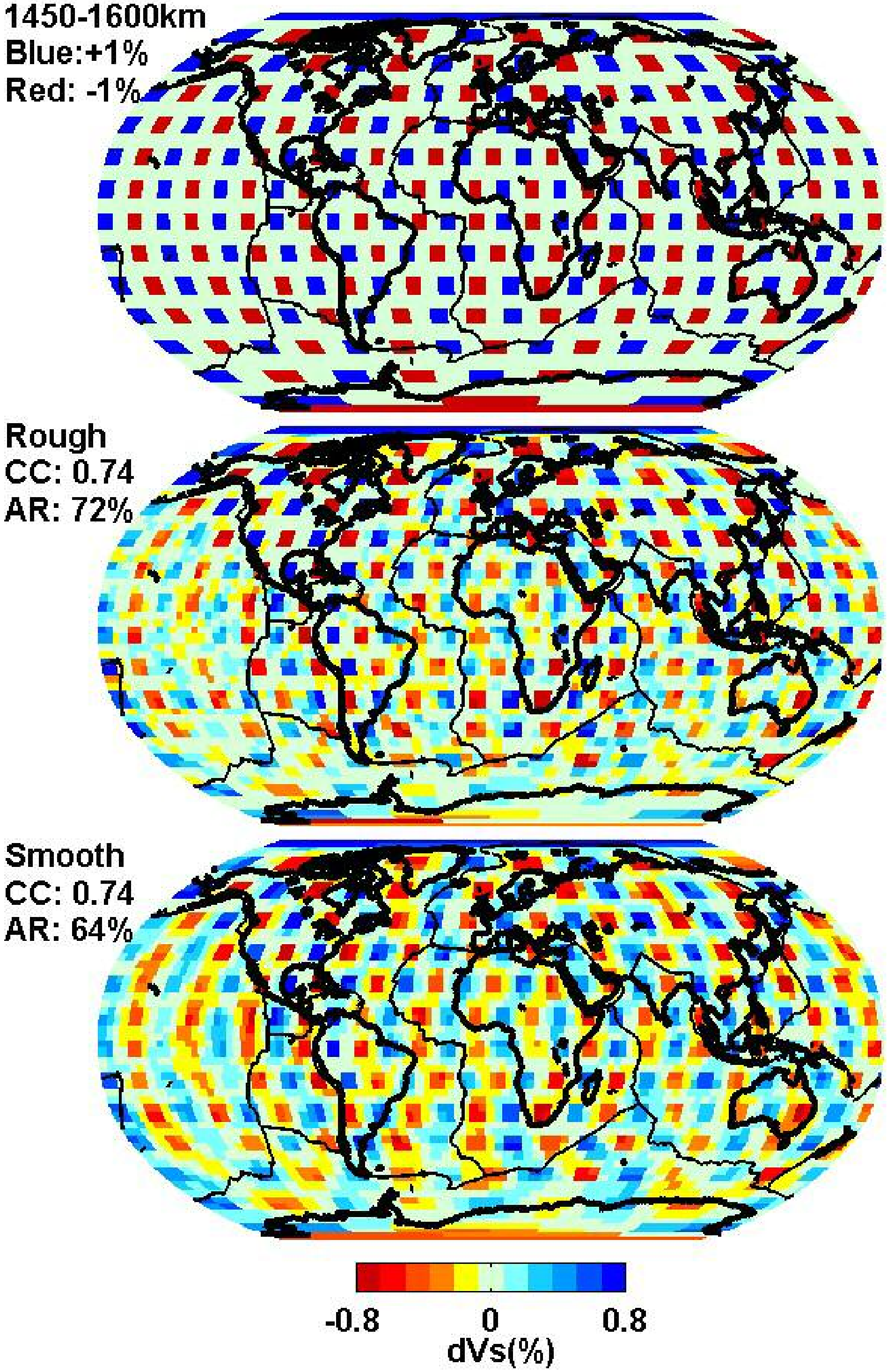

Figure B1 (continued)

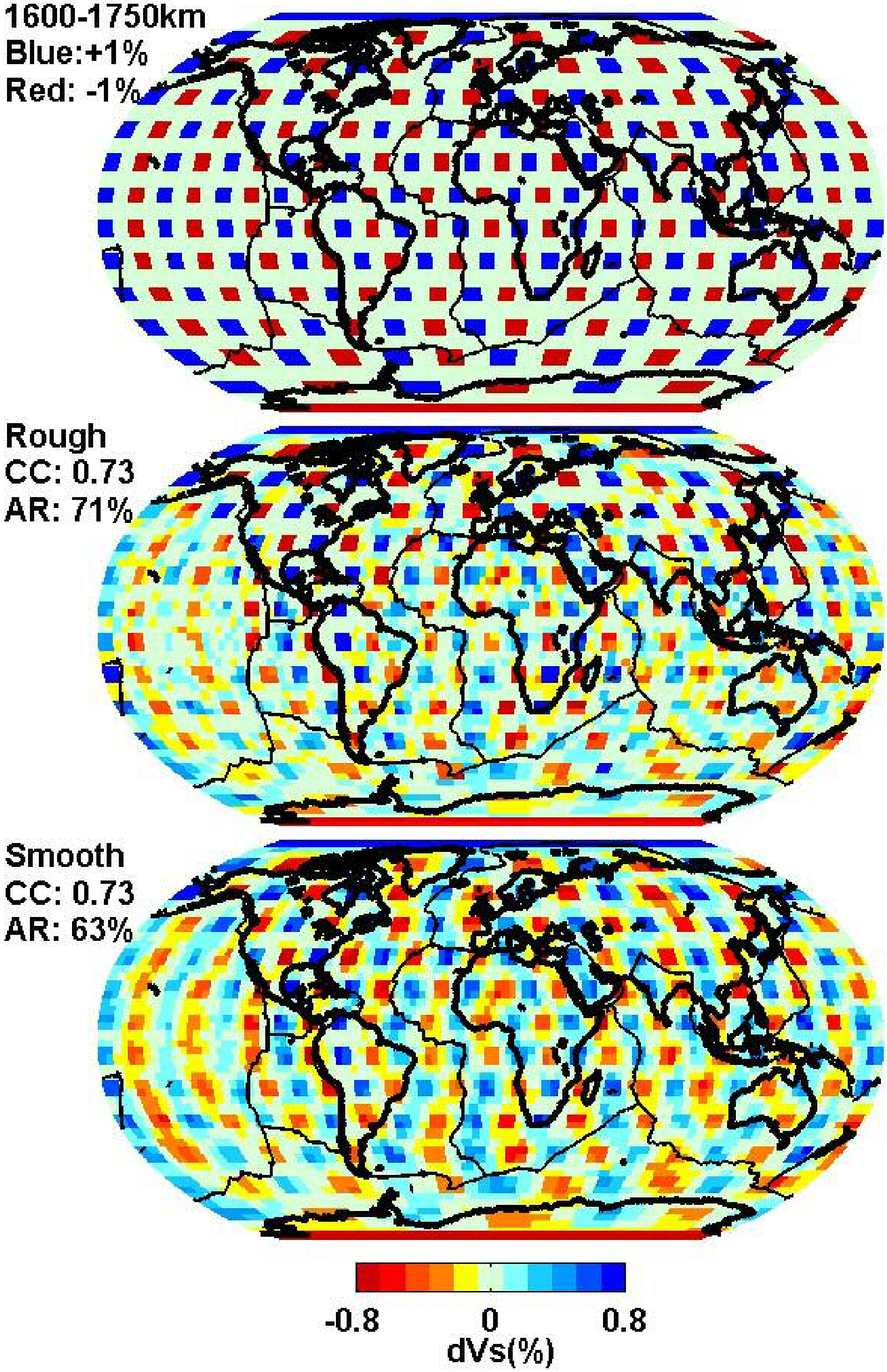

Figure B1 (continued)

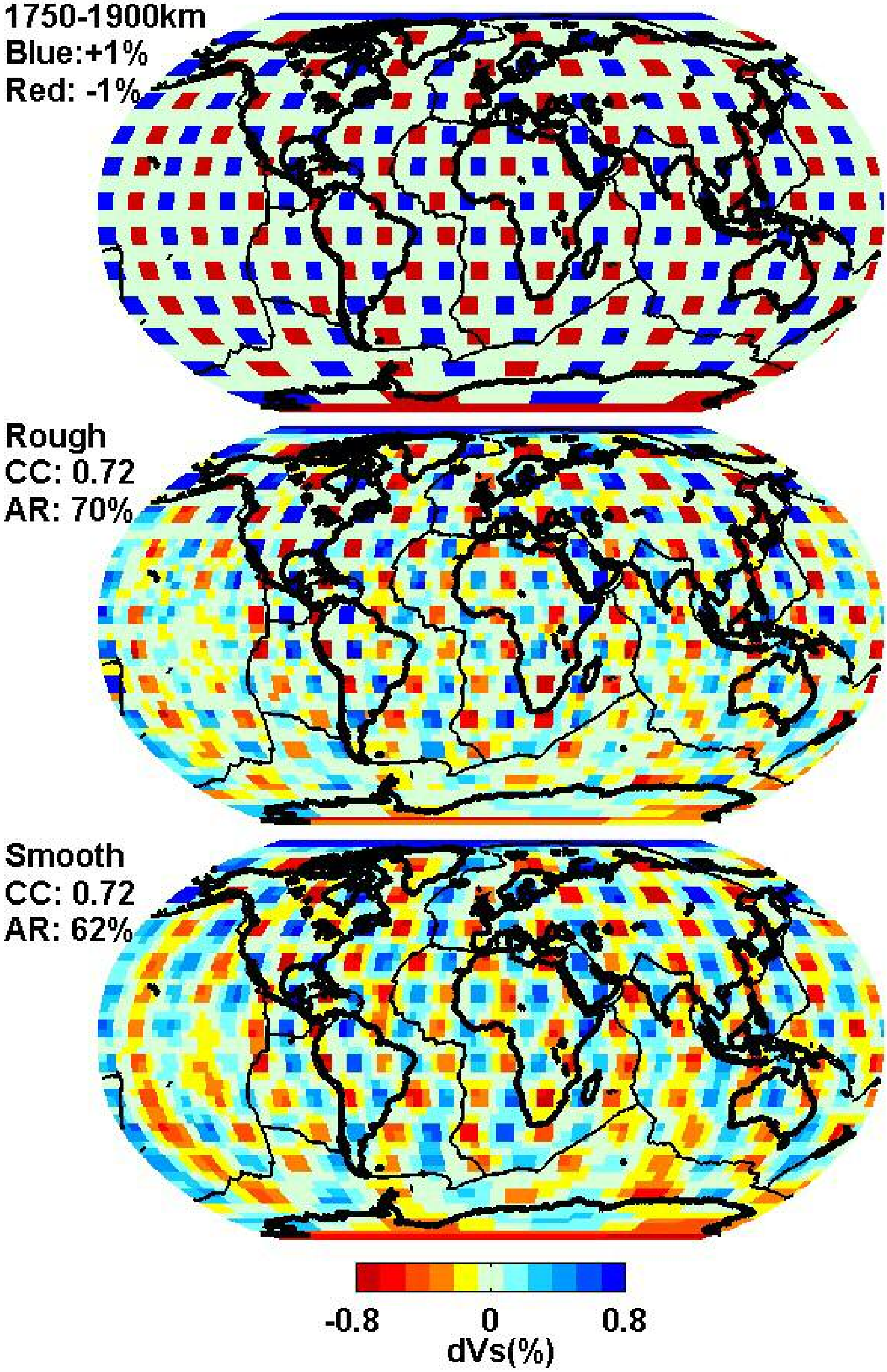

Figure B1 (continued)

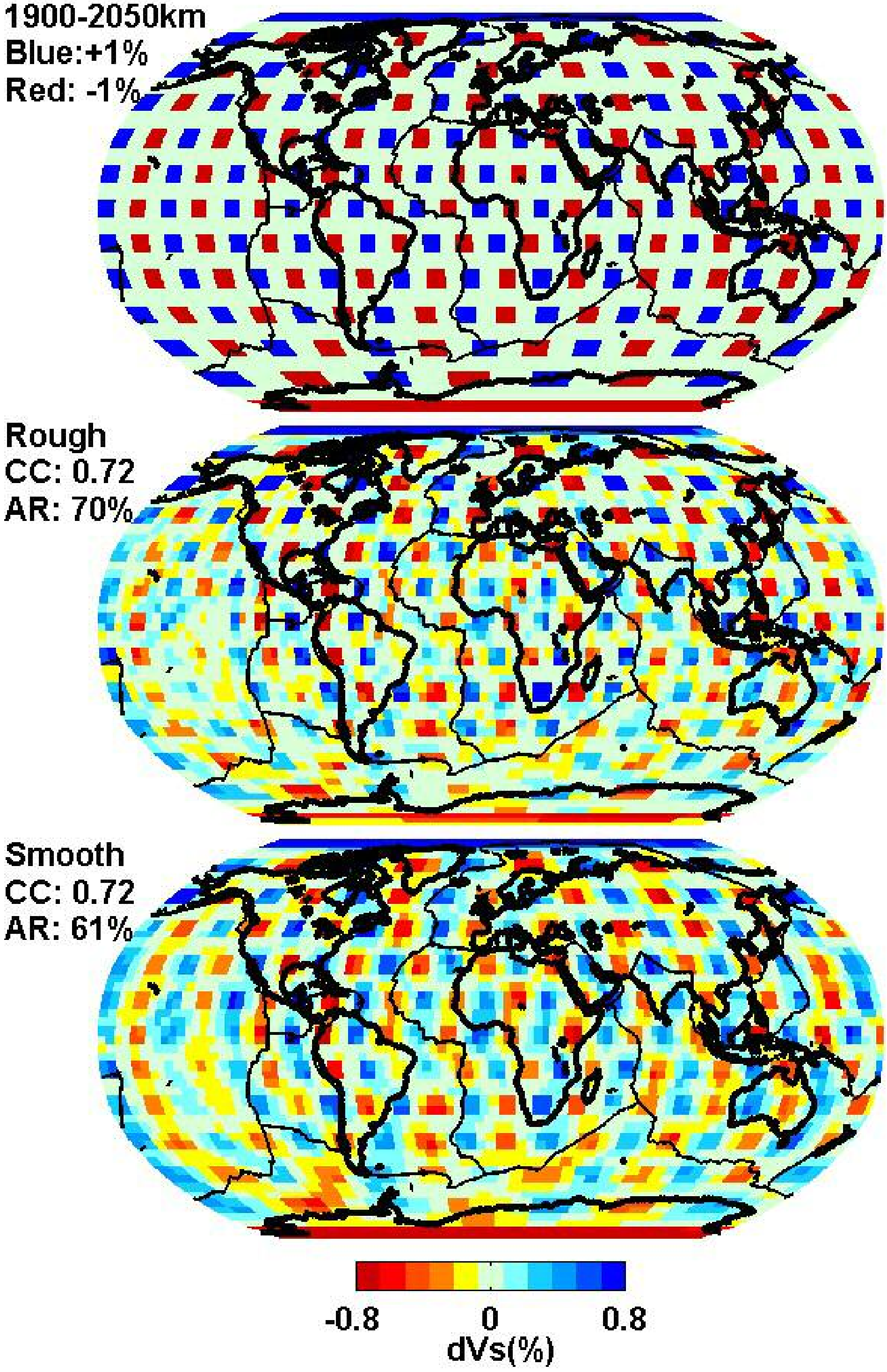

Figure B1 (continued)

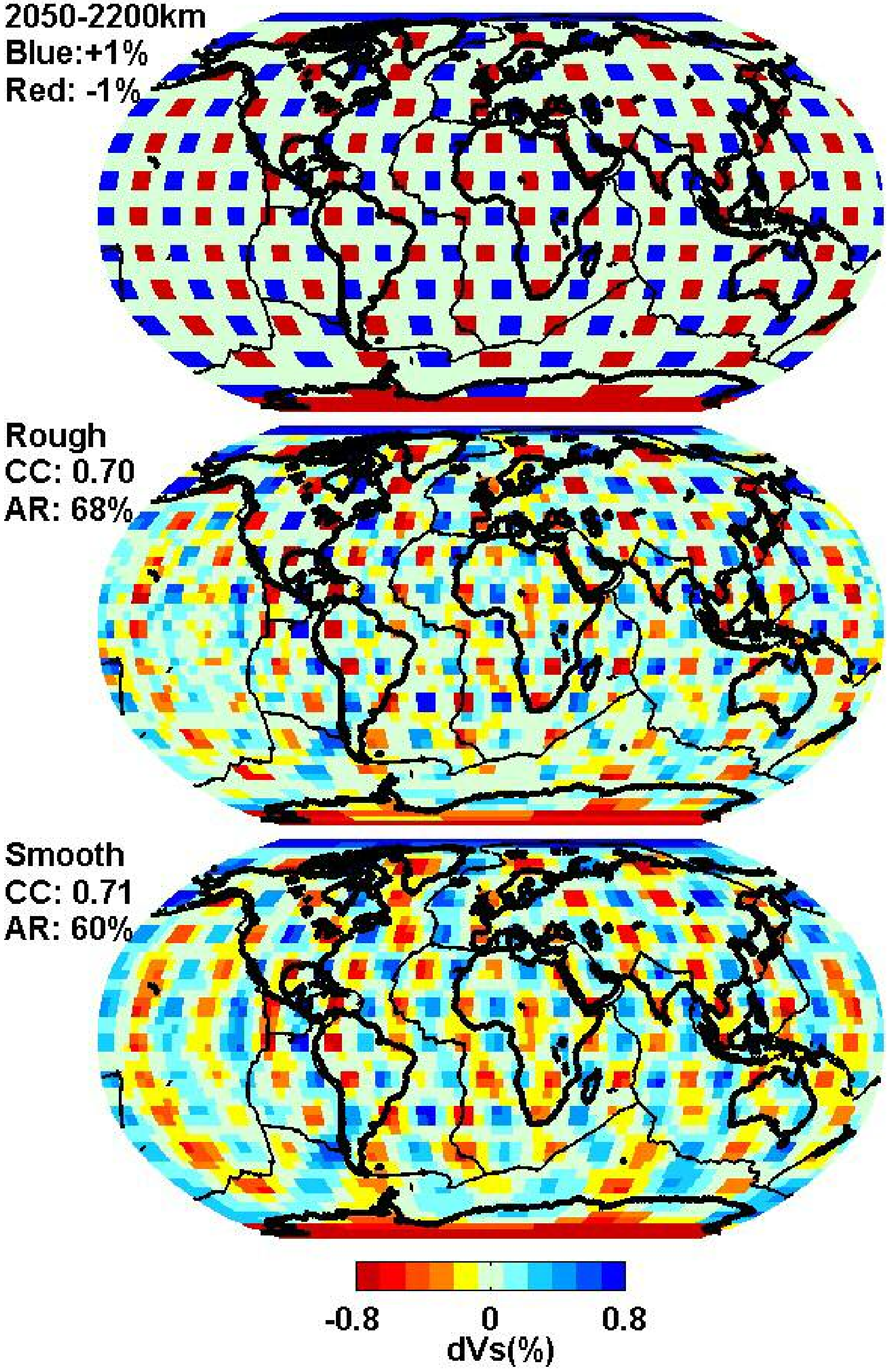

Figure B1 (continued)

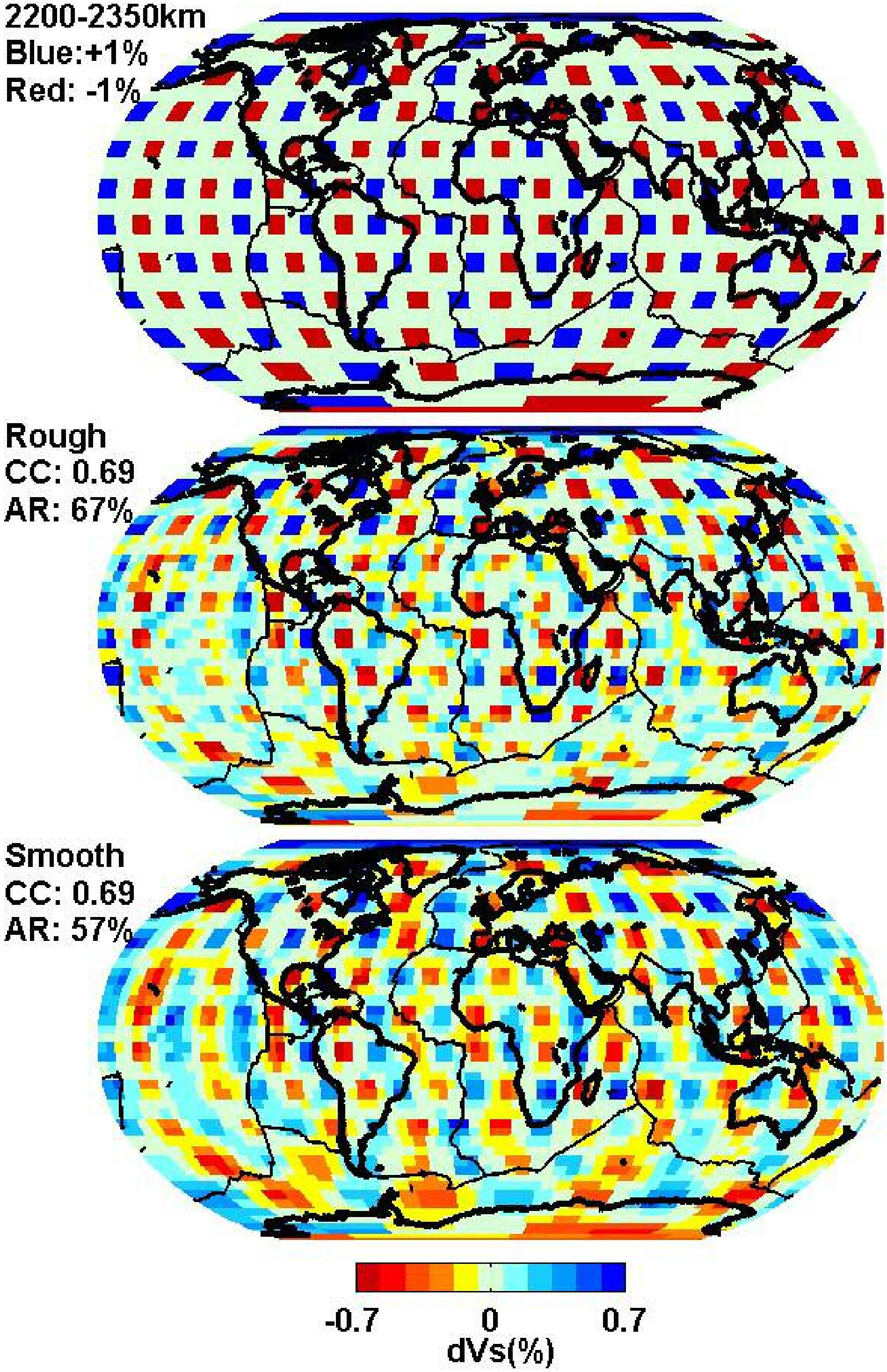

Figure B1 (continued)

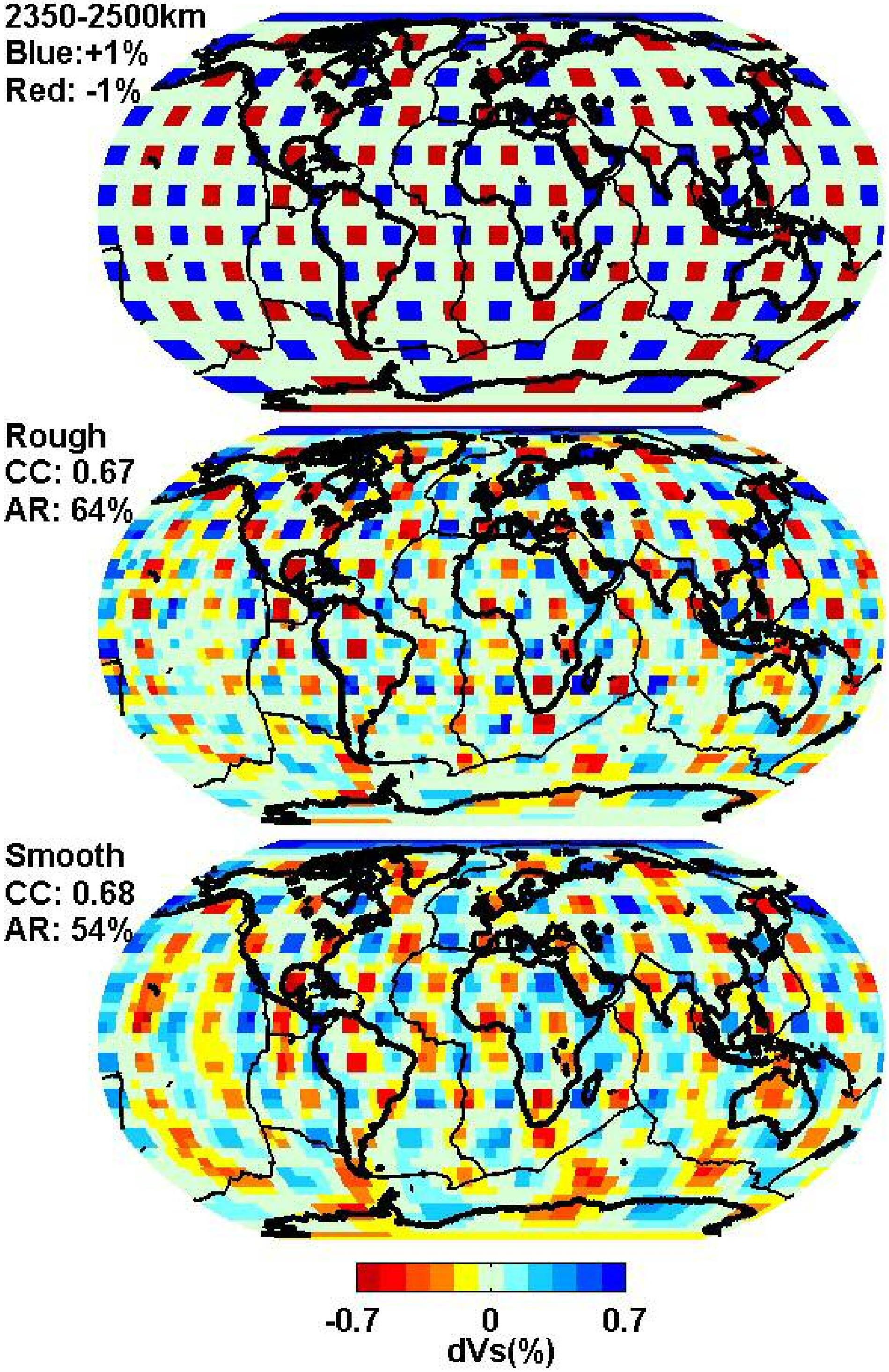

Figure B1 (continued)

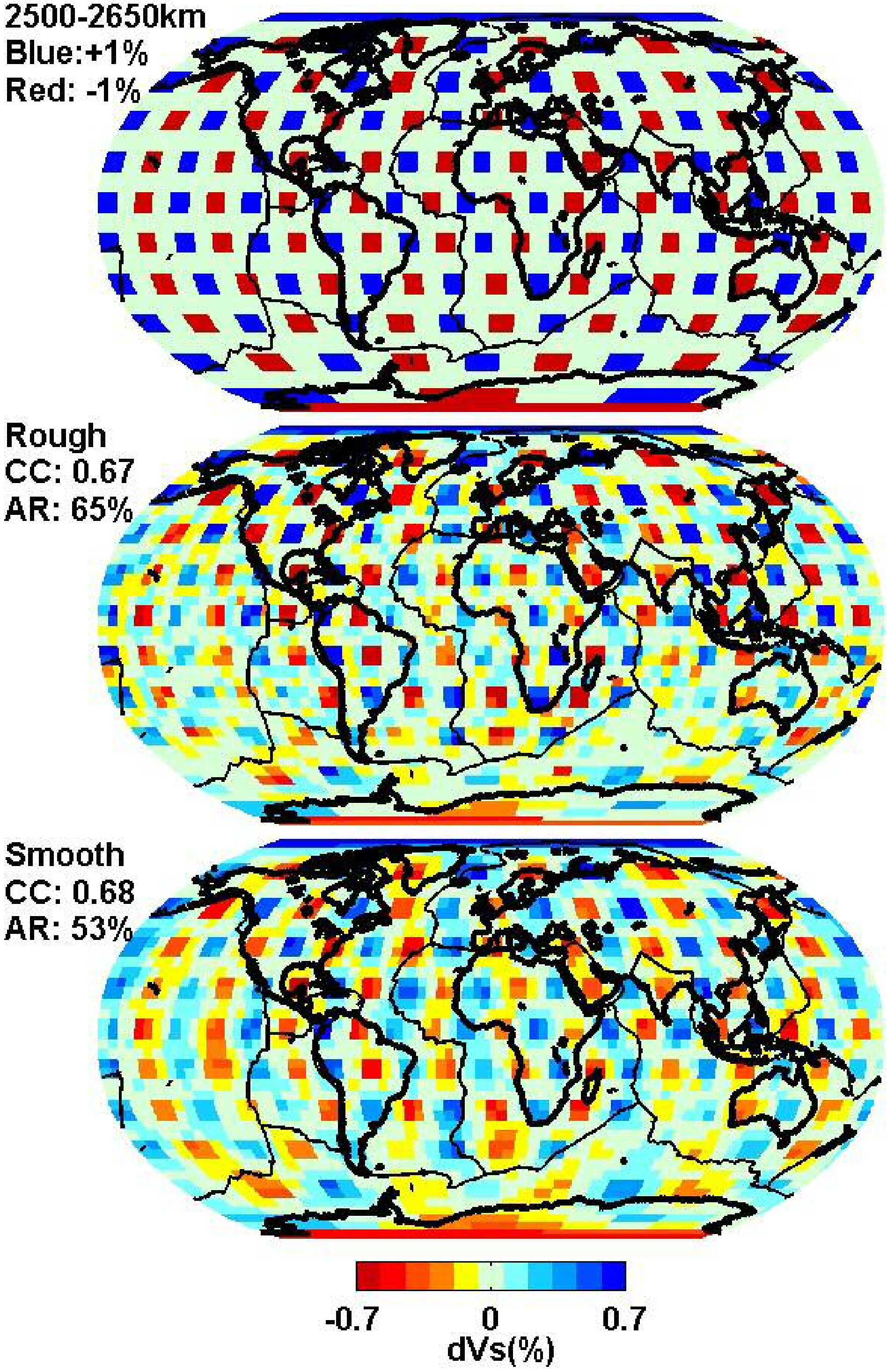

Figure B1 (continued)

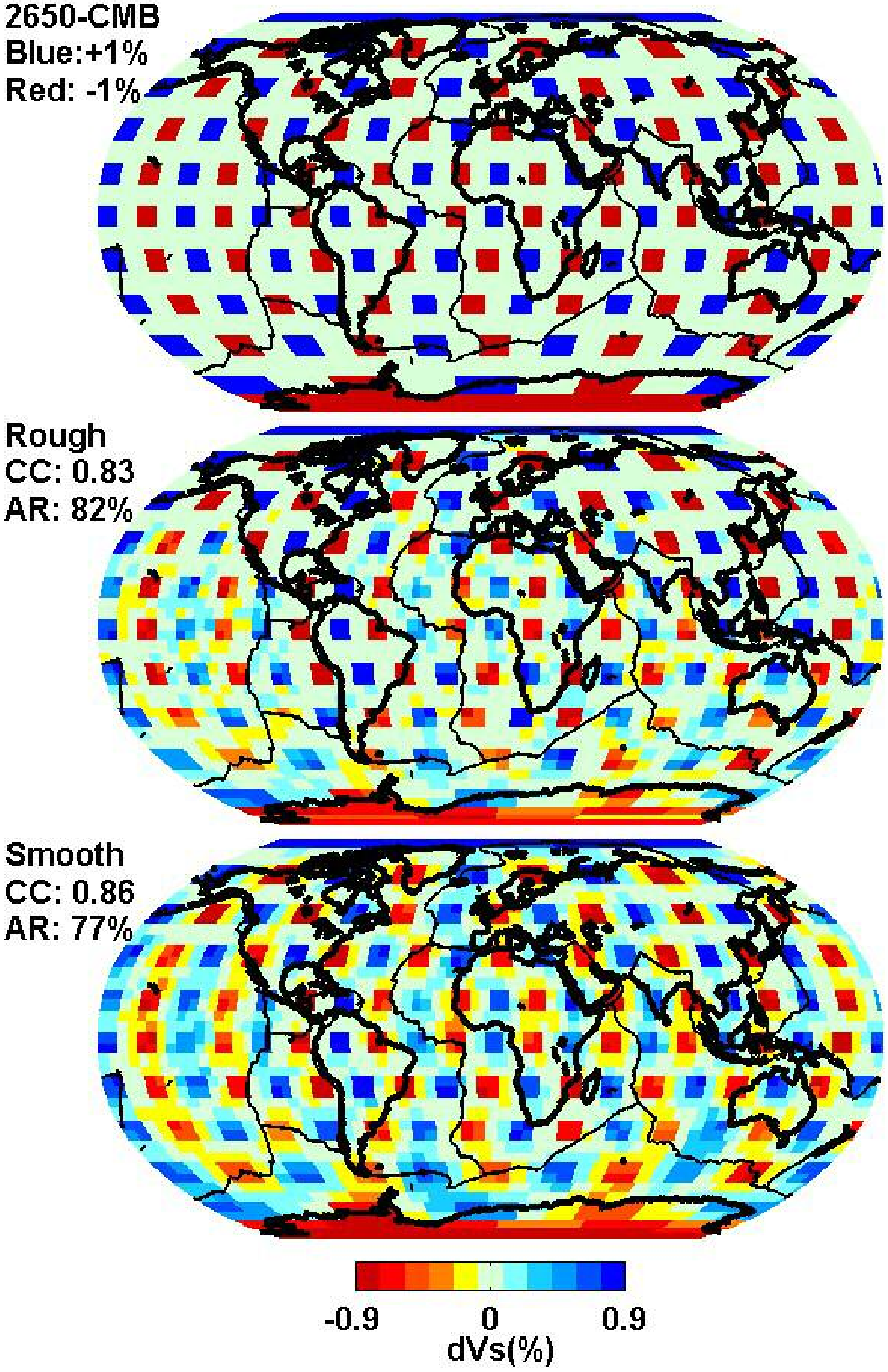

Figure B1 (continued)

Appendix C

Complete Shear-wave Tomography Model

This is the complete shear-wave tomographic model of the mantle produced using the data and methods fully described in Chapter 2. The mantle was divided into 22 depth layers and each is presented. Using L-curve analysis, I determined the optimal trade-off between data misfit and model complexity (roughness). The definitions of misfit and model complexity as well as the L-curve can also be found in Chapter 2. In addition to the optimal model, I also present a smoother and a rougher solution to give insight on how anomalies vary with overall model smoothness. Each of the models are presented in term of shear-wave velocity perturbations and it should be noted that the amplitude scale varies with each depth.

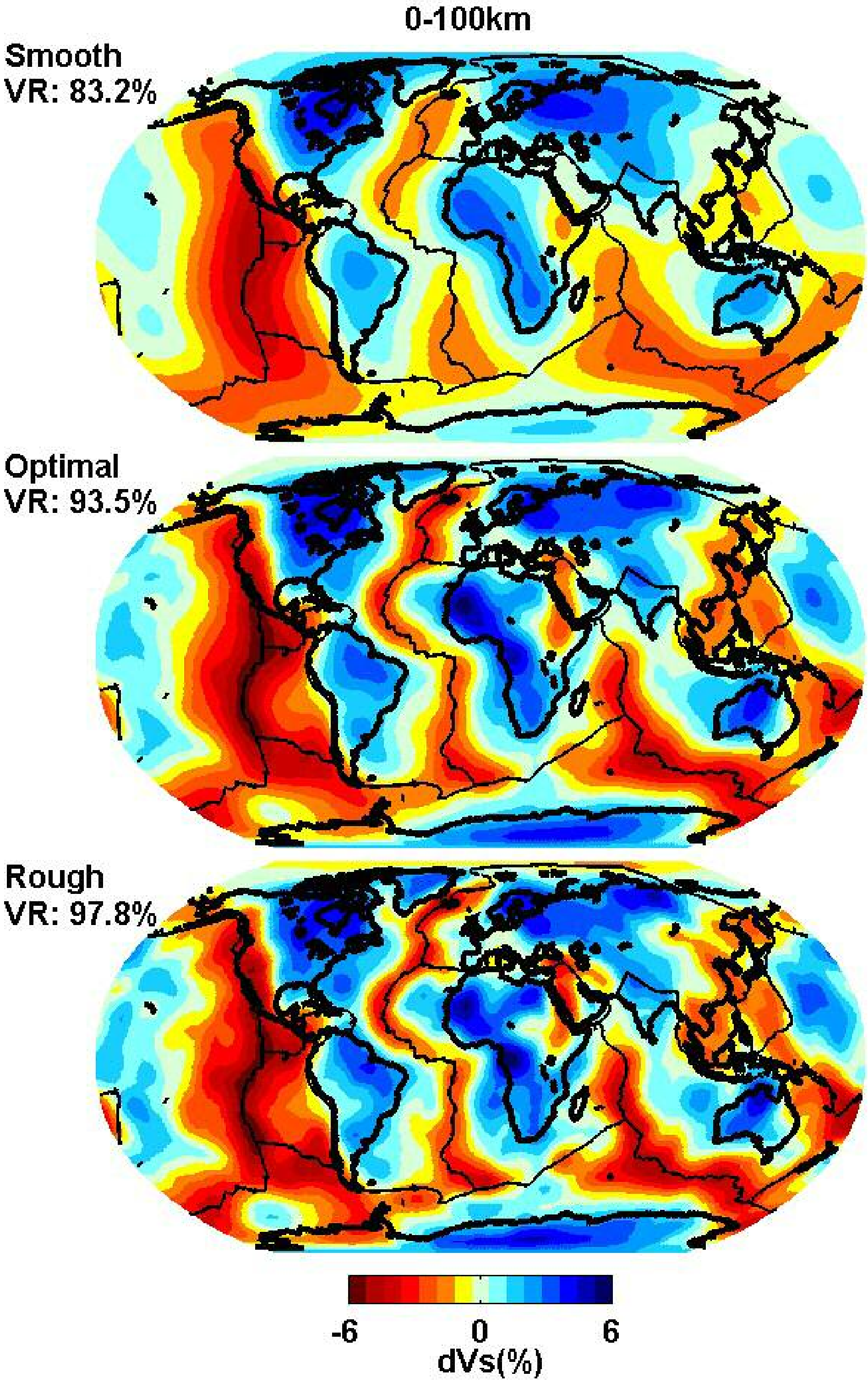

Figure C1 Shear-wave tomographic model described in Chapter 2.

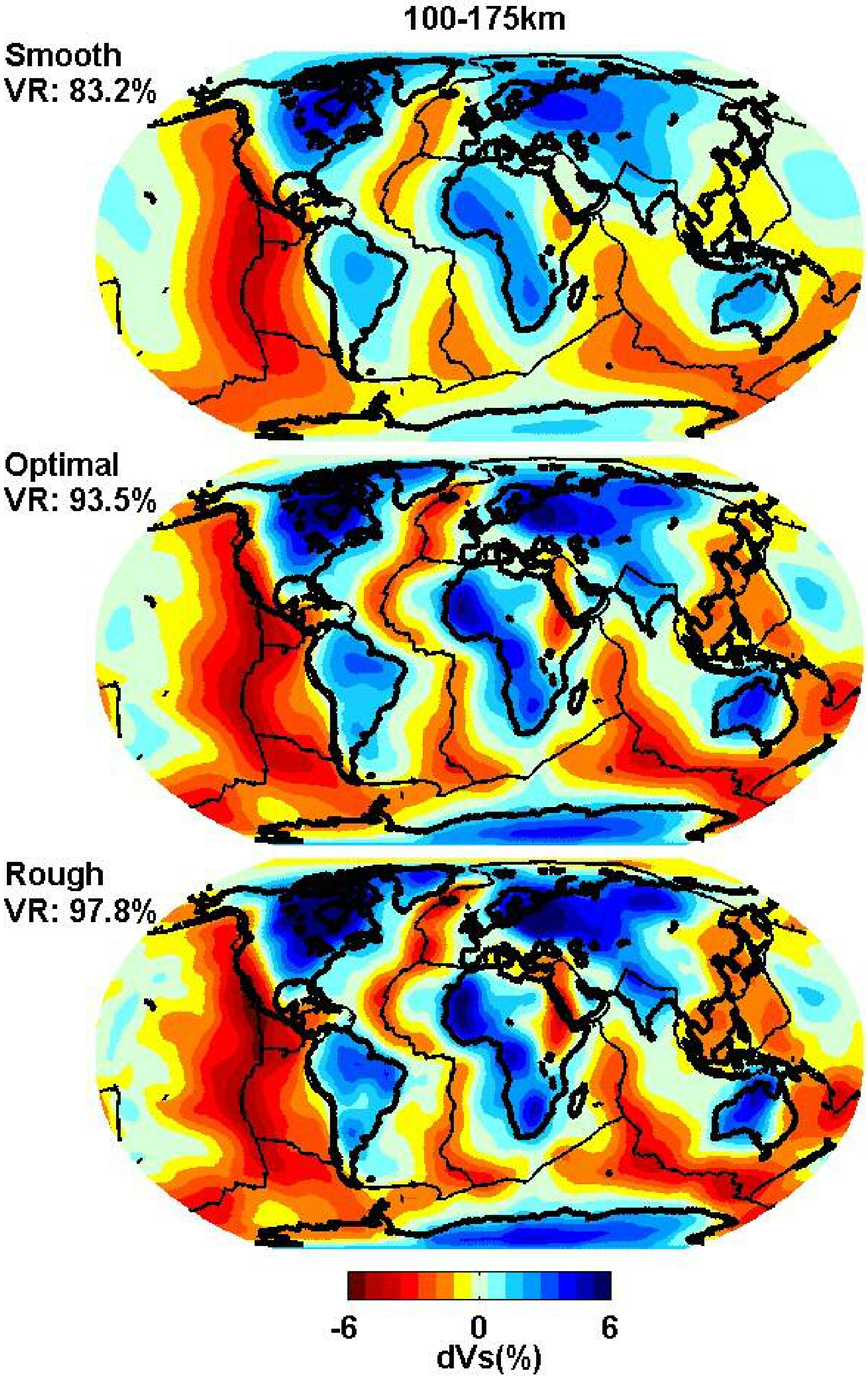

Figure C1 (continued)

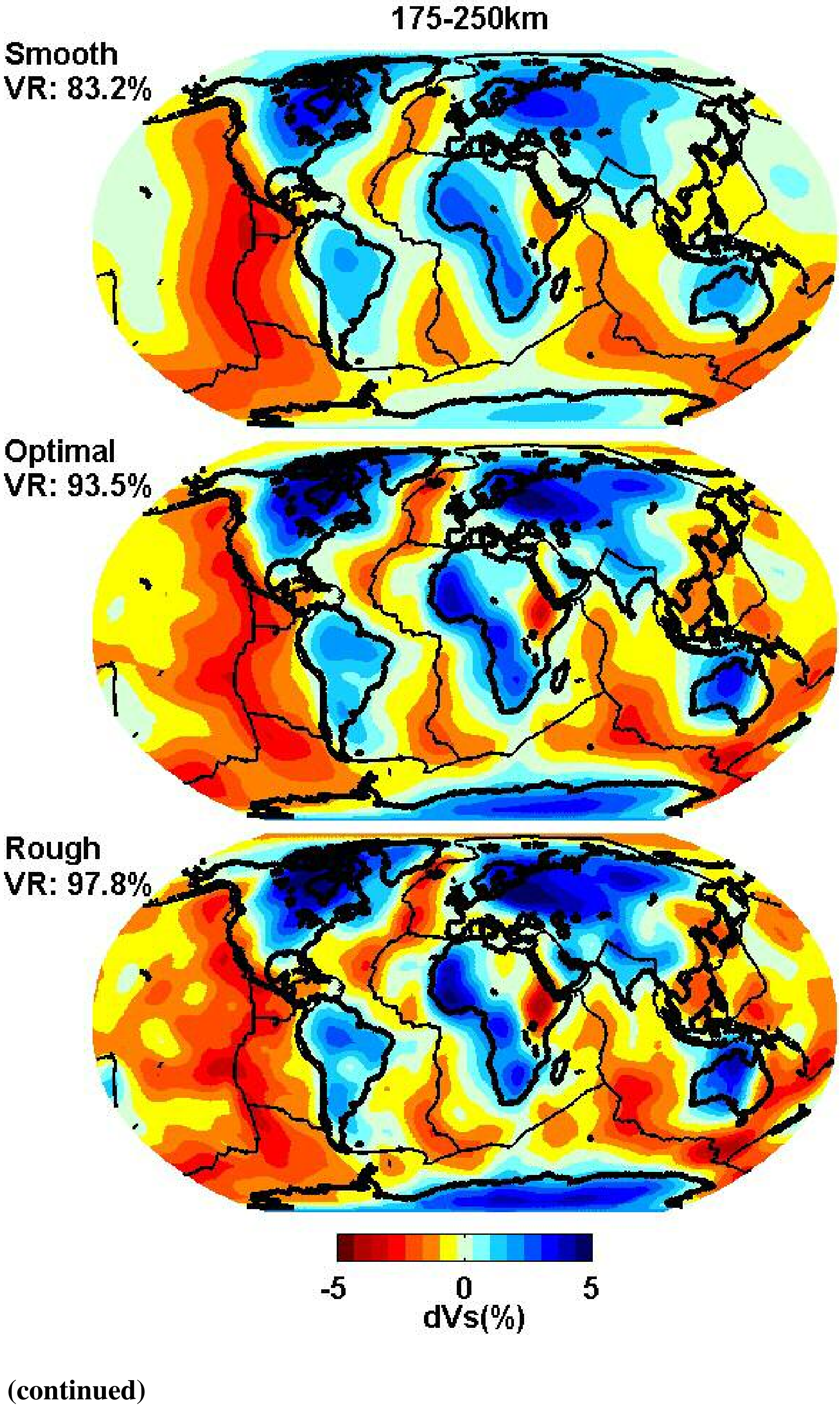

Figure C1 (continued)

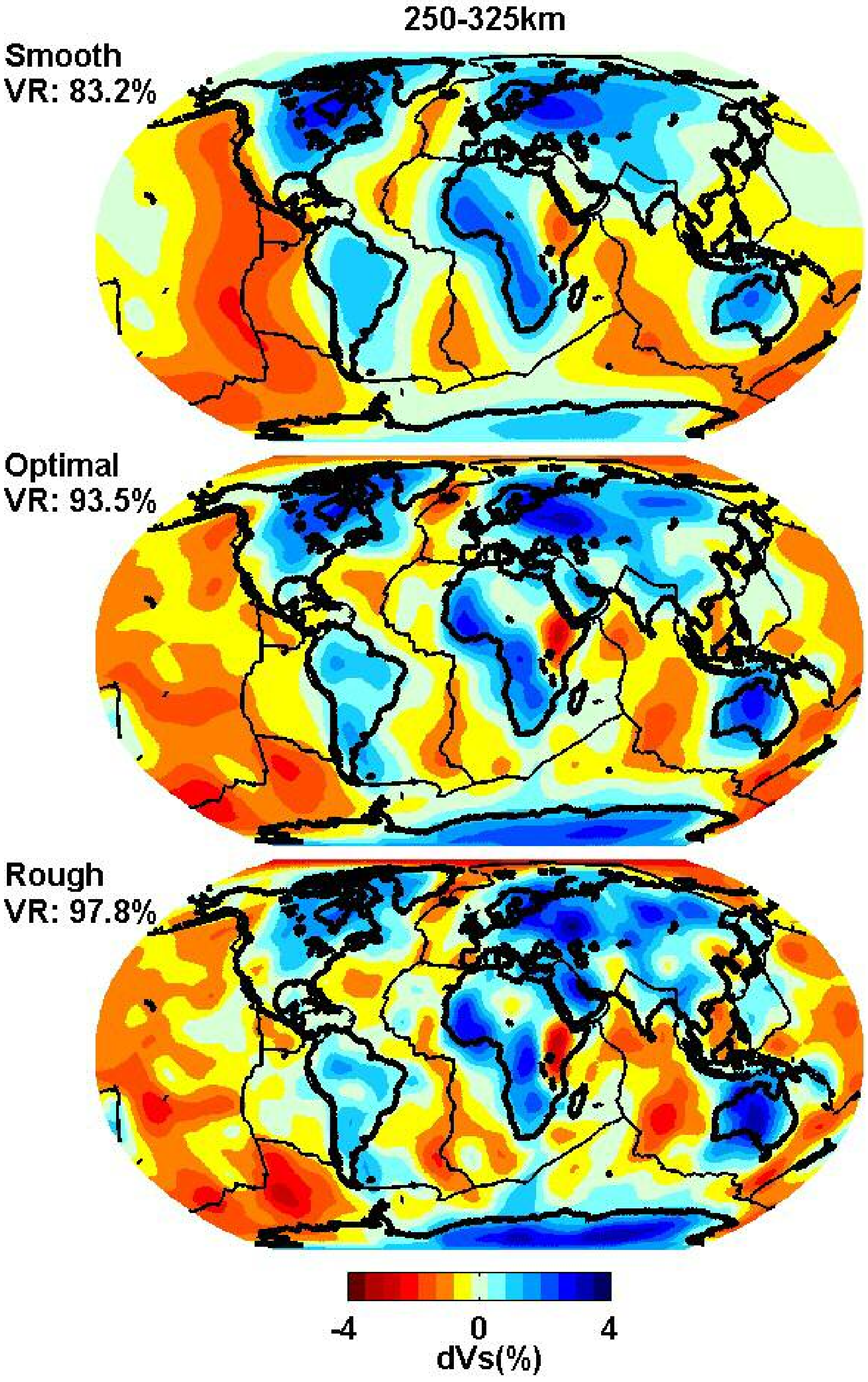

Figure C1 (continued)

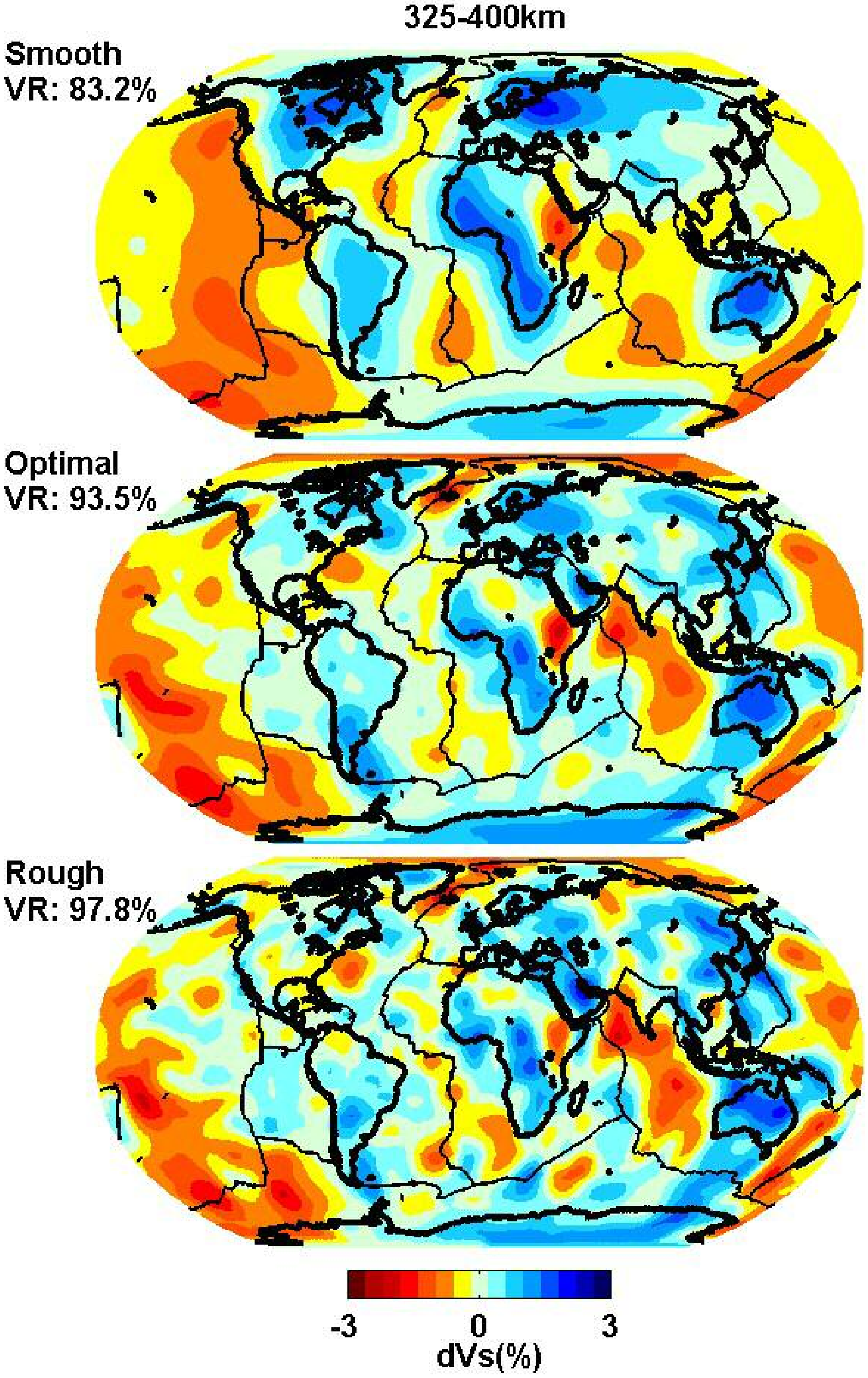

Figure C1 (continued)

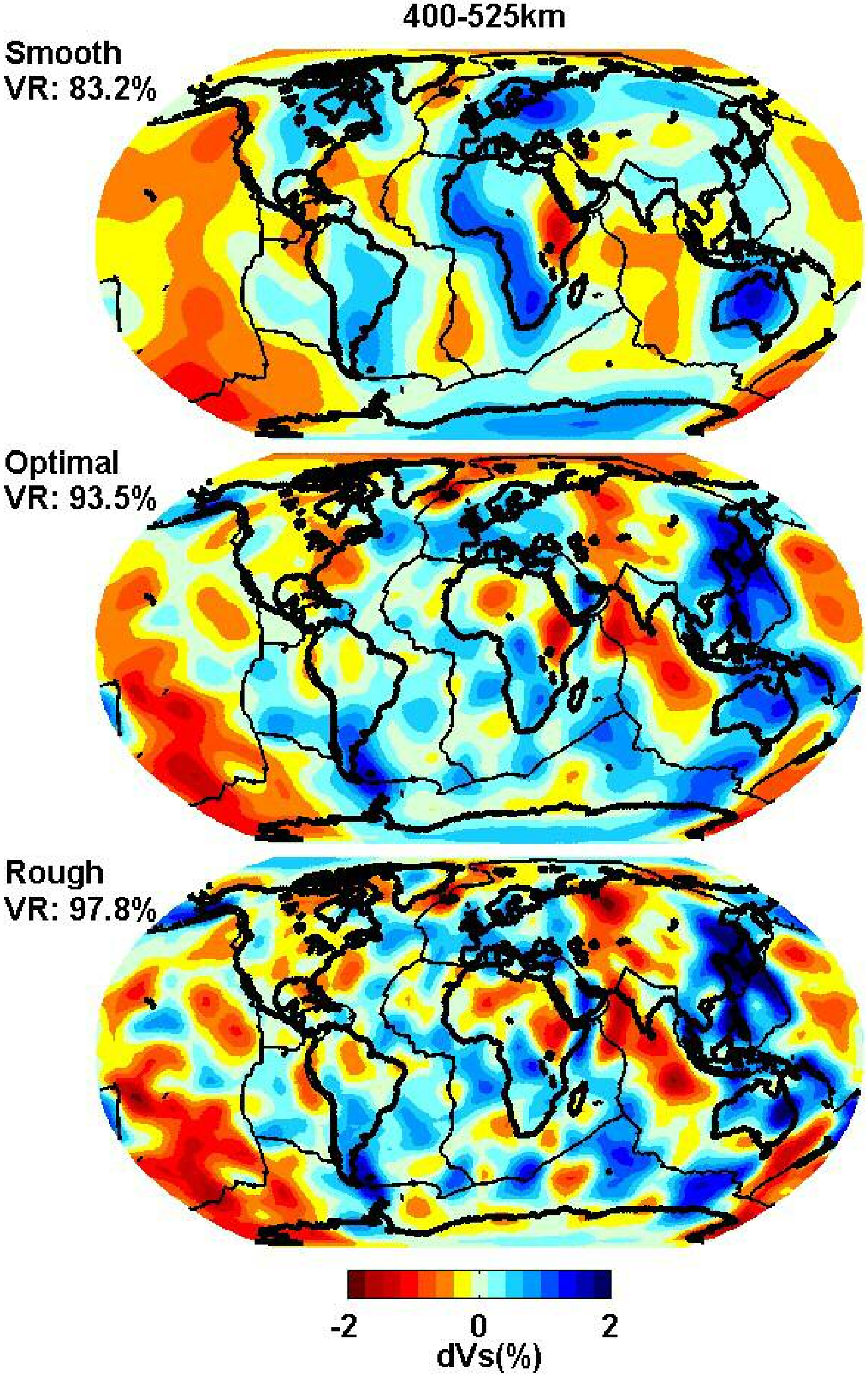

Figure C1 (continued)

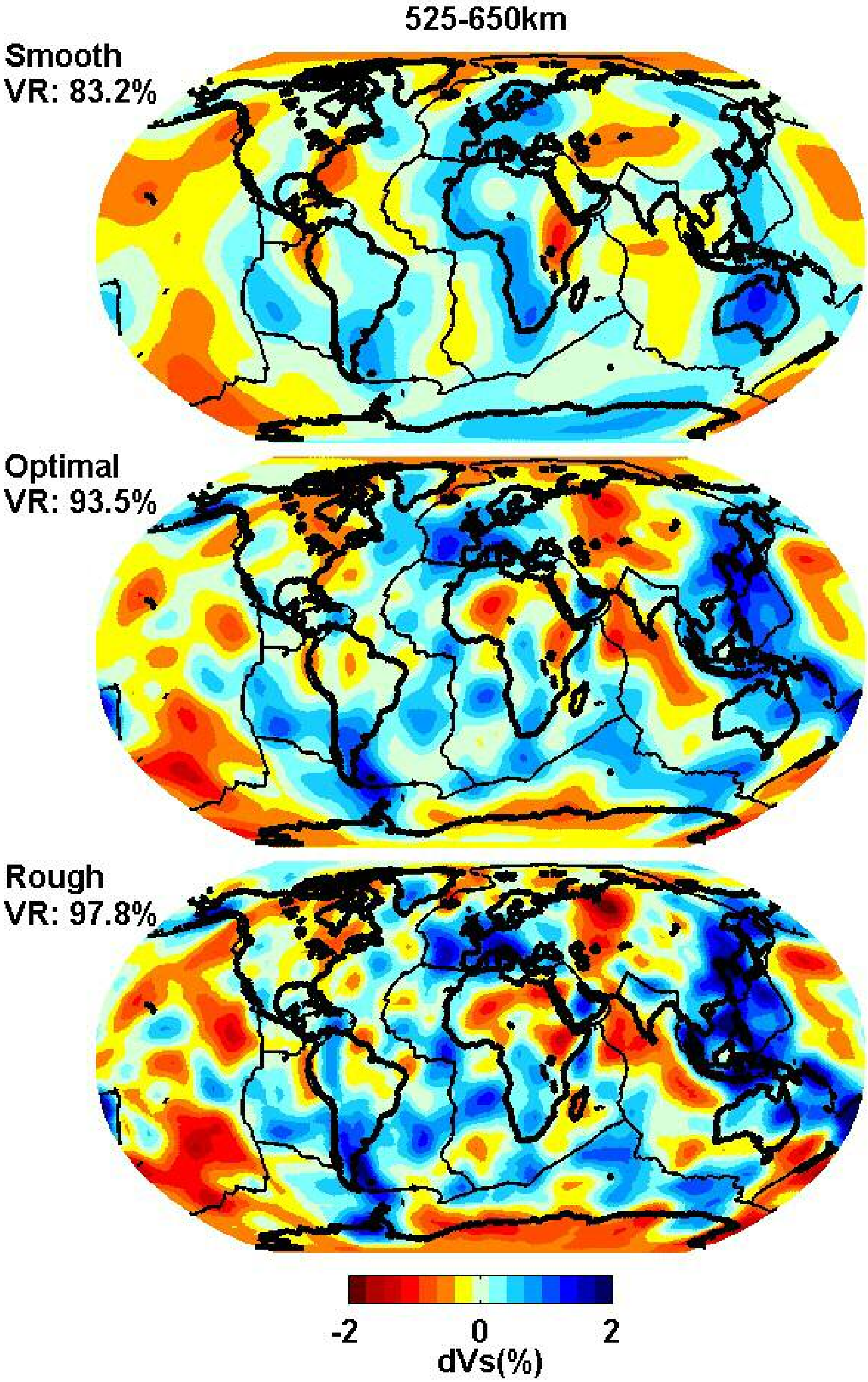

Figure C1 (continued)

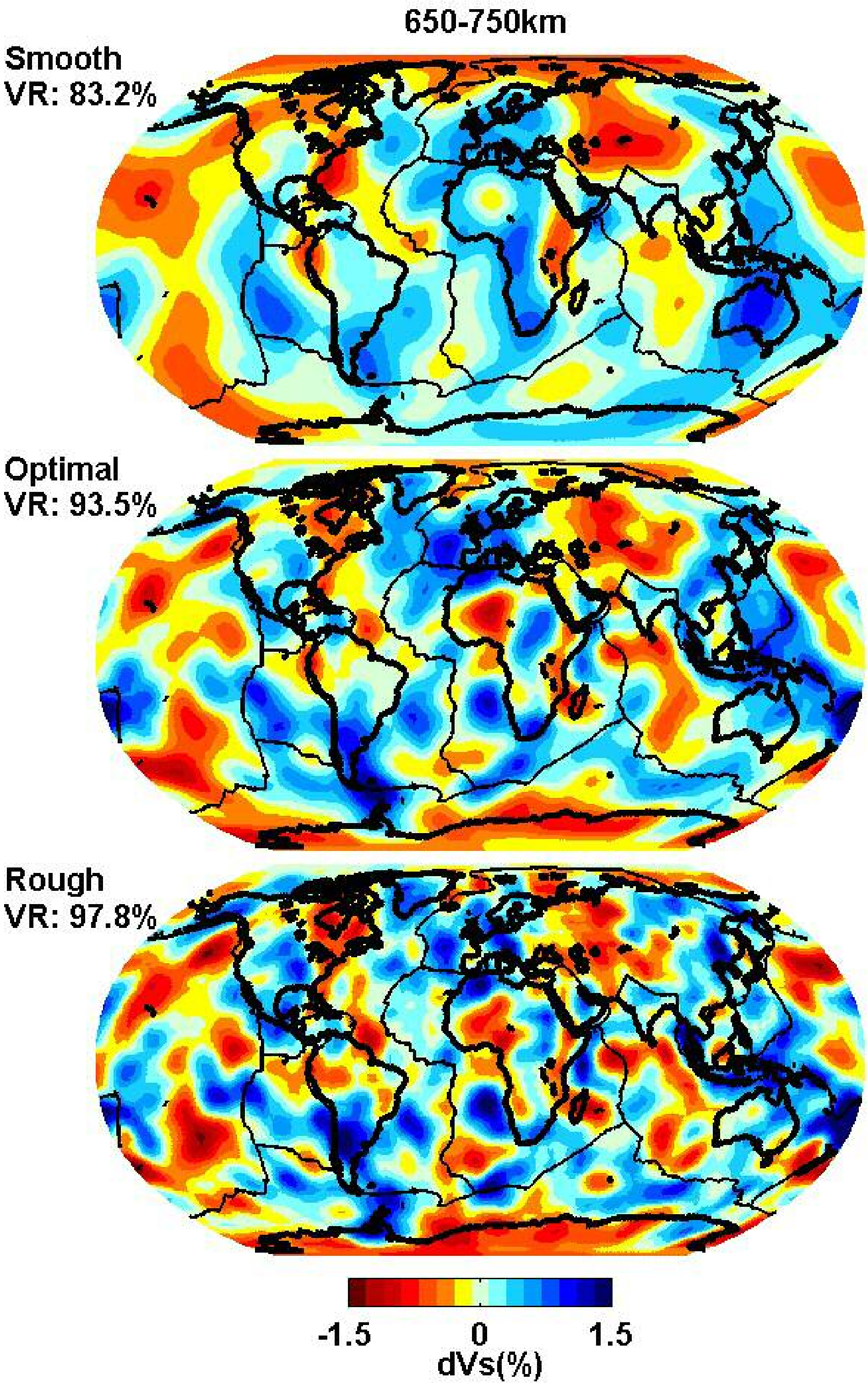

Figure C1 (continued)

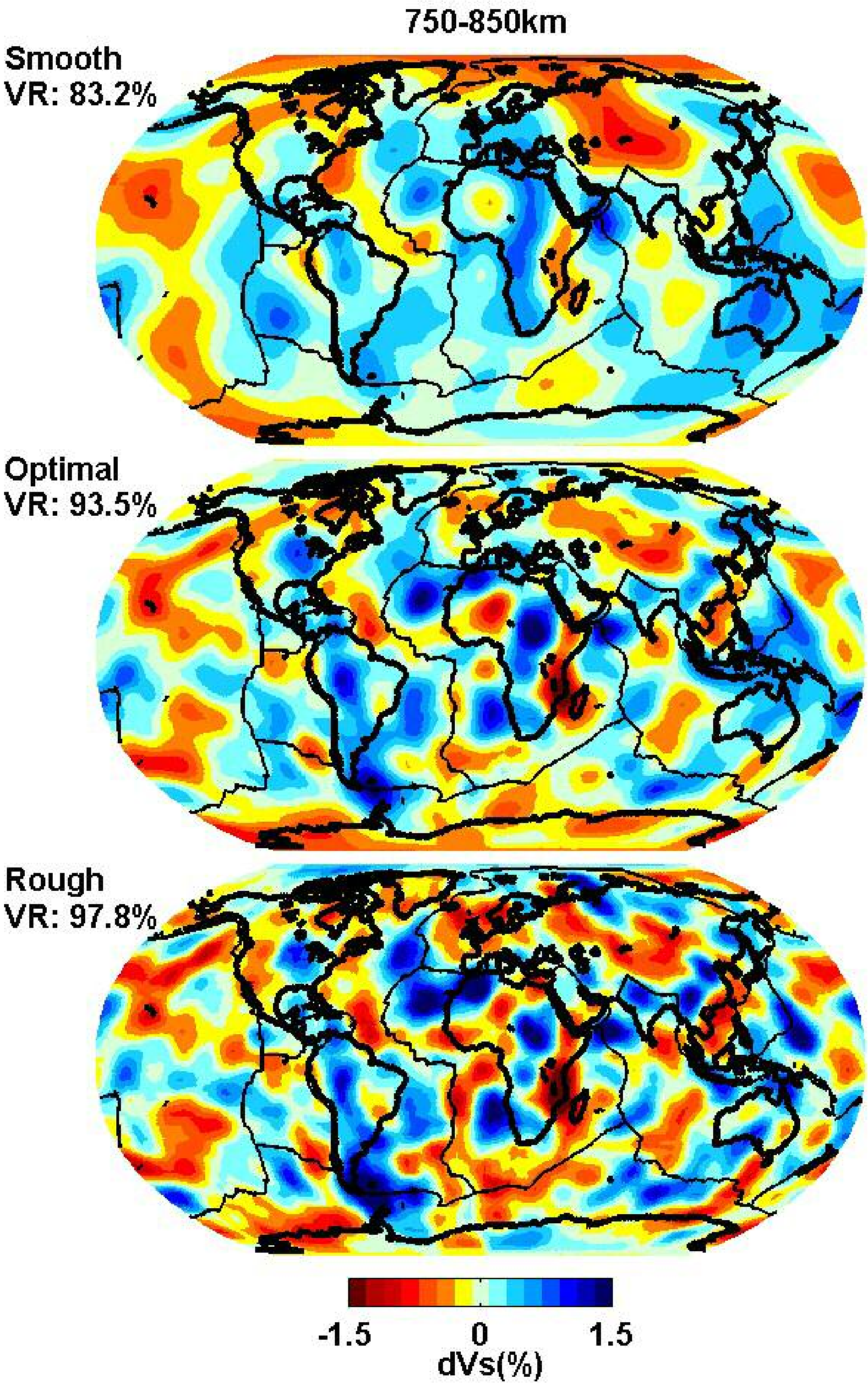

Figure C1 (continued)

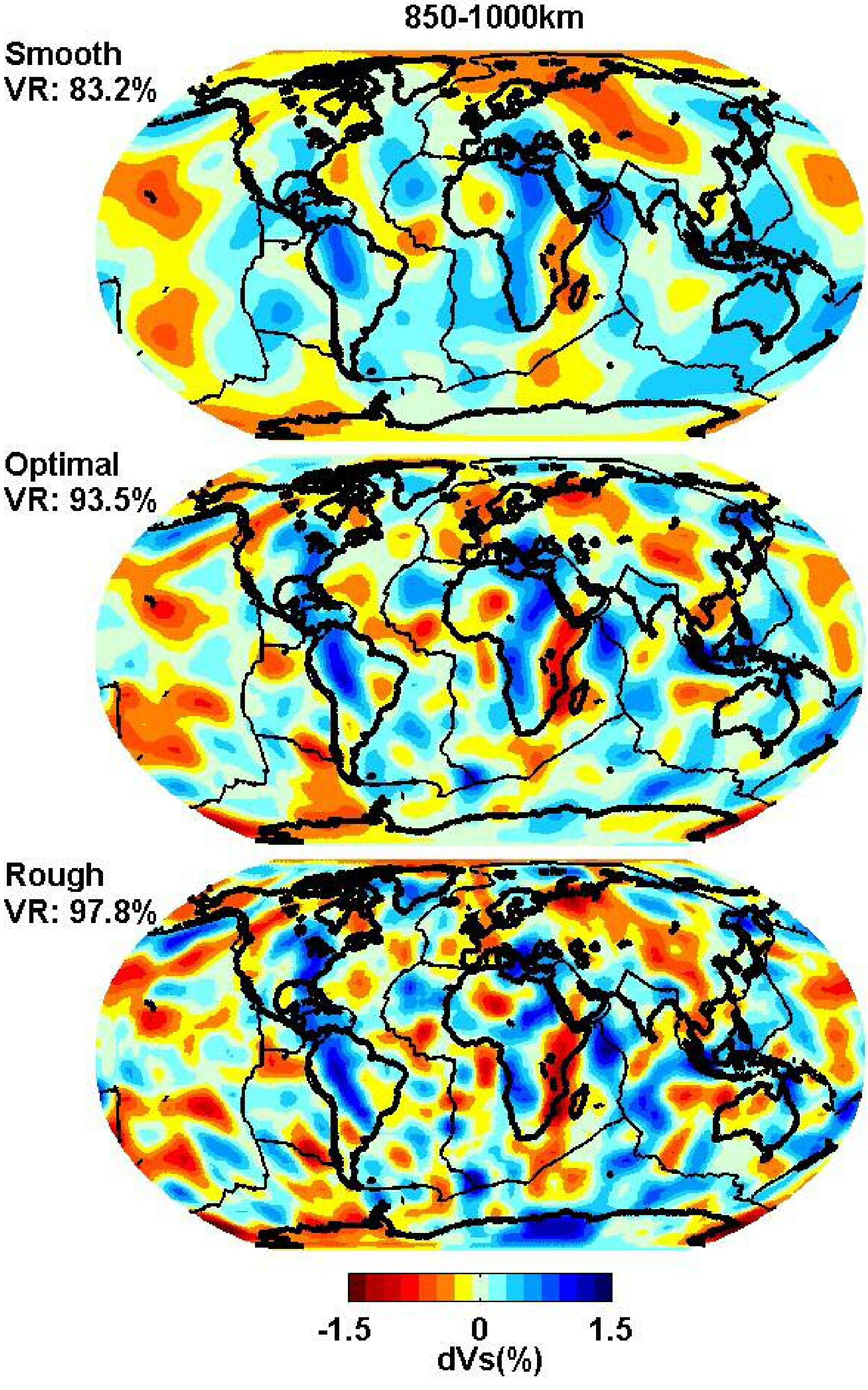

Figure C1 (continued)

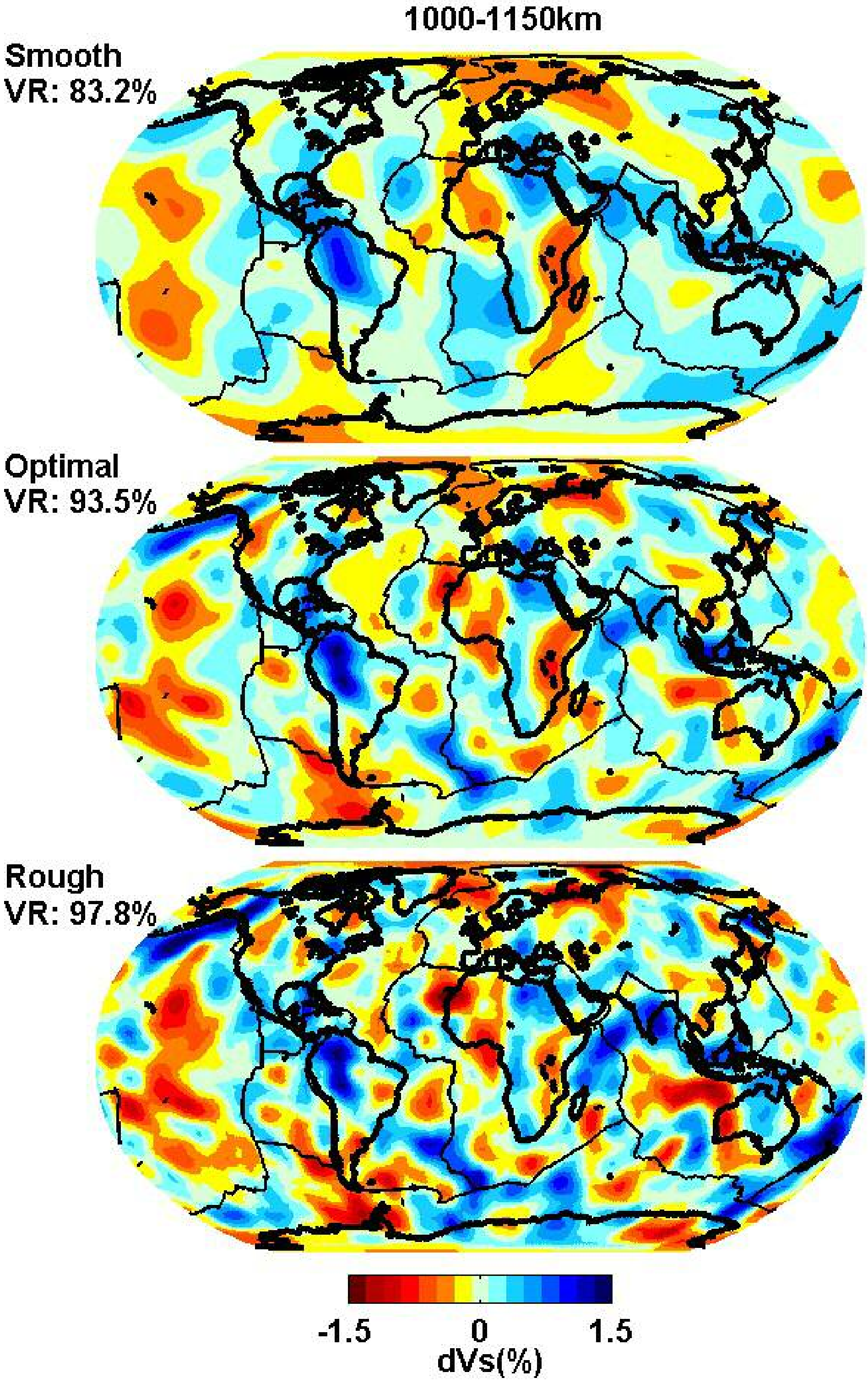

Figure C1 (continued)

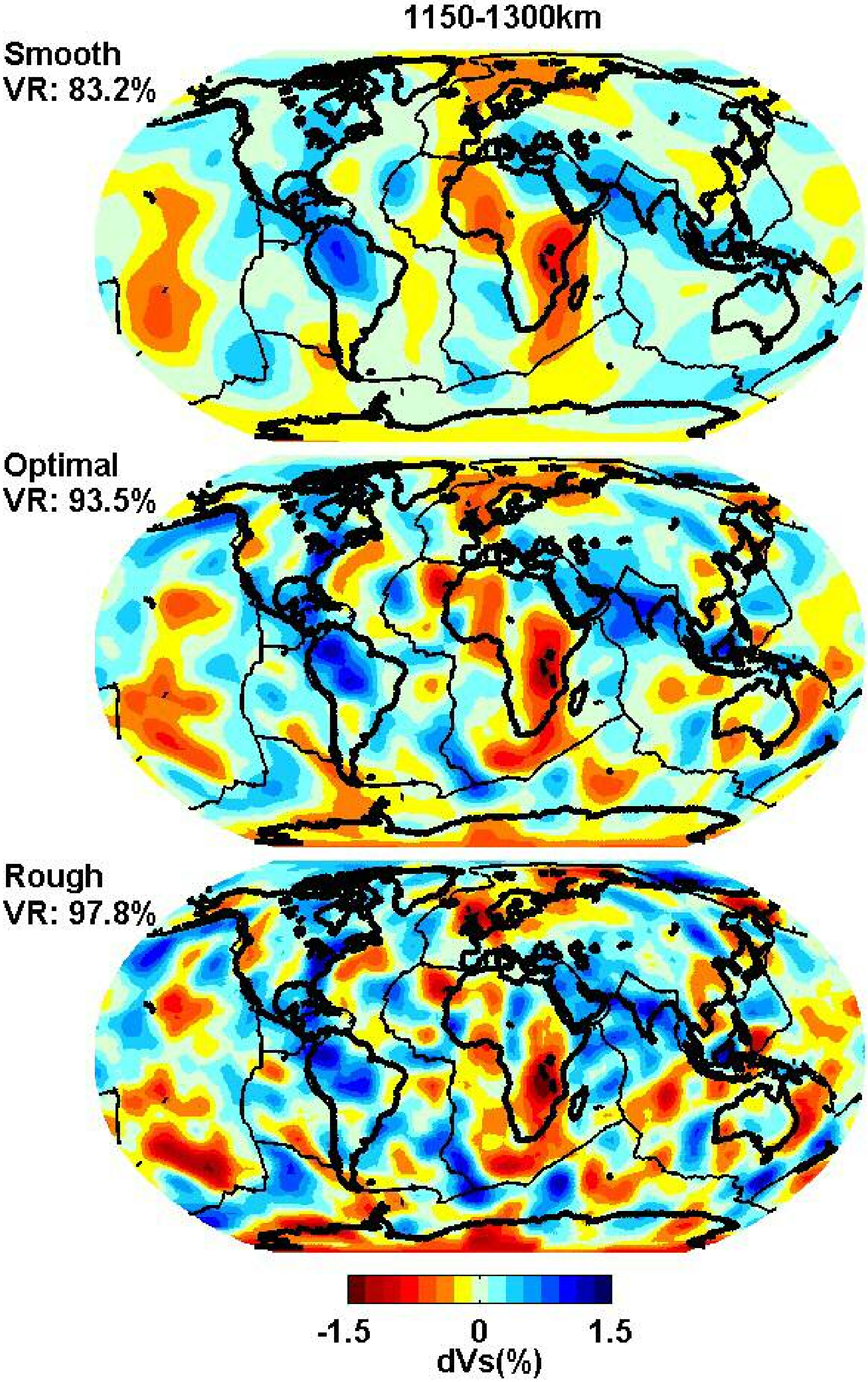

Figure C1 (continued)

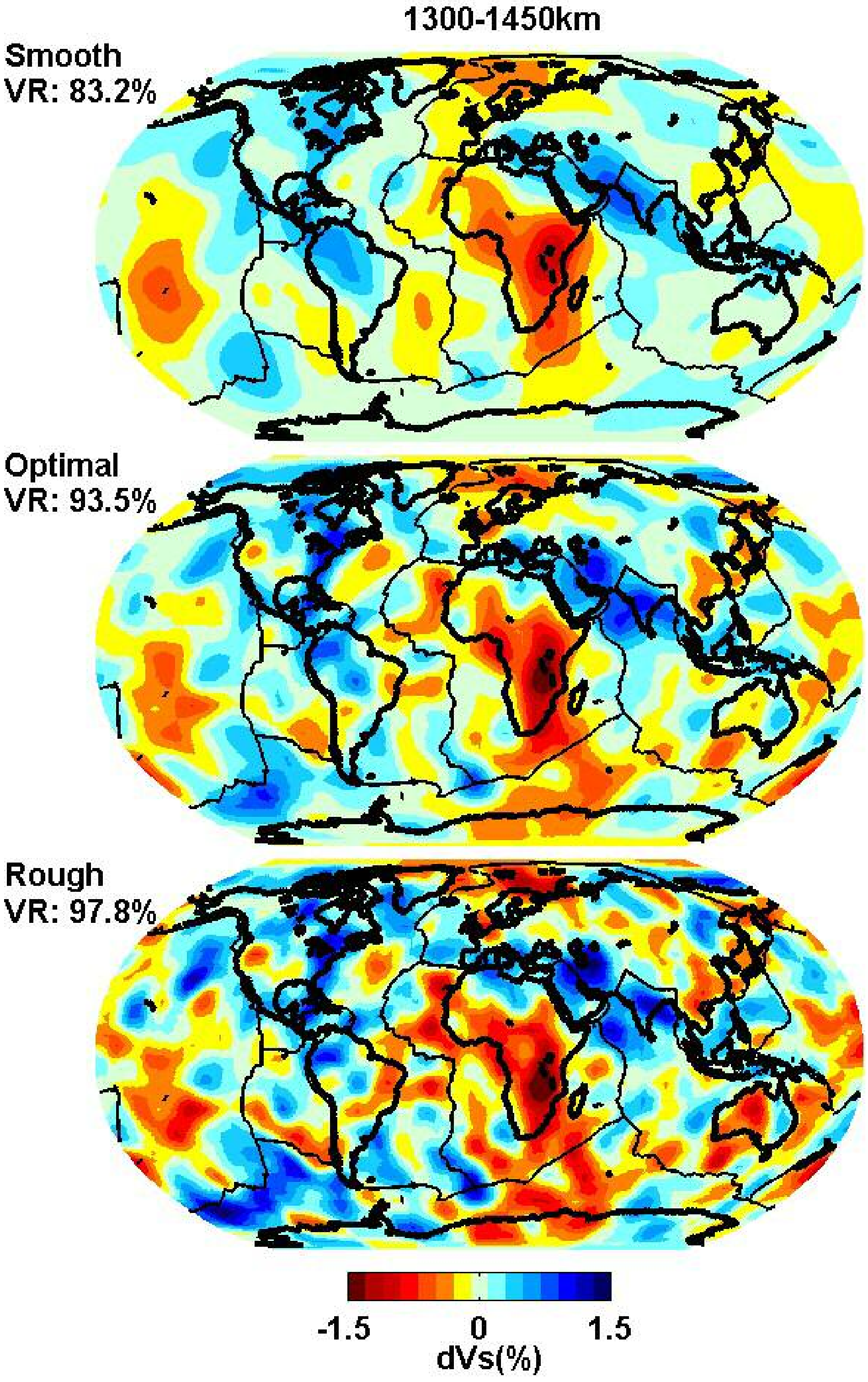

Figure C1 (continued)

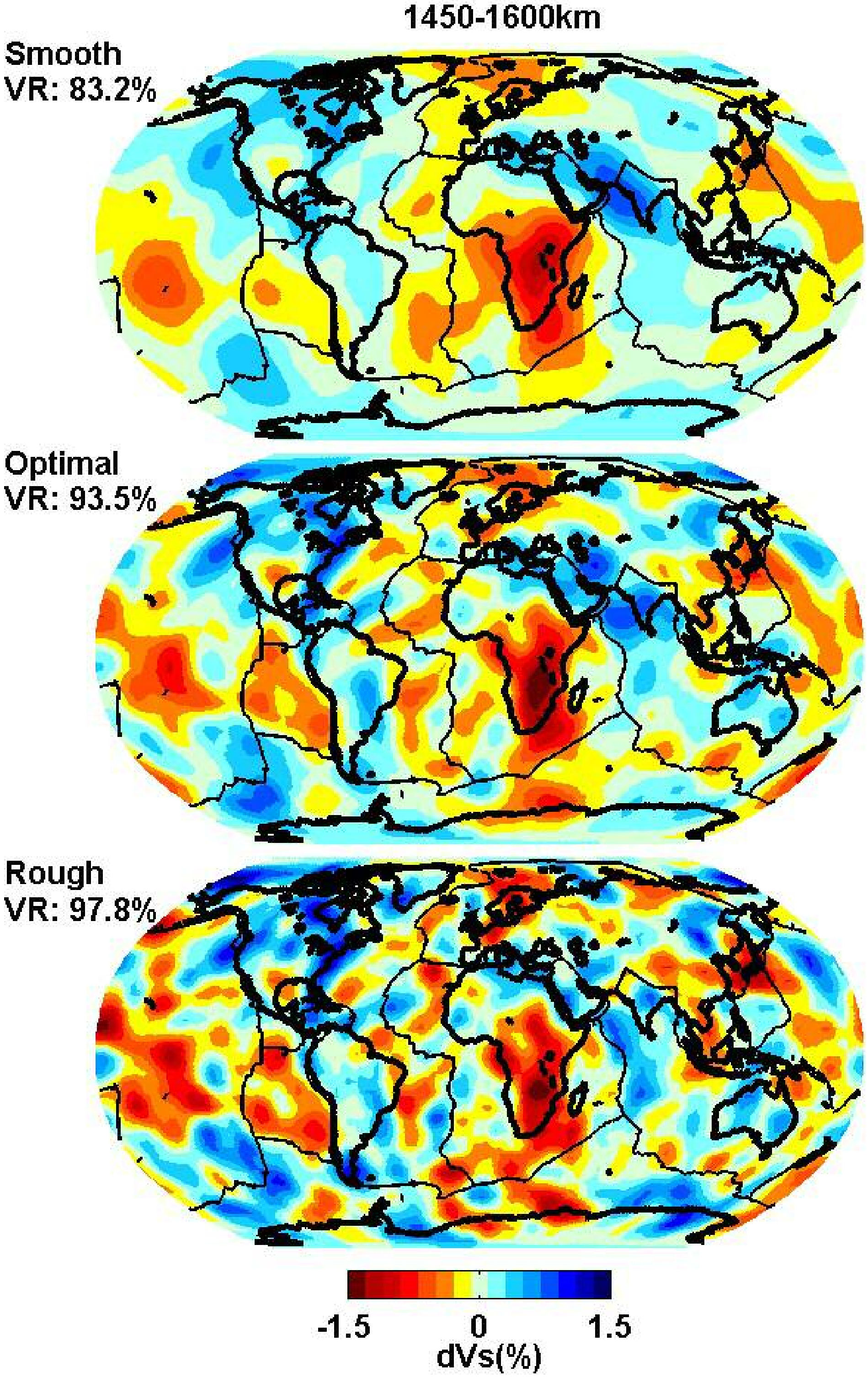

Figure C1 (continued)

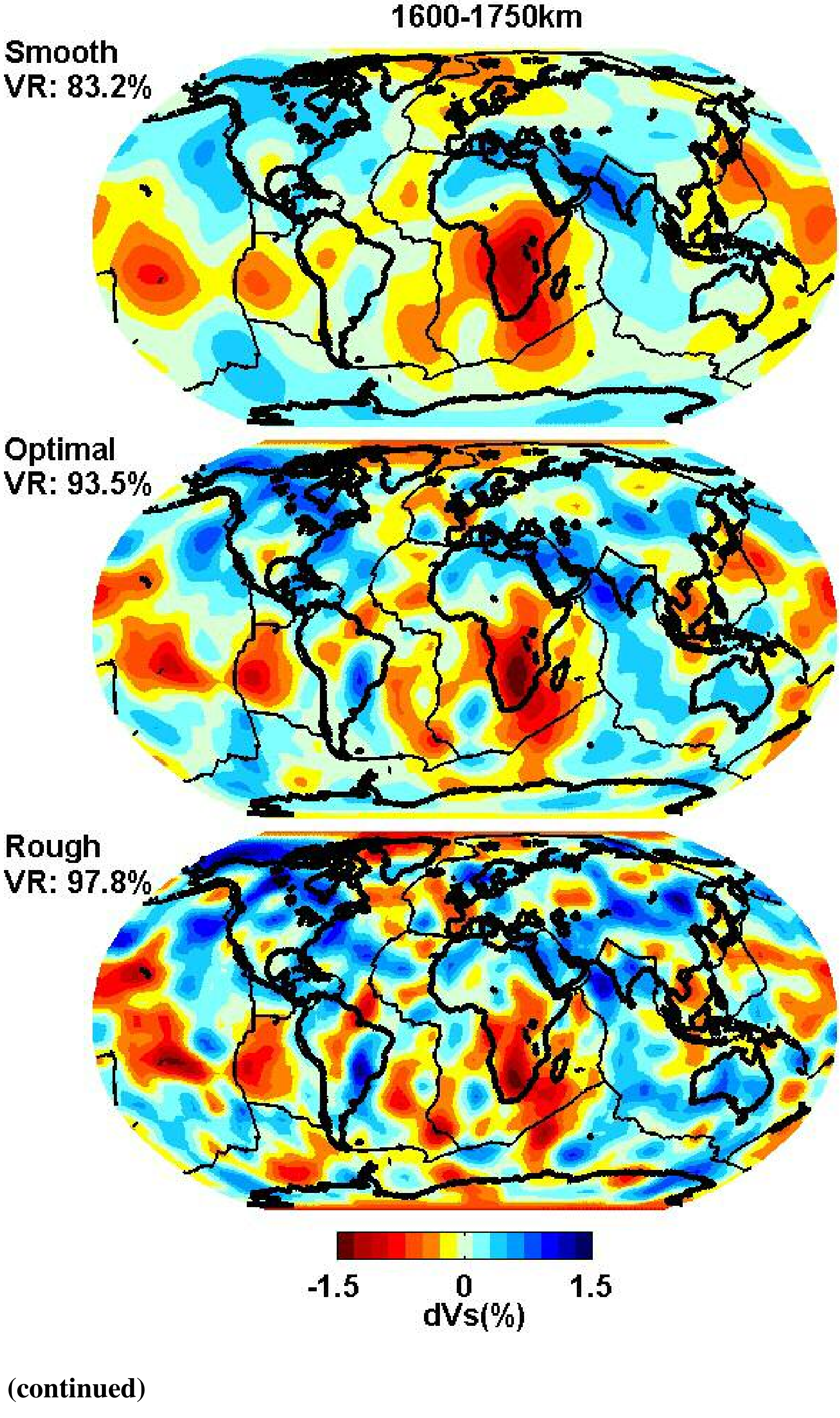

Figure C1 (continued)

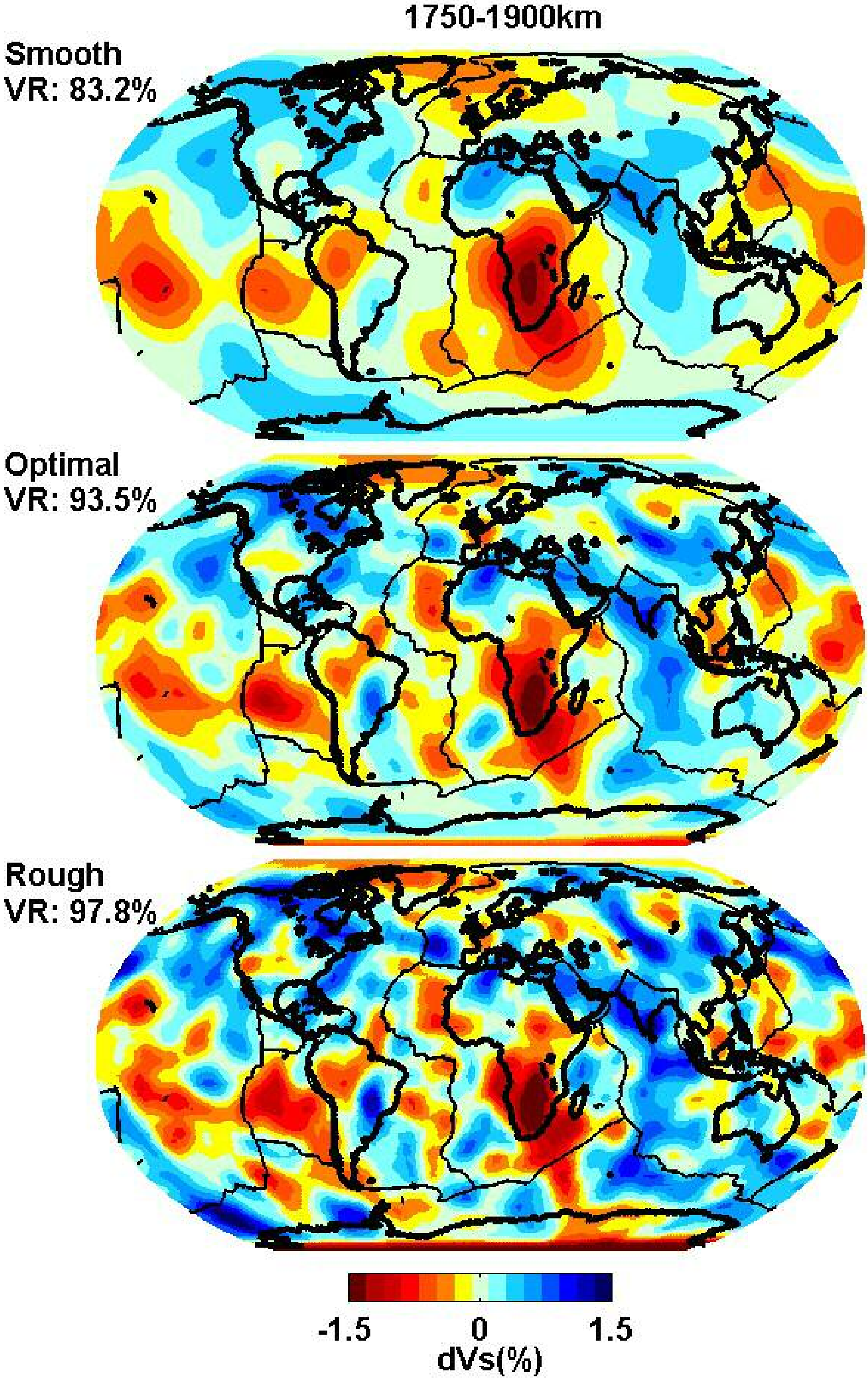

Figure C1 (continued)

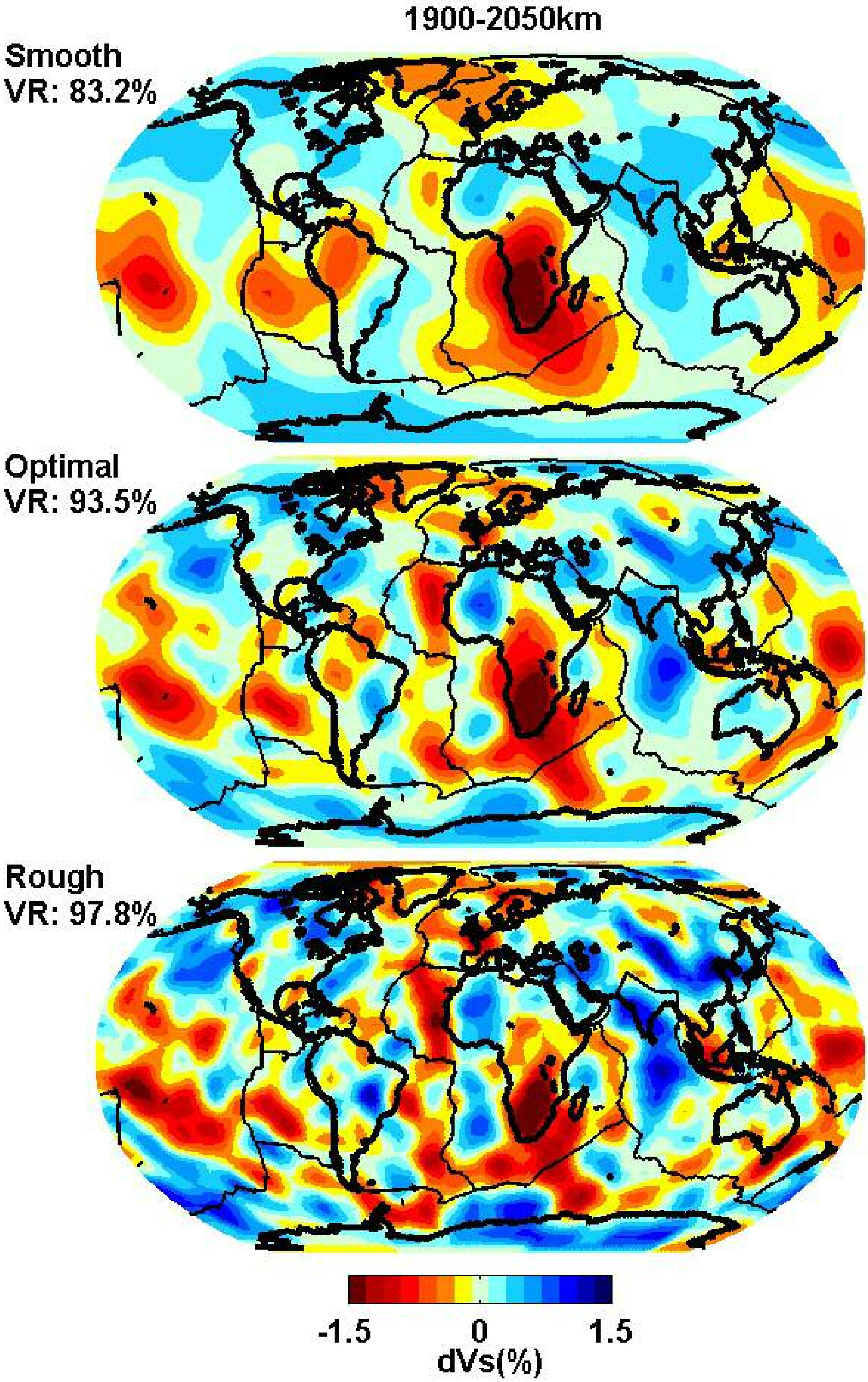

Figure C1 (continued)

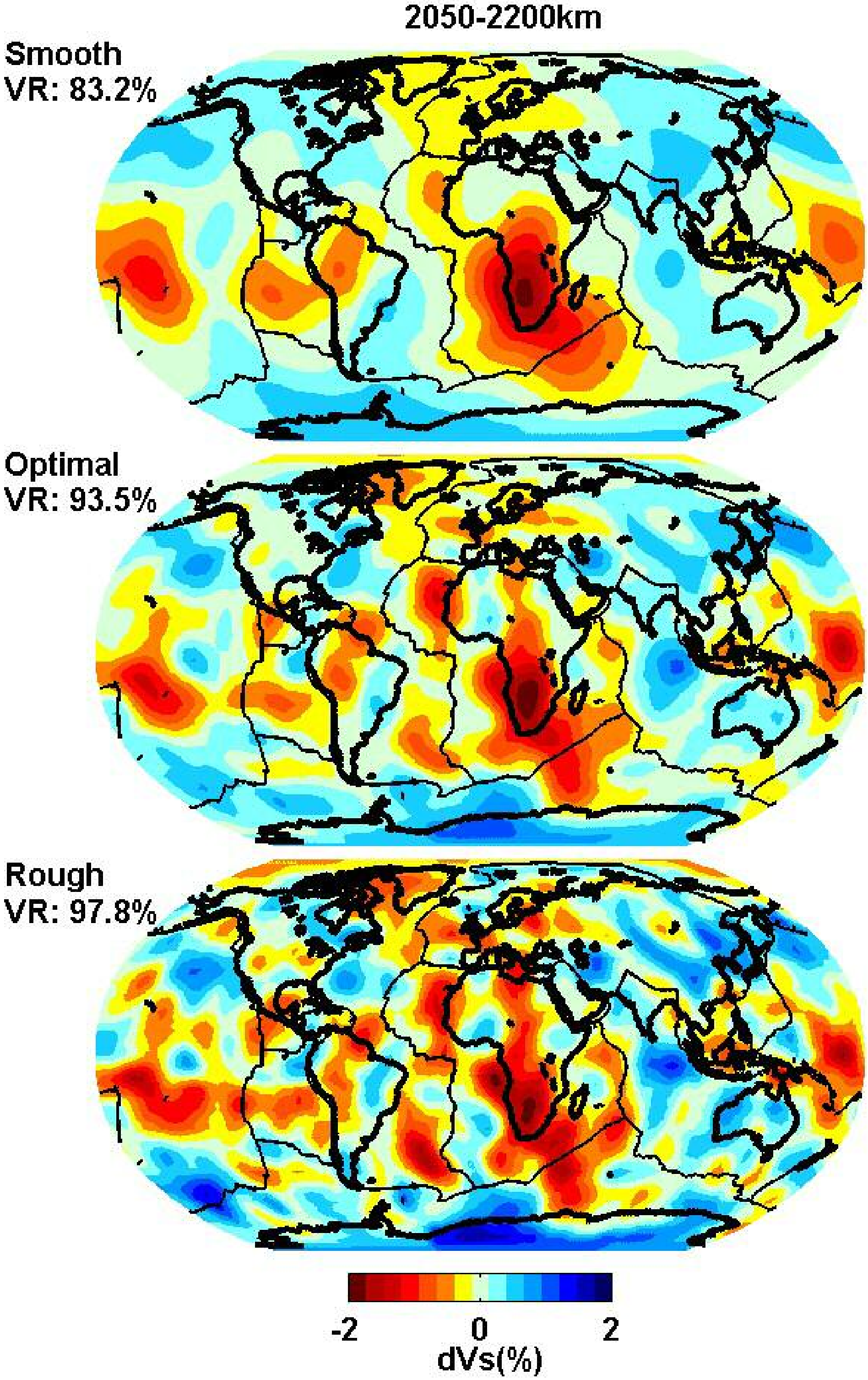

Figure C1 (continued)

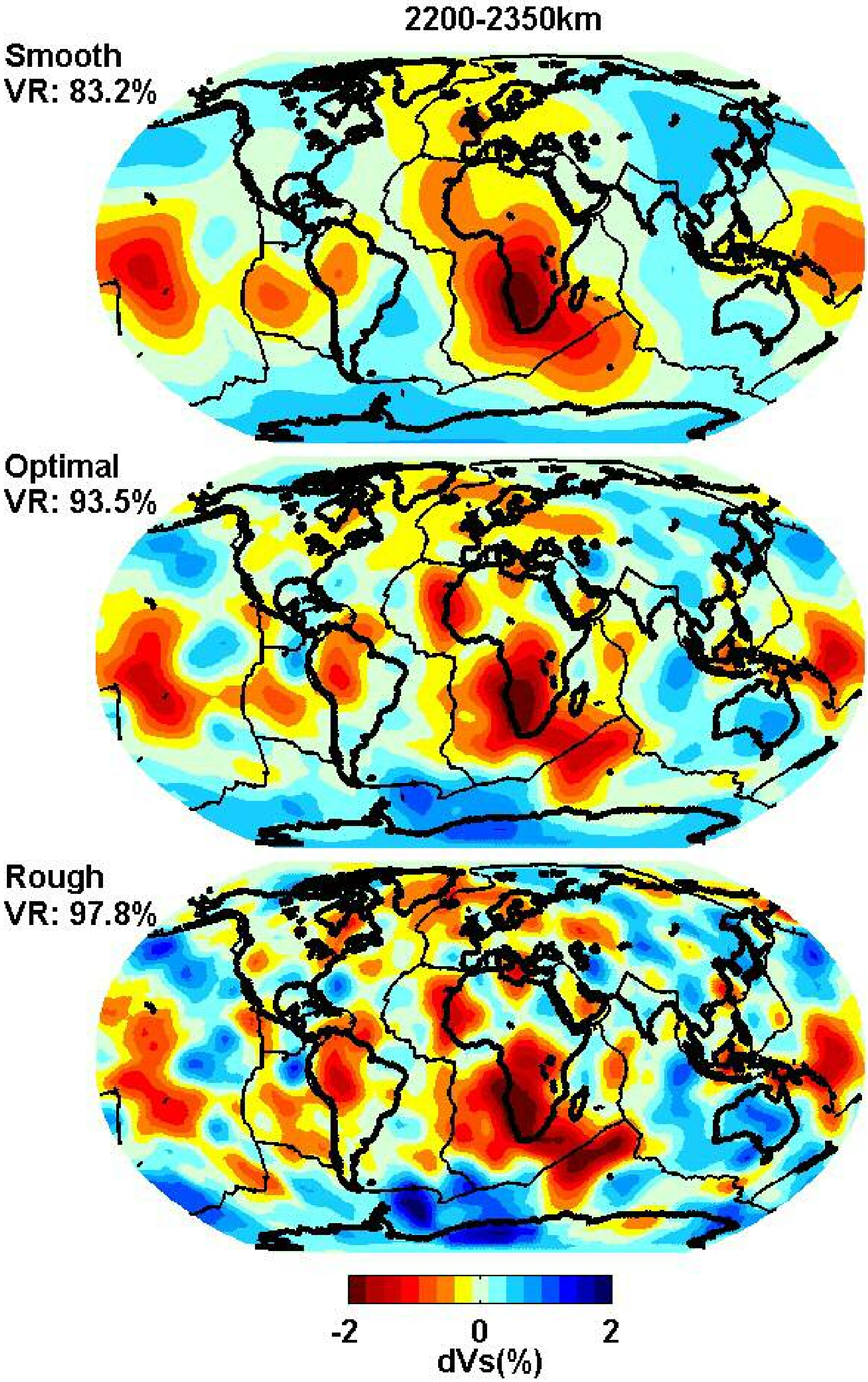

Figure C1 (continued)

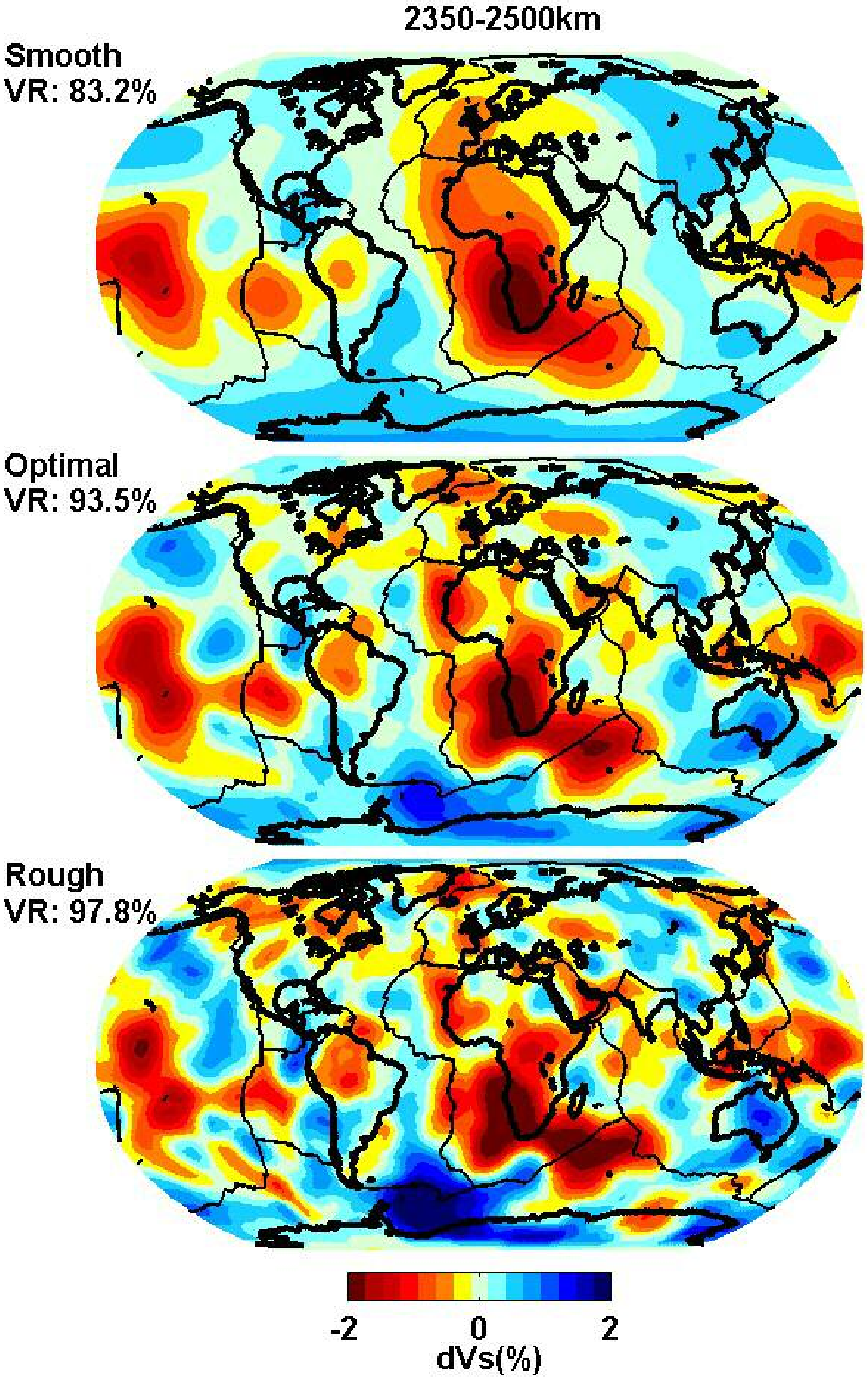

Figure C1 (continued)

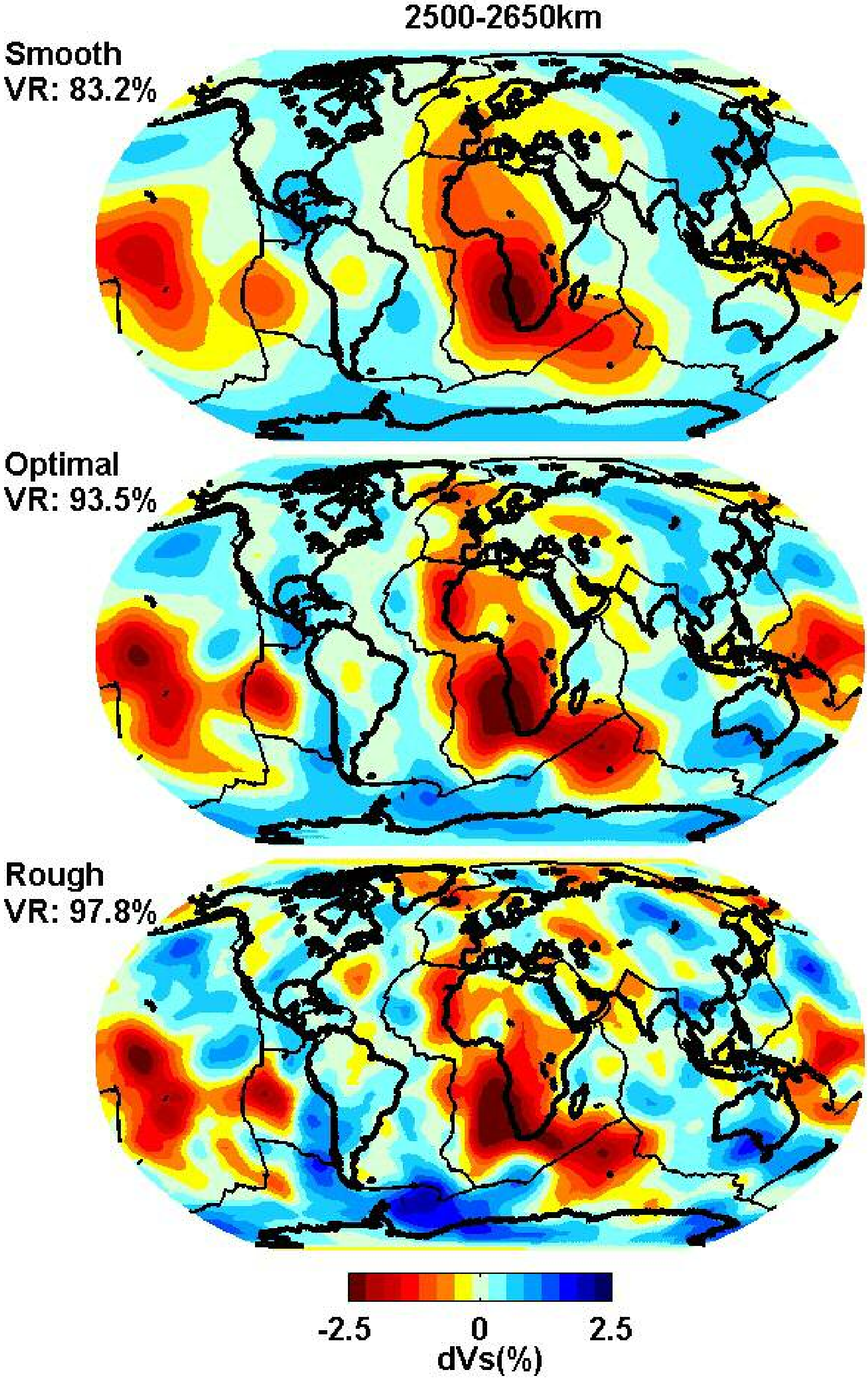

Figure C1 (continued)

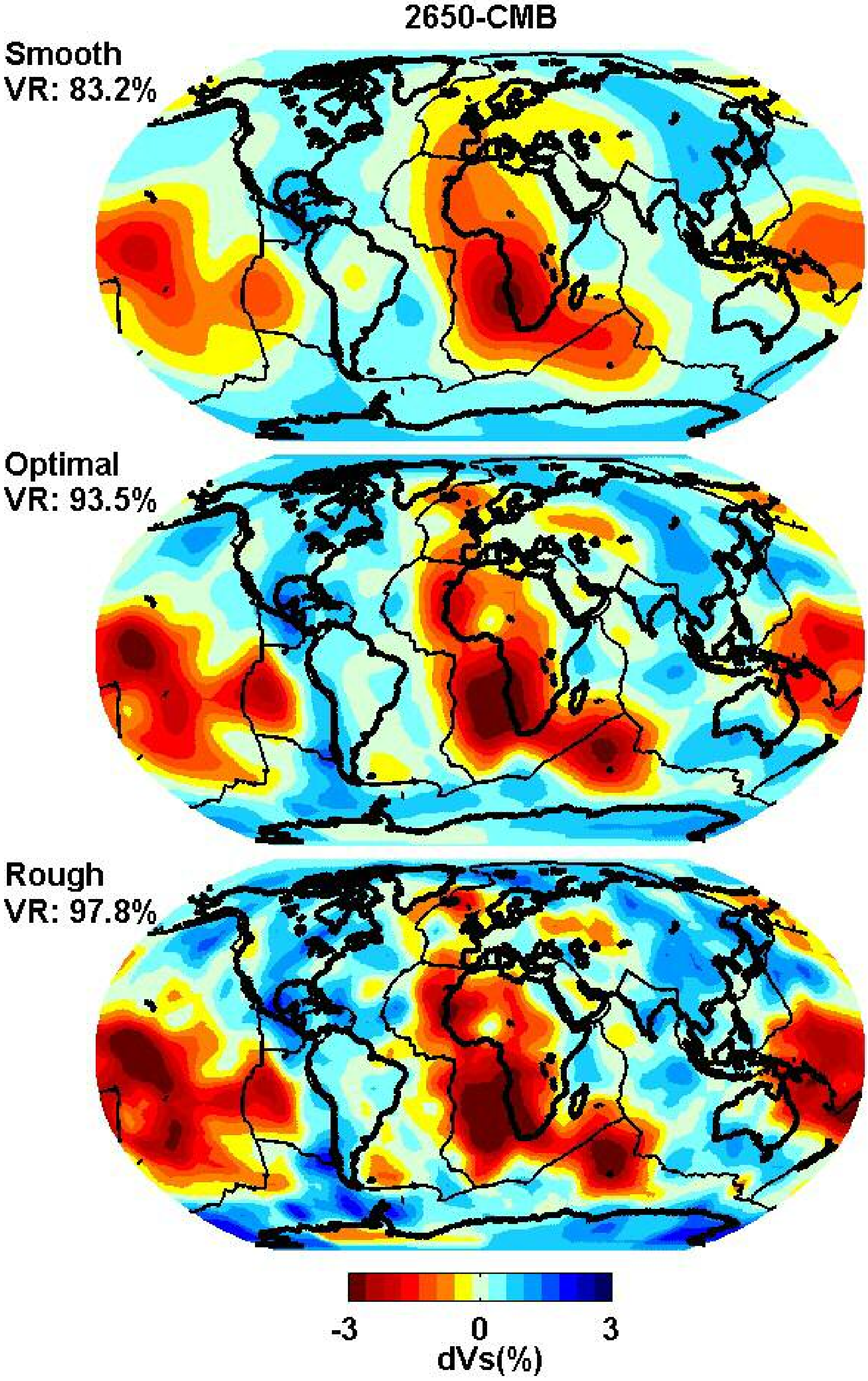

Figure C1 (continued)

Appendix D

Comparison of Seismic and Joint Velocity Models

The following set of images illustrate the shear-wave velocity model produced using only the seismic data (Chapter 2) compared to the jointly derived model described in Chapter 5. For each selected depth range, the top panel contains the purely seismic model, the middle panel illustrates the final joint model and the bottom panel is the model difference (joint – seismic). Full descriptions of the development of each model can be found in the text.

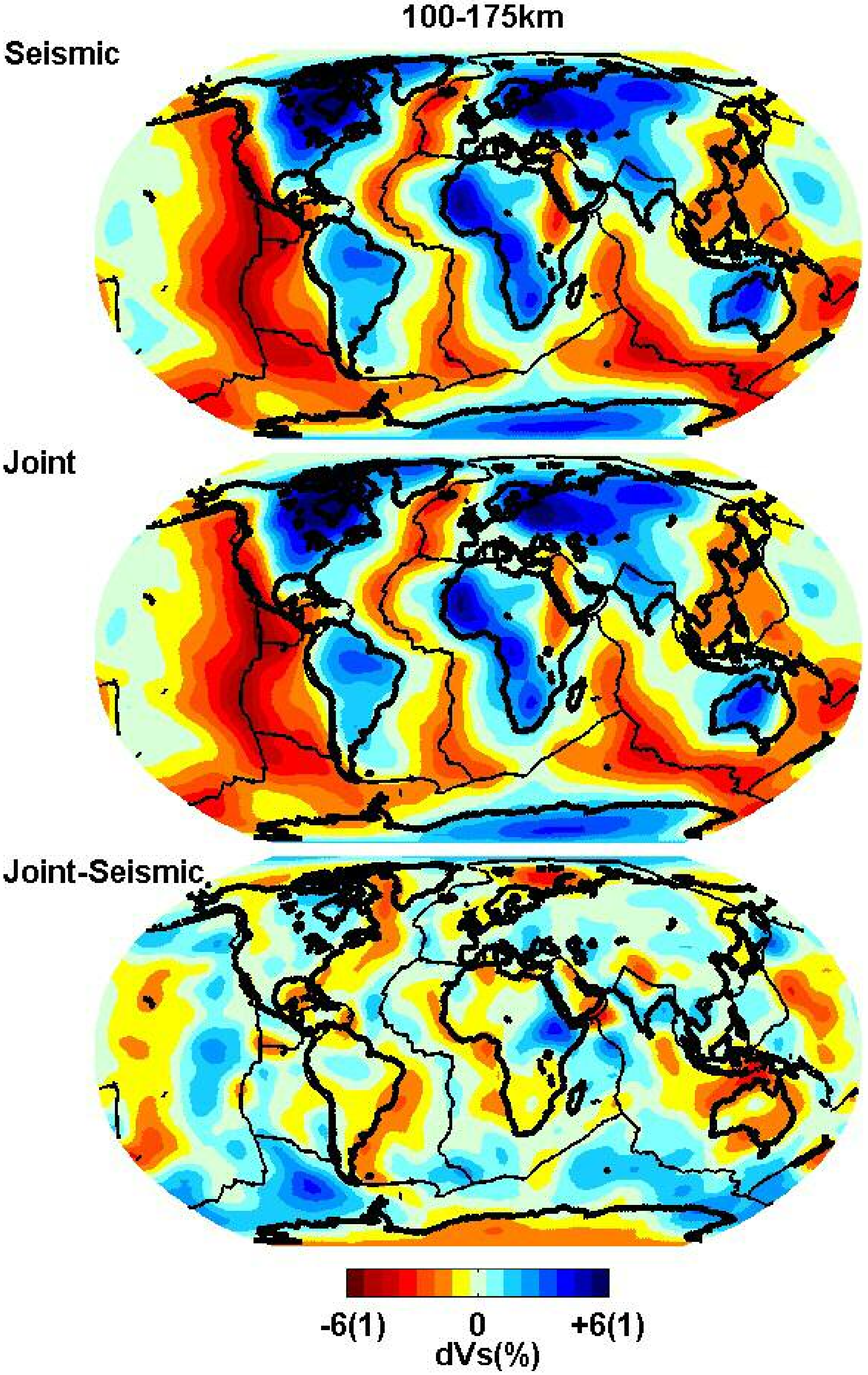

Figure D1 Comparison of seismic and joint shear-wave velocity models at 100-175km depth. Note that the amplitude scales for the upper two panels are ±6% and the bottom panel is ±1% (shown in parentheses).

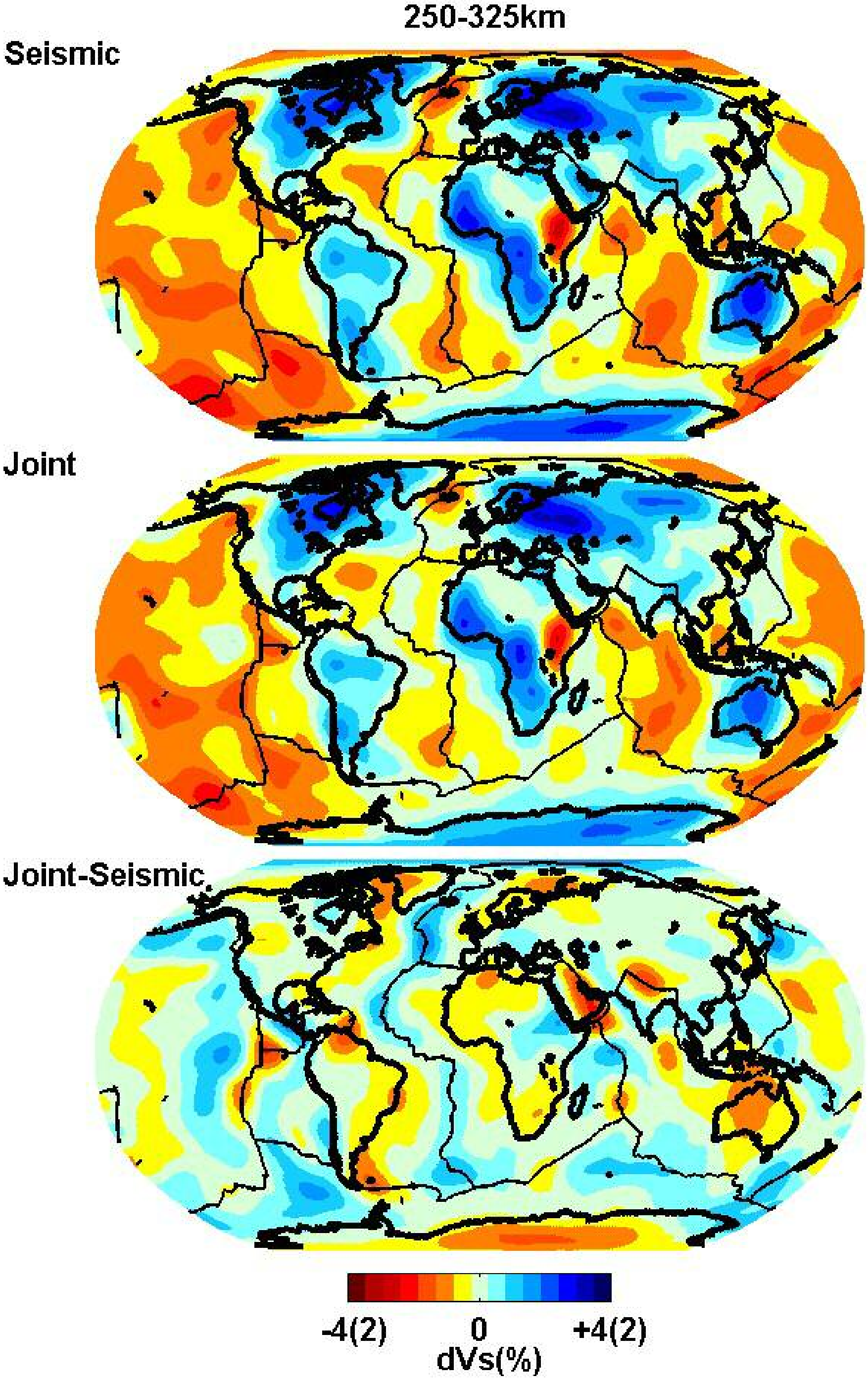

Figure D1 (continued) Comparison of seismic and joint shear-wave velocity models at 250-325km depth. Note that the amplitude scales for the upper two panels are ±4% and the bottom panel is ±2% (shown in parentheses).

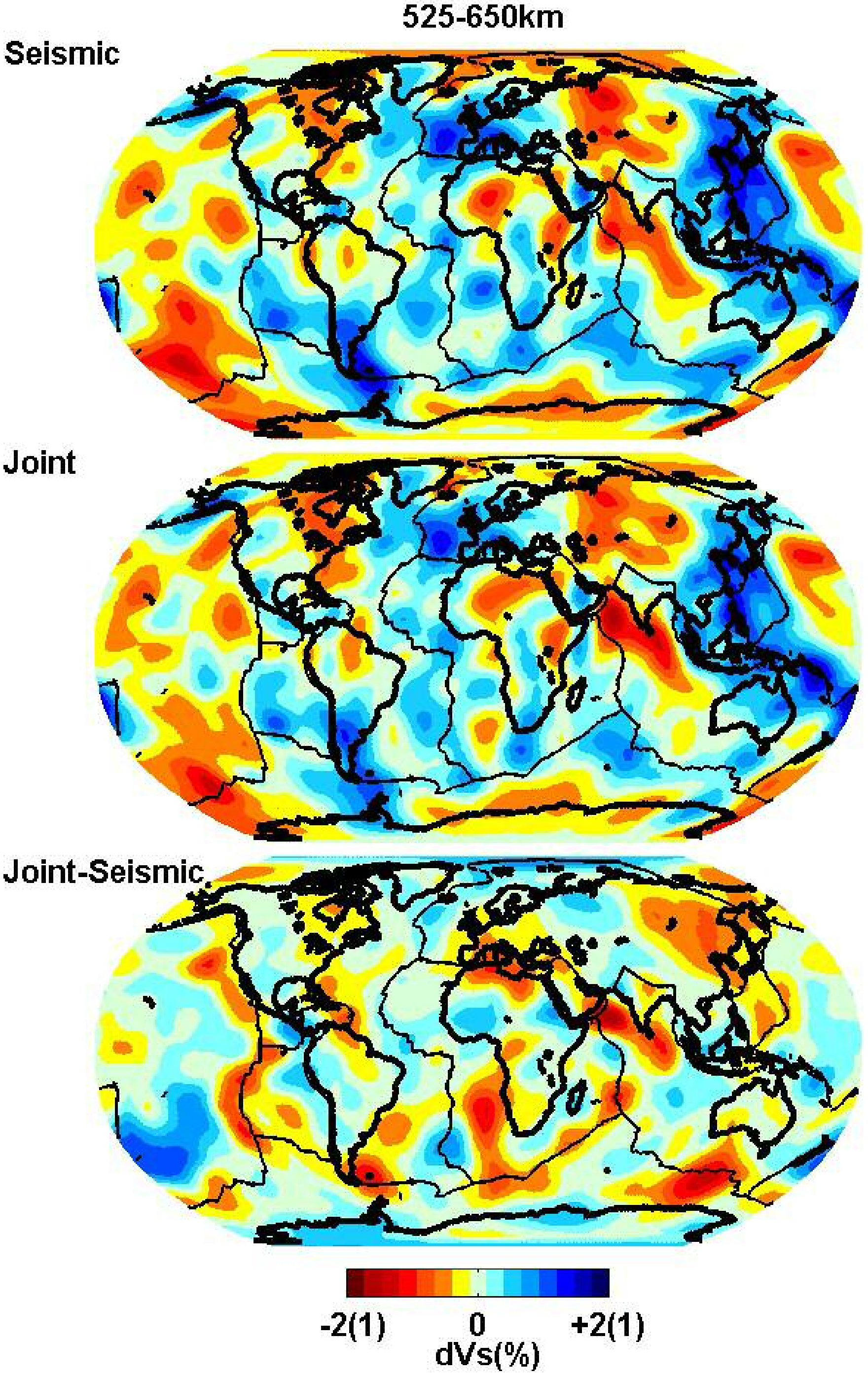

Figure D1 (continued) Comparison of seismic and joint shear-wave velocity models at 525-650km depth. Note that the amplitude scales for the upper two panels are ±2% and the bottom panel is ±1% (shown in parentheses).

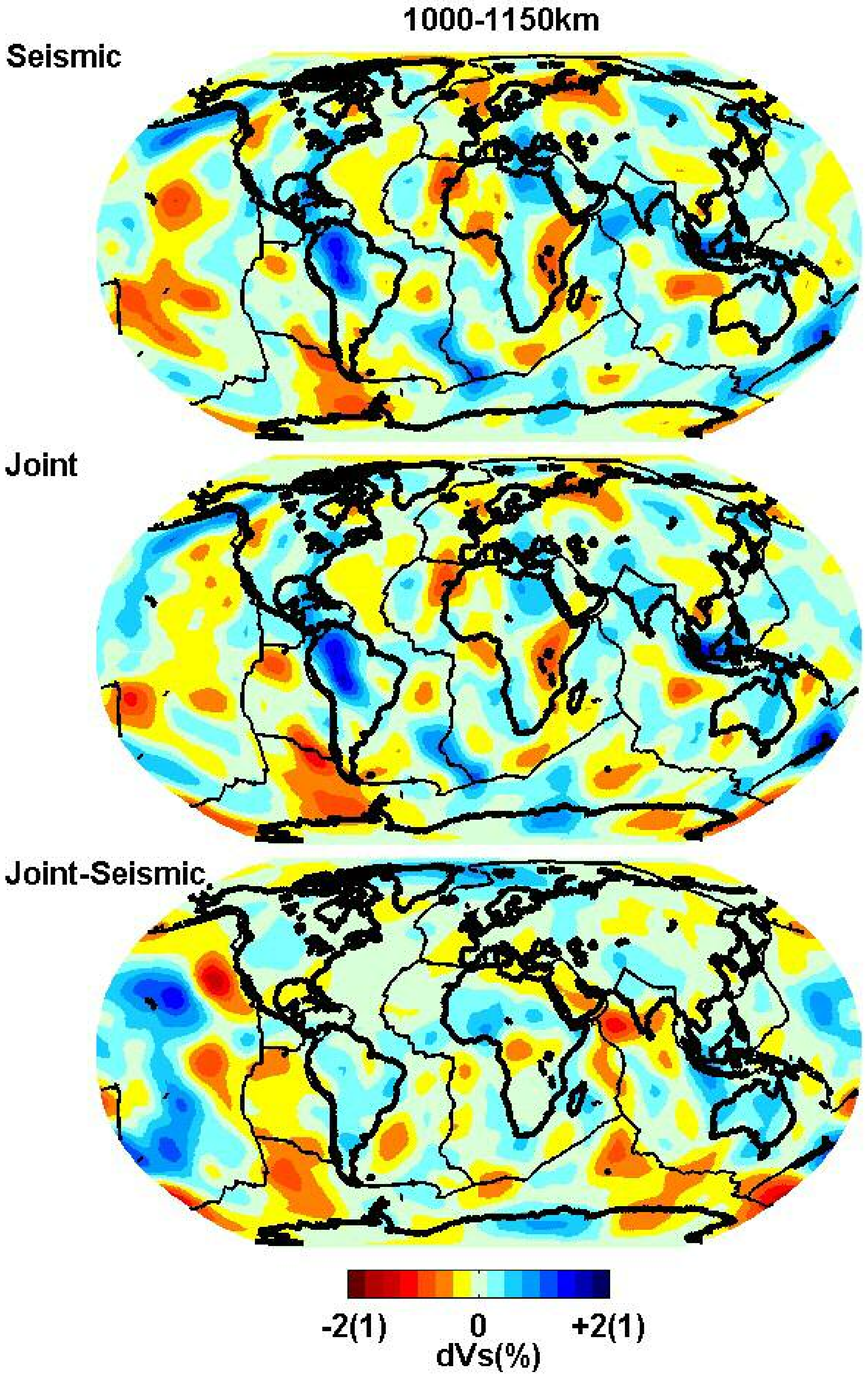

Figure D1 (continued) Comparison of seismic and joint shear-wave velocity models at 1000-1150km depth. Note that the amplitude scales for the upper two panels are ±2% and the bottom panel is ±1% (shown in parentheses).

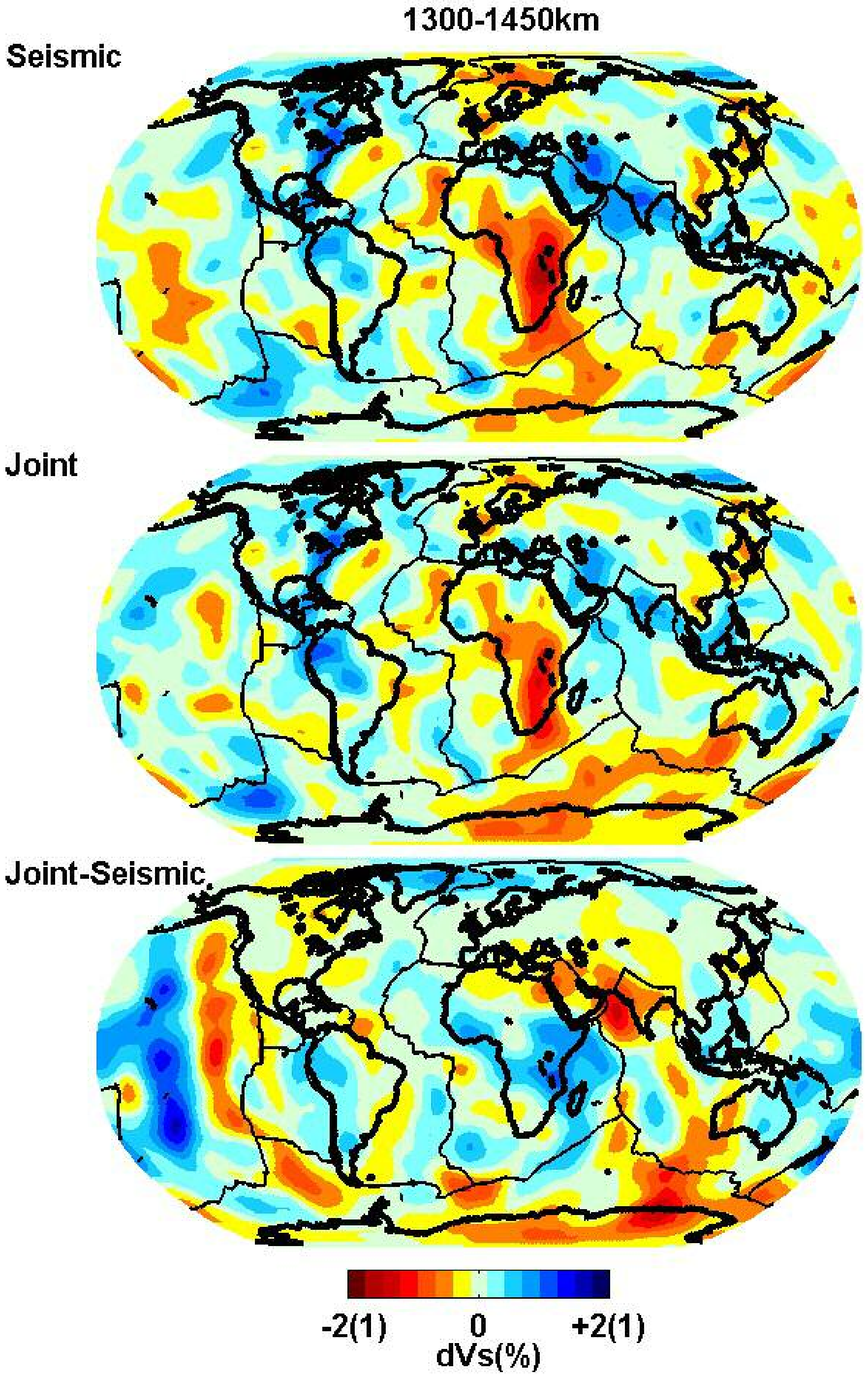

Figure D1 (continued) Comparison of seismic and joint shear-wave velocity models at 1300-1450km depth. Note that the amplitude scales for the upper two panels are ±2% and the bottom panel is ±1% (shown in parentheses).

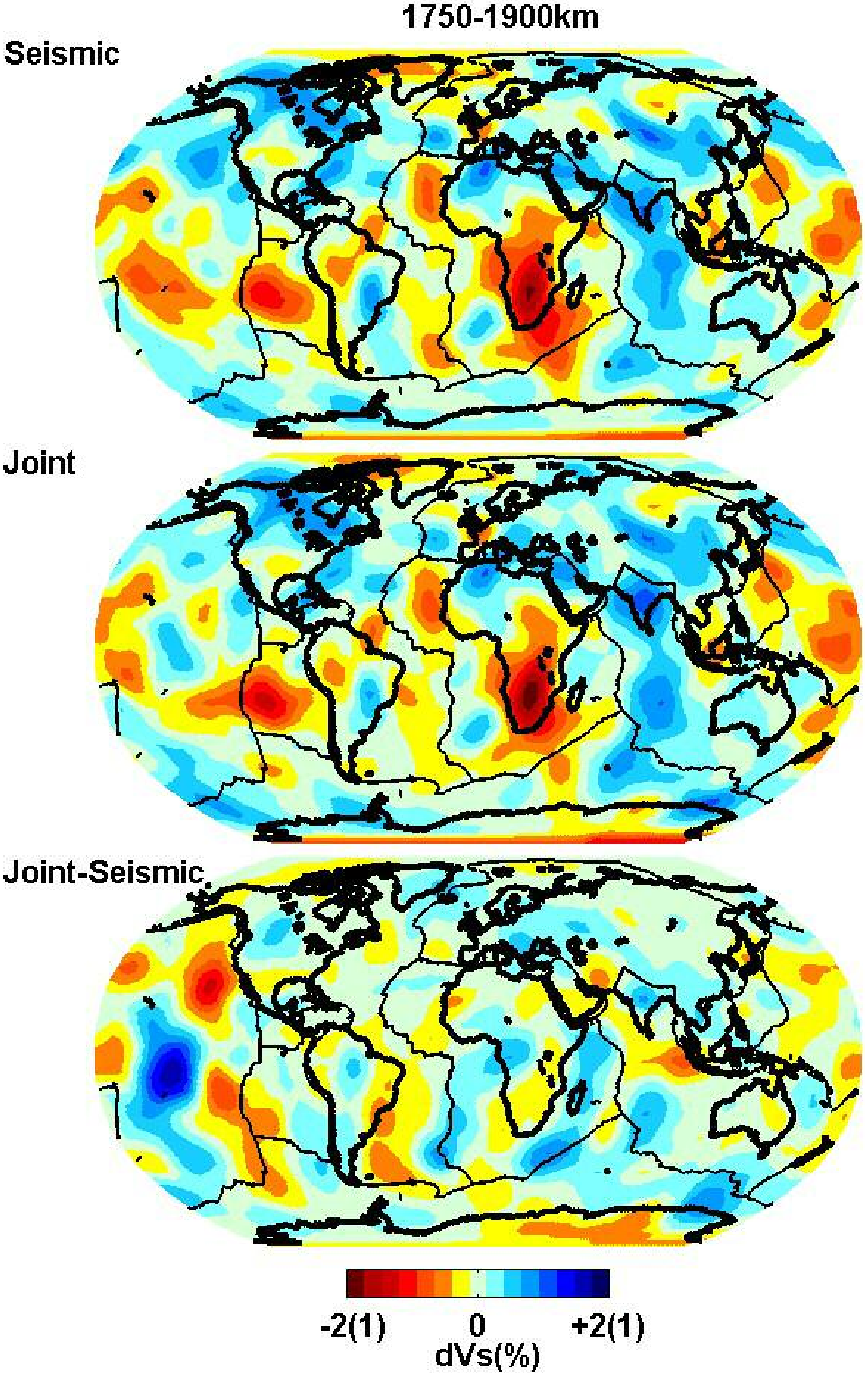

Figure D1 (continued) Comparison of seismic and joint shear-wave velocity models at 1750-1900km depth. Note that the amplitude scales for the upper two panels are ±2% and the bottom panel is ±1% (shown in parentheses).

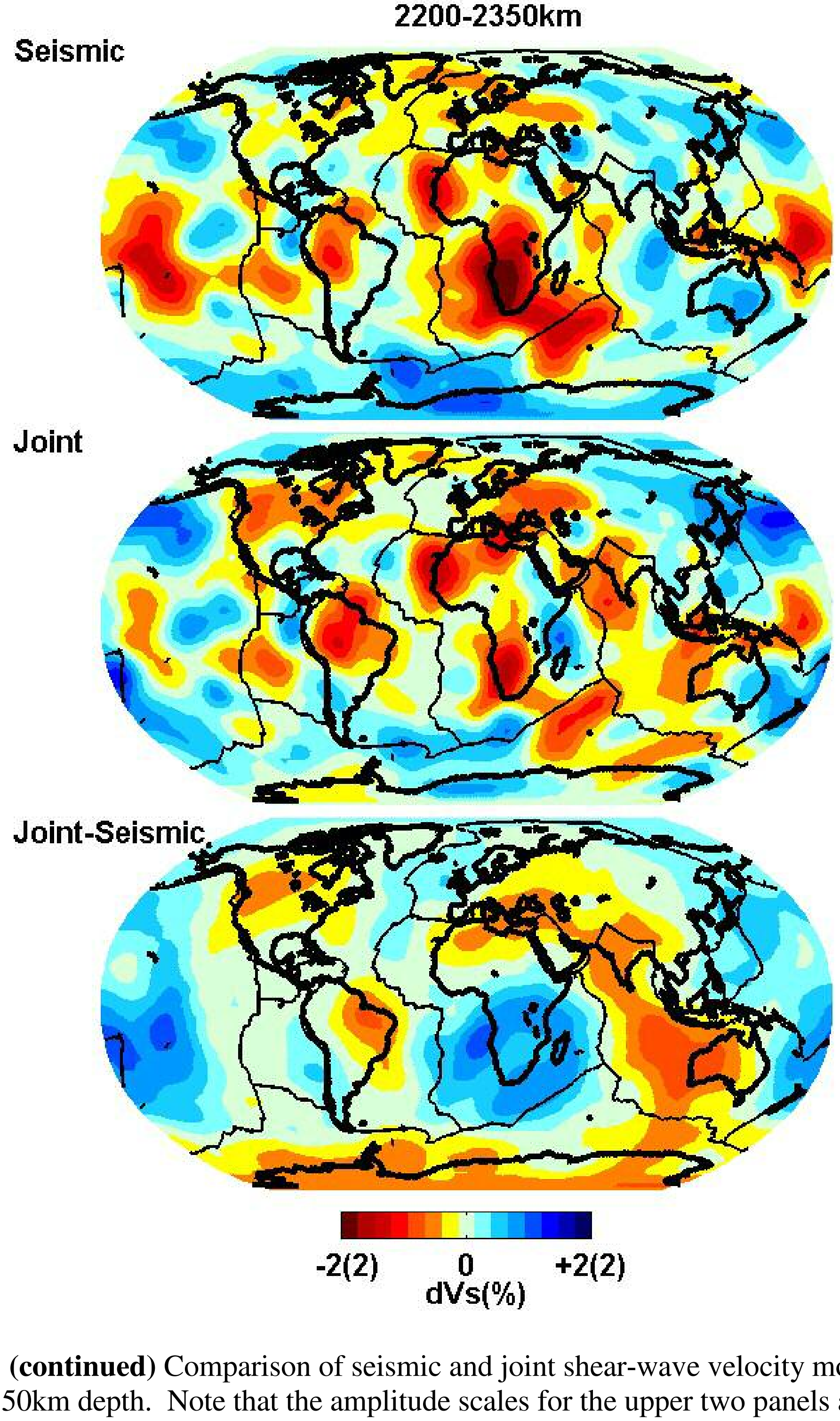

Figure D1 (continued) Comparison of seismic and joint shear-wave velocity models at 2200-2350km depth. Note that the amplitude scales for the upper two panels are ±2% and the bottom panel is ±2% (shown in parentheses).

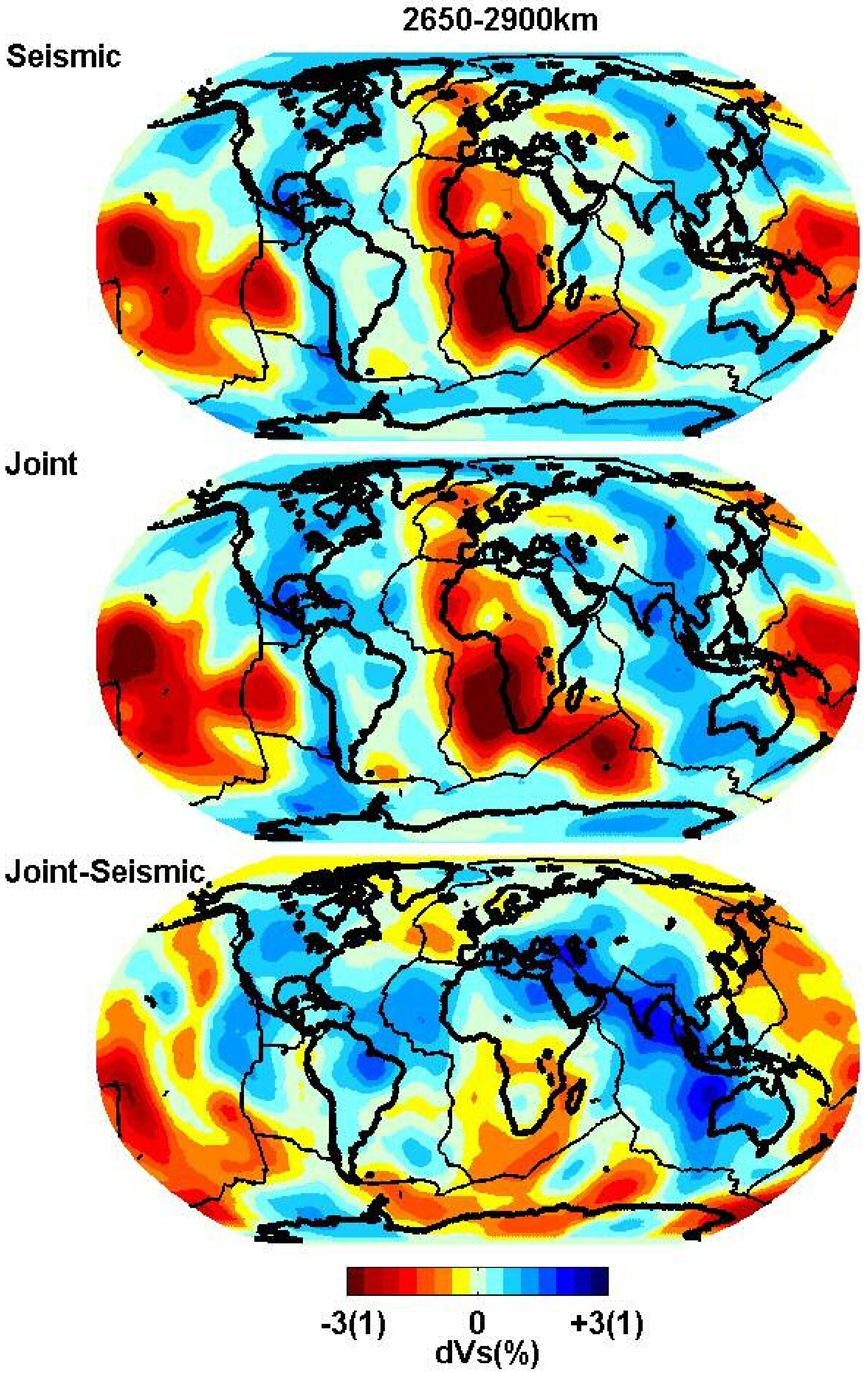

Figure D1 (continued) Comparison of seismic and joint shear-wave velocity models in the D'' layer. Note that the amplitude scales for the upper two panels are ±3% and the bottom panel is ±1% (shown in parentheses).

Reference List

Aki, K., A. Christofferson & E.S. Husebye (1977), Determination of the three-dimensional seismic structure of the lithosphere, *J. Geophys. Res.*, *82*, 277-296.

Bassin, C., G. Laske & G. Masters (2000), The current limits of resolution for surface wave tomography in North America, EOS Trans AGU 81(48) 897.

Čadek, O., L. & Fleitout (1999), A global geoid model with imposed plate velocities and partial layering, *J. Geophys. Res. 104*, 29055-29075.

Čadek, O., L. & Fleitout (2003), Effect of lateral viscosity variations in the top 300 km on the geoid and dynamic topography, *Geophys. J. Int. 152*, 566-580.

Cammarano, F., S. Goes, P. Vacher & D. Giardini (2003), Inferring upper-mantle temperatures from seismic velocities, *Phys. Earth Planet. Inter.*, *138*(3-4), 197-222.

Chapman, C.H. (1978), A new method for computing synthetic seismograms, *Geophys. J. R. Astron. Soc.*, *54*, 481-518.

Chopelas, A. & R. Boehler (1992), Thermal expansivity in the lower mantle, *Geophys. Res. Lett.*, *19*, 1983-1986.

Čižková, H. O. Čadek, A.P. Van den Berg & N.J. Vlaar (1999), Can lower mantle slab-like seismic anomalies be explained by thermal coupling between the upper and lower mantles?, *Geophys. Res. Lett. 26*, 1501-1504.

Constable, S.C. R.L. Parker & C.G. Constable (1987), Occam's inversion; a practical algorithm for generating smooth models from electromagnetic sounding data, *Geophys. 52*, 289-300.

Davaille, A., M. Le Bars & C. Carbonne (2003), Thermal convection in a heterogeneous mantle, *C. R. Geoscience*, *335*(1), 141-156.

DeMets, C.R., Gordon, R.G., Argus, D.F. & S. Stein (1990), Current plate motions, *Geophys. J. Int.*, *101*(2), 425-478.

Dziewonski, A.M. & F. Gilbert (1976), The effect of small, aspherical perturbations on travel times and a re-examination of the corrections for ellipticity, *Geophys. J. R. Astron. Soc. 44*, 7-17.

Dziewonski, A.M. & D.L. Anderson (1981), Preliminary reference Earth model, *Phys. Earth Planet. Inter.*, *25*, 297-356.

Dziewonski, A.M. (1984), Mapping the lower mantle: determination of lateral heterogeneity in P velocity up to degree and order 6, *J. Geophys. Res.*, *89*, 5929-5952.

Forte, A.M. & W.R. Peltier (1987), Plate tectonics and aspherical Earth structure; the importance of poloidal-toroidal coupling, *J. Geophys. Res. 92*, 3645-3679.

Forte, A.M. & W.R. Peltier (1991), Viscous flow models of global geophysical observables; 1, Forward problems, *J. Geophys. Res. 96*, 20131-20159.

Forte, A.M. & W.R. Peltier (1994), The kinematics and dynamics of poloidal-toroidal coupling in mantle flow; the importance of surface plates and lateral viscosity variations, *Adv. Geophys. 36*, 1-119.

Forte, A.M., R.L. Woodward & A.M. Dziewonski (1994), Joint inversions of seismic and geodynamic data for models of three-dimensional mantle heterogeneity, *J. Geophys. Res. 99*, 21857-21877.

Forte, A.M. & R.L. Woodward (1997), Seismic-geodynamic constraints on three-dimensional structure, vertical flow, and heat transfer in the mantle, *J. Geophys. Res. 102*, 17981-17994.

Forte, A.M. (2000), Seismic-geodynamic constraints on mantle flow: implications for layered convection, mantle viscosity, and seismic anisotropy in the deep mantle, *in Earth's Deep Interior: Mineral Physics and Tomography from the Atomic to the Global Scale*, edited by S.-I. Karato et al., pp. 3-36, AGU, Washington, DC.

Forte, A.M. & H.K.C. Perry (2000), Geodynamic evidence for a chemically depleted continental tectosphere, *Science*, *290*, 1940-1944.

Forte, A.M. & J.X. Mitrovica (2001), Deep-mantle high-viscosity flow and thermochemical structure inferred from seismic and geodynamic data, *Nature*, *410*(6832), 1049-1056.

Forte, A.M., J.X. Mitrovica, R. Moucha, N.A. Simmons & S.P. Grand (2007), Descent of the ancient Farallon slab drives localized mantle flow below the New Madrid seismic zone, *Geophys. Res. Lett.*, *34*, doi: 10.1029/2006GL027895.

Fuchs, K. & G. Muller (1971), Computation of synthetic seismograms with the reflectivity method and comparison with observations, *Geophys. J. R. Astron. Soc. 23*, 417-433.

Fukao, Y., S. Widiyantoro, M. Obayashi (2001), Stagnant slabs in the upper mantle transition region, *Rev. Geophys. 39*, 291-323.

Grand, S.P. & D.V. Helmberger (1984), Upper mantle shear structure of North America, *Geophys. J. R. Astron. Soc*. 76, 399-438.

Grand, S.P. (1994), Mantle shear structure beneath the Americas and surrounding oceans, *J. Geophys. Res.*, *99*, 11591-11621.

Grand, S.P., R.D. Van der Hilst & S. Widiyantoro (1997), Global seismic tomography: a snapshot of convection in the Earth, *GSA Today*, *7*, 1-7.

Grand, S.P. (2002), Mantle shear-wave tomography and the fate of subducted slabs, *Phil. Trans. R. Soc. Lond. A*, *360*(1800), 2475-2491.

Gu, Y.J., A.M. Dziewonski, W. Su & G. Ekstrom (2001), Models of the mantle shear velocity and discontinuities in the pattern of lateral heterogeneities, *J. Geophys. Res.*, *106*, 11169-11199.

Gurnis, M., J.X. Mitrovica, J. Ritsema & H.J. Van Heijst (2000), Constraining mantle density structure using geological evidence of surface uplift rates: The case of the African Superplume, *Geochem. Geophys. Geosys.*, *1*(7), doi: 1999GC000035.

Hamilton, W.B. (2002), The closed upper-mantle circulation of plate tectonics, in S. Stein, J.T. Freymueller (Eds.), Plate Boundary Zones, AGU, Washington, DC, pp. 359-410.

Hansen, P.C. (1992), Analysis of discrete ill-posed problems by means of the L-curve, *SIAM Rev.*, *34*, 561-580.

Helmberger, D.V., S. Ni, L. Wen & J. Ritsema (2000), Seismic evidence for ultralow-velocity zones beneath Africa and eastern Atlantic, *J. Geophys. Res.*, *105*, 23865-23878.

Herring, T.A., P.M. Mathews & B.A. Buffett (2002), Modeling of nutation-precession; very long baseline interferometry results, *J. Geophys. Res. Solid Earth*, *107*(B4), doi: 10.1029/2001JB000165.

Hofmann, A.W. (1997), Mantle geochemistry: the message from oceanic volcanism, *Nature 385*, 219-229.

Ishii, M. & J. Tromp (1999), Normal-mode and free-air gravity constraints on lateral variations in velocity and density of Earth's mantle, *Science*, *285*(5431), 1231-1236.

Ishii, M. & J. Tromp (2004), Constraining large-scale mantle heterogeneity using mantle and inner-core sensitive normal modes, *Phys. Earth Planet. Inter.*, *146*(1-2), 113-124.

Jordan, T.H. (1978), Composition and development of the continental tectosphere, *Nature*, *274*, 544-548.

Jordan, T.H. (1981), Continents as a chemical boundary layer, *Phil. Trans. Roy. Soc. London A*, *301*(1461), 359-373.

Karason, H. & R.D. van der Hilst (2000), Constraints on mantle convection from seismic tomography, in: M.R. Richards, M.R. Gordon, R.D. van der Hilst (Eds.), The History and Dynamics of Global Plate Motion, AGU, Washington, DC, pp. 277-288.

Karato, S.I. (1993), Importance of anelasticity in the interpretation of seismic tomography, *Geophys. Res. Lett.*, *20*, 1623-1626.

Karato, S.-I. & P. Wu (1993), Rheology of the upper mantle; a synthesis, *Science 260*, 771-778.

Karato, S.I. & B.B. Karki (2001), Origin of lateral variation of seismic wave velocities and density in the deep mantle, *J. Geophys. Res. Solid Earth*, *106*(B10), 21771-21783.

Kawakatsu, H. & F. Niu (1994), Seismic evidence for 920-km discontinuity in the mantle, *Nature 371*, 301-305.

Kellogg, L.H., B.H. Hager & R.D. Van der Hilst (1999), Compositional stratification in the deep mantle, *Science*, *283*(5409), 1181-1184.

Kennett, B.L.N. & A. Gorbatov (2004), Seismic heterogeneity in the mantle—strong shear wave signature of slabs from joint tomography, *Phys. Earth Planet. Inter.*, *146*, 87-100.

Lay, T. & T. C. Wallace (1995), “Modern Global Seismology”, Academic Press, San Diego, 521pp.

Le Stunff, Y. & Y. Ricard (1997), Partial advection of equidensity surfaces: A solution for the dynamic topography problem? *J. Geophys. Res. 102*, 24655-24667.

Lithgow-Bertelloni, C. & P.G. Silver (1998), Dynamic topography, plate driving forces and the African superswell, *Nature*, *395*(6699), 269-272.

Loper, D.E. & T. Lay (1995), The core-mantle boundary region, *J. Geophys. Res.*, *100*, 6397-6420.

Machetel, P. & P. Weber (1991), Intermittent layered convection in a model mantle with and endothermic phase change at 670 km, *Nature 350*, 55-57.

Marsh, J.G., *et al*. (1990), The GEM-T2 gravitational model, *J. Geophys. Res. Solid Earth*, *95*(13), 22043-22071.

Masters, G., G. Laske, H. Bolton & A.M. Dziewonski (2000), The relative behavior of shear velocity, bulk sound speed, and compressional velocity in the mantle: implications for chemical and thermal structure, *in Earth's Deep Interior: Mineral Physics and Tomography from the Atomic to the Global Scale*, edited by S.-I. Karato et al., pp. 63-87, AGU, Washington, DC.

Mathews, P.M., T.A. Herring & B.A. Buffett (2002), Modeling of nutation and precession: new nutation series for nonrigid Earth and insights into the Earth's interior, *J. Geophys. Res. Solid Earth*, *107*(B4), doi: 10.1029/2001JB000390.

McNamara, A.K. & S. Zhong (2005), Thermochemical structures beneath Africa and the Pacific Ocean, *Nature*, *437*(7062), 1136-1139.

Megnin, C. & B. Romanowicz (2000), The three-dimensional shear velocity structure of the mantle from the inversion of body, surface and higher-mode waveforms}, *Geophys. J. Int.*, *143*, 709-728.

Mitrovica, J.X. & A.M. Forte (1997), Radial profile of mantle viscosity; results from the joint inversion of convection and postglacial rebound observables, *J. Geophys. Res. 102*, 2751-2769.

Mitrovica, J.X. & A.M. Forte (2004), A new inference of mantle viscosity based upon joint inversion of convection and glacial isostatic adjustment data, *Earth Planet. Sci. Lett.*, *225*(1-2), 177-189.

Mitrovica, J.X., A.M. Forte & M. Simons (2000), A reappraisal of postglacial decay times from Richmond Gulf and James Bay, Canada, *Geophys. J. Inter. 142*, 783-800.

Montelli, R., G. Nolet, F.A. Dahlen, G. Masters, R.E. Engdahl & S.H. Hung (2004), Finite-frequency tomography reveals a variety of plumes in the mantle, *Science*, *303*, 338-343.

Mooney, W.D., G. Laske & G. Masters (1998), CRUST 5.1: a global crustal model at 5 x 5 degrees, *J. Geophys. Res. Solid Earth*, *103*(B1), 727-747.

Moucha, R., A.M. Forte, J.X. Mitrovica & A.L. Daradich (2004), Geodynamic implications of convection-related surface observables: the role of lateral variations in mantle rheology, *Eos Trans. AGU 85*, T11E-1325.

Moucha, R., A.M. Forte, J.X. Mitrovica & A.L. Daradich (2005), Geodynamic implications of lateral variations in mantle rheology on convection related observables and inferred viscosity models, *Geophys. J. Inter*. submitted.

Ni, S. & D.V. Helmberger (2001a), Horizontal transition from fast to slow structures at the core-mantle boundary; South Atlantic, *Earth Planet. Sci. Lett.*, *187*, 301-310.

Ni, S. & D.V. Helmberger (2001b), Probing an ultra-low velocity zone at the core mantle boundary with P and S waves, *Geophys. Res. Lett.*, *28*, 2345-2348.

Ni, S.D., E. Tan, M. Gurnis & D.V. Helmberger (2002), Sharp sides to the African superplume, *Science*, *296*(5574), 1850-1852.

Ni, S.D. & D.V. Helmberger (2003a), Ridge-like lower mantle structure beneath South Africa, *J. Geophys. Res. Solid Earth*, *108*(B2), doi:10.1029/2001JB001545.

Ni, S.D. & D.V. Helmberger (2003b), Seismological constraints on the South African superplume; could be the oldest distinct structure on Earth, *Earth Planet. Sci. Lett.*, *206*(1-2), 119-131.

Ni, S.D., D.V. Helmberger & J. Tromp (2005), Three-dimensional structure of the African superplume from waveform modeling, *Geophys. J. Int.*, *161*, 283-294.

Niu, F., H. Kawakatsu (1997), Depth variation of the midmantle seismic discontinuity, *Geophys. Res. Lett. 24*, 429-432.

O'Reilly, S.Y., W.L. Griffin, Y.H. Proudjom & P. Morgan (2001), Are lithospheres forever? Tracking changes in subcontinental lithospheric mantle through time, *GSA Today*, *11*, 4-10.

Paige, C.C. & M.A. Saunders (1982), LSQR: an algorithm for sparse linear equations and sparse least squares, *ACM Transactions on Mathematical Software*, *8*, 43-71.

Panasyuk, S.V. & B.H. Hager (1998), A model of transformational superplasticity in the upper mantle, *Geophys. J. Inter. 133,* 741-755.

Panasyuk, S.V. & B.H. Hager (2000), Inversion for mantle viscosity profiles constrained by dynamic topography and the geoid, and their estimated errors, *Geophys. J. Int. 143*, 821-836.

Panning, M. & B. Romanowicz (2004), Inferences on flow at the base of Earth's mantle based on seismic anisotropy, *Science*, *303*(5656), 351-353.

Perry, H.K.C., D.W.S. Eaton & A.M. Forte (2002), LITH5.0: A revised crustal model for Canada based on Lithoprobe results, *Geophys. J. Int. 150*, 285-294.

Quéré, S. & A.M. Forte (2006), Influence of past and present-day plate motions on spherical models of mantle convection: implications for mantle plumes and hotspots, *Geophys. J. Int.*, *165*, 1041-1057.

Ricard, Y., L. Fleitout & C. Froidevaux (1984), Geoid heights and lithospheric stresses for a dynamic Earth, Ann. *Geophys. 2*, 267-286.

Ricard, Y. & C. Vigny (1989), Mantle dynamics with induced plate tectonics, *J. Geophys. Res. 94*, 17543-17559.

Richards, M.A. & B.H. Hager (1984), Geoid anomalies in a dynamic earth, *J. Geophys. Res. Solid Earth*, *89*(B7), 5987-6002.

Richards, M.A. & D.C. Engebretson (1992), Large-scale mantle convection and the history of subduction, *Nature 355*, 437-440.

Ritsema, J., S. Ni, D.V. Helmberger & H.P. Crotwell (1998), Evidence for strong shear velocity reductions and velocity gradient in the lower mantle beneath Africa, *Geophys. Res. Lett.*, *25*(23), 4245-4248.

Ritsema, J., H.J. Van Heijst & J.H. Woodhouse (1999), Complex shear wave velocity structure imaged beneath Africa and Iceland, *Science*, *286*(5446) 1925-1928.

Robertson, G.S & J.H. Woodhouse (1996), Ratio of relative S to P velocity heterogeneity in the lower mantle, *J. Geophys. Res.*, *101*, 20041-20052.

Romanowicz, B. (2003) Global mantle tomography: progress status in the last 10 years, *Ann. Rev. Earth Plan. 31*, 303-328.

Saltzer, R.L., R.D.Van der Hilst & H. Kárason (2001), Comparing P and S wave heterogeneity in the mantle, *Geophys. Res. Lett.*, *28*(7) 1335-1338.

Shapiro, N.M. & M.H. Ritzwoller (2002), Monte-Carlo inversion for a global shear-velocity model of the crust and upper mantle, *Geophys. J. Int.*, *151*, 88-105.

Simmons, N.A., A.M. Forte & S.P. Grand (2006), Constraining mantle flow with seismic and geodynamic data: A joint approach, *Earth Planet. Sci. Lett.*, *246*(1-2), 109-124.

Simmons, N.A., A.M. Forte & S.P. Grand (2007), Thermochemical structure and dynamics of the African superplume, *Geophys. Res. Lett. 34*(2), L02301, doi: 10.1029/2006GL028009.

Solheim, L.P. & W.R. Peltier (1994), Avalanche effects in phase transition modulated thermal convection: a model of Earth's mantle, *J. Geophys. Res. 99*, 6997-7018.

Spakman, W. & G. Nolet (1988), Imaging algorithms, accuracy and resolution in delay time tomography, in "Mathematical Geophysics" (eds. Vlaar, Nolet, Wortel and Cloetingh), *D. Reidel Publishing Company*, pp. 155-187.

Su, W. & A.M. Dziewonski (1997), Simultaneous inversion for 3-D variations in shear and bulk velocity in the mantle, *Phys. Earth Planet. Inter.*, *100*(1-4), 135-156.

Tackley, P.J., D.J. Stevenson, G.A. Glatzmaier & G. Schubert (1994), Effects of multiple phase transitions in a three-dimensional spherical model of convection in Earth's mantle, *J. Geophys. Res. 99*, 15877-15901.

Tackley, P.J. (2000), Mantle convection and plate tectonics: toward an integrated physical and chemical theory, *Science 288*, 2002-2007.

Tackley, P.J. (2002), Strong heterogeneity caused by deep mantle layering, *Geochem. Geophys. Geosys.*, *3*, doi: 10.1029/2001GC000167.

Tan, E., & M. Gurnis (2005), Metastable superplumes and mantle compressibility, *Geophys. Res. Lett.*, *32*, doi: 10.1029/2005GL024190.

Thompson, P.F. & P.J. Tackley (1998), Generation of mega-plumes from the core-mantle boundary in a compressible mantle with temperature-dependent viscosity, *Geophys. Res. Lett.*, *25*(11), 1999-2002.

Thorne, M.S., E.J. Garnero & S.P. Grand (2004), Geographic correlation between hot spots and deep mantle lateral shear-wave velocity gradients, *Phys. Earth. Planet. Int.*, *146*, 47-63.

Thoraval, C. & P. Machetel (1995), Locally layered convection inferred from dynamic models of the Earth's mantle, *Nature 375*, 777-780.

Trampert, J., F. Deschamps, J. Resovsky & D. Yuen (2004), Probabilistic tomography maps chemical heterogeneities throughout the lower mantle, *Science*, *306*(5697), 853-856.

Van der Hilst, R.D., S. Widiyantoro & E.R. Engdahl (1997), Evidence for deep mantle circulation from global tomography, *Nature*, *386*, 578-584.

Van der Hilst, R.D. & H. Kárason (1999), Compositional heterogeneity in the bottom 1000 kilometers of the Earth's mantle: Toward a hybrid convection model, *Science*, *283*, 1885-1888.

Wen, L. & D.L. Anderson (1997), Layered mantle convection: a model for geoid and topography, Earth Planet. *Sci. Lett. 146,* 367-377.

Wen, L.X. (2001), Seismic evidence for a rapidly varying compositional anomaly at the base of the Earth's mantle beneath the Indian Ocean, *Earth Planet. Sci. Lett.*, *194*(1-2), 83-95.

Woodhouse, J.H. & A.M. Dziewonski (1984), Mapping the upper mantle; three-dimensional modeling of Earth structure by inversion of seismic waveforms, *J. Geophys. Res.*, *89*, 5953-5986.

Zhao, D. (2001), Seismic structure and origin of hotspots and mantle plumes, *Earth Planet. Sci. Lett. 192*, 251-265.

Zhou, H. & R.W. Clayton (1990), P and S wave travel-time inversions for subducting slab under the island arcs of the northwest Pacific, *J. Geophys. Res. 95*, 6829-6851.

Vita

Nathan Alan Simmons was born in Dallas, Texas on September 20, 1975, the son of Valerie Hawkinson and Joseph Simmons. He was raised on farms and ranches throughout northeast Texas. He completed high school in Kaufman, Texas and entered Texas Tech University in 1994 where he received a Bachelor of Science degree in field of geological sciences in 1998. He continued his studies at Texas Tech and completed his Master of Science degree in geophysics in 2000. After leaving Lubbock, Texas in 2000, he entered the Graduate School of the University of Texas at Austin where he continued studying Earth's internal structure.

Permanent Address: 8913 Taline Circle, Austin, Texas 78748

This dissertation was typed by the author.